Accepted by the Graduate Faculty, Indiana University, in partial fulfillment of the requirements for the degree of Doctor of Philosophy.

Andrzej T. Zieminski, Ph.D.

Benjamin B. Brabson, Ph.D.

Doctoral Committee

Roger G. Newton, Ph.D.

Daria B. Zieminska, Ph.D.

27 June 1996

To Grandpa's Memory

Para mis queridos padres
afectuosas hermanas y
cariñosos sobrino y sobrina

Acknowledgements

The completion of a doctoral degree is a grand individual accomplishment, however it is a goal not achieved alone. Professional assistance and personal support from many people are required to complete the degree. With utmost humility, I shall attempt to thank those people who helped me fulfill my dream of becoming a scientist.

To thank my family with words on this page would never truly convey the gratitude I feel in my heart and soul. Without their unyielding love and support throughout my entire life I would not have become the person I am today. To genuinely thank my parents, sisters, nephew and niece I must honor them with my best as a person. *Recuerda, mi vida siempre será tuya.*

This thesis would not have been attempted, nevermind completed, if it was not for Christopher R. Murphy—the person who inspired me to continue my graduate studies, and who served as my role model and mentor. Chris was a valuable resource throughout my graduate career. His physics intuition and knowledge clarified many of my misunderstandings, and his meticulous methodical research skills were my example for scientific integrity. Above all, Chris is an exceptional person. His friendship helped me maintain my sense of humor and sanity throughout our stay at *FermiHell.* Thank you "compadre"!

Of all the lessons I have learned in life, the importance of friendship has been the most valuable. I have been extremely lucky during my graduate school years to have made many dear and close friends. They are...Todd Foxford for being the brother I never had, and understanding my unique sense of humor and mental state. Shanna Bunce for her example of strength and perseverance. Janet Lee for being a great pen-pal with timely words of support. Jon Schuler for being himself. Regina Demina, Sergey Korjenevski and Polina Raye Demina for welcoming me into their family. "Lord" Jim Cochran for sharing an important interest and certain perspectives on life. Paul Russo for his tolerance of my insenitivity and his help with all my computer related questions. Christine Tarazi for being my confidant and social coordinator. Jamal Tarazi for his infectious enthusiasm and optimism. Greg Griffin for being my "partner in crime". Elizabeth Brillhart for being a beacon of light. Terry and Molly Geld for accepting me.

Many others I would like to thank are the "insuffer-abulls": Ssu-Min Chang, Freedy Nang, David Cullen-Vidal, and Cary Yoshikawa. All of my sailing buddies, in particular Rich Astur and Terry Heuring. My cultural brothers: José Luis González, Leonel Magaña, Alberto Sánchez-Hernández and Raul Hernandez Montoya. John Balderston for our excellent adventure to L.A. The Northeastern Persian connection: Erfan Amidi and Hossein Johari. Bruce Hoeneisen for personifying the scientific ideal. The other Run 1A b-physics students (John Balderston, Regina Demina, David Fein, Thorsten Huehn, Eric James, Guilherme Lima, Chris Murphy, Vitor Oguri, Alex Smith) for accomplishing almost the impossible with the data given to us. Joey Thompson for being an exemplary human being. Elizabeth Gallas for her great MTC package and warm smile. Kathy Streets for her outgoing nature. Srini Rajagopalan for his sense of humor and laugh. Bob Kehoe for being so "special". Jan and Joan Guida for always taking an interest in my work and well being. The Fermilab gym rats: Ray Fonseca, Dale Knapp, and Carl Penson. Importantly,

the 1995–1996 Fermilab Indoor Soccer League Champions PRERNA[1].

Naturally, this thesis would not have been possible without the assistance of many individuals for their technical expertise. First, the many members of the DØ collaboration in building, testing and monitoring the detector. In particular, Jan and Joan Guida for their never ending dedication to the smooth data collection throughout Run 1. Susumu Igarashi for being the first to help me get started with the analysis of dimuons. Lee Leuking for being patient in helping me stream the B2M data set. The b-physics group for their support, especially Marc Baarmand, Dave Hedin, Arthur Maciel and Ken Johns. Furthermore, Andrzej Zieminski for supervising my research and demonstrating great patience throughout the years we worked together.

I would like to thank the remaining members of my doctoral committee, Benjamin Brabson, Roger Newton and Daria Zieminska, for performing their committee responsibilities conscientiously.

The Fermilab security force for making my stay at Fermilab interesting.

The administrative assistance of Beverly Carson and June Dizer in minimizing the Indiana University bureaucracy in my life was greatly appreciated. Finally, I would like to thank the Indiana University Department of Physics for giving me the opportunity to pursue my dream.

[1] See appendix B.

BEAUTY AT DØ

Gene Álvarez

Department of Physics
Indiana University
Bloomington, Indiana 47405

Abstract

We have studied the bottom quark production in $p\bar{p}$ collisions at $\sqrt{s} = 1.8$ TeV. The results are based on 6.73 pb^{-1} of data collected by the DØ detector at the Fermi National Accelerator Laboratory Tevatron collider. The $b\bar{b}$ events were identified by the presence of two or three energetic muons in the final state. We measure the inclusive b-quark and the $b\bar{b}$ correlated production cross sections, analyze event topologies and search for high mass resonances decaying into $b\bar{b}$ pairs. Our measurements are compared to Next-to-Leading-Order Quantum Chromodynamics (NLO QCD) calculations and are used to extract the strong coupling constant, α_s.

Contents

List of Figures

List of Tables

Chapter 1

INTRODUCTION

"Science walks forward on two feet, namely theory and experiment. Sometimes it is one foot which is put forward first, sometimes the other, but continuous progress is only made by the use of both—by theorizing and then testing, or by finding new relations in the process of experimenting and then bringing the theoretical foot up and pushing it on beyond, and so on in unending alternations." Robert Millikan

Physics is the science that endeavors to comprehend the structure of matter and the interactions between the fundamental constituents of the observable universe—to discover and formulate the fundamental laws of nature. In the broadest sense physics (from the Greek physikos), which was long called natural philosophy, is concerned with all aspects of nature from the macroscopic down to the submicroscopic levels. Its scope of study encompasses not only the behaviour of objects under the action of given forces but also the nature and origin of the forces. Physics ultimate objective is the formulation of a few comprehensive principles that bring together and explain all disparate physical phenomena, *i.e.* a unified set of laws, typically expressed with economy and precision in the language of mathematics, governing energy, matter and motion.

1.1 A Brief History of Particle Physics

A branch of contemporary physics is the study of the fundamental subatomic constituents of matter, the elementary particles. This field, also called high-energy physics,

emerged in the 1930s out of the developing experimental areas of nuclear and cosmic-ray physics. In the proceeding sections we will give a brief historical overview of the intellectual development to determine the composition of matter.

1.1.1 Ancient Greece

Physics was derived from the rationalistic materialism [1] that emerged in classical Greece, itself an outgrowth of ancient Greece's magical and mythical views of the world. The Greek philosophers of the 6th and 5th centuries BC abandoned the animism[1] of the poets and explained the world in terms of ordinarily observable natural processes. These early philosophers posed the broad questions that still underlie physics (and all of science) [1]: *How did the world order emerge from chaos? What is the origin of multitude and variety in the world? How can motion and change be accounted for? What is the underlying relation between form and matter?* Greek philosophy answered these questions in terms that provided the framework for science for approximately 2000 years.

Two physical theories emerged from ancient Greece. First, attempting to reconcile the differences between the underlying unity and apparent multitude and diversity of nature, the Greek atomists Leucippus (mid-5th century BC), Democritus (late 5th century BC), and Epicurus (late 4th and early 3rd century BC) asserted that nature consisted of *atoma* (things too minute to be visible that cannot be cut or divided) moving in empty space. According to this theory, the various motions and configurations of atoms and clusters of atoms are the causes of all the phenomena of nature[2]. The Greek atomists took a general view of nature which fostered a *scientific attitude*[3]. Third, Aristotle (mid-3th century BC) had regarded the four elements earth, water, air, and fire as the constituents of all things.

[1] The belief that all natural objects and the universe itself possess a soul.

[2] Other forms of atomism existed and differed mainly in two points. First, some atomists did not restrict the differences between the atoms to purely quantitative ones but accepted also differences in quality. Secondly, some atomists regarded atoms as divisible.

[3] Objective experimentation and reproduction of experimental measurements.

Transmutable each into the other, all four elements were believed to exist in every substance.

1.1.2 First Scientific Revolution

The reintroduction of Epicurus' atomic theory of matter[4] [1] in Lucretius' *De rerum natura*, by Pierre Gassendi in 1649, galvanized the first revolution of scientific thought during the 15th century, which subsequently cascaded into the following two centuries. A new view of nature emerged—the rational and the empirical. Science became an autonomous discipline, distinct from philosophy, having pragmatic goals. From the womb of the Renaissance and Reformation came forth a new sense of science, bringing about the following changes [2]: the reeducation of common sense in favor of abstract reasoning; the substitution of a quantitative for a qualitative view of nature; the view of nature as a machine rather than as an organism; the development of an experimental method that sought definite answers to certain limited questions within in the framework of specific theories; the acceptance of new criteria for explanation, stressing the "how" rather than the "why" that had characterized the Aristotelian way of thought.

The work of Sir Isaac Newton at the end of the 17th century represents the culmination of the first scientific revolution. His monumental work, *Philosophiae Naturalis Principia Mathematica*, solved the major problems posed by the scientific revolution in mechanics and in cosmology[5]. By means of the concept of *force*, Newton was able to synthesize two important components of the scientific revolution, the mechanical philosophy and the mathematization of nature [3]. In his other seminal work, *Opticks*, Newton expressed the typical 18th century view of the atom[6]:

[4] Epicurus combined moral urgency, intellectual force, and precise observation of the physical world to argue men should be free from superstition and the fear of death.

[5] Newton provided a physical basis for Kepler's laws, unified celestial and terrestrial physics under one set of laws, and established the problems and methods that dominated much of astronomy and physics for well over a century.

[6] After Robert Boyle comprehensive study of air in 1658, he explained that all things are "made of one Catholick Matter common to them all, and...differ but in the shape, size, motion or rest, and texture of the small parts they consist of."

> "All these things being considered, it seems probable to me that God in the Beginning form'd Matter in solid, massy, hard, impenetrable, moveable Particles, of such Sizes and Figures, and with such other Properties, and in such Proportion to Space, as most conduced to the End for which he form'd them; and that these primitive Particles being Solids, are incomparably harder than any porous Bodies compounded of them; even so very hard, as never to wear or break in pieces; no ordinary Power being able to divide what God himself made one in the first Creation."

Therefore, by the 17th century it was generally accepted that all matter was composed of solid indivisible particles arranged into molecules to give materials their different properties.

A prelude to the second Scientific Revolution, to be discussed in the next section, was the fundamental revision of the theories of electricity, magnetism and light by Michael Faraday and James Clerk Maxwell in the mid 1800s. Their views were the first recension of the Newtonian framework for physical science. Faraday's extraordinary insight led him to propose that magnetic force was composed of field lines emanating from and concluding with the magnetic object. Thus, Faraday introduced the concept of *fields*. Furthermore, Faraday declared that electrical and magnetic forces were not transmitted instantaneously but required a finite time of transmission. Maxwell's contribution was expressing Faraday's physical intuition about electricity and magnetism into the language of mathematics which linked the rudiments of electricity and magnetism into the theory of *electromagnetism*, and the connection of eletromagnetism with the speed of light.

The seminal works of Faraday and Maxwell greatly influenced the development of particle physics, however not immediately. The adaption of Faraday's idea that forces propagate via fields and Maxwell's example of the unification of two apparently different physical phenomenoa led the way to revolutionary approaches in the theoretical developments describing

matter in the 20th century.

1.1.3 Second Scientific Revolution

During the years 1896–1932 the foundations of physics changed so radically that this period began the second most important scientific revolution in human history. The 20th-century revolution changed many of the ideas about space, time, mass, energy, atoms, light, force, determinism, and causality that had apparently been firmly established by Newtonian physics during the 18th and 19th centuries.

The discovery of radioactivity by the French physicist Henri Becquerel in 1896 is generally regarded as the beginning of 20th-century physics. The successful isolation of radium and other radioactive substances by Marie and Pierre Curie focused the attention of scientists to radioactivity and promoted a wide range of experiments, many of which addressed the question of "*What is matter made of?*".

At the University of Manchester (England), Ernest Rutherford led a group that developed a new theory about atomic structure. Based on an experiment conducted by Hans Geiger and Ernest Marsden, Rutherford scattered alpha particles on a thin film of gold. From the results he proposed a nuclear model of the atom (1911). In this model, Rutherford purported that the atom consisted mostly of empty space, with a tiny, positively charged nucleus that contains most of the mass, surrounded by one or more negatively charged electrons[7].

The Danish physicist Niels Bohr pioneered the use of Max Planck's quantum hypothesis[8] (1900) in developing a successful theory of atomic structure. Adopting Rutherford's nuclear model, Bohr proposed in 1913 that the atom is like a miniature solar system, with the electrons moving in orbits around the nucleus just as the planets move around the Sun. Al-

[7]Discovered in 1897 by J. J. Thompson [69].

[8]A blackbody only emits and absorbs energy in *quanta* of energy—in discrete amount of energy.

though the electrical attraction between the electrons and nucleus is mathematically similar to the gravitational attraction between the planets and the Sun, the quantum hypothesis was needed to restrict the electrons to certain orbits and to forbid them from radiating energy except when jumping from one orbit to another. In that same year, Henry G. J. Moseley, an English physicist, demonstrated that the systematic increase of X-ray energies with atomic number was explained by Bohr's atomic structure proposition.

Bohr's model provided a good description of the spectra and other properties of atoms containing only one electron—neutral hydrogen and singly ionized helium—but could not be satisfactorily extended to multi-electron atoms or molecules. The model relied on an inconsistent mixture of old and new physical principles, hinting but not clearly specifying how a more adequate general theory might be constructed.

In 1926 the Austrian physicist Erwin Schrödinger developed an equation that yielded the properties of the hydrogen atom but it also allowed the use of simple approximating methods for more complicated systems even though the equation could not be solved exactly. Schrödinger's equation was the birth of quantum mechanics. Essentially a wave equation, the Schrödinger equation describes the form of the probability waves (or wave functions) that govern the motion of small particles, and it specifies how these waves are altered by external influences. Later in 1926, the German physicist Werner Heisenberg proposed an alternate mathematical approach to describe atomic phenomena. Heisenberg's theory was called *matrix mechanics*. The significant consequence of Heisenberg's theory was the realization that position and momentum of a particle cannot be determined exactly. This is called the *uncertainty principle*[9]. Heisenberg's work established the physical basis of quantum mechanics.

[9]Mathematically, the uncertainty principle is written as

$$\Delta p \Delta q \geq \hbar,$$

where $\hbar$ is Planck's constant divided by 2π.

The next great intellectual advancement came in 1927 when P. A. M. Dirac combined the theory of relativity and electrodynamics with quantum mechanics. Dirac's union of two of the most recent theories of his time laid the foundation of modern high energy physics—quantum field theory. Developments came quickly after Dirac unified the theory of radiation with his relativistic theory of the electron thus creating *Quantum Electrodynamics* (QED). A revolutionary consequence of Dirac's theory was the prediction of the *positron*[10]—identical to the electron but opposite in charge. This led to the general concept of *antimatter.* In 1949, Feynman, Schwinger and Tomonaga demonstrated the computational power and conceptual scope of QED by extracting meaningful physical information from the theory. For example, QED's prediction of the interaction between electrons and photons agrees with experimental measurements to within one part in 10^8.

The successful application of quantum field theory to describe the electromagnetic force encouraged physicists to apply this physical framework to the weak and strong forces. However, one problem prevented progress. The theories were plagued by infinities. QED had its infinities but they were resolved in 1949. Theoretical progress was slowed down until 1971 when G. 't Hooft, then a graduate student, proved that Yang-Mills gauge theories—a particular type of quantum field theory—were *renormalizable.* In other words, the infinities can be dealt with. This important breakthrough lead to tremendous developments in understanding the weak and strong forces.

During recent decades a coherent picture has evolved of the underlying structure of matter involving three types of particles called *leptons, quarks* and *field quanta.* The theoretical framework which encompasses the three constituents of matter is called the Standard Model.

[10]The positron was discovered in 1932 [4].

1.2 Our Present Day Understanding of Matter

Ordinary matter consists of electrons surrounding the nucleus, which is composed of neutrons and protons, each of which contain three quarks. Leptons and quarks occur in pairs, *e.g.* one lepton pair consists of the electron and the neutrino. Each quark and each lepton have an antiparticle with properties that mirror those of its partner. Quarks have charges that are either positive two-thirds or negative one-third of the electron charge, while antiquarks have the opposite charges. In addition to the particles in ordinary matter and their antiparticles, which are referred to as the first generation, there are two additional generations of quarks and leptons, more massive than the first. Evidence exists for the second and third generation. In addition to their electric and magnetic properties, quarks have strong nuclear forces and also participate in the weak nuclear interaction, while leptons take part in only the weak interaction.

The quantum fields through which quarks and leptons interact with each other and with themselves consist of particle like objects called quanta. The first known quanta were those of the electromagnetic field—the photons. A modern unified theory of weak and electromagnetic interactions, known as the electroweak theory, proposes that the weak nuclear interaction involves the exchange of particles about 100 times as massive as protons. These massive quanta have been observed[11]—namely, two charged particles, W^+ and W^-, and a neutral one, Z°.

In the theory of strong nuclear interactions known as Quantum Chromodynamics (QCD), eight quanta, called gluons, bind quarks to form protons and neutrons and also bind quarks to antiquarks to form mesons, the force itself being dubbed the *color force.* Quarks are said to come in three colors—red, blue, and green. Only certain color combinations, namely color neutral, or "white", *i.e.* mixtures of three colors or color anticolor pairs, cancel out

[11] In 1983 [5].

one another resulting in no net color, are conjectured to exist in nature in an observable form. The gluons and quarks themselves, being colored, are permanently confined (bound within the particles of which they are a part), while the color-neutral composites such as protons can be directly observed. One consequence of color confinement is that the observable particles are either electrically neutral or have charges that are integral multiples of the charge of the electron. A number of specific predictions of QCD have been experimentally tested and found correct. In the next chapter a brief account of our current understanding of QCD and discussion of a few experimental measurements that verify the theory's predictive power will be presented.

1.3 The Aim of This Thesis

Both experiment, the observation of phenomena under conditions that are controlled as precisely as possible, and theory, the formulation of a conceptual framework, play essential and complementary roles in the advancement of physics. Physical experiments result in measurements, which are then compared to theoretical predictions. A theory that reliably predicts the results of experiments to which it is applicable is said to embody a law of physics. However, a law is always subject to modification, replacement, or restriction to a more limited domain, if a later experiment makes it necessary.

Continuing in the tradition of our ancient forefathers—to understand what is matter—, the aim of this thesis was to test our present understanding of nature. QCD describes the force that binds quarks and gluons together. Bound states of quarks and gluons decay into various different types of particles, in particular leptons. Leptons are readily experimentally observable due to their unique physical characteristics. As a result, leptons are used to identify decayed quarks. In the case of the b-quark, it decays approximately 20% of the time into a lepton. Occasionally, quarks decay into two leptons. Our research rests upon

the identification of multilepton events, namely events with two and three muons. From our multimuon sample, the author will present various experimental results which corroborate QCD. In particular, the analyses carried out by the author have achieved:

1. An understanding of the different dimuon production mechanisms;
2. Measurement of the b-quark production cross section;
3. A quantitative separation of leading-order and next-to-leading-order QCD processes of b-quark production using dimuons as a b-quark tag;
4. The identification of $b\bar{b}$ states with trimuon events;
5. The verification of the "running nature" of the strong coupling constant.

The author has concluded that his thesis results add to the confirmation of QCD's remarkable description of nature.

Chapter 2

THEORETICAL SURVEY

> *"One should try to construct a theory in terms of quantities which are provided by experiment, rather than building it up, as people had done previously, from an atomic model which involved many quantities which could not be observed."* Werner Heisenberg

Quantum Field Theory (QFT) is the most successful conceptual framework describing particle physics. Dirac's [6] union of nonrelativistic quantum mechanics with the special theory of relativity and electrodynamics laid the foundation of modern high energy physics. One can argue their merger was natural because particle physics is concerned with the quantum of action and the finite speed of light. The application of QFT ideas have lead to the description of three of the four known fundamental forces in nature. The theory which explains the subatomic forces is called the Standard Model (SM). In this chapter we will briefly discuss the SM and its implication to heavy quark production.

2.1 An Overview of The Standard Model

The Standard Model is a Quantum Field Theory based on the idea of *local gauge invariance*[1][7, 8]. The gauge symmetry group of the SM is $SU(3)_C \times SU(2)_L \times U(1)_Y$, where $SU(3)_C$ and $SU(2)_L \times U(1)_Y$ are the respective symmetry groups describing the strong and electroweak interactions.

[1]The Lagrangian is invariant under a transformation that changes at every space-time point.

There are two general classes of particles in the theory: 1) fermions which have spin $\frac{1}{2}$; and 2) gauge vector bosons which have spin 1. Fermions are further subdivided into particles called leptons and quarks. Leptons and quarks are grouped into three families, or generations, with each family consisting of two members. Quarks may exist in one of three color states—an internal degree of freedom. Because of their color property, the theory which describes the strong interaction between the quarks is named *Quantum Chromodynamics* (QCD). Tables 2.1 and 2.2 summarizes the basic properties of leptons and quarks.

Lepton	Charge	Mass (MeV/c^2)
Electron (e)	-1	0.511
Electron Neutrino (ν_e)	0	$< 7.3 \times 10^{-3}$
Muon (μ)	-1	105.7
Muon Neutrino (ν_μ)	0	< 0.27
Tau (τ)	-1	1784
Tau Neutrino (ν_τ)	0	< 35

Table 2.1: Lepton Properties

Quark	Charge	Mass (GeV/c^2)
Down (d)	$-1/3$	0.005–0.015
Up (u)	2/3	0.002–0.008
Strange (s)	$-1/3$	0.1–0.3
Charm (c)	2/3	1.3–1.7
Bottom (b)	$-1/3$	4.7–5.3
Top (t)	2/3	166–184

Table 2.2: Quark Properties

Local gauge invariance requires the introduction of massless vector gauge bosons—the particles that mediate the force between the particles. For the strong force, the quarks interact via the gauge bosons of $SU(3)_C$ called gluons. In total, there are eight gluons. Due to the non-abelian nature of the color symmetry gluons are allowed to interact among themselves. The observed strongly interactive particles in nature are called hadrons, which themselves are classified into mesons (quark-antiquark pairs) and baryons (triplets of quarks). How-

ever, up to now no free quarks have been observed. Consequently, it is hypothesized that only color singlet states exist in nature (this will be expanded in Section 2.2.3).

The Electroweak sector of the SM unites the weak and electromagnetic interactions [9] and it has four gauge vector bosons. In order to describe the weak force phenomenology, it is required that some of the vector bosons acquire a nonzero mass. The masses are generated by *spontaneously breaking* the symmetry of the $SU(2)_L \times U(1)_Y$ group. This is implemented by the Higgs Mechanism [10] via the introduction of complex scalar fields. By allowing the scalar field to acquire a nonzero vacuum expectation value, three of the four vector gauge bosons gain mass. The three bosons are identified as follows: a) two that mediate charged current weak interactions ($W^{\pm}$); and b) one that mediates neutral current weak interactions (Z^0). The remaining massless gauge boson mediates the electromagnetic interactions—the photon. However, one neutral scalar field remains from the broken symmetry called the Higgs boson. To date, the Higgs boson has not been observed.

2.2 Quantum Chromodynamics

Quantum Chromodynamics (QCD) is a gauge field theory of the strong interaction between quarks and gluons. The $SU(3)$ color symmetry group provided an explanation for the interaction quarks, whereas the gluons mediate the force between quarks. In the proceeding sections we will discuss various aspects of QCD.

2.2.1 Renormalization

Quantum Field Theory has a serious complication. Namely, the theory is divergent. When higher order corrections are calculated one finds that the integrals diverge in the ultraviolet region corresponding to large momentum p. The divergent nature of QFT reflects the fact that the divergent graphs probe extremely small distance region of space-time, or equivalently, the high momentum region. Because almost nothing is known about the nature

of physics at very small distances "we are disguising our ignorance of this region by cutting off the integrals at small distances" [11]. However, not all is lost. One can manipulate these infinite quantities such that the divergent integrals are absorbed into an infinite rescaling of the coupling constants and masses of the theory. This is called *renormalization.*

Although renormalization schemes differ in their approach, the essential idea is that there is a set of bare physical parameters that are divergent, such as the coupling constants and masses. However, these bare parameters are unmeasurable. The divergences of these parameters are chosen so that they cancel against the ultraviolet infinities coming from infinite classes of Feynman diagrams, which probe the small distance behavior of the theory. After these divergences have been absorbed by the bare parameters we are left with the physical, "renormalized", parameters that are measurable. Since there are a finite number of bare physical parameters one is only allowed to make a finite number of such redefinitions. Hence, Renormalization Theory is a set of rules where, after a finite number of redefinitons, one can render the theory finite to any order. One must note that renormalization is necessary even if the theory has no divergences because the bare parameters are unmeasureable. Renormalization results in observable quantities [12].

Two commonly used renormalization schemes are the *minimal subtraction scheme* (MS) and the *modified minimal subtraction scheme* ($\overline{\text{MS}}$). The two schemes are linked to *dimensional regularization*[2]. These schemes produces the function β (to be discussed in Section 2.2.3) independent of the renormalized mass. The difference between MS and $\overline{\text{MS}}$ is how the schemes handle the poles in complex d.

A significant breakthrough in physics occurred in 1971 when G. 't Hooft [18] proved that

[2]The internal momenta over which one has to integrate in a Feynman diagram are taken to have d components. After certain formal manipulations it is possible to interpret the result as holding for arbitrary complex d. For small enough d the result is finite and the divergences that one originally had when $d = 4$ now show up as singularities when one continues analytically in d up to $d = 4$. These singularities can be eliminated by allowing the parameters of the theory to depend on d. In fact, the integrals are regularized with a dimensionless parameter ϵ defined to be $\epsilon = \frac{1}{2}(4 - d)$ [16].

spontaneously broken Yang-Mills [8] theory was renormalizable. This monumental success led to the successful application of QFT to the weak interaction (Electroweak Theory) and the strong interaction (Quantum Chromodynamics).

2.2.2 Renormalization Group Equations

The renormalization group equations constrain the renormalized vertex functions [83]. They are based on the simple observation that the physical theory cannot depend on the subtraction point μ at which one regularizes the theory. μ was introduced purely as a mathematical device to begin the process of renormalization and that no physical consequences can emerge from the subtraction point. This implies that in order to keep the physics invariant, the subtraction point must be offset by changes in the renormalized physical parameters, such as the masses and the coupling constant, as a function of the energy.

Without going into the details of its derivation (the reader is referred to [22]), the renormalization group equations for QCD[3] is

$$\left(\mu\frac{\partial}{\partial\mu}+2\beta\frac{\partial}{\partial\alpha_s}-n_A\gamma^A-n_\psi\gamma^\psi+2\gamma_{m_f}\frac{\partial}{\partial\ln m_f^2}\right)\Gamma^{(n_a,n_\psi)}\Big(p;\alpha_s(\mu^2),\mu,m_f\Big)=0\,. \quad (2.1)$$

Γ^n are the "amputated" n-leg momentum space Green's Functions G^n. What is meant by amputated is that Γ^n are the G^n without the propagators for the external legs. μ is the arbitrary mass parameter for the renormalization scheme. The Γ^n are functions of momentum p, the coupling constant α_s, μ and the bare mass of a quark of flavor f.

n_A and n_ψ specify the number of gluon and quark fields. Both fields are renormalized as

$$\begin{aligned}\psi_B &= Z_\psi^{\frac{1}{2}}(\lambda)\psi\\ (A_B^a)_\mu &= Z_A^{\frac{1}{2}}(\lambda)A_\mu^a\,,\end{aligned} \quad (2.2)$$

[3] In the Landau gauge, $\partial_\mu A^\mu = 0$.

where λ is the regularization cutoff, and A^a_μ is the gluon vector potential, with the octet color labeled $a = 1 \ldots 8$. β is defined to be

$$\beta\left[\alpha_s(\mu^2)\right] = \frac{\mu}{2}\frac{\mathrm{d}\alpha_s(\mu^2)}{\mathrm{d}\mu}\,, \tag{2.3}$$

while γ^A, γ^ψ and γ_{m_f} are

$$\gamma^A = \frac{\mu}{2}\frac{\mathrm{d}\ln Z_A}{\mathrm{d}\mu} \qquad \gamma^\psi = \frac{\mu}{2}\frac{\mathrm{d}\ln Z_\psi}{\mathrm{d}\mu} \qquad \gamma_{m_f} = \frac{\partial \ln m_f^2}{\partial \ln \mu^2}\,. \tag{2.4}$$

The importance of the renormalization group equations 2.1 is that they show how the renormalized functions change as one varies the subtraction point μ. The renormalization group equations perform the book-keeping necessary to keep track of how the renormalized coupling constant and masses change when μ changes.

2.2.3 The Running of Alpha Strong

From our perspective, the most important function of 2.1 is β. Knowledge of β determines the behavior of the coupling constant as a function of the mass scale.

Re-expressing Equation 2.3 and performing the integration one has

$$\ln\left(\frac{\mu^2}{\mu_\circ^2}\right) = \int_{\alpha_s(\mu_\circ^2)}^{\alpha_s(\mu^2)} \frac{\mathrm{d}\alpha_s}{\beta(\alpha_s)}\,. \tag{2.5}$$

Equation 2.5 expresses the exact relationship between couplings defined at scales μ and $\mu_\circ$.

Expanding β in a Taylor series of α_s

$$\beta(\alpha_s) = -b\alpha_s^2[1 + b'\alpha_s + \cdots]\,,$$

substituting the expansion into the integral Equation 2.5, and integrating to lowest order we arrive at

$$\alpha_s(\mu^2) = \frac{\alpha_s(\mu_\circ^2)}{1 + b\alpha_s(\mu_\circ^2)\ln(\mu^2/\mu_\circ^2)}\,, \tag{2.6}$$

where b is a constant determined from the structure constants f_{abc} of the $SU(3)_C$ group. The value for b is

$$b = \frac{11N_C - 2N_f}{12\pi} = \frac{33 - 2N_f}{12\pi} . \tag{2.7}$$

The b' in the expansion of β is another constant which depends on f_{abc}. Its value is

$$b' = \frac{153 - 19N_f}{2\pi(11N_C - 2N_f)} = \frac{153 - 19N_f}{2\pi(33 - 2N_f)} . \tag{2.8}$$

N_C is the number of colors and N_f is the number of light flavors. Terms proportional to N_f can be traced back to vacuum polarization due to quark loops, while term proportional to N_C correspond to vacuum polarization due to gluon loops involving the non-abelian three gluon vertex [27].

Equation 2.6 shows that as μ^2 increases $\alpha_s(\mu^2)$ decreases—*running of the coupling constant.* This important property, known as asymptotic freedom, was first recognized by Gross, Wilczek, and Politzer [19], and independently by 't Hooft [20], as being a consequence of the non-abelian nature of QCD (and for all renormalizable gauge theories). Asymptotic freedom allows the treatment of quarks and gluons as effectively free particles in high energy collisions. In Section 10.4 we will demonstrate with DØ's inclusive b-quark production cross section the running nature of α_s. Our measurement improves upon UA1's published result [21].

In addition, for standard QCD ($N_C = 3$ and $N_f = 3$–6) α_s increases with decreasing μ^2. This implies that α_s is not bounded for large distances and can exceed the value of one, therefore rendering perturbation theory meaningless. Nonperturbative calculations indicate that an infinite amount of energy is required to separate bound quarks and gluons from each other. Hence, quarks and gluons cannot exist as free particles but must be inevitably bound as color singlet states. This inseparablity is called *confinement.*

One can rewrite the leading order expression 2.6 as

$$\alpha_s(\mu^2) = \frac{1}{b\ln(\mu^2/\Lambda^2)}\,, \tag{2.9}$$

where

$$\Lambda^2 = \mu_o^2 \exp^{-1/b\alpha(\mu^2)}\,. \tag{2.10}$$

Λ is a parameter that tells one about the strength the QCD coupling. Naturally, Λ has to be found experimentally and its value will depend upon the number of flavors used in expression 2.7 for b. N_f is usually defined to become $N_f + 1$ when a heavy flavor threshold is crossed. α_s should be continuous across the threshold. Consequently, there are different values of Λ for the various energy regions where dissimilar numbers of light flavors are active. We will use throughout this thesis the number of light flavors to be five. Note that the value of α_s will depend on the renormalization scheme utilized.

For QCD, given that there is no specially favored scale at which one could define α_s, it is reasonable to regard Λ as the *fundamental measure* of the strong coupling. Therefore, one can give an exact definition by noticing that $\mu^2 = \Lambda^2$ corresponds to the point at which $\alpha_s(\mu^2) \to \infty$. Thus we can define Λ by

$$\ln\left(\frac{\Lambda^2}{\mu_o^2}\right) \equiv \int_{\alpha_s(\mu_o^2)}^{\infty} \frac{dx}{\beta(x)}\,. \tag{2.11}$$

In next-to-leading-order one has

$$\ln\left(\frac{\Lambda^2}{\mu_o^2}\right) = -\int_{\alpha_s(\mu_o^2)}^{\infty} \frac{dx}{bx^2(1+b'x)}\,. \tag{2.12}$$

Performing the integration yields

$$\frac{1}{\alpha_s(\mu_o)} + b'\ln\left[\frac{b'\alpha_s(\mu_o)}{1+b'\alpha_s(\mu_o)}\right] = b\ln\left(\frac{\mu_o}{\Lambda^2}\right) \tag{2.13}$$

from which a numerical value for α_s or Λ can be calculated given one of them. The Particle Data Group recommends the following solution to Equation 2.13

$$\alpha_s(\mu_o) = \frac{1}{b\ln(\mu_o/\Lambda^2)}\left\{1 - \frac{b'}{b}\frac{\ln[\ln(\mu_o/\Lambda^2)]}{\ln(\mu_o/\Lambda^2)}\right\}\,. \tag{2.14}$$

The corresponding expression for Λ is

$$\Lambda^2 = \mu_o \exp\left\{-\frac{1}{b}\left[\frac{1}{\alpha_s(\mu_o)} + b' \ln[b\alpha_s(\mu_o)]\right]\right\} . \tag{2.15}$$

2.2.4 The Naive Parton Model

If hadrons are thought of as atoms (or molecules), then inner structure probing at high energies and momentum transfers reveal a relatively simple picture of almost free (but nonetheless confined) point-like constituents. The idea that hadrons possess a structure is called the Parton Model (PM) [23]. The PM was motivated from the SLAC-MIT experiments of the late 1960s [24].

The PM assumes that at sufficiently high momentum transfer reactions the projectile sees the target hadron as made up of almost free components and is scattered by a single, free, effectively massless constituent. Moreover, the scattering from individual components is incoherent. In addition, the PM relates physically measurable high energy cross sections between interacting hadrons to theoretically calculable partonic cross sections through a set of parton distribution functions[4] (PDF). This is expressed as

$$\sigma_{AB}(p,p') = \sum_{ab} \int dx_a dx_b \hat{\sigma}_{ab}(x_a p, x_b p') f_{\frac{a}{A}}(x_a) f_{\frac{b}{B}}(x_b) , \tag{2.16}$$

where p is the momentum of hadron A which collides with hadron B having momentum p'. We sum over all partons of type a and b which contribute to the process for producing the desired final state. Furthermore, x_a represents the fraction of momentum of parton a within hadron A, and similarly for parton b and meson B. The f_i are the PDFs and $\hat{\sigma}_{ab}$ is the corresponding cross section for the scattering of partons a and b to produce the desired final state.

One can define a parameter Q^2 that is characteristic of the reaction. For example, one can take $Q^2 = -q^2$, where q is the momentum transfer between the two interacting

[4]Parton distribution functions describe the density distribution of the partons within the interacting hadrons.

particles with momenta k and k' respectively ($q^\mu = k^\mu - k'^\mu$). As one can readily see in Equation 2.16 the structure functions have no explicit dependence on the strength of the hard scattering Q^2. Therefore, the PM discussed thus far assumes that the structure functions are independent of Q^2; expressed differently, exact scaling holds [28]. We refer to this particular PM as the "Naive Parton Model". To account for scaling violations we need structure functions with Q^2 dependence. This is described by the "QCD Improved Parton Model".

2.2.5 QCD Improved Parton Model

The QCD Improved Parton Model allows one to express the hadronic cross sections as a product of the hard scattering parton subprocess cross section, computed up to a certain order in α_s, and the PDFs as a function of Q^2. Applying renormalization techniques, the Q^2 dependence of the structure functions are accounted for in the Altarelli-Parisi evolution equations [83]. These equations introduce the radiative corrections due to the interactions of the constituent quarks and gluons among themselves (gluon emission or splitting). Suppose $\Phi_{i/h}(x)$ represents a generic parton distribution function for partons of type i relative to hadrons h, then the evolution equations can be written as

$$\mu\frac{d}{d\mu}\Phi_{i/h}(x,\mu) = \sum_j \int_x^1 \frac{d\xi}{\xi} P_{ij}(\frac{x}{\xi}, \alpha_s(\mu))\Phi_{j/h}(\xi,\mu)\,, \tag{2.17}$$

where the evolution kernels $P_{ij}(x)$ are referred to as splitting functions and are given by perturbative expansions in α_s since the coupling constant is asymptotically free. The Q^2 dependence has been absorbed into μ—*factorization scale.* The factorization scale is an arbitrary parameter which is generally chosen to be of the order of the hard scale Q. Typically, the higher order corrections of the parton scattering cross section $\hat{\sigma}_{ij}$ are removed and factored into the parton functions. These corrections involve ratios of Q/m. Suppose we know $\Phi_{j/h}(\xi,\mu)$ for $\xi > x$ at some initial scale $\mu = Q_0$, then the evolution equations

allow us to calculate $\Phi_{j/h}(x,\mu)$ at a higher scale $\mu = Q$.

An application of the QCD improved parton model is the calculation of hadronic cross sections of heavy quarks.

2.2.6 Heavy Quark Production

The term "heavy flavor" refers to a parton with mass large compared to the QCD scale Λ. A heavy quark may be generated through electroweak interactions at lepton colliders or by deep inelastic scattering. At hadron colliders the production of heavy quarks is described by QCD. The creation of heavy quarks through the reaction $p\bar{p} \rightarrow Q\bar{Q}X$ is hypothesized to occur via the interaction of the partons of the colliding hadrons. These partons are the light valence quarks of the hadron and the *sea* quarks and gluons. In Electroweak Theory, the production of a heavy flavor occurs at a WQQ' or $ZQ\bar{Q}$ vertex, while QCD perturbation theory only allows a heavy quark pair to be produced from a gluon vertex.

The hard scattering cross section is usually expressed as a perturbative expansion in $\alpha_s(Q^2)$. At the parton level, the lowest order production of heavy quarks in a hadronic collision is given by two processes

$$q\bar{q} \rightarrow Q\bar{Q} \, ,$$

$$gg \rightarrow Q\bar{Q} \, .$$

The massive quark assures that the lowest order Feynman diagrams do not diverge and that perturbation theory is valid. The only ambiguities involve the choice of the renormalization/factorization scale and PDFs.

At higher orders, heavy quark production is non-negligible. In kinematic regimes where gluon distributions are large and gluon-gluon scattering is important, the production of $Q\bar{Q}$ pairs are significantly increased by gluon splitting in either the initial or final state. These events include the virtual corrections to the Born diagrams and incorporate the following

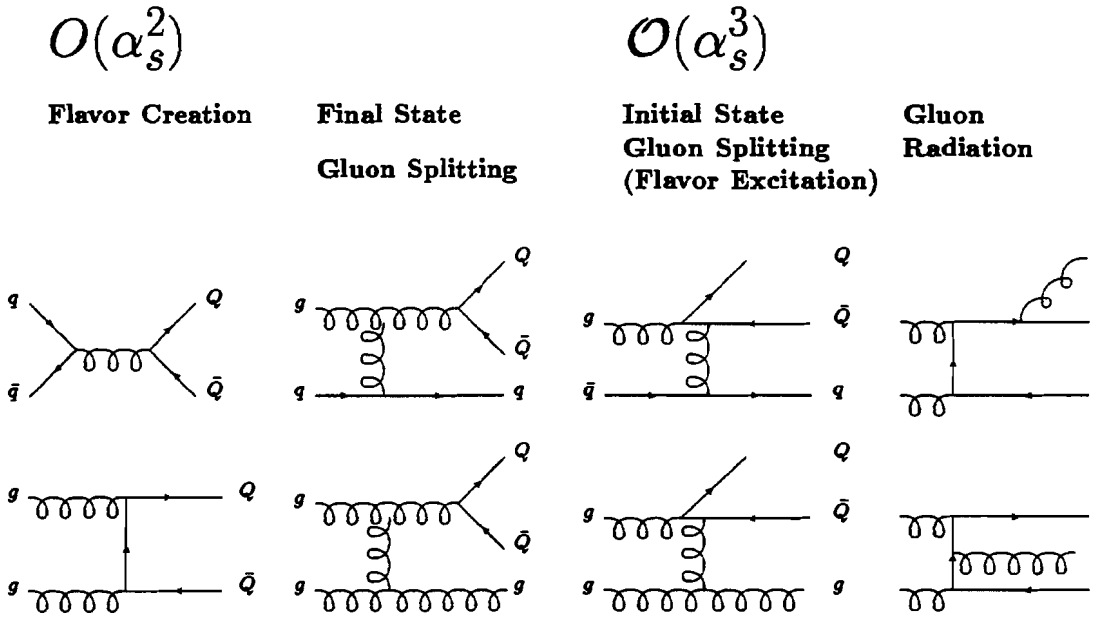

Figure 2.1: Feynman Diagrams for Leading-Order and Next-to-Leading Order Heavy Quark Production

processes

$$q\bar{q} \to Q\bar{Q}g\,,$$
$$gq \to Q\bar{Q}q\,,$$
$$g\bar{q} \to Q\bar{Q}\bar{q}\,,$$
$$gg \to Q\bar{Q}g\,.$$

A representative number of the leading-order and next-to-leading-order Feynman diagrams are shown in Fig. 2.1.

The analytic next-to-leading order $\mathcal{O}(\alpha_s^3)$ calculation for the production of heavy quarks was carried out by Nason, Dawson and Ellis (NDE) [25]. Virtual corrections include gluon loops and vertex corrections. NDE use two-loop structure functions in their calculation to maintain consistency with the $\mathcal{O}(\alpha_s^3)$ computation of the hard scattering cross section. Higher order contributions to the total heavy quark cross section were found to be important in two regions of parton center of mass energy $\hat{s}$: near threshold and very far above

threshold. The threshold effects are explained by initial state gluon radiation and Coulomb enhancement from the virtual gluon exchange between the heavy quarks. The enhancement of the cross section is due to the exchange of a spin 1 gluon in the $\hat{t}$ channel. Lowest order diagrams only have spin 1/2 exchange. The heavy flavor cross section changes only in the normalization, not the shape, between leading-order and next-to-leading-order. Also, NDE warns that for $P_T >> m_Q$ logarithmic terms of the form $\ln(P_T^2/m^2)$ lead to theoretical uncertainty. In this limit, the heavy flavor is effectively massless leading to collinear divergences.

The confidence in the predictive power of any perturbative QCD calculation depends on a comprehension of the theoretical uncertainties that arise. One uncertainty issue is the choice of the Q^2 scale. When the total lowest order and next-to-leading-order bottom quark cross section are plotted as a function of Q^2 one finds that the next-to-leading-order result becomes unstable and increases as Q goes to zero for $Q < 5$ Gev [26]. This value is a natural lower bound for Q set by the b-quark mass. One also observes less scale dependence as Q increases [26]. This implies that the choice of a function dependent on the transverse momentum of the heavy quark is a reasonable choice for Q. As a result, NDE choose $Q^2 = P_{T\,q}^2 + m_q^2 = \mu^2$. In will be shown in Section 10.3.1 that we prefer Q^2 ranging from $\mu/4$ to $\mu/2$.

Another theoretical uncertainty is the choice of parton density functions. These functions depend on the energy scale at which they are evaluated, called the factorization scale. The scale dependence is described by the Altarelli-Parisi equations. Since the splitting functions in the Altarelli-Parisi evolution equations are perturbatively expanded in α_s the gluon density now appears indirectly as a correction to the sea quark content. Moreover, the gluon structure functions can only be derived assuming the validity of QCD.

Bottom quark production has been measured in hadronic reactions by UA1 [29], CDF

[30] and DØ [31]. Although UA1 results were in reasonable agreement with NLO QCD calculations at $\sqrt{s} = 630$ GeV, earlier CDF results have tended to be a factor of five higher than the theoretical central values. The CDF results prompted theorists either to reevaluate the validity of the fixed target flavor perturbative expansions at Tevatron (section 3.1) energies or to modify the proton gluon structure functions [32]. In Section 10.1.1 we will present DØ's latest set of inclusive b-quark cross section points from low mass dimuons. As will be shown, these new measurements are consistent with DØ's previously published results and they support NLO QCD calculations.

Chapter 3

EXPERIMENTAL APPARATUS

"Keep your #%& detector in good workin' order." Forrest Gump

The DØ detector is located at the DØ interaction region of the Fermi National Accelerator Laboratory (*Fermilab*) Tevatron Collider—hence, the name. The detector was proposed in 1983, installed and commissioned in early 1992 and started taking proton-antiproton ($p\bar{p}$) data on 12 May 1992. DØ [33] is a general purpose detector with excellent calorimetric energy and spatial resolution, good electron and muon identification, and a high degree of hermeticity—4π of the solid angle coverage. Naturally, the design of the detector greatly influenced the physics topics to be studied at DØ. The physics topics studied by the DØ collaboration include: B-physics, the top quark, electroweak physics (production of intermediate bosons $W^{\pm}$ and Z°), quantum chromodynamics (QCD) (production of jets and prompt photons), and search for new particles and phenomena (*e.g.* supersymmetry). The detector has three major components:

1. the central detector system, used for tracking and electron identification;
2. the calorimetry system, which includes a Central Calorimeter, two End Calorimeters, and the Intercryostat Detector;
3. the muon system, which includes both the large and small angle muon drift tubes.

DØ's auxiliary member is a scintillator detector, Level Ø, mounted on each End Calorimeter cryostat, which measures an approximate position of the primary interaction point used in DØ's hardware and software triggers, and monitors the luminosity. However, before one proceeds with a general overview of the DØ detector one must discuss the apparatus which generates the elementary particles used to probe the fundamental forces of nature—the Fermilab Tevatron.

3.1 The Tevatron Collider

The Fermilab Tevatron[1] [34, 35, 36, 37] is currently running as the highest energy particle accelerator in the world with a center of mass energy of the colliding proton-antiproton ($p\bar{p}$) system of 1.8 TeV. The basic principle behind a particle accelerator is simple: a charged particle is given an energy boost as it crosses a gap with an electromagnetic field. Many such gaps can be arranged in a linear configuration (*linear* accelerator). Alternately, a single gap can be reused by containing the particles in a circular orbit such that the particles pass through the gap many times per second, as is done at the Tevatron. A synchrotron is a cyclic machine in which the particles are confined to a closed orbit by a series of magnets that bend the particles' trajectory along the orbit. On each pass around the ring the particles' energy is increased by acceleration in a synchronized radio frequency cavity. As the particles' momentum increases, the magnetic field in the bending magnets must be increased in a synchronized fashion in order for the particles to remain in the ring.

After acceleration in a synchrotron, a primary beam of accumulated particles can be used in one of two ways: 1) fixed target mode or 2) collider mode. Each mode is used for specific purposes. In fixed target mode, the accelerated particles are extracted in bunches and steered magnetically either directly into detectors or onto various targets to produce a wide

[1] In Batavia, Illinios ... about 40 miles west of Chicago

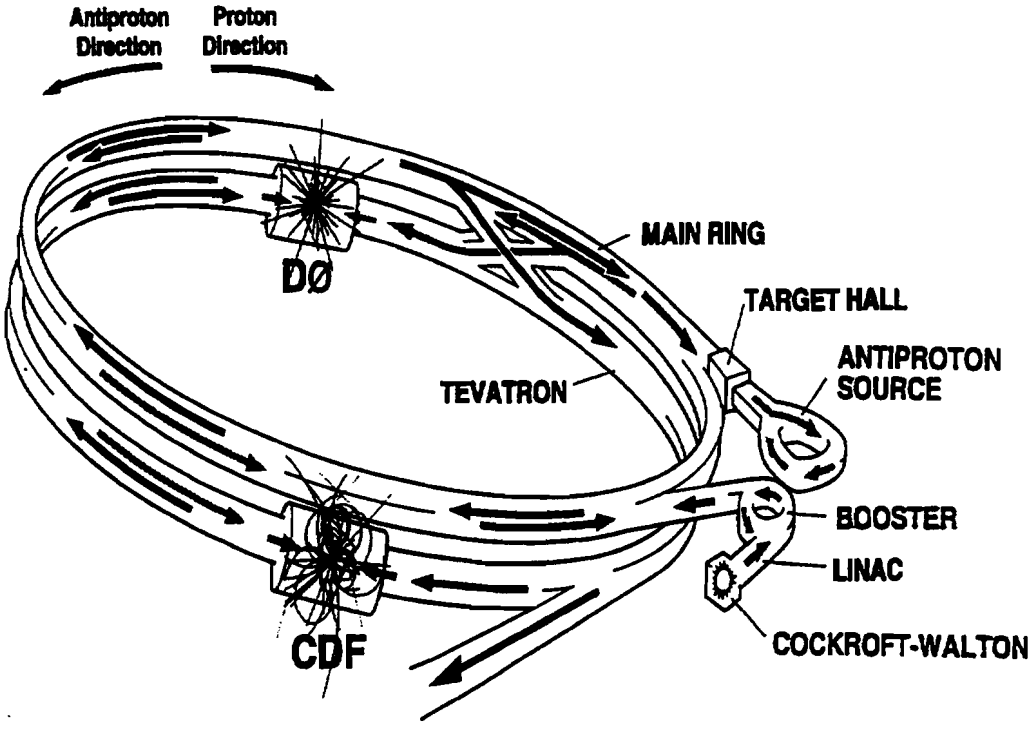

Figure 3.1: FermiLab's Tevatron Collider

range secondary beams of charged and neutral particles. These beams are then delivered to detectors. The major advantage of the fixed target mode is the control available to the researcher to change the particle type and energy. In collider mode, the circulating beams of particles are strongly focussed to a head-on collision at an interaction region which is surrounded by a detector which catches the resultant debris. The advantage of the collider mode is that much higher center of mass energies are available than in fixed target mode.

The Tevatron[2] is a synchrotron of immense complexity and sophistication. It is composed of seven parts (Fig. 3.1):

1. A Cockroft-Walton Accelerator
2. The Linac

[2]For a good detailed discussion see [38].

3. The Booster Synchrotron
4. The Main Ring
5. The Target Hall
6. The Antiproton Source
7. The Tevatron

To begin the acceleration process one needs a source. At the Tevatron, a bottle of pressurized hydrogen gas begins the acceleration process. The hydrogen atoms are ionized by the addition of electrons thus creating H^- ions. The resulting ions are then accelerated to an energy of 750 keV in the Cockroft-Walton accelerator after which the ions are expelled into the Linac, an Alvarez[3] drift tube linear accelerator. Within the Linac the ions are raised to an energy of 200 MeV due to an induced oscillating electric field between a series of electrodes. Once the ions are raised to 200 MeV they are put through a carbon foil which extracts the protons from the H^- ions. The protons are then steered into the Booster Synchrotron Ring in which they are ramped to an energy of 8 GeV. The next stage of the acceleration process is the injection of the protons into the Main Ring. As the protons are accelerated to an energy of 120 GeV in the Main Ring they are concurrently focused into short bunches. In collider mode, these proton bunches are then extracted onto a nickel/copper target creating about twenty million antiprotons per bunch (approximately 10^7 antiprotons can be produced from each batch of 1.8×10^{12} protons). The antiprotons are initially focused with the aid of a lithium lens (a cylinder of liquid lithium that transforms a current pulse of 600,000 amperes into a focusing magnetic field) after which the antiprotons, with energies of 8 GeV, are injected into the first of two antiproton storage rings.

The first ring, known as the Debuncher, uses sophisticated radiofrequency and cooling techniques to *squeeze* the incoherent antiproton beam into a *clean*, coherent set of bunches.

[3]Luis Alvarez (1911–1988): 1967 Physics Nobel Laureate—no relation to the author.

The antiprotons are rotated in phase space from a configuration with a small time and large momentum spread to one with a large time but small momentum spread; then they are stochastically cooled [39] to further reduce the momentum spread. This squeezing process runs continuously and sends about twenty billion clean antiprotons in bunches into the second antiproton storage ring, the Antiproton Accumulator. Further cooling within the accumulator reduces the antiproton population by a factor of about one million thus yielding twenty thousand antiprotons. During Fermilab operations for Run 1A[4], approximately four hours were required to accumulate the 200 billion antiprotons necessary to commence antiproton injection into the Main Ring. Once in the Main Ring, the antiprotons are ramped to 150 GeV with conventional magnets. By this juncture in time, the protons have already been accelerated to 150 GeV and transferred into the Tevatron. When the antiprotons reach 150 GeV they are also injected into the Tevatron.

The Main Ring and Tevatron beam pipes share the same tunnel with the Main Ring approximately 1 m above the Tevatron beam pipe. The Tevatron uses superconducting magnets (operating at a temperature of just 4.7 Kelvin they produce a field of approximately 3 Telsa). Therefore the Tevatron can achieve a much higher energy. In the final leg of the acceleration process, six bunches of protons (roughly 7×10^{10} protons/bunch) and six bunches of antiprotons (roughly 6×10^{10} antiprotons/bunch) are simultaneously focussed and raised to full energy (0.9 TeV for Run 1A). Once at full energy, the beams are squeezed and collided at two beam crossing points: BØ (the location of CDF—Collider Detector at Fermilab) and DØ. The proton and antiproton beams are kept from colliding at other points in the Tevatron by electrostatic separators. Over time the beams decrease in size and density due to scattering with residual beam gases in the vacuum tube. The typical beam lifetime for Run 1A was approximately twenty hours. Antiprotons are produced continuously during

[4]May 1992 to May 1993.

collisions, barring any technical difficulty, in order for a *stack* of antiprotons to be ready when the preceeding stack is depleted.

Thanks to improvements in several aspects of the accelerator system [40], the Tevatron achieved three accelerator records in Run 1A: (1) an instantaneous luminosity of 7.48×10^{30} cm^{-2}sec^{-1}; (2) a record stacking rate of 4.54×10^{10}/hour; and (3) a record integrated luminoisty of 1.48 pb^{-1}/week.

3.2 Determination of the Amount of Data Collected

The principal aim of a high energy experiment is to study the fundamental forces of nature. This is attempted from the analysis of the data. However, to obtain quantitative results one must know the amount of data one has collected.

3.2.1 Luminosity and Integrated Luminosity

An important measurement is the particle flux, or *luminosity*, after a $p\bar{p}$ collision. This measurement is used to determine the amount of data collected. The luminosity is proportional to the number of particles passing through a unit area per unit time. Expressing the luminosity in terms of beam parameters one has

$$L = \frac{N_p N_{\bar{p}}}{\tau A} \ , \tag{3.1}$$

where N_p and $N_{\bar{p}}$ respectively denote the number of protons and antiprotons, τ is the time between collisions, and A is the geometrical area of the interaction point. τ is determined by

$$\tau = \frac{C_{\rm Tev}}{cN_{\rm bunch}} \ ,$$

where $C_{\rm Tev}$ is the circumference of the Tevatron (6.28 km), c is the speed of the beams (roughly the speed of light), and $N_{\rm bunch}$ is the number of bunches. During Run 1A

τ was 3.5 μs. The typical luminosity range for the data set used for this thesis was 1–7 $\times 10^{30}$ cm^{-2}sec^{-1}.

The quantity of interest to high energy experimentalists is the total amount of luminosity collected during a run. This is called the integrated luminosity, which is expressed as

$$\mathcal{L} = \int L dt \ . \tag{3.2}$$

3.2.2 Cross Section

An equally important quantity is the interaction probability per unit flux called the *cross section*. This reaction rate is measured by the experimentalist to determine "how often" a certain transition rate occurs from a collision. Knowing the number of observed events of interest (N) and the integrated luminosity corresponding to the data set which yielded the N events, the cross section (σ) is expressed as

$$\sigma = \frac{N}{\mathcal{L}} \ . \tag{3.3}$$

The cross section is expressed in *barns* (1 barn = 10^{-24} cm^2).

From Equation 3.3 one can also estimate the yield for a certain reaction if one knows the predicted theorectical cross section and the integrated luminosity.

3.3 DØ Coordinate System

Before we can proceed with a description of the DØ detector we must define the coordinate system we shall be using. DØ uses a right-handed coordinate system, with the positive z-axis aligned along the direction of the proton beam and the positive y-axis vertical. The angular coordinates (azimuthal (ϕ) and polar (θ) angles) are defined such that $\phi = \pi/2$ is parallel to the positive y-axis and $\theta = 0$ is coincident with the positive z-axis. Radial distances are measured perpendicularly to the beam line.

The center of mass of the partons involved in the hard scatter is not necessarily at rest in the laboratory frame. Such being the case, for a parton of energy E and momentum p, one defines a Lorentz invariant quantity, the *rapidity*, as

$$y = \frac{1}{2}\ln\left(\frac{E+p_z}{E-p_z}\right) , \tag{3.4}$$

where p_z is the z component of the parton's momentum. If the mass of the parton is much less than its energy, then the rapidity can be approximated by the pseudorapidity and is defined as

$$\eta = -\ln\left(\tan\left(\frac{\theta}{2}\right)\right) . \tag{3.5}$$

Trajectories within the detector are thus described by ϕ and η.

Practically, one projects the momentum vector onto a plane perpendicular to the beam axis because one can apply momentum conservation in the transverse plane (see Section 4.7). Therefore, one defines the transverse momentum to be

$$P_{\mathrm{T}} = P\sin\theta , \tag{3.6}$$

where P and θ are the respective physics object's mometum and polar angle as measured from the collision point to the point of observation. Similarly, one can define the transverse energy as

$$E_{\mathrm{T}} = E\sin\theta . \tag{3.7}$$

3.4 The DØ Detector

In high energy experiments one has to detect four types of physics objects: 1) jets; 2) muons; 3) electrons; and 4) missing transverse energy. To optimize the detection of the four object types and maximize the number of physics topics the design of the DØ detector (Fig. 3.2) centered on several important features:

- Uniform response;

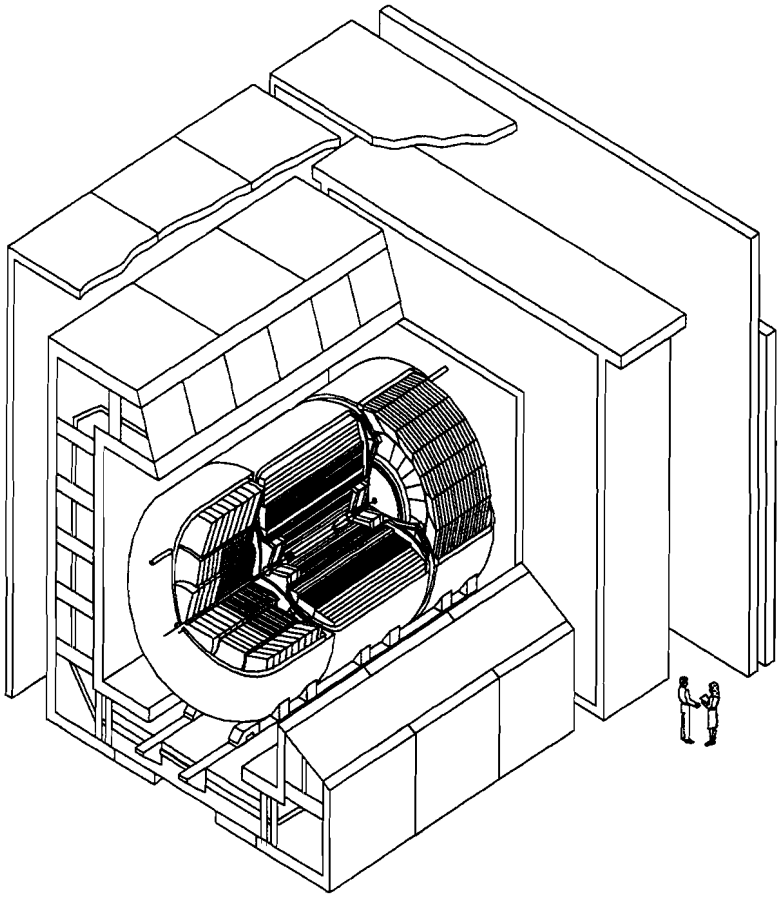

Figure 3.2: The DØ Detector (cross section view)

- Good calorimetric energy and spatial resolution;
- Good energy resolution for jets and electrons;
- Good missing transverse energy measurement;
- Good electron to hadron ratio;
- Fine pseudorapidity and azimuthal segmentation;
- Maximum possible muon coverage and identification;
- Compactness and hermeticity.

The mantel piece of the detector was decided to be the calorimetry system. Therefore, it was imperative to have the calorimeter respond to electromagnetic and hadronic energy as similarly as possible since it is impossible to discern at the trigger level how much of a jet's energy is either electromagnetic and hadronic. The electromagnetic/hadronic (e/h) ratio measures the calorimeter's response to each type of energy. Ideally, e/h should be 1.0 (optimization of electron and hadron energy response is called compensation). To maximize muon identification, the calorimeter had to be compact and dense to minimize background from punch throughs and light meson decays. All of the above goals led to a choice of a uranium/liquid argon calorimeter, muon coverage up to a pseudorapidity of approximately 3.5, and a central tracking without a central magnetic field. The overall dimensions of the DØ detector are extremely impressive. The entire assembly is 13 m high $\times$ 11 m wide $\times$ 17 m long with a total weight of 5500 tons.

3.4.1 Central Tracking Detectors

DØ's Central Tracking Detectors (CD) is comprised of four subsystems. The Vertex Drift Chamber (VTX), Transition Radiation Detector (TRD) and the Central Drift Chambers (CDC) are cylindrical devices concentrically arranged around the beryllium beam pipe that traverses the detector. The fourth subsystem consists of two Forward (backward) Drift Chambers (FDC) which are oriented perpendicular to the beam pipe. The active detection volume of the CD is bounded by a radius of approximately 75 cm and a length of 270 cm. A cutaway view of the central detectors can be seen in Fig. 3.3. The major design motivation of the central traking detectors was the fact that DØ has no central magnetic field. Consequently, the primary requirements for the traking detectors are:

- Good spatial resolution of individual particles;
- High efficiency;

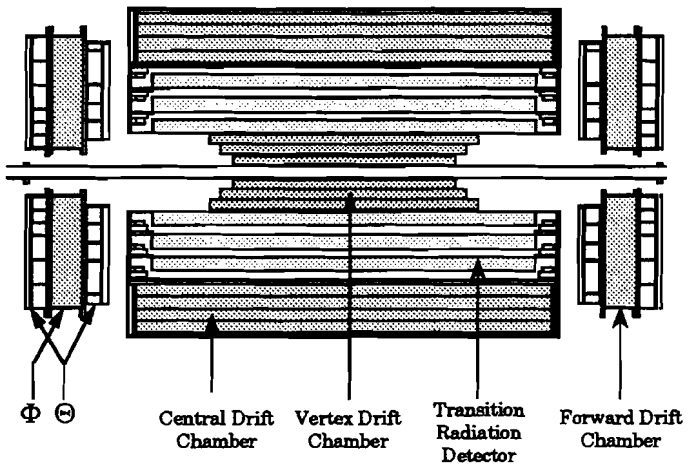

Figure 3.3: A cutaway view of the DØ Tracking Chambers

- Good two-track resolving power;
- Good dE/dx measurements to distinguish between electrons and closely spaced conversion pairs ($\pi^\circ \rightarrow \gamma\gamma$).

Three of the four tracking detectors, VTX, CDC, and FDC, are wire drift chambers. The basic working principle behind tracking detectors is as follows [41, 42]. When a charged particle travels through a drift chamber it liberates electrons and thus creates ions from the gas mixture within the chamber. Within statistical fluctuations of a macroscopic scale, the number of ions produced is proportional to the magnitude of the charge of the particle and independent of its energy in the relativistic limit. Separation of the electrons and ions is accomplished by an electric field. Electrons will drift to the positive electrode wire commonly known as a *sense wire*. A multiwire drift chamber has several sense wires strung in parallel forming a plane which divides the chamber in two symmetric halves. The electrostatic field in a cell divides the cell's active volume into parts bearing a one-to-one correspondence with the sense wires. In other words, an ionization electron will find its way to the sense wire closest to its point of creation. The small diameter of a sense wire produces a very strong electrostatic field in its immediate vicinity. As a result, the electric field accelerates the

drift electrons to high enough energies to induce further ionization which leads to a large electrical pulse (avalanche).

The velocity of the drift electrons is independent of the particle that initiates the ionization; it is dependent on the strength of the electric field, and the composition, pressure and temperature of the gas mixture. The drift time, defined to be the difference between the known time of the collision and the arivial time of the electrical pulse at the readout, combined with the drift velocity leads one to calculate the drift distance of the drift electrons. In order to obtain a linear relationship between distance and time, it is necessary to have a constant electric field over as large a volume of the chamber as possible. From the drift time and distance the trajectory of the charge particle can be reconstructed (Section 4.1).

3.4.1.1 Vertex Drift Chamber

The Vertex Drift Chamber (VTX) [43, 44, 45] is DØ's innermost tracking detector. A cross sectional view of the detector is shown in Fig. 3.4. The designed specifications were to provide precise position determination of primary and secondary vertices and large η coverage. Also, one must keep in mind that the DØ detector is in a high luminosity environment. Therefore wire placement accuracy should be minimally 25 μm and the readout electronics be capable of measuring drift times on the order of one nanosecond.

The VTX is comprised of three mechanically independent concentric, cylindrical layers of cells parallel to the beam pipe (radial extension of 3.7 cm $\leq r \leq$ 16.2 cm). The innermost layer has 16 cells in azimuth; the outer two layers have 32 cells. Each cell has eight 25 μm nickel-colbolt-tin (NiCoTn) sense wires to provide measurement of the $r\phi$ coordinates. A measurement of the z-coordinate is achieved from readouts at both ends of the sense wires. Resolution of left/right ambiguity (Section 4.1) is achieved by staggering adjacent sense wires by $\pm$ 100 μm. Enhancement of pattern recognition is accomplished by offset cells in ϕ in each layer. To obtain good spacial resolution and track pair resolving power, the

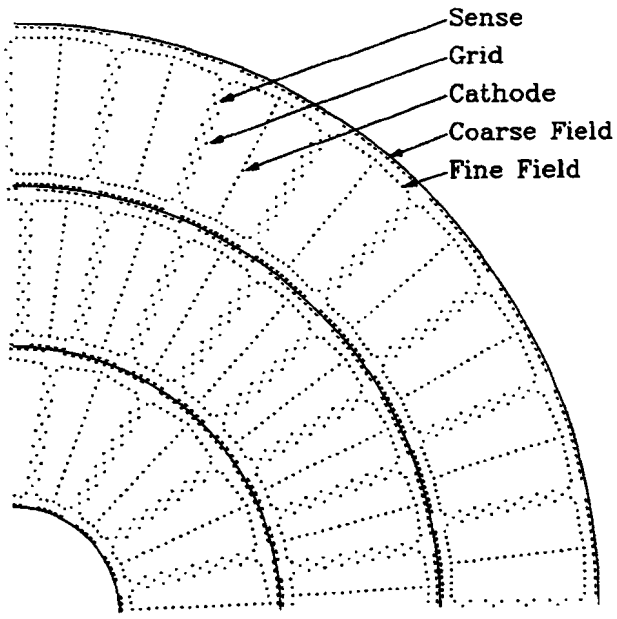

Figure 3.4: Cross Sectional View of the Vertex Drift Chamber

Length of Active Volume: Layer 1	96.6 cm
Layer 2	106.6 cm
Layer 3	116.8 cm
Phi sectors/layer	16, 32, 32
Radial Interval (active)	3.7-16.2 cm
Radial Wire Interval	4.57 mm
Number of Sense Wires/Cell	8
Number of Sense Wires	640
Stagger of Sense Wires	$\pm$ 100 μm
Gas Mixture	CO_2(95%)-Ethane(5%)
Gas Pressure	1 atm
Drift Field	1.0-1.6 kV/cm
Average Drift Velocity	7.3-12.8 μm/ns
Gas Gain at Sense Wires	4×10^4
Sense Wire Potential	+2.5 kV
Sense Wire Diameter	25 μm NiCoTin
Guard Wire Diameter	152 μm Au-plated Al

Table 3.1: Vertex Chamber Parameters

VTX's gas mixture is carbon dioxide (CO_2) and ethane (C_2H_6) (95% : 5%) at atmospheric pressure. The average drift velocity under normal DØ running conditions is approximately 7.3 μm/ns. The $r\phi$ and z-coordinate design spatial resolutions are approximately 60 μm and 1.5 cm. A summary of the VTX design specifications are listed in Table 3.1.

3.4.1.2 Transition Radiation Detector

After the VTX, along the radial direction, is the Transition Radiation Detector (TRD) [46, 47]. The physical principle behind the TRD is the emission of transition X-rays by highly relativistic particles when they traverse boundaries between media with different dielectric constants. The X-rays are detected when they ionize the gas. The magnitude and arrival time of charged clusters are used to distinguish between electrons and hadrons. Distinguishability of electrons and hadrons is the TRD's utmost responsilbility since DØ has no central magnetic field (see Fig. 3.6).

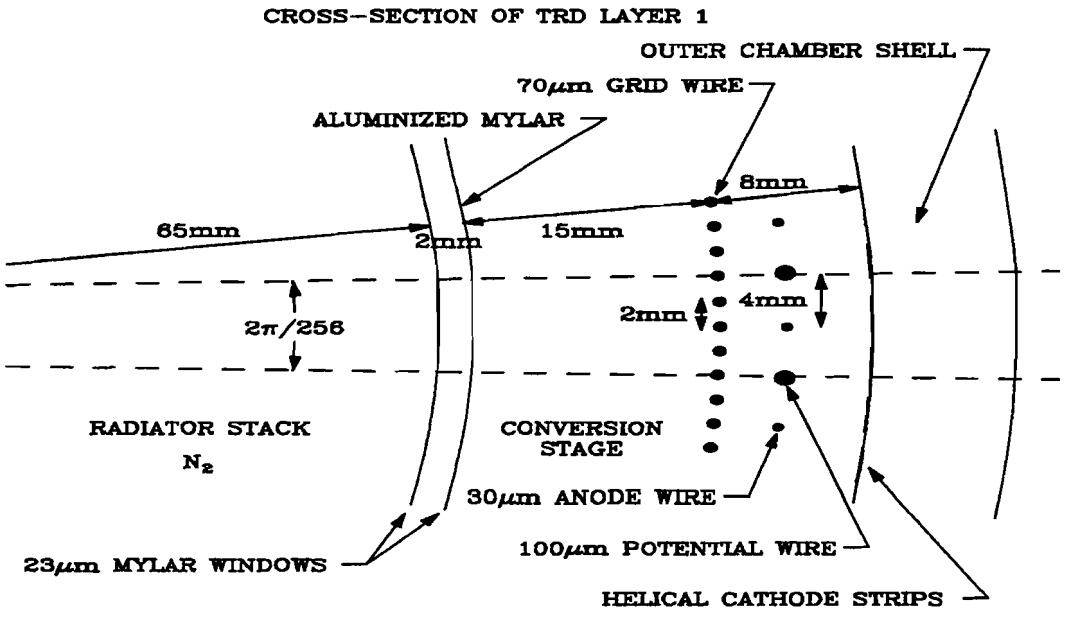

Figure 3.5: Cross Sectional View of the First Transition Radiation Detector Layer

Similar to the VTX, the TRD consists of three concentric, cylindrical layers. Each layer

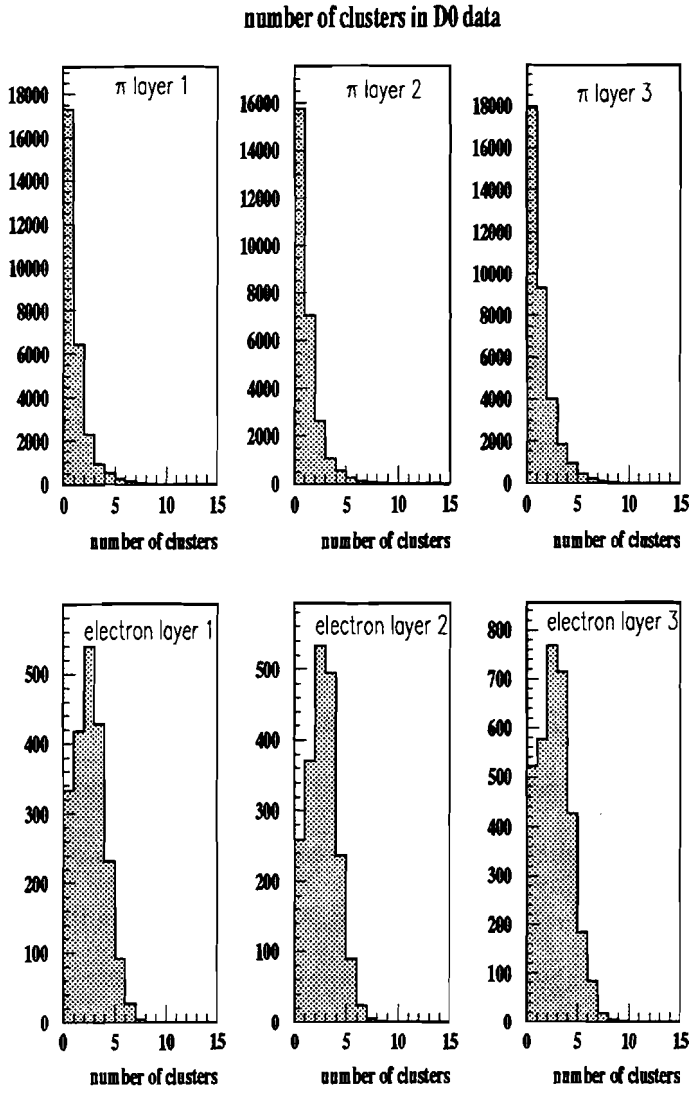

Figure 3.6: Number of associated clusters per TRD layer for electrons and pions.

has a radiator and an X-ray detection chamber. A radiator consists of 393, 18 μm, thick polypropylene foils separated by a mean gap of 150 μm between each foil. The volume is filled with nitrogen (N_2) gas. The X-ray detector is a two stage time-expansion radial-drift proportional wire chamber (PWC) mounted just after the radiator. It is composed of a 15 mm conversion and 8 mm amplification stages separated by a cathode grid of 70 μm gold plated tungsten (W) wire. The radiator and detector volumes are separated by a pair of 23 μm windows. Dry CO_2 flows through the gap between the two windows to prevent the N_2 in the radiator to leak into the detector volume and pollute the xenon (Xe), methane (CH_4), ethane (C_2H_6) (91% : 7% : 2%) chamber gas mixture. Ideally, the TRD offers a factor of ten rejection against pions while keeping 90% of isolated[5] electrons.

3.4.1.3 Central Drift Chamber

Beyond the TRD are the four cylindrical, concentric rings of the Central Drift Chamber (CDC) [44, 48] (Fig. 3.7). The CDC provides trajectory dE/dx information on isolated charged particles for the region $|\eta| \leq 1.2$.

Each of the four layers is divided into 32 modular, azimuthal cells in $r\phi$ with seven 30 μm gold plated W sense wires and two delay lines parallel to the beam direction per cell. The sense wires are split between the inner and outer walls of each layer; five of the sense wires are located along the inner radius while the other two are along the outer radius. The delay lines are embedded in the outer and inner walls of each cell for measurement of the longitudinal coordinate. This is accomplished when an avalanche occurs on an outer sense wire; pulses are induced on the delay line and the difference in arrival times at the two ends determines the z-coordinate. Adjacent wires within a cell are staggered in ϕ by $\pm$ 200 μm to remove cell level left/right ambiguity (see Section 4.1). Pattern recognition is further aided with alternate cells in radius offset by half of a cell. Thus a particle traversing

[5]Electrons not associated with jets.

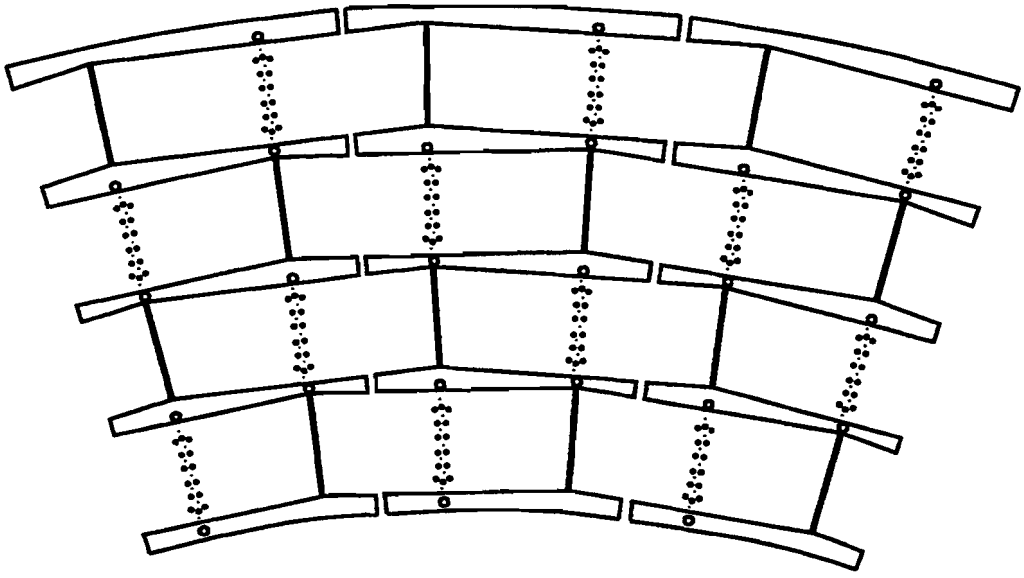

Figure 3.7: Cross Sectional View of the Central Drift Chamber

Length of Active Volume	179.4 cm
Radial Interval (active)	51.8-71.9 cm
Number of Layers	4
Radial Wire Interval	6 mm
Number of Sense Wires/Cell	7
Number of Sense Wires	896
Stagger of Sense Wires	± 200 μm
Number of Delay Lines	256
Gas Mixture	Ar(93%)-CH_4(4%)-CO_2(3%)
Gas Pressure	1 atm
Drift Field	620 V/cm
Average Drift Velocity	34 μm/ns
Gas Gain at Sense Wires	$2,6 \times 10^4$
Sense Wire Potential	+1.5 kV
Sense Wire Diameter	30 μm Au-plated W
Guard Wire Diameter	125 μm Au-plated CuBe

Table 3.2: Central Drift Chamber Parameters

the CDC will be seen by a maximum of 28 sense wires and 8 delay lines. The CDC uses a gas mixture of argon (Ar), CH_4, and CO_2 (93% : 4% : 3%) at atmospheric pressure. The average drift velocity is about 34 μm/ns under normal DØ running operation. The $r\phi$ and z-coordinate design spatial resolutions are approximately 180 μm and 2.9 mm. Table 3.2 lists the relavent design specifications of the CDC.

3.4.1.4 Forward Drift Chambers

The Forward Drift Chambers (FDC) [44, 48], which cap both ends of the CD system, are a composition of two distinct chambers. Each consists of three in total: the φ chamber with sense wires oriented radially to measure the ϕ-coordinate, sandwiched between two ϑ chambers, composed of four separate quadrants, whose sense wires are oriented parallel to the x-axis for the top/bottom subchambers and parallel to the y-axis for the left/right subchambers to measure the θ-coordinate. Figure 3.8 is an illustration of the FDC.

The φ chamber has 36 sectors over the full azimuth, each with 16 sense wires of length 50 cm parallel to the beam pipe. The four quadrants of the ϑ module contain six rectangular cells at increasing radii. Each cell has eight sense wires and one delay line. Similar to the CDC, the sense wires in both the φ and ϑ modules are staggered by $\pm$ 200 μm to help resolve left/right ambiguity. The two ϑ chambers are rotated by 45° in ϕ with respect to each other. The φ and ϑ chambers use the same gas mixture as the CDC. The φ and ϑ chambers design spatial resolutions are approximately 200 μm and 300 μm. A design specification overview of the FDC is listed in Table 3.3.

3.4.2 Calorimetry System

The strongest aspect of the DØ detector is the liquid argon sampling calorimeter [49, 50] with uranium, copper and stainless steel absorbers (Figs. 3.9, 3.10). Since there is no central magnetic field, the Calorimeter must provide energy measurement for electrons, photons

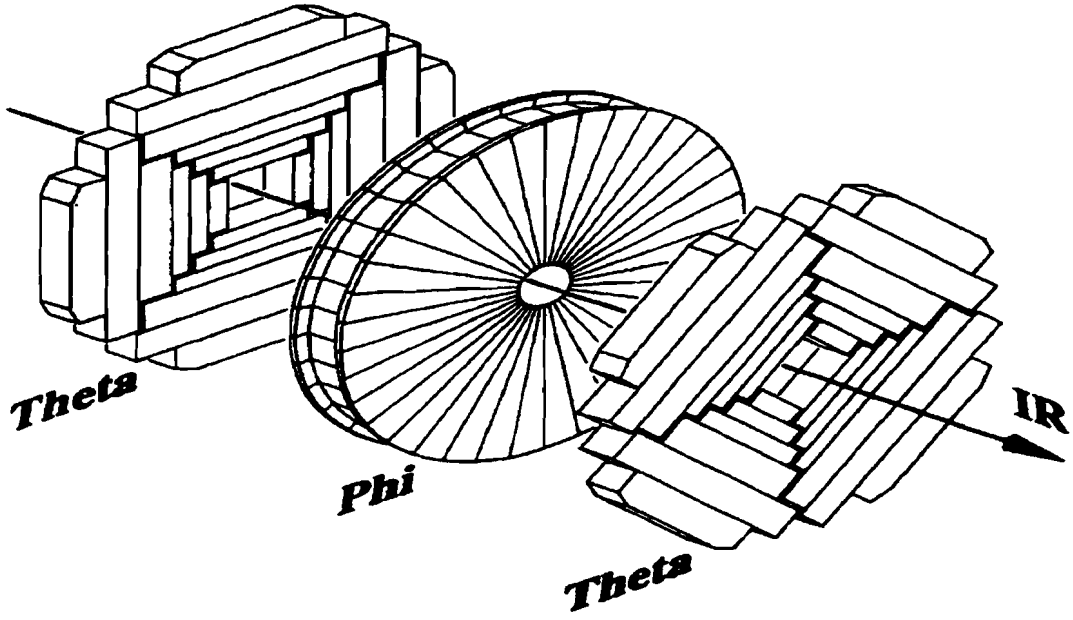

Figure 3.8: Layout of the Forward Drift Chambers

	Θ *modules*	Φ *modules*
z interval	104.8-111.2 cm	113.0-127.0 cm
	128.8-135.2 cm	
Radial Interval	11-62 cm	11-61.3 cm
Number of Cells in Radius	6	
Maximum Drift Distance	5.3 cm	5.3 cm
Stagger of Sense Wires	0.2 mm	0.2 mm
Sense Wire Separation	8 mm	8 mm
Angular Interval/cell		10°
Number of Sense Wires/Cell	8	16
Number of Delay Lines/Cell	1	0
Number of Sense Wires/End	384	576
Number of Delay Lines Read out/End	96	
Gas Mixture	Ar(93%)-CH_4(4%)-CO_2(3%)	
Gas Pressure	1 atm	1 atm
Drift Field	1.0 kV/cm	1.0 kV/cm
Average Drift Velocity	37 μm/ns	40 μm/ns
Gas Gain at Sense Wire	$2.3, 5.3 \times 10^4$	3.6×10^4
Sense Wire Potential	+1.5 kV	+1.5 kV
Sense Wire Diameter	30 μm NiCoTin	
Guard Wire Diameter	163 μm Au-plated Al	

Table 3.3: Forward Drift Chamber Parameters

and jets. Furthermore, the Calorimeter is vital in lepton[6], photon and jet identification, transverse energy balance measurement and missing transverse energy resolution in the event.

In a sampling calorimeter the energy deposited by particles is detected only in sensitive layers via ionization of the active medium. The "live" layers are interspread with layers of passive absorbers. Only a small fraction of the particle's energy is read out, which serves to sample the entire energy deposition. A correction, called the sampling fraction,

$$sf = \frac{E_{active}}{E_{inactive} + E_{active}} ,$$

is used to obtain the full energy loss of the particle.

The sampled energy is typically a result of an *electromagnetic* and/or *hadronic shower.* Electromagnetic showers are primarily produced from the emission of photons due to the interaction of highly energetic electrons with the Coulomb field around the nucleus of the Calorimeter's absorbers (Bremsstrahlung)[7], or the creation of electron-positron pairs (pair production) from photons. The energy loss of an electromagnetic particle through a specified amount of material is determined by the material's *radiation length* (x_o), given by:

$$E(x) = E_o e^{x/x_o} .$$

The radiation length is a characteristic of the medium. Uranium's typical radiation length is 3.2 mm. Ionization and atomic excitation begin to dominate energy loss for electrons and photons below 10 GeV.

Hadronic showers are produced from the inelastic collisions of hadrons with the nuclei of the medium. These collisions create secondary hadrons, where the daughter hadrons can undergo inelastic collisions. Obviously, the hadrons lose most of their energy due to

[6]Especially for our muon identification (Section 6.2.2).

[7]The Bremsstrahlung cross section is inversely proportional to the square of the incident particle's mass and increases logarithmically with the square of its Lorentz γ factor.

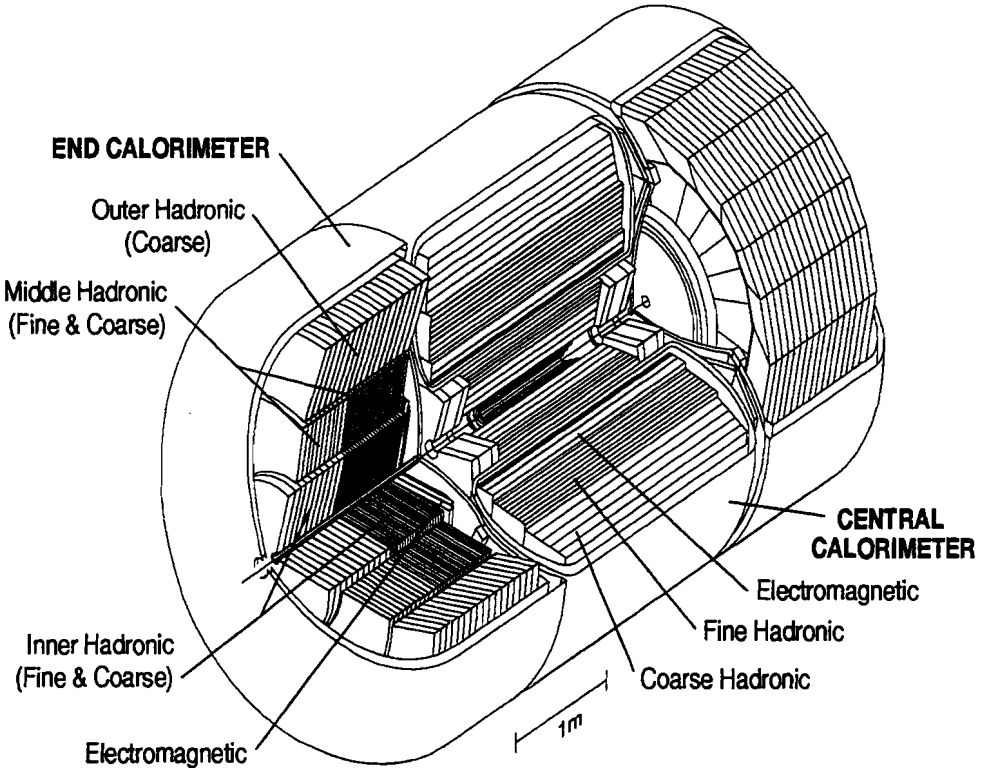

Figure 3.9: A cutaway view of the DØ calorimeter system.

these collisions. The hadron's mean free path between collisions in the medium is called the nuclear interaction (or absorption) length, λ_o. The interaction length for uranium is 10.5 cm. Consequently, hadron showers are generally larger, both longitudinally and transversely, than electromagnetic showers.

DØ's calorimeter is made of dense, passive absorbers (copper, stainless steel or depleted uranium—U^{238}) and an active material (liquid argon—LAr) sandwiched in layers (Fig. 3.10). Typically, 5–10% of an incident particle's energy is deposited in the active layers through

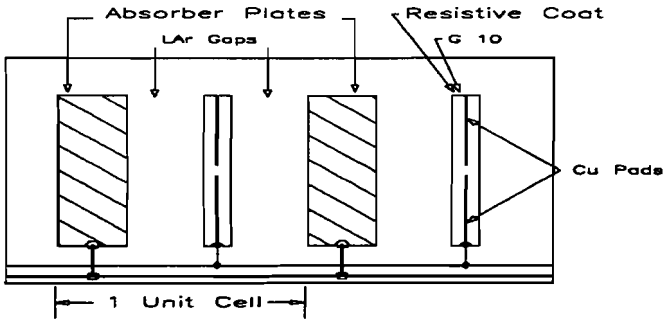

Figure 3.10: Schematic of DØ calorimeter cell

ionization of the liquid. Also, DØ's calorimeter design achieves good electromagnetic and hadronic shower resolution along with electron to hadron response (compensation). The e/h ratio of the Calorimeter falls from about 1.11 at 10 GeV to about 1.04 at 150 GeV. Another important aspect of LAr calorimetry is the nondegradation of the signal if the liquid argon is maintained reasonably pure (less than two parts per million of O_2), since LAr is not susceptible to radiation damage. This is important because the calorimeter was designed to produce electronic signals proportional to the deposited energy. DØ's calorimeters are the Central Calorimeter, End Calorimeters, Massless Gaps and Intercryostat Detector.

3.4.2.1 Central Calorimeter

The Central Calorimeter (CC) is comprised of three cylindrical concentric shells parallel to the beam axis with radial coverage of $75 < r < 222$ cm from the beam pipe, longitudinal range of 226 cm and angular coverage of $35° \leq \theta \leq 145°$. The three sections are an electromagnetic (32 modules), a fine hadronic (16 modules) and a coarse hadronic (16 modules) ring. Each concentric ring is rotated azimuthally by $\Delta\phi = 0.2$ radians to avoid continuous cracks. The lateral segmentation of the calorimeters is 0.1×0.1 in $\eta \times \phi$, space except for

	EM	FH	CH
Rapidity Coverage	± 1.2	± 1.0	± 0.6
Number of Modules	32	16	16
Absorber[a]	Uranium	Uranium	Copper
Absorber Thickness (cm)	0.3	0.6	4.65
Argon Gap (cm)	0.23	0.23	0.23
Number of Cells/Module	21	50	9
Longitudinal Depth	20.5 X_0	3.24 λ_0	2.93 λ_0
Number of Readout Layers	4	3	1
Cells/Readout Layer	2, 2, 7, 10	21, 16, 13	9
Total Radiation Lengths	20.5	96.0	32.9
Radiation Length/cell	0.975	1.92	3.29
Total Absorption Lengths (Λ)	0.76	3.2	3.2
Absorption Length/Cell	0.036	0.0645	0.317
Sampling Fraction (%)	11.79	6.79	1.45
Segmentation ($\phi \times \eta$)[b]	0.1 × 0.1	0.1 × 0.1	0.1 × 0.1
Total Number of Readout Cells	10, 368	3456	768

Table 3.4: Central Calorimeter Parameters

[a]Uranium is depleted and FH absorbers contain 1.7% Niobium alloy
[b]Layer 3 of the EM has 0.05 × 0.05

the third readout layer of the electromagnetic calorimeter. For the third layer, the segmentation in $\eta \times \phi$ space is 0.05 × 0.05 to optimize the distinguishability between electron and hadron showers. The electromagnetic modules have 21 radial cells arranged in four readout layers. Each cell is composed of a 3 mm depleted uranium absorber plate and 2.3 mm LAr gaps for a sampling fraction of 12.9%. The fine hadronic modules, each divided into three readout layers, have 50 radial cells, 6 mm uranium-niobium alloy absorber plate with 2.3 mm LAr gaps for a sampling fraction of 6.9%. The coarse hadronic section also has 16 modules but only one readout layer. It uses nine 4.75 cm copper absorber plates with 2.3 mm LAr gaps for a sampling fraction of 1.7%. The CC is contained in a double walled steel cryostat. Table 3.4 lists the major design specfications of the CC.

3.4.2.2 End Calorimeters

The two End Calorimeters (EC) are divided into four sections: the forward electromagnetic (EM), the inner hadronic (IH), the middle hadronic ring (MH), and the outer

hadronic ring (OH). The ECEM consists of two circular modules with angular coverage of $3° < \theta < 27°$ and radial coverage of an inner radius of 5.7 cm to an outer radius varying between 84 cm to 104 cm. The modules have 18 radial cells with, as in the CC, the absorber material being 4 mm of depleted uranium. The transverse segmentation is the desired $\Delta\phi = \Delta\eta = 0.1$. However, above $|\eta| = 3.2$, the pad size is too small so the segmentation is increased to $\Delta\phi = \Delta\eta = 0.2$. As in the CCEM, the third ECEM layer is more finely segmented to improve electron/hadron shower resolution. The segmentation is $\Delta\eta = \Delta\phi = 0.05$ for $|\eta| < 2.7$, 0.10 for $2.7 < |\eta| < 3.2$, and 0.2 for $|\eta| > 3.2$.

The IH module that is directly behind the ECEM is cylindrical with inner and outer radii 3.92 cm and 86.4 cm. Longitudinally, the IH is divided into a fine (IFH) and course hadronic (ICH) section. The IFH uses sixteen 6 mm semicircular uranium plates arranged in four readout layers. Alternate plates have their boundary rotated by 90° to avoid cracks. The ICH uses thirteen 46.5 mm stainless steel plates arranged in a single readout layer. Transversely, the IH matches the ECEM segmentation. For $|\eta| < 3.2$, the segmentation is $\Delta\eta = \Delta\phi = 0.1$; for $|\eta| > 3.2$, the IH pad size increases to $\Delta\eta = \Delta\phi = 0.2$; above $|\eta| = 3.8$ (beyond ECEM coverage) the pad size is increased to $\Delta\eta = 0.4, \Delta\phi = 0.2$.

The MH ring consists of sixteen wedge-shaped modules surrounding the IH. The ring extends from an inner radius of 33 cm to an outer radius of 1.52 m. Each module subtends an angle of 22.5° and is divided longitudinally into a fine hadronic and coarse hadronic section (MFH and MCH) as in the IH. The MFH consists of 60 radial cells arranged in four readout layers. The first cell uses the front plate of the module as its absorber plate; all other cells use 6 mm U-Nb alloy plates. The transverse segmentation follows the usual convention. The ECMCH is a single readout layer of 14 cells, which use 46.5 mm steel absorber plates.

The OH ring consists of sixteen modules, all of which are coarse hadronic (OCH).

	EM	IFH	ICH	MFH	MCH	OH
Rapidity Coverage	1.3-4.1	1.6-4.5	2.0-4.5	1.0-1.7	1.3-2.0	0.7-1.4
Number of Modules/End Calor.	1	1	1	16	16	16
Absorber[a]	U	U	SS[b]	U	SS	SS
Absorb Thickness (cm)	0.4	0.6	4.6	0.6	4.6	4.6
Argon Gap (cm)	0.23	0.21	0.21	0.22	0.22	0.22
Number of Cells/Module	18	64	12	60	12	24
Longitudinal Depth	$20.5X_0$	$4.4\lambda_0$	$4.1\lambda_0$	$3.6\lambda_0$	$4.4\lambda_0$	$4.4\lambda_0$
Number of Readout Layers	4	4	1	4	1	3
Cells/Readout layer	2, 2, 6, 8	16	12	15	12	8
Total Radiation Lengths	20.5	121.8	32.8	115.5	37.9	65.1
Total Absorption Length (Λ)	0.95	4.9	3.6	4.0	4.1	7.0
Sampling Fraction (%)	11.9	5.7	1.5	6.7	1.6	1.6
$\Delta\phi$ Segmentation[c]	0.1	0.1	0.1	0.1	0.1	0.1
$\Delta\eta$ Segmentation[d]	0.1	0.1	0.1	0.1	0.1	0.1
Total Number of Readout Ch.[e]	14976	8576	1856	2944	768	1784

Table 3.5: End Calorimeter Parameters

[a]Uranium is depleted and FH (IFH and MFH) absorbers contain 1.7% Niobium alloy
[b]Stainless Steel
[c]Layer 3 of the EM has $\Delta\phi \times \Delta\eta = 0.05 \times 0.05$ for $|\eta| < 2.6$
[d]For $|\eta| > 3.2, \Delta\phi = 0.2$ $\Delta\eta \approx 0.2$
[e]MCH and OH are summed together at $|\eta| = 1.4$

The modules have an inner and outer radii of 1.62 m and 2.26 m. Each module forms a parallelogram with the inner face at an angle of 27.4° with respect to the xy plane. There are 25 radial cells, read out in three layers. Each cell uses 46.5 mm steel absorber plates except for the first and last cells. These cells use stainless steel plates. Each EC is contained within its own double set of cryostat walls. The design specifications for the EC are tallied in Table 3.5.

3.4.2.3 Massless Gaps and the Intercryostat Detector

In the crossover region from CC to EC, there are several rapidity regions where a particle must travel through mostly support structures (e.g. cryostat walls, end support plates, etc.) before (or after) reaching the sampling calorimeter modules. To partially compensate for the energy loss in these support walls two different types of detectors were adopted. First, an additional layer of LAr sampling was included on the face of each

ECMH and ECOH module and on each end of the CCFH modules. These *massless gaps* (MG) have no significant absorber material but do sample the shower energy before and after the dead material between the cryostats. The CCMG, ECMH and ECOH η coverage are $0.7 < |\eta| < 1.2$, $1.1 < |\eta| < 1.4$, and $0.8 < |\eta| < 1.1$. The segmentation is the typical $\Delta\eta = \Delta\phi = 0.1$. The second, Intercryostat Detector (ICD), are two arrays of 384 scintillation counter tiles mounted on the front surface of each EC cryostat. The tiles match the LAr calorimeter cells in size. The ICD readout uses 1.3 cm diameter phototubes.

3.4.3 Muon System

Muons are identified by their very penetrating property since muons do not interact strongly and for energies less than approximately 500 GeV do not readily produce electromagnetic showers. The Muon System (Fig. 3.11) plays an integral part in DØ's lepton identification.

Surrounding the calorimeters, the Muon System (Fig. 3.11) is broken into two subsystems: the wide angle muon spectrometer (WAMUS) [51, 52] and the small angle muon spectrometer (SAMUS) [53]. Each subsystem uses three layers of proportional drift tubes (PDT) with magnetized toroids after the first layer of drift tubes. In all, there are five toroids. The central toroid (CF) covers the region $|\eta| \leq 1$ while the two end wall toroids (EF) cover the region $1 < |\eta| < 2.5$. The two SAMUS toroids cover the region $2.5 < |\eta| < 3.3$. All five toroids are magnetized to a field of 1.9 telsa. The magnetic field is perpendicular to the beam axis; hence, muon trajectories are bent in the rz plane. In order to measure the bend, and thus determine the momentum, the muon trajectory is reconstructed both before and after the iron. A very clean environment is provided for muon identification and momentum measurement because the combined interaction lengths of the calorimeters and muon toroids minimizes the punchthrough probability (Fig. 3.12). For example, the minimum momentum required for a muon to pass through the calorimeter and iron varies

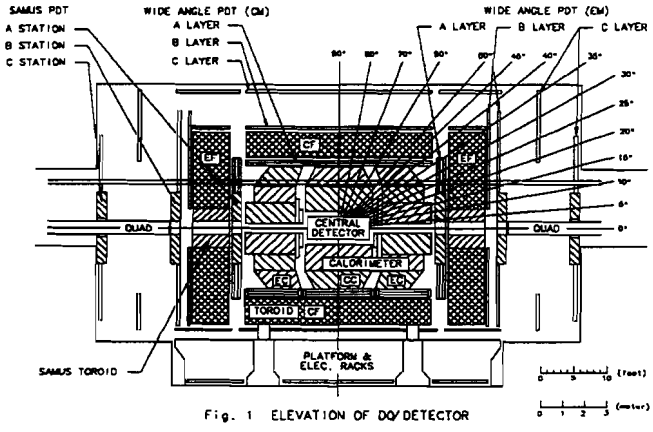

Figure 3.11: Cross Section View of the DØ Muon System

	WAMUS	SAMUS
Rapidity Coverage	$\|\eta\| \leq 2.3$	$2.3 \leq \|\eta\| \leq 3.6$
Magnetic Field	2 T	2 T
Number of Chambers	164	448
Interaction Lengths	13.4	18.7
Bend View Resolution[a]	$\pm$ 0.53 mm	$\pm$ 0.35 mm
Non-Bend Resolution	$\pm$ 3 mm	3.5 mm
$\delta P/P$[b]	18%	18%
Gas	Ar(90%)-CF_4(5%)-CO_2(5%)	CF_4(90%)-CH_4(10%)
Average Drift Velocity	6.5 cm/μs	9.7 cm/μs
Anode Wire Voltage	+4.56 kV	+4.0 kV
Cathode Pad Voltage	+2.3 kV	-
Number of Cells	11,386	5308
Sense Wire Diameter	50 μm	50 μm

Table 3.6: Muon System Parameters

[a]The diffusion limit is 0.2-0.3 mm.

[b]Multiple Coulomb Scattering limit - assumes 100% chamber efficiency.

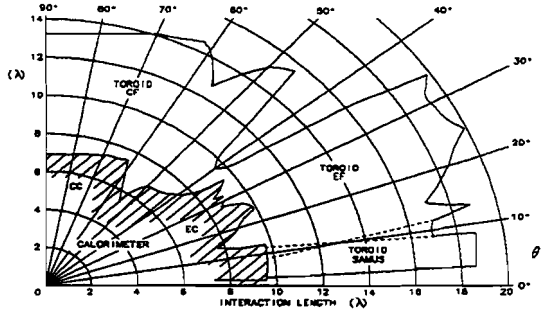

Figure 3.12: Thickness of the Calorimeter and Muon System in Terms of Interaction Length

from roughly 3.5 GeV/c at $\eta = 0$ to about 5 GeV/c at larger η. However, because of the thickness of the detector, Multiple Coulomb Scattering contributes to the muon momentum resolution. The WAMUS and SAMUS design specifications are listed in Table 3.6.

3.4.3.1 Wide Angle Muon Spectrometer

Muon position is determined by three layers of proportional drift tubes (PDT). A schematic drawing of a PDT is shown in Fig. 3.13. In WAMUS, each layer consists of 3 or 4 planes of PDT's. The first layer, A layer, is inside the toroids and has four PDT planes. Layers B and C are both outside of the toroids and each has three PDT planes. In all, there are 164 WAMUS chambers which differ in PDT depth (3 or 4), width (14 and 24 cm) and length (between 1.91 and 5.59 m). The total number of WAMUS PDT's is 11,386. The PDT's are oriented almost parallel to the direction of the magnetic field of the toroid. As a result, the deflection due to the magnet is measured by the drift time. The WAMUS PDT's are made from alumium (Al) extrusion unit cells with the extrusions cut to the appropriate lengths. The unit cell for each PDT is 10.1 cm wide by 5.5 cm high. The top and bottom of each Al tube have vernier cathode pads and a central 50 μm gold plated tungsten sense wire. The hit resolution from the sense wire is approximately 0.5 mm.

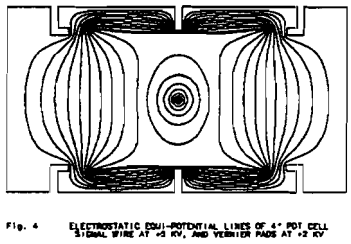

Figure 3.13: WAMUS PDT cell structure

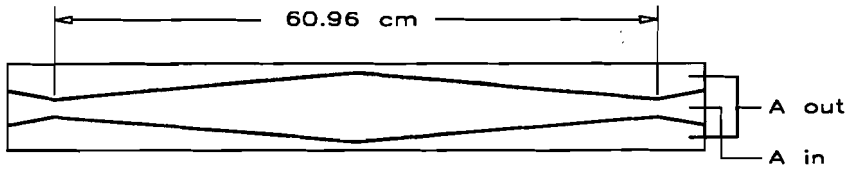

Figure 3.14: Top View of a WAMUS PDT cathode pad structure

The cathodes are copper-clad Glasteel (polyester and epoxy based plastic sheets with a fiber glass mat) which are cut into a repeating diamond pattern (Fig. 3.14). This pattern repeats itself every 61 cm. A relative transverse offset between the planes of the chambers allows one to solve the left/right drift-time ambiguity (Section 4.1). If there were any hits on the cathode pad in that tube, then a single bit output is set which is used in the Level 1 muon trigger; this bit is called the *pad latch* (Section 3.5.1.1). The tubes are filled with a mixture of Ar, CF_4 and CO_2 (90% : 5% : 5%) for a drift velocity of approximately 6.5 cm/μs.

The coordinate (ξ) along the wire direction is measured by the use of cathode pad signals and timing information from the anode wires. Wires from adjacent cells are jumpered at one end. A rough measurement of ξ is obtained by the measured time difference for a specific anode signal from the two ends of the paired wires. Finer calculation of ξ is achieved with the use of cathode pad signals. The two inner pads of a given cell are added and read independently of the sum from the outer pads. Sum and difference ratio calculations of the inner and outer signals give the ξ coordinate, modulo 30 cm half wavelength of the diamond pattern.

3.4.3.2 Small Angle Muon Spectrometer

The small angle muon spectrometer (SAMUS) consists of six stations of PDT's. Each station consists of three doublets of 29 mm diameter PDT's. These doublets are oriented in x, y and u directions (u is rotated 45° with respect to the xy plane to resolve multiple tracks). Individual PDT's in a doublet form a close packed array with adjacent tubes offset by half of a tube diameter. The unit cell is a 3 cm diameter stainless steel tube with a 50 μm gold plated W sense wire. The gas mixture is CF_4 and CH_4 (90% : 10%) with an average drift time of 9.7 cm/μs.

3.4.4 Level Ø Detector

The Level Ø (LØ) [54] Detector provides the lowest order trigger for DØ. It serves several important roles for DØ, namely:

- To provide luminosity monitoring;
- To detect multiple interactions within a beam crossing;
- To identify actual beam-beam interactions;
- To determine the z-coordinate of the interaction vertex.

LØ consists of two arrays of hodoscopes which are mounted on the face of the EC cryostats. The hodoscopes have a checker-board like pattern of scintillation counters, 1.6 cm thick, within a 45 cm radius circle that surround the beam pipe. The LØ detector provides nearly complete rapidity coverage over the range $2.2 \leq |\eta| \leq 3.9$, with partial coverage extending the overall range to $1.9 \leq |\eta| \leq 4.3$. The rapidity coverage is set by the requirement that a coincidence of both LØ detectors be $\geq$ 99% efficient in detecting non-diffractive inelastic collisions. The hodoscope arrays consist of two different types of counters. Eight long counters, 65 cm $\times$ 7 cm, cover the entire length of the array. The long counters are read out by two photomultiplier tubes, one at each end, and have a time-of-flight resolution of 80 picoseconds. Twenty short counters, 7 cm $\times$ 7 cm, have a single phototube on the outer edge and a time-of-flight resolution of 120 ps. Each array is made of two sub-planes, one arranged vertically and the other horizontally of short and long counters. Light guides are used to transport the light to photomultiplier tubes (PMT) situated on the outside of the array.

In addition to identifying inelastic collisions, the LØ trigger provides information on the z-cooordinate of the primary collision vertex to improve E_{T} calculations in the trigger system (Sections 3.5.1 and 3.5.2). This is of absolute necessity due to the large spread of

the Tevatron vertex distribution ($\pm$ 30 cm). The z-coordinate is determined from the time arrival difference for particles hitting the two arms of the LØ detector. A fast z-cooordinate determination, with a resolution of $\pm$ 15 cm, is available 800 ns after the collision. After 2.1 μs of the collision a more accurate determination of the z-cooordinate is available with a resolution of $\pm$ 3.5 cm.

3.5 Trigger and Data Acquisition

For Run 1A, the Tevatron was operated at a center of mass energy of 1.8 TeV with an average luminosity of 5×10^{30} cm^{-2}s^{-1}. The total cross section (elastic plus inelastic) for $p\bar{p} \rightarrow X$ at 1.8 TeV is approximately 70 mb. This yields roughly a hard scattering rate of 350,000 events per second (hertz—Hz). Unfortunately, from a physics perspective, an overwhelming number of these interactions are uninteresting to us! The trick is to pick out and save the interesting events. Muon bit patterns and the calorimeter variables for a given event are compared to logical programmable thresholds. A programmable threshold is called a trigger. Hence, the DØ trigger and data acquisition systems are used to select and record physics events of interest, for example multi muon events. Figure 3.15 is a schematic overview of the trigger and data acquisition systems.

There are three levels of the trigger system which are used to decipher relevant physics events. The Level Ø scintillator hardware indicates the occurance of an inelastic collision, *i.e.* distinguishes between beam-beam ($p\bar{p}$) and beam-gas collisions. For the data recorded for this analysis, the LØ rate was about 150–200 KHz.

Hardware elements arranged in a flexible software architecture comprise the Level 1 trigger. Most Level 1 triggers operate within the 3.5 μs time interval between beam crossings. However, several Level 1 triggers require several beam crossings to complete; they are referred to as the Level 1.5 triggers. The rate after both Level 1 and 1.5 is roughly

100–120 Hz.

Events that pass the hardware trigger are sent to a farm of 48 microprocessors—the Level 2 system (Section 3.5.2). The microprocessors reconstruct those events with a simplified version of DØ's standard reconstruction algorithms. The function of Level 2 is the reduction of the data rate to approximately 2 Hz before they are send along to the host computers for event monitoring and recording on permanent, magnetic storage media.

3.5.1 Level 1 Trigger

The Level 1 (L1) Trigger is a hardware trigger used to select physics events of interest. Its purpose is to provide a fast decision to keep or discard an event by comparing hit centroids from the muon system and/or energy sums in the Calorimeter in the event to programmable conditions. Triggers are a logical combination of AND-OR terms (latched bits). There are 256 different AND-OR terms. Each latched bit represents a specified detector information, *e.g.* two muon candidates within $|\eta| < 1$, $P_T^\mu > 3$ GeV/c, two calorimeter clusters over 10 GeV, *etc.* The gathering of the AND-OR terms and the determination whether a particular event satisifes one of the 30 possible triggers is done by the Level 1 Framework. The L1 Trigger processing stages are illustrated in Fig. 3.16.

3.5.1.1 Muon Level 1

The input for the muon L1 trigger [55] is based on one latch bit for each of the 16,700 drift cells of the system. The output separately consists of 16 L1 and L1.5 trigger bits. These bits represents the number of coarse muon candidates found within the five distinct trigger regions of the muon system (CF, EF North and South, SAMUS North and South). Each trigger region is divided azimuthally into quadrants, except for the CF which is divided into octants. When a charged particle traverses muon PDT's the electronic signal travels to one of the 24 Versibus Modular Eurocard (VME) digitizing crates, which contains a

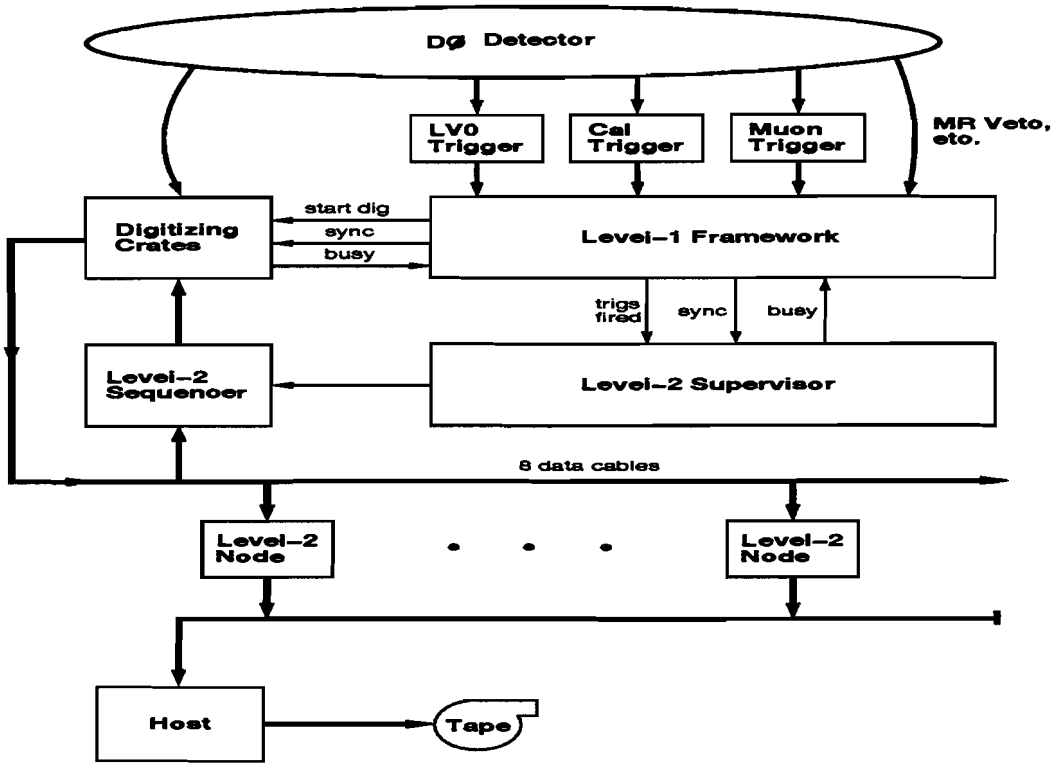

Figure 3.15: DØ Trigger and Data Acqusition System

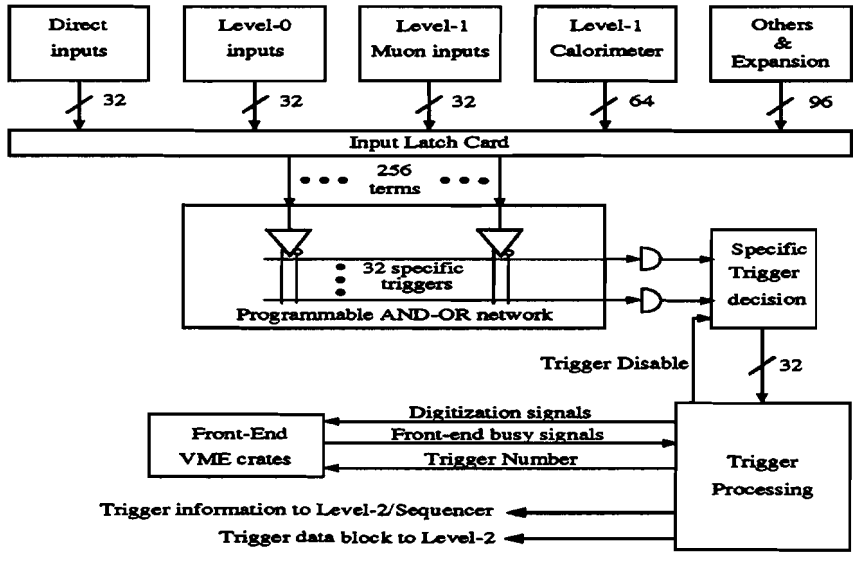

Figure 3.16: Level 1 Trigger processing stages

Motorola 68020 microprocessors and several module address cards (MAC) (200 MAC's in total). The microprocessors are used for downloading data and crude event building. Each muon module has a MAC to interface the module with the L1 Framework. The MAC acts to supply timing signal to the module front end, receive the latch bits, perform zero suppression for the data acquisition and generate trigger patterns. The latch bits are sent to the MAC in groups of three or four, respectively for each layers, at 10 MHz. The bit patterns from the MAC's corresponds to hit *centroids* for the muon trigger electronics.

Centroids represent probable intersections of tracks with a muon PDT. One assumes that a particle will hit at least two of the three tubes within a three column band—99% of the particles passing within 45° of normal incidence do. In WAMUS the tracks are projected to a single plane with resolution equal to half the width of a 10 cm cell. For three deck chambers, the track is projected to the center line of the middle deck and for four deck chambers the track is projected to the midplane of the third deck, nearest the toroid. All combinations of pairs of cells in different decks are tallied and assigned to the most likely half cell. Since SAMUS has only two layers of tubes, the centroid logic is simpler than WAMUS. For example, if a single isolated hit is reported, the centroid is assigned to the midpoint of the hit pair of tubes.

The centroids are produced with two granularities. Half-cell localization centroids are termed *fine* centroids. In WAMUS the fine centroids are localized to 5 cm and in SAMUS to 1.5 cm, except in the SAMUS u plane where the fine centroid is localized to 3 cm. Logical electronic grouping of fine centroids produces *coarse* centroids. In WAMUS, a the coarse centroid is a group of three fine centroids, while in SAMUS they are groups of four fine centroids. The coarse centroids from the MAC are transmitted to a Coarse Centroid Trigger (CCT) card. Each CCT is uniquely programmed to reflect the geometry of the chamber. The CCT logically combines the coarse centroids for each layer, which results in 20 coarse

centroids in the B and C-layers, and 12 coarse centroids in the A-layer. The coarse centroid resolution is 60 cm. An additional component of the muon trigger is implemented for a limited rapidity range—Level 1.5. L1.5 provides a more precise muon track and transverse momentum (P_T) information by comparing the course centroids to look-up tables stored in Octant Trigger Cards (OTC), which correspond to possible tracks with P_T thresholds. Once a coarse centroid has been determined and passed a programmed CCT logic, the event data is sent to the muon supervisor crate which interfaces with the muon clock system and the Trigger Framework.

3.5.1.2 Calorimeter Level 1

The Calorimeter L1 trigger [56, 57] adds adjoining cells in $\Delta\eta \times \Delta\phi$ (0.2×0.2) space to form trigger towers out to $|\eta| = 3.2$. Separate trigger inputs are provided for the electromagnetic and hadronic sections of the calorimeters. These trigger towers are summed to produce seven variables:

1. Global corrected electromagnetic transverse energy (E_T)
2. Global corrected hadronic E_T
3. Global corrected total E_T
4. Missing E_T
5. Global uncorrected electromagnetic E_T
6. Global uncorrected hadronic E_T
7. Global uncorrected total E_T.

The transverse energies are calculated from the energy sum of the Calorimeter cells within the respective trigger towers times the sine of the trigger tower's polar angle with respect to the interaction vertex provided by LØ. These seven variables are each compared with up to 32 programmable thresholds.

In addition to the above sums, each individual electromagnetic and hadronic trigger tower is compared to four programmable reference values. Also, the sum of the electromagnetic and hadronic transverse energies for each trigger tower is compared to four programmable thresholds.

3.5.1.3 Trigger Framework

The overall control for comparison of the L1 trigger bit patterns to the preset thresholds, the organization for the readout of the digitized crates and the interface to Level 2 resides in the Level 1 Framework [56, 57]. The Framework gathers digital information for each of the specific L1 triggers and determines whether a particular event is to be kept for further examination, all within the 3.5 μs beam crossing interval. If a specific trigger requires a L1.5 decision, the Framework starts the digitization cycle and holds the event waiting upon the L1.5 decision. If a trigger is satisfied, the results of the comparisons are used to set a trigger bit which is logically added to the information from the other detector systems (*e.g.* muon, TRD) to digitize the event and pass it through to the Level 2 system so that the microprocessors can recompute the input information to confirm the L1 decision. Also, the Framework coordinates various vetos which can inhibit triggers, provides the prescaling of triggers[8], correlates the triggers and readout functions, manages the communication tasks between the front-end electronics (the DØ detector) and the Trigger Control Computer (TCC), and provides a large number of scalers which allow monitoring of trigger rates and dead-times (time when the trigger and data acquisition system is unable to select or record events).

The digitizing hardware is 86 front-end VME crates. In Run 1A these crates were grouped into 32 *geographic sectors*. This grouping was necessary in order for the Framework to command the appropriate set of sectors to begin digitization when a trigger was satisfied.

[8] A prescale is some value N such that the acceptance for a satisfied trigger is 1:N.

When one of the sector's crate was unable to digitize another triggered event the sector sent a buzy signal back to the Framework. Under normal operational conditions, a crate can start digitizing a second event while a previous event is being transferred to Level 2 (a double buffered crate).

3.5.2 Level 2 System and Data Acquistion Architecture

The Level 2 (L2) System's [58, 59] function is to collect the digitized data from the L1 Framework, format the data into a dynamic data structure called Zebra[9] and apply software event filtering algorithms (fast preliminary reconstruction) on the data to reduce the rate from the approximate 100–120 Hz input to about 2 Hz output to the host computers.

The DØ data acquisition (DAQ) system and the L2 trigger hardware are closely intertwined. The system is based on a farm of 48 parallel microprocessors connected to the detector electronics and the L1 Framework by a set of eight 32-bit wide high speed data cables. The data cables are each a loop originating and terminating at a Sequencer card. All of the digitizing hardware VME crates contain a VME buffer/driver (VBD) card. The VBD card is connected to one of the eight data cables. The microprocessors are Digital Equipment Corporation 4000/60 workstations (nodes). The bus (a set of cables which connects two or more devices) of each node is extended out to its own VME crate. Each crate contains four dual multiport memory (MPM) boards which are connected to the data cables. the VAXELN real time operating system[10].

The eight data cables are controlled by the Sequencers and Supervisor processors. When there is a valid L1 trigger, the Supervisor prepares the event number, the crate readout, and polls the L2 processors to find one available to be the target for the data and enables

[9] An extension of FORTRAN [61] that allows for data memory usage to be set and incremented as a program is being executed.

[10] VAXELN is designed to gaurantee a precise and reliable response time to every system task. This operating system has no swapping and page faulting.

the node's MPMs to receive data from the cable. The information is sent to the Sequencers which start the circulation of *tokens* on the data cables. Tokens are network packets (collection of bytes) that are used to arbitrate access to the data cable. For example, a VBD may only transmit data while it is in possession of a readout token. When a VBD receives the readout token and has data to send, it grabs the token and dumps the data onto the cable. The data is stored in the available MPMs on the cable. After a crate has been read out, the VBD modifies another token. Once the target node has received the complete event, the event is converted into Zebra format. At this point, the filtering process begins. To monitor the performance and function of the L2 nodes, the Sequencer and Supervisor processors and the data flow a special processor, the Surveyer, collects statistics on the full system and provides diagnostics which are available for real-time displays and alarms.

3.5.2.1 Level 2 Filter

The filtering process [60] in each node is accomplished by a series of filter tools. Each tool has a specific function related to identification of a type of particle or event characteristic. Muons, jets, calorimeter electromagnetic clusters, track association with calorimeter clusters, E_{T} and missing E_{T} have their own filtering tools. For example, a muon filter tool may depend on a minimum number of tracks, minimum P_{T} for each track, and the maximum allowed pseudorapidity coverage. The tools are associated in particular combinations and ordered into *scripts*. Every one of the 30 programmable L1 triggers is associated with one or more scripts. For example, a single muon plus jet L1 trigger can have several L2 scripts depending on the muon and/or jet features present in the event. In all, there are a maximum of 128 software filters. Once an event passed its scripted filter the event is sent to the online cluster across a special high speed data cable link ($\approx$ 1500 Kbytes per second) to be logged and recorded onto 8 mm double density tapes from which point the *raw* event can be reconstructed with DØ's standard reconstruction algorithms.

3.6 Online Cluster

DØ's online cluster [33] serves as the interface to the detector systems. The cluster, comprised of three DECVAX microprocessors for Run 1A, is responsible for high level control data-taking system, downloading of all set table parameters (*i.e. trigger configuration*), specifying hardware monitoring activities and the recording and displaying of data collected by the detector ($p\bar{p}$ interactions, calibrations, monitoring information and alarms). The event data-taking system is designed to support flexible defined partitions of the detector, allowing for the collection of many tailored data streams. When the cluster receives the collected data from the Level 2 output cables, it logs these events to a staging disk, dispatches a sample for on-line monitoring purposes and spools the events from the staging disk to 8 mm tapes.

Chapter 4

EVENT RECONSTRUCTION

Once the raw events are recorded one must process the digital and analog[1] signals, with the inclusion of detector geometry and calibration information, to identify the final physics objects in the events, namely jets, leptons, photons, missing transverse energy. This conversion process is done by DØ's reconstruction software package DØReco. The primary function of DØReco is to identify and measure the kinematic properties of the physical objects that presumably originated from a $p\bar{p}$ collision.

There are three steps in the event reconstruction procedure.

1. Hit Finding: the raw digitized counts in the calorimeter cells and the counts per time bin for the tracking chamber wires are unpacked and converted into energy deposits and spatial locations;
2. Tracking and Clustering: spatially associated hits are joined together to produce tracks in the tracking chambers and clusters in the calorimeter;
3. Particle Identification: the tracks and energy clusters are constructed as candidate physics objects with their respective kinematic characteristics calculated. The particle identification criteria used at this stage are loose to minimize the loss

[1]The detector monitoring constants, *e.g.* high voltages, gas systems, *etc.*

of efficiency. Identifiers and quality flags are defined for each candidate object to aid the various analyses.

Following is a brief overview of DØReco's functionality as was implemented in version 11.

4.1 Central Tracking

In general, the track reconstruction outlined below is applied for all three central drift chambers (VTX, CDC, FDC). A more detailed discussion of algorithms used for each specific tracking chamber can be found in [62]. The prescription to be expanded is categorized as follows:

- Pulse and Hit Finding
- Segment Finding
- Segment Matching and Global Track Fit

First, the raw FADC (Fast Analog to Digital Converter) data, for a given sector and layer, were unpacked. The data contained the digitized information on charge versus time bin together with the associated wire address. For a given wire a pulse was recognized by the determination of leading and trailing edges. The leading edge of the pulse was determined by obtaining the center of gravity of the cluster between the beginning and the peak of the pulse. The trailing edge was found by comparing the pulse height of each bin with preset thresholds in conjunction with the difference between pulse heights of two adjacent bins. Hit finding represent the conversion of the pulse's corrected drift time information into the position of the pulse. The conversion was done by using known drift velocities measured during test beam. The drift velocities were corrected by calibration constants which took into account the channel-to-channel variations. These calibration constants were recorded when there were no $p\bar{p}$ collisions and were stored in a database accessed by

DØReco. Hits were found by determining the beginning and end position of a pulse from the difference between adjacent FADC bins and comparing them to threshold conditions. Each FADC bin was given a weight so that more importance was given to FADC bins from drift electrons which improved the resolution. Each signal on a sense wire was mapped onto two hits in the plane containing the wire and perpendicular to the direction of the incoming charged particle. Since the drift volume was divided by the sense wire into two symmetric halves, individual drift times cannot allow one to distinguish from which side of the wire the electrons drifted. This is called commonly left/right ambiguity. One hit corresponded to the true track while the other is its mirror image. In practice, left/right ambiguity was resolved in this detector by staggering the sense wires; the staggering breaks the symmetry between the two halves. The set of hits originating from the true track lended itself to a better straight line fit than the set from mirror images. Once all hits were found track segment finding began.

Segments were found by checking all of the hits along the wires of a given azimuthal sector. The *first* and *last* wire of an azimuthal sector defined a road in which one checked their respective hits in an attempt to search for best straight line fit in the r-ϕ plane. One then included hits from the intermediate wires if they were within a ϕ tolerance interval. When a sufficient predetermined number of matching hits were found an overall fit was performed. All matched hits were tagged because the segment finding process was repeated but this time the numerical ordering of the wires was reversed, *i.e.* first becomes last, last is first, *etc.* When all first-last wire combinations had been considered, matched hits which had the best line fit were kept as segment candidates. For each tracking chamber, segment candidates that match in ϕ and were within a predetermined distance of the midplane were considered to be track candidates. Once the track was fully reconstructed in three dimensions, the measure of ionization per unit length (dE/dx) was determined from a

truncated pulse height analysis. Succinctly stated, the truncated pulse height analysis computed the integrated pulse area[2] for each hit lying on a track and one took the average of the lowest 70% of the pulse height samples in order to minimize the effect of delta ray production. The dE/dx value was then the mean of the gaussian fit, where one employed a convoluted gaussian and exponential function to fit the resulting Landau distribution of the pulse area. Finally, track candidates from the respective tracking chambers were matched in a similar fashion within a given sub-detector.

The spatial resolution of a drift chamber was determined from the standard deviation of the residuals, which was the difference in the position of a hit between track candidates with and without the hit in question, and to the sense wires. Several contributors affect the spatial resolution. They were:

- Time resolution limited due to digitization resolution of the signal;
- Variation of electron diffusion with drift distance;
- Statistical fluctuations in the production of the primary ion pairs can cause the pulse to shift leading to a mismeasurement of the time;
- Non-uniform electric field especially at cell boundaries;
- Fluctuations in the gas mixture;
- Changes in pressure and temperature.

The first three listed effects were the primary contributors to the spatial resolution and were functionally represented by

$$\sigma^2 = \sigma_E^2 + \sigma_D^2 + \sigma_S^2 \ , \tag{4.1}$$

where σ_E^2, σ_D^2 and σ_S^2 denote the respective resolutions for electronic contribution, longitudinal diffusion and the statistical fluctuation in the number of ions produced close to the

[2]Gains, geometric and drift distance corrections were applied to the average pulse area.

sense wire [63].

The dE/dx resolution is sensitive to fluctuations in pulse height, such as pressure fluctuations, glow flow, *etc.*, and is expressed as

$$\left(\frac{\sigma}{E}\right) = 31.953n^{-0.428}\left(\frac{\alpha t}{I}\right)^{-0.32} , \tag{4.2}$$

where αt measured the number of primary ionization in the gas layer of thickness t, I is the effective ionization potential and n is the number of hits (pulse areas) on the track candidate.

The reconstruction resolution for tracks in the central region of the detector is approximately 0.014 cm in azimuth and 0.15 cm in the polar angle.

4.2 Vertex Finding

In order to calculate momentum components of the physics objects in an event, one must associate them with one of the interaction vertices in order to determine their azimuthal and polar angles. For the typical luminosity of Run 1A of 5×10^{30} cm^{-2}sec^{-1} there were 1.2 interactions per event. The vertex with the largest track multiplicity was considered the primary vertex of the $p\bar{p}$ interaction and all high P_T physics objects were assumed to originate from that point. The remaining vertices were most likely due to additional minimum-bias[3] $p\bar{p}$ interactions, irrelevant for our studies.

The z coordinate of the interaction vertex was extended along the beam direction with a width of approximately 30 cm. As a result, it was necessary to measure the z coordinate on a event-by-event basis. This was accomplished by the use of tracks from the central drift chamber (CDC). The procedure was as follows:

- Projected CDC track candidates to the center of the detector in the xy-plane;
- Removed tracks if their impact parameter was greater than 2.5 cm;

[3]Events which satisfied a trigger with maximum acceptance.

- Projected each track into the r-z plane and compute their intersection with the z-axis. Histogramed the z positions of the intersections. Searched for peaks of clustered tracks. One filled a new histogram for the largest peak with the mean of the histogram an estimate for the z coordinate of the primary vertex. Secondary vertices were found from any other peaks.

The z coordinate resolution was about 1–2 cm. Multiple vertices were separated if they were at least 7 cm apart.

The x and y coordinates of the vertex were known very well because the cross sectional area of the beam was minimized in this plane in order to achieve maximum luminosity. The average collision cross section at the collision point was roughly 50 μm with a location of 3–4 mm from the center of the detector. The measured deviation from the nominal beam spot location over the duration of Run 1A was less than 50 μm. Nonetheless, a precise xy position determination was still performed. CDC candidate tracks which had $r\phi$ impact parameter less than 2 cm and rz impact parameter less than 4 cm were extrapolated into the vertex chamber (VTX). The xy position, (x_o,y_o), was determined from the minimization of

$$S = \sum_{i=1}^{\text{tracks}} (1/\sigma_{\phi_i}^2)((y_i - y_o - \frac{dy}{dz} \cdot z_i)\cos\phi_i + (x_i - x_o - \frac{dx}{dz} \cdot z_i)\sin\phi_i)^2 \ , \qquad (4.3)$$

where x_i, y_i, ϕ_i are the center of gravity and angle of each VTX track in the $r\phi$ view, and σ_{ϕ_i} is the error associated with the ϕ measurement. The z position of the vertex to which the i^{th} track was associated was determined from the above paragraph's description, while dx/dz and dy/dz were the beam slopes in DØ coordinates. This minimization procedure was iterated three times and it gave a resolution of 60 μm for the beam's xy coordinate.

4.3 Calorimetric Towers

The deposited energy recorded as digitized counts in each calorimeter cell had to be converted back to a physical energy in units of GeV. The conversion factors were determined from the responses of the modules to the known energies of test beam particles. Cell-by-cell corrections were made for the variations in the electronic gain and pedestal values. These corrections were time dependent and retrieved by DØReco from a database which was updated from calibration runs without $p\bar{p}$ collisions. In other words, towers were energy deposits in localized calorimeter cells. DØ defined for each calorimeter cell i the directed energy vector $\vec{E}_i$ as

$$\vec{E}_i = \hat{n} E_i \ ,$$

where $\hat{n}$ was the unit vector pointing from the interaction point to the center of cell i and E_i was the magnitude of the energy deposit in cell i. The electromagnetic and hadronic cells with the same η and ϕ coordinates formed *towers*. From the cells that constitute a tower, the transverse energy of a tower was defined to be

$$E_T^{\text{tower}} = \sqrt{(E_x^{\text{tower}})^2 + (E_y^{\text{tower}})^2} \ , \tag{4.4}$$

with

$$E_x^{\text{tower}} = \sum_i^{ncells} E_i \sin\theta_i \cos\phi_i \tag{4.5}$$

$$E_y^{\text{tower}} = \sum_i^{ncells} E_i \sin\theta_i \sin\phi_i \ , \tag{4.6}$$

where θ_i and ϕ_i were the respective polar and azimuthal coordinate for cell i. The other kinematic quantities were calculated as follows

$$\phi_{\text{tower}} = \arctan(E_y^{\text{tower}}/E_x^{\text{tower}}) \tag{4.7}$$

$$\theta_{\text{tower}} = \arccos(E_z^{\text{tower}}/E^{\text{tower}}) \tag{4.8}$$

$$\eta_{\text{tower}} = -\ln\left(\tan\frac{\theta_{\text{tower}}}{2}\right) \ , \tag{4.9}$$

where

$$E_z^{\text{tower}} = \sum_i^{\text{ncells}} E_i^{\text{tower}} \cos\theta_i \tag{4.10}$$

and

$$E^{\text{tower}} = \sum_i^{\text{towers}} E_i^{\text{tower}} \ . \tag{4.11}$$

Towers were the building blocks for jet and electron/photon reconstruction.

4.4 Jet Reconstruction

The products of fragmentation or hadronization of quarks and gluons (partons) into collimated colorless, hadron collections are called jets[4]. To construct the jet's kinematic features from the localized energy cluster detected by the Calorimeter, DØReco used a fixed-cone algorithm. Specifically, the algorithm used a fixed-cone radius $\mathcal{R}$ in $\eta \times \phi$ space, where $\mathcal{R}$ was defined as $\mathcal{R} = \sqrt{\Delta\eta^2 + \Delta\phi^2}$. Four cone sizes were used, $\mathcal{R} = 0.3$, 0.5, 0.7, and 1.0. The implementation of DØ's fixed-cone algorithm was performed in three steps:

1. Preclustering of towers;
2. Cone clustering of preclusters;
3. Splitting/Merging of cone clusters.

The first stage of preclustering was the ordering of towers by decreasing E_{T}. This list only included towers which had a minimum deposited energy of 1 GeV. The highest $E_{\text{T}}^{\text{tower}}$ was taken as the starting point (*seed*) for the precluster. Adjacent towers were added to the precluster if they were within ± 0.3 units in $\eta \times \phi$ space from the seed. The towers included in the precluster were removed from the list of calorimeter towers. The remaining tower with the highest E_{T} was used as the next seed. This procedure was followed until all towers

[4]Experimentally observed in 1975 [66].

were exhausted. Once all towers were assigned to a precluster, the preclusters were ordered by E_T, the scalar sum of the towers' E_T, and cone clustering began.

The highest E_T precluster was used first. For each precluster one determined the E_T weighted center of gravity in η and ϕ coordinates, which was defined to be the axis of the precluster. All towers within a radius $\mathcal{R}$ of the axis were assigned to the cone cluster. Again the center of gravity was calculated with the previous procedure iterated until the axis moved less than 0.001 in $\eta \times \phi$ space. A maximum of 50 iterations was allowed in to order prevent the rare case of oscillation between multiple solutions from using an unreasonable amount of computer processing time. When an axis was stable in $\eta \times \phi$ space and if the cone cluster had an $E_T > 8$ GeV the cone cluster was kept and identified as a jet. The jet's axis was defined to be the stable cone cluster axis.

Jets were not allowed to share energy. When the second and subsequent jets were found a check was made if any of the jets shared any towers. At this point splitting/merging was performed. If two jets shared one or more towers the jet axes were compared. If the jets were separated by a distance less than 0.01 in $\eta \times \phi$ space the most recently constructed jet was dropped. If the jets had a distance greater than 0.01, then the ratio of the E_T sum of the common towers divided by the lowest E_T jet was calculated. If the fraction was less than or equal to 0.5, then the two jets were preserved with each shared cell assigned to the nearest jet. Otherwise, the pair of jets was considered to be a single jet with all towers assigned to the combined jet. Regardless, the jet axis and relevant kinematic variables were recalculated for all appropriate clusters. Approximately, 5% of jets were merged and 30% were split. When splitting/merging was completed the next precluster was used. Cone clustering continued until all preclusters were exhausted.

Once all the preclusters were used, the kinematic quantities for the reconstructed jets were determined. The E_T of a jet was defined to be

$$E_T^{\rm jet} = \sum_i^{\rm towers} E_{T_i} \ . \tag{4.12}$$

The remaining kinematic quantities for the jets were defined by

$$\phi_{\rm jet} = \arctan(E_y^{\rm jet}/E_x^{\rm jet}) \tag{4.13}$$

$$\theta_{\rm jet} = \arccos(E_z^{\rm jet}/E^{\rm jet}) \tag{4.14}$$

$$\eta_{\rm jet} = -\ln\left(\tan\frac{\theta_{jet}}{2}\right) \ , \tag{4.15}$$

with

$$E_x^{\rm jet} = \sum_i^{\rm towers} E_i \sin\theta_i \cos\phi_i \tag{4.16}$$

$$E_y^{\rm jet} = \sum_i^{\rm towers} E_i \sin\theta_i \sin\phi_i \tag{4.17}$$

$$E_z^{\rm jet} = \sum_i^{\rm towers} E_i \cos\theta_i \ , \tag{4.18}$$

where θ_i and ϕ_i were the respective polar and azimuthal coordinates for tower i.

DØ defined three "standard" jet quality variables for reconstructed jets with cone size of $\mathcal{R} = 0.7$ [67, 68]. They are:

1. Electromagnetic Fraction: this is the fraction of the jet energy which is contained by the electromagnetic portion of the Calorimeters. The EM fraction was required to be between 5–95% (Fig. 4.1);
2. Fine Coarse Hadronic Fraction: this is the fraction of the jet energy deposited in the coarse hadronic modules. This requirement was designed to remove fake jets introduced by main ring particles depositing energy in the Calorimeter. The FCH fraction was required to be less than 40% (Fig. 4.2);

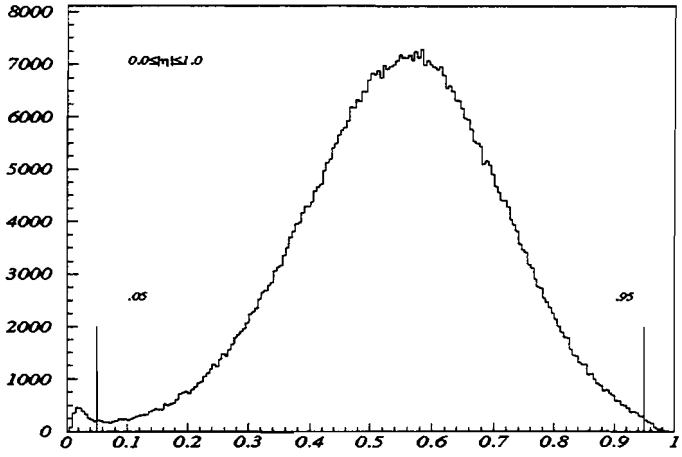

Figure 4.1: Electromagnetic Fraction Distribution for Jets with $\eta < 1$.

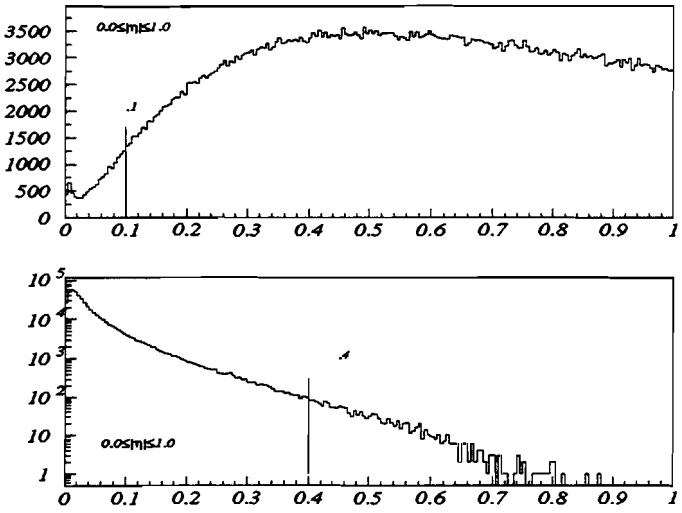

Figure 4.2: Hot Cell Ratio (top) and Fine Coarse Hadronic Fraction (bottom) for Jets with $\eta < 1$.

3. Hot Cell[5] Ratio: this is the ratio between the 2nd most energetic cell of a jet over the most energetic one. HC ratio was required to be greater than 10% (Fig. 4.2).

The jet energy resolution had been studied in the test beam from the transverse momentum balance in DØ's dijet events. The empirical formula for the jet E_T resolution was

$$\left(\frac{\sigma}{E_T}\right)^2 = C^2 + \frac{S^2}{E_T} + \frac{N^2}{E_T^2} \quad , \tag{4.19}$$

where C was an error term from the calibration, S represented the shower fluctuations in the sampling gap, and N denoted the contribution due to noise and the underlying event. S was the most important term to the jet resolution. Naively speaking, since the number of ions produced in the LAr was proportional to the traversing particle's energy ($\langle N_{\text{ions}} \rangle = \alpha E$) and the detected signal was proportional to the number of ions ($\langle D \rangle = \beta N_{ions}$), applying a Gaussian approximation to the Poisson distribution of N_{ions} one obtained

$$\frac{\sigma(D)}{\langle D \rangle} = \langle N_{ions} \rangle^{-1/2} = \alpha^{-1/2} \langle E \rangle^{-1/2} \ .$$

The parameters for jets located within the Central Calorimeter were determined to be: $C = 0$, $S = 0.74 \pm 0.005\ \sqrt{\text{GeV}}$ and $N = 1.9 \pm 0.2$ GeV.

4.4.1 Jet Corrections

The basic principle of event reconstruction was to rebuild the event identifying all physics objects. However, neither detector nor reconstruction program was perfect. Therefore, corrections were made, which will included corrections for hardware imperfections and systematic biases. In our present discussion, one would like the measured jet energy to give

[5] In DØReco "hot cells" were removed. Hot cells were defined to be:

(a) If a cell's $E_T \geq 10$ GeV and the cell's energy was more than 10 times the sum of the energies in the cell immediately above and immediately below, in the same tower; or

(b) If the candidate hot cell was in the first electromagnetic layer or the outer most course hadronic cell, then if its energy was 10 times the energy of one adjacent cell in the tower.

back the original parton energy. However, due to the extended, multiparticle nature of jets the reconstructed jet's energy was not necessarily the parent parton's energy. A few of the correction factors for reconstructed jets were:

- The calorimeter's energy scale;
- The non-linearity of the calorimeter's response at energies below 5 GeV. The sum of the calorimeter cells will give the incorrect total energy since jets are comprised of particles of varying energies, including many low P_T particles;
- The addition of energy from partons in the hadrons which do not participate in the hard scatter but do deposit energy into the calorimeter (*underlying event*), and from the calorimeter itself, *i.e.* uranium decay, hardware pedestal cut (*zero-suppression*), *etc.*;
- Energy from final state radiation of the parent parton which were not fully contained in the fixed-cone of the jet.

To correct for the energy scale, DØ first calibrated the electromagnetic layers of the central calorimeter by constraining the $Z \rightarrow e^+e^-$ mass to the measured LEP value[6]. This was roughly a 5% correction in the central calorimeter. Afterwards, the central hadronic layers were calibrated to the electromagnetic section by a procedure called *missing transverse energy projection fraction* (MPF). MPF assumed that the missing E_T ($\not\!\!E_T$) in an event was primarily due to jet energy mismeasurement. One studied events which consist solely of an electromagnetic jet (a single isolated photon) and a hadronic jet lying opposite in azimuth. Ideally, there should be no neutrinos in the event assuring us that any $\not\!\!E_T$ in the event was ascribed to the energy mismeasurement of the hadronic jet. By projecting

[6] 91.187 GeV/c^2

the MEt along the electromagnetic jet axis one derived the necessary correction. That was,

$$E_{\mathrm{T}}^{\mathrm{meas}} = \left(1 + \frac{\vec{\not{E}}_{\mathrm{T}} \cdot \hat{n}_{\mathrm{T}}^{\mathrm{EM-jet}}}{E_{\mathrm{T}}^{\mathrm{EM-jet}}}\right) \cdot E_{\mathrm{T}}^{\mathrm{true}} \ , \tag{4.20}$$

where $\hat{n}_{\mathrm{T}}^{\mathrm{EM-jet}}$ was the unit vector of the electromagnetic jet axis. The ratio

$$\frac{\vec{\not{E}}_{\mathrm{T}} \cdot \hat{n}_{\mathrm{T}}^{\mathrm{EM-jet}}}{E_{\mathrm{T}}^{\mathrm{EM-jet}}}$$

was the missing E_{T} projection fraction. Finally, the end calorimeters were calibrated to the central region. This was accomplished by the balance of missing E_{T} in dijet events where one jet was centrally located and the other was in one of the end calorimeters.

The energy contributions due to spectator events and detector effects were measured from single minimum-bias runs. The underlying event's E_{T} was found to be constant in η and ϕ with a measured value of $\mathrm{d}^2E_{\mathrm{T}}/\mathrm{d}\eta\mathrm{d}\phi = 0.55 \pm 0.1$ GeV, whereas the energy due to detector effects was parametrized to be constant in η and ϕ with a value of $\mathrm{d}^2E_{\mathrm{T}}/\mathrm{d}\eta\mathrm{d}\phi = 1.36 \pm 0.2$ GeV [65]. An integration over η and ϕ within each fixed-cone determined the corrected E_{T} due to detector effects.

Corrections to the Calorimeter's non-linearities and out-of-cone showering were obtained from Monte Carlo events. It was found that for $\mathcal{R} = 0.5$, 96% of the jet's energy was reconstructed independent of the input Monte Carlo jet energy [64]. A detailed discussion concerning the non-linearity of the Calorimeter can be found in [65].

4.5 Electron/Photon Reconstruction

In contrast to the fixed-cone algorithm used for jet construction, electron[7]/photon[8] construction and identification used a nearest-neighbor algorithm. Electromagnetic (EM) towers, defined to be the four EM Calorimeter layers plus the first layer of the Fine Hadronic

[7]Experimentally observed in 1897 [69].

[8]Robert A. Millikan in 1915 experimentally verified Einstein's hypothesis that light *is* quanta.

Calorimeter, were ordered by decreasing E_T. From the highest E_T tower, the nearest-neighbor algorithm formed clusters by the addition of adjacent towers above 50 MeV. The summation of adjacent towers, with each included tower appropriately tallied, continued until there were no adjacent towers above 50 MeV. From the next energetically allowable tower, not previously associated with a cluster, started the next cluster search. After all the energetically permissable towers were clustered, electron/photon identification proceeded as follows for clusters above 1.5 GeV:

- Each energy cluster was required to have a minimum of 90% of its total energy deposited in the EM layers;
- At least 40% of the energy was contained in a single tower;
- For an electron candidate, a minimum of one associated central track, CDC or FDC, matching the cluster within a road of typically 0.1×0.1 radians in $\eta \times \phi$ space about the axis defined by the vertex and the cluster centroid. If no central track was associated with the cluster, then the cluster was considered a photon candidate.

For all electromagnetic cluster candidates the centroid of the cluster was determined. The necessity of the centroid was apparent. Without a central magnetic field to help identify tracks that may be mistakenly matched to a photon from a neutral meson decay (*e.g.* π^0, η), thus creating a *fake electron* background for electron candidates, one needed to know the center of gravity for the showers to allow a precise match with a central track to accomplish the desired rejection of fake candidates. The cells in the third electromagnetic layer were used for the centroid calculation because of that layer's fine segmentation, 0.05×0.05 in $\eta \times \phi$ space. The centroid was defined to be the log-weighted center of gravity (COG),

$$\vec{x}_{COG} = \frac{\sum_i w_i \vec{x}_i}{\sum_i w_i} \ ,$$

where $\vec{x}_i$ and w_i were the respective center position and weight of cell i. The weight was defined as

$$w_i = \max\left(0, w_o + \ln\left(\frac{E_i}{\sum_j E_j}\right)\right) ,$$

where E was the deposited energy of a cell and w_o was a cell dependent parameter chosen such that to optimize the position resolution. The resolution of the centroid was position, energy and angle dependent. Typical resolution values for high P_T electrons in the Central and End Calorimeters were 6 mm and 2 mm respectively. From $\vec{x}_{COG}$ the various kinematic relations were determined.

To aid in the identification of electrons/photons DØReco used the correlations between energy depositions in the calorimeter cells based on the longitudinal and transverse shower shapes of typical electrons/photons determined from Monte Carlo and test beam events. The correlations were related by a covariance matrix called the H-matrix. DØ defined the covariance matrix as

$$M_{ij} = \frac{1}{N}\sum_{n=1}^{N}(x_i^n - \langle x_i\rangle)(x_j^n - \langle x_j\rangle) , \tag{4.21}$$

where N was the number of electrons/photons used in the test beam, $x_{i,j}^n$ was the value of observable $i(j)$ for electron/photon n and $\langle x_{i,j}\rangle$ was the mean value of the observable $i(j)$ for the sample. In all, there are 41 variables used for the covariant matrix. If M was invertible, then one defined $H \equiv M^{-1}$. To determine the degree in which a given electron candidate had a shower shape consistent with that of an electron one computed the covariance parameter

$$\chi^2 = \sum_{i,j}(x_i^k - \langle x_i\rangle)H_{ij}(x_j^k - \langle x_j\rangle) . \tag{4.22}$$

This χ^2 was extremely powerful in the separation of electromagnetic and hadronic showers as illustrated in Fig. 4.3. Furthermore, to ensure good electron/photon identification, qualifiers, such as track match significance, number of cells in the cluster, isolation variables,

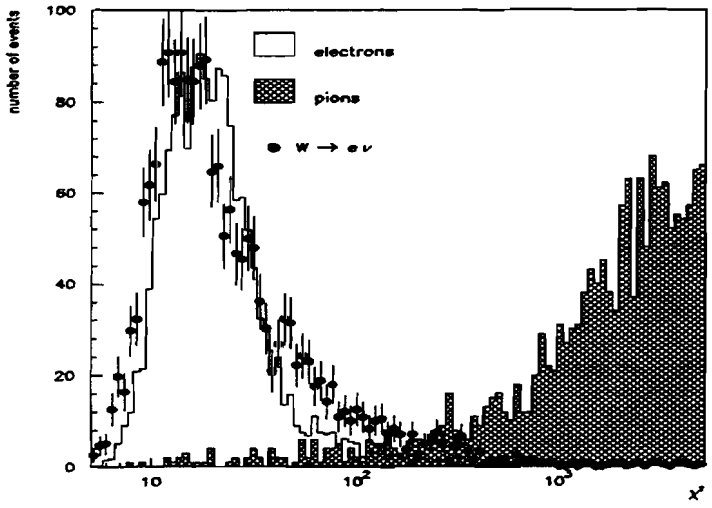

Figure 4.3: χ^2 distribution for test beam electrons (unshaded), test beam pions (shaded), and electrons from W's (dots).

track ionization, *etc.*, were calculated for each candidate.

The Calorimeter's response was linear as a function of energy to better than 0.3% for electron energies greater than 10 GeV. The resolution for the electron/photon candidate was given by Equation 1.2. For electrons in the central region of the Calorimeter test-beam studies showed $C = 0.003 \pm 0.002$, $S = 0.157 \pm 0.005\ \sqrt{\text{GeV}}$ and $N = 0.3 \pm 0.2$ GeV.

4.5.1 Electron/Photon Corrections

Since the electromagnetic shower initiated by an electron or a photon was concentrated in a much smaller volume than a typical hadronic shower, the primary correction to electron/photon reconstruction was the energy scale, which was discussed in detail in Section 4.4.1. Another correction of vital importance was the position resolution for the COG of a cluster. Detailed studies of Monte Carlo events and $Z \rightarrow e^+e^-$ data had been carried out to parametrize and correct biases associated with the log-weighted centroid.

4.6 Muon Reconstruction

The reconstruction of muon[9] candidates was similar in principle to track finding in the central detectors but the differences lied in the geometry and the front-end electronics of the muon system. The raw muon data consisted of a digital pad-latch information indicating a possible hit and its associated series of analogue signals that corresponded to the drift time, delta time and cathode pad charges. Muon reconstruction was performed in three steps:

1. Hit Sorting: the muon system's digitized and analog counts were unpacked and converted into spacial locations;
2. Segment and Track Finding: the hits were assigned to obtain the best muon track candidate;
3. Global Fit: the muon track candidate were associated to tracks in the Central Tracking System.

One began with the identification of hit chambers. The time and delta time for the hit chambers were corrected for channel-to-channel variations from electronic calibration constants measured when no $p\bar{p}$ collisions occurred. These constants were stored and later retrieved by DØReco in databases. Charge values were corrected for pedestals and gains, while the drift times were corrected for time-of-flight and then converted to drift distances. Hits with at least one pad-latch and a physical drift time were kept. To obtain space points in the DØ global coordinate system survey constants were used to translate the hits from chamber coordinates. However, due to left/right ambiguity in the drift cell there were two space points associated with each hit (Section 4.1).

The next step in the construction of muon candidates was the pattern recognition of the hits. The assignment of hits into line segments, via a least squares fit algorithm,

[9]Experimentally observed in 1936 [70].

was done separately for the bend (r-z plane—drift measured) and non-bend (r-ϕ plane) views. Furthermore, A-layer and BC-layer hits were fitted separately (due to the physical separation by the toroids). The differance in the time measurements were used to seed the list of vernier pad solutions. Pad solutions that minimized a goodness of fit test were assumed to be the correct pad solutions. Drift distances were also used in the fit thus resolving the left-right ambiguity. The bend view assumed two straight line fits with both of the lines constrained to meet in the magnet center, while the non-bend view assumed a straight line fit through the magnet. BC-segments required a minimum of four planes out of six and A-layer segments required a minimum of two out of four planes. At this stage, all segments were required to have an impact parameter to the primary interaction vertex within 3–5 m.

To find candidate muon tracks a road algorithm was used. BC-layer hits were fitted first with the resultant track segment extrapolated to the midplane of the magnet from which a pseudo-point in the plane was used to help fit the hits in the A-layer. If no A-layer segment was found, then the pseudo-point, in conjunction with the vertex point, was used to define the segment inside the magnet. If no BC-segment existed, then the track finding started with A-layer segments extended into the B or C-layers. In order to have a muon track candidate hits were required to be on tracks in both views. Once a track candidate was made its kinematic variables were calculated from the direction cosines inside the toroids.

The track candidate momentum was determined from the bend angle in the bend view. In the non-bend view a straight line was fitted through the magnet with the track constrained to originate from the vertex. The preliminary momentum value was corrected for muon energy loss by employing look-up tables determined from Monte Carlo events. However, if a muon track was associated with a central detector (CD) track (thus knowing the trajectory of the muon before the magnet more accurately), then muon momentum was

measured more precisely. The final correction to the momentum was done by a *global fit*.

The idea of a global fit is intuitive—use all the available information for a muon track candidate to check its consistency and to improve the track momentum measurement. The global fit was a seven parameter least squares fit, which in addition to track segments took into account the Multiple Coulomb Scattering in the Calorimeter and constrained the track to the interaction point. There were 16 inputs to the global fit which were:

- 2 VTX measurements of the vertex point—(Y,Z);
- 4 CD measurements which gave the slope and intercept of the best matched CD track in XY and RZ views;
- 2 angle measurements (set to mean values which are equal to zero) which described the Multiple Coulomb Scattering that occurred in the Calorimeter;
- 4 tracking measurements which gave the slope and intercept in both views for A-layer tracks;
- 4 tracking measurements which gave the slope and intercept in both views for BC-layer tracks.

The resultant 7 parameters were:

- 4 parameters for the muon track in the CD;
- 2 parameters that described the deflection of the muon in the Calorimeter due to Multiple Coulomb Scattering;
- 1 parameter for the inverse of the muon momentum ($1/p$).

For the data set studied for this analysis, approximately 70% of the muon track candidates were globally fitted.

Muon momentum resolution was limited by various effects, namely chamber alignment uncertainties, geometric design constraints, resolution of measured space points and Multiple Coulomb Scattering in the Calorimeter and toroid. Resolution of low momentum tracks was dominated by multiple scattering. High momentum track resolution was primarily hampered by the measurement limitations of space points due to the uncertainty of the deflection angle through the magnetic field. The muon momentum resolution was parametrized as

$$\left(\frac{\delta p}{p}\right)^2 = \left(\frac{0.18(p-2)}{p}\right)^2 + (0.008p)^2 \ . \tag{4.23}$$

The first term characterized the limit on the resolution due to Multiple Coulomb Scattering, while the second term described space point drift resolution and chamber alignment errors.

Several quality flags were determined for all muon track candidates to help discriminate against spurious tracks. One evaluated the goodness of the track, by looking at the quality of fit in bend and non-bend views, layers used for track, vertex projection and hit combination. These quality indicators were combined into a single global quality word, IFW4. Another tool to aid in identifying good muons was the measured energy deposition of the track within the Calorimeter. A minimum ionizing particle (MIP), such as a muon, had a characteristic energy deposition signature. For muons, most of the energy was deposited in the hadronic layers of the calorimeter. Furthermore, a muon that originates from the interaction point will have hit calorimeter cells tracing back to the vertex. Hence, the combined calorimetric information just mentioned were used to verify the integrity of the muon track along its projected path through the Calorimeter. Another useful parameter was the path length through the toroids—the amount of magnetic field trasversed by the muon ($\int \vec{B} \cdot d\vec{l}$). Other quality parameters, such as *isolation parameter*, *impact parameter*, *track timing*, were also calculated. Specific muon quality requirements will be discussed in Chapter 6.

4.6.1 Muon Corrections

The reprocessing of the raw data with improved versions of DØReco was the only available method to correct muons for this analysis. With each new reconstruction software version, improvements were implemented because of a better understanding of the muon system: more reliable alignment constants of the muon chambers with respect to each other and to the other subdetectors, more accurate time-to-distance relations, and clever methods to include information from the other subdetectors.

4.7 Neutrinos: Missing E_T

Neutrinos[10] are not directly detected because they are neutral and weakly interacting. Their existence were originally postulated by Wolfgang Pauli [72] to ensure momentum and angular momentum conservation in weak decays. At DØ we inferred the presence of neutrinos in an interaction by imposing transverse momentum conservation in an event. The longitudinal momenta of the final state cannot be precisely measured because many forward particles are lost in the beam pipe. These lost particles carry a negligible fraction of the total transverse momentum, which was calculated from the vector sum of all observed entities in the event. Any presence of an energy imbalance was defined as missing transverse energy ($\not\!\!E_T$). Hence, the "detection" of neutrinos was done via $\not\!\!E_T$.

DØReco introduced three different types of missing transverse momentum measurements. The first was based on the energy imbalance in the Calorimeter alone. The second was a correction to the first which includes information from the ICD and Massless Gaps. The third type of $\not\!\!E_T$ incorporated muons to the known measured energy of the event. Since the Calorimeter measured energy and not momentum, DØ defined the Calorimeter

[10] Experimentally observed in 1956.

$\not\!\!E_T$ as follows

$$\not\!\!E_x^{\rm Cal} = -\sum_{i=1}^{ncells} E_i \sin\theta_i \cos\phi_i \tag{4.24}$$

$$\not\!\!E_y^{\rm Cal} = -\sum_{i=1}^{ncells} E_i \sin\theta_i \sin\phi_i \tag{4.25}$$

$$\not\!\!E_T^{\rm Cal} = \sqrt{(\not\!\!E_x^{Cal})^2 + (\not\!\!E_y^{Cal})^2}\,, \tag{4.26}$$

where E_i, θ_i and ϕ_i were the respective deposited energy, and polar and azimuthal angles (measured from the center of the cell in relation to the primary vertex of the event) of cell i. The cells of the ICD and Massless Gaps were included in the summed cells for the first correction to the $\not\!\!E_T$. It was this value of $\not\!\!E_T$ which was typically quoted as the Calorimeter missing energy. If muon candidates were present in the event, then the final $\not\!\!E_T$ estimate was the subtraction of the transverse momenta and energy deposit of all muon tracks. Hence, the muon corrected missing E_T was

$$\not\!\!E_x = \not\!\!E_x^{\rm Cal} - \sum_\mu (P^\mu - E^{\rm dep}) \sin\theta_\mu \cos\phi_\mu \tag{4.27}$$

$$\not\!\!E_y = \not\!\!E_y^{\rm Cal} - \sum_\mu (P^\mu - E^{\rm dep}) \sin\theta_\mu \sin\phi_\mu \tag{4.28}$$

$$\not\!\!E_T = \sqrt{\not\!\!E_x^2 + \not\!\!E_y^2}\,, \tag{4.29}$$

where P_μ, $E^{\rm dep}$, θ_μ, and ϕ_μ were the muon momentum, expected muon calorimeter energy deposition (determined from Monte Carlo simulation), and polar and azimuthal angles, respectively. The other kinematic quantities were calculated for each distinctive $\not\!\!E_T$ from their respective momentum components.

The $\not\!\!E_T$ resolution of the DØ Calorimeter had been parametrized as

$$\sigma_T = a + b \cdot S_T + c \cdot S_T^2 \quad , \tag{4.30}$$

with $a = 1.89 \pm 0.05$ GeV, $b = (6.7 \pm 0.7) \times 10^{-3}$, $c = (9.9 \pm 2.1) \times 10^{-6}$ GeV^{-1}, and where S_T was the summed transverse energy in the calorimeter.

4.7.1 Missing E_T Corrections

By definition, $\not\!\!E_T$ was the vector sum of calorimeter cells not associated with any reconstructed candidate object which contributed to the energy imbalance in the event. If the energy of any candidate object was mismeasured, then the $\not\!\!E_T$ was mismeasured by the same amount. Any corrections made to jet and electron/photon candidates (except for detector noise, underlying event and out-of-cone effects), or rejection of bad muon candidates, were also propagated to the $\not\!\!E_T$. In practice, as each object was corrected one added the uncorrected object's $\vec{E}_T$ to $\vec{\not\!\!E}_T^{\,\mathrm{Cal}}$ and then subtracted the corrected object's $\vec{E}_T$.

4.8 Reconstruction Verification

Our understanding of the DØ detector was constantly evolving since data taking started in April of 1992. The education still continues and is reflected in a multitude of versions of DØReco. Each version of DØReco required a thorough verification of the algorithms. The author was personally involved in the verification process of the muon reconstruction code for all of the Run 1A data. The events used for muon reconstruction verification were selected J/ψ candidates. We studied the difference between many versions of DØReco for muon and J/ψ momenta, mass resolution of the J/ψ, and muon criteria quality flags. Similar verification on different event samples was done for the other DØReco algorithms. At the end of the run, all the events of Run 1A were processed with the DØReco version 11. This was the reconstruction version used for this analysis and applied to the Monte Carlo simulated events.

4.9 Reconstruction Output Files

There were two output files from DØReco [33] used for the different analyses, and greatly used for this analysis. They were:

4.9. *RECONSTRUCTION OUTPUT FILES*

- STA File: Contained the raw data plus the complete results of the reconstruction. STA files were on the average 600 kilobytes/event. They were used for event reprocessing and event displays.

- DST (Data Summary Tape) File: Contained a compressed version of the full reconstruction results. A DST contained summaries of central detectors and muon tracks, calorimeter clusters, and all parameters for electron, photon, muon, tau and jet candidates, and missing E_T. The DST event size was approximately 20 kilobytes.

Chapter 5

MONTE CARLO EVENT SIMULATION

"The essence of life is statistical improbability on a colossal scale." Richard Dawkins

To study the signatures of and backgrounds to various physics processes and to include detector effects, high energy experimentalists use computer simulations of physics events, generically known as *Monte Carlo* simulations. Monte Carlo techniques are used to generate complete events, from partonic state to the observable particles. Monte Carlo algorithms calculate integrals by performing $\mathcal{N}$ random samplings of the integrand to determine a resultant average. Such integrals arise from constraints on phase space and other continuous variables which describe the event. Furthermore, Monte Carlos programs must incorporate detector response in order to understand effects such as detector and trigger acceptances and efficiencies. The simulated physics events are reconstructed and analyzed the same way as experimental data. However, one must be forewarned. The reliability of the Monte Carlo events is strongly dependent on the physics model one has implemented as the computer algorithm. No one calculational technique contains all of the possibly relevant physics processes. For example, perturbative QCD provides a good description of hard interactions with momentum transfers greater than 1 GeV/c but one experimentally observes hadrons, not basic objects, quarks and gluons, of perturbative QCD. The formation of hadrons is theoretically described by nonperturbative QCD processes characterized by small momen-

tum transfers. At present, nonperturbative QCD is not understood in any fundamental way although there exist a variety of phenomenological models which attempt to explain nonperturbative hadronization, *e.g.* string fragmentation [73], independent fragmentation [74] and cluster fragmentation [75][76]. Since very few problems in physics are exactly solvable theoretical uncertainties naturally arise. Such being the case, Monte Carlo generators have inherent uncertainties. One should be aware of all liabilities of the Monte Carlo when estimating rates or background to the physics process one is studying. The following quote from J. D. Bjorken chides the experimentalist's reliance on Monte Carlo [77].

> "Another change that I find disturbing is the rising tyranny of Carlo[1]. No, I don't mean that fellow who runs CERN, but the other one, with first name Monte. The simultaneous increase in detector complexity and in computation power has made simulation techniques an essential feature of contemporary experimentation. The Monte Carlo simulation has become the major means of visualization of not only detector performance but also physics phenomena. So far so good. But it often happens that the physics simulations provided by the Monte Carlo generators carry the authority of data itself. They look like data and feel like data, and if one is not careful they are accepted as if they were data. All Monte Carlo codes come with a GIGO (garbage in, garbage out) warning label. But the GIGO warning label is just as easy for a physicist to ignore as that little message on a pack of cigarettes is for a chain smoker to ignore. I see nowadays experimental papers that claim agreement with QCD (translation: someone's simulation labeled QCD) and/or disagreement with an alternative piece of physics (translation: an unrealistic simulation), without much evidence of the inputs into those simulations."

[1] Carlo Rubbia: director of CERN from 1989–1993. 1983 Physics Nobel Laureate for the discovery of the W/Z vector bosons.

In this chapter we will describe the event generator, detector simulations and the different types of Monte Carlo samples used for this thesis. We will also discuss the program used for the calculation of next-to-leading order heavy quark cross sections.

5.1 Event Generator: ISAJET

Since the pioneering work of Feynman and Field to simulate high P_T physics events [74], Monte Carlo programs used in high energy physics combine perturbative and nonperturbative QCD. All QCD Monte Carlo programs must describe the complete range of momentum transfer (Q^2) from the initial hard scatter to the formation of hadrons at $Q^2 \leq 1$ GeV^2/c^2. Furthermore, high energy Monte Carlo programs must take into account the specific experimental environment, such as fixed target, hadron-hadron and electron-positron collisions, in order to model the physics process under investigation. At DØ three event generators were used to aid the diverse data analyses—HERWIG, ISAJET and PYTHIA. For this thesis ISAJET [78] was used exclusively to generate all Monte Carlo events. Event simulation in ISAJET followed four distinct steps (like all hadron-hadron generators) (see Fig. 5.1). The four steps were:

1. The Initial Hard Scatter
2. QCD Evolution
3. Hadronization
4. Beam Jet Fragmentation

In the following subsections we will present a brief overview of the above mentioned event generator steps.

5.1.1 The Hard Scatter

The initial step to simulate events at the Tevatron was to numerically calculate the $p\bar{p}$ cross section from the QCD perturbative leading order two body hard scattering interaction

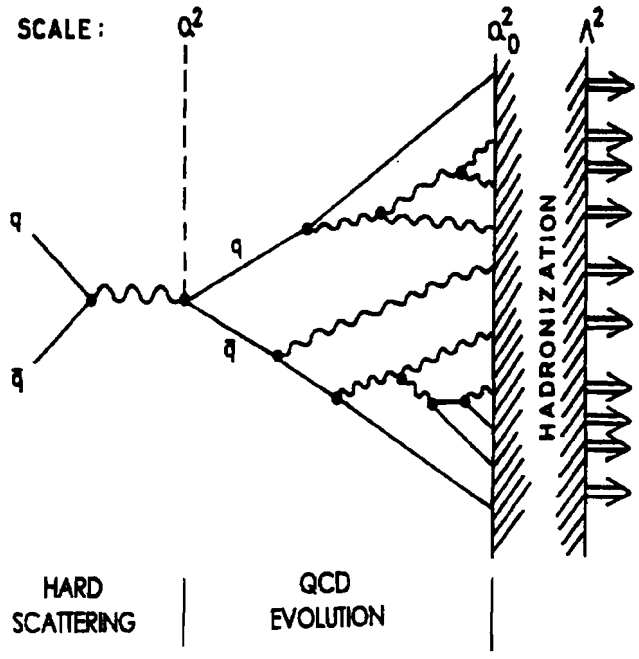

Figure 5.1: Schematic illustration of a $q\bar{q}$ collision.

cross section ($\hat{\sigma}_{ij\to k}$), convoluted with the product of parton distribution functions which incorporate leading-log approximations[2]. The cross section is written as

$$\sigma_{ij\to k} = \int dx_i \int dx_j \; f_i(x_i, Q^2) f_j(x_j, Q^2) \hat{\sigma}_{ij\to k} \; , \tag{5.1}$$

where $x_i = p_i/p$ is the momentum fraction of parton i, Q^2 is the momentum transfer, and $f_i(x_i, Q^2)$ and $f_j(x_j, Q^2)$ are the parton density distribution functions which measures the probability that parton i, j is found with a momentum p between $x_{i,j}p$ and $(x_{i,j} + dx_{i,j})p$. The Monte Carlo samples used for this thesis were generated with ISAJET's default struction functions EHLQ (Eichten, Hinchliffe, Lane and Quigg) [78]. ISAJET allowed the user to specify the kinematic limits for the primary partons, *e.g.* transverse momenta, pseudorapidity and azimuthal angle ranges, in order to bound the cross section within these

[2]In the leading-log approximation terms of the form $\alpha_s^n \left(\ln\left(Q^2/Q_o^2\right)^m\right)$ are retained only for $m \leq n$.

kinematic limits. To simplify the numerical calculations, the perturbative expansion was truncated at low order in the strong coupling constant (α_s) because if the value of Q^2 was of the order for the scale of the hard scatter, then there would be no large logarithms in the expansion of Equation 2.1 [79].

5.1.2 QCD Evolution

After the primary hard scatter was generated, QCD radiative corrections were added to model jet multiplicity in order to obtain the correct event structure. This is especially important at Tevatron energies. All partons involved in the hard scatter were evolved through repeated parton branchings, as modeled in ISAJET by Sjostrand's branching approximation for initial state gluon radiation [80], and by Fox and Wolfram's branching approximation for final state radiation [81]. Approximate QCD radiative corrections to arbitrary order were included by the emission of gluons and gluon splitting into $q\bar{q}$ pairs for both initial and final state partons.

Parton showers are based on an iterative use of the basic $q \to qg$, $g \to gg$ and $g \to q\bar{q}$ branching processes. In general, the branching approximation was calculated as follows [82]. The probability $\mathcal{P}$ that a branching $a \to bc$ will take place during a small change in the evolution parameter dt ($t = \ln(Q^2/\Lambda^2_{\rm QCD})$) is given by the Altarelli-Parisi equations [83]

$$\frac{d\mathcal{P}}{dt} = \frac{1}{2\pi}\int dz\ \alpha_s(Q^2)P_{a\to bc}(z)\ , \tag{5.2}$$

where $P_{a\to bc}(z)$ are the standard Altarelli-Parisi splitting functions, z is the momentum fraction of the initial parton a carried off by b/c, and $\alpha_s(Q^2)$ is the strong coupling constant (typically evaluated only to first order). From the maximum allowed mass for parton a, t was successively degraded until a branching occurred. The value of t at which a branching occurred (t_b) was determined from the probability $\Pi(t_o, t_b)$ for evolving from an initial value

t_o to a final value t_b while emitting no parton radiation. Specifically, if

$$\Pi(t_o, t_b) = \frac{\alpha_s(t_o)}{\alpha_s(t_b)}^{2\gamma(z_c)/b_o} , \tag{5.3}$$

where

$$\gamma(z_c) = \int_{z_c}^{1-z_c} dz P(z) ,$$

with z_c expressed in terms of a suitable cutoff value for t (t_c) to avoid infrared and collinear singularities, then t_b may be derived from the derivative

$$\Xi(t_b) = \frac{\partial \Pi(t_o, t_b)}{\partial t_b} ,$$

since this gives the distribution for the mass t_b at which the first resolvable radiation occurs. The products, b and c, were then allowed to branch with a new z selected from $P(z)$ and their respective masses were evolved starting from zt_b and $(1-z)t_b$.

The cutoff value t_c, know as the regularization scale, was introduced in the branching process to avoid a breakdown with perturbation theory at low energy scales. t_c prevents the evolution of parton masses below some minimum value $t < \ln(Q^2_{\rm min}/\Lambda^2_{\rm QCD})$. The cutoff divided the parton evolution into a perturbative region, where radiated gluons with $p^2 > t_c$ are included in the cascade explicitly, and a non-perturbative region, where radiated gluons with $p^2 < t_c$ are handled by the hadronization model. In ISAJET, the cutoff was chosen to be 6 $\mathrm{GeV}^2/\mathrm{c}^2$ [78]. Due to this cutoff the threshold for gluon splitting into $c\bar{c}$ pairs and soft final state gluon radiation was raised. Also, gluons were not produced colinearly with a heavy quark within the cone $\Delta\mathcal{R} < 1$ around the heavy quark axis. Hence, heavy quarks were produced within ISAJET as *bare* quarks with soft radiation applied at the hadronization stage. One must note that the branching approximation overestimates the multiplicity of jets at large Q^2 because it does not sum the next to leading terms which are of comparable order to the leading terms [81].

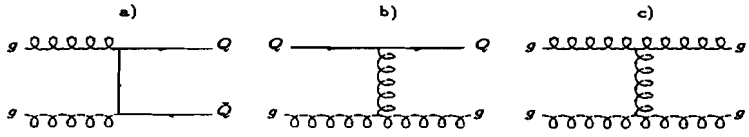

Figure 5.2: Feynman graphs for some of the lowest order matrix elements used in ISAJET for heavy quark production.

Since the scope of this thesis was the study of beauty production at DØ one needed to describe the production mechanism of $b\bar{b}$ pairs. ISAJET simulated heavy quark production via three mechanisms:

1. Flavor Creation
2. Flavor Excitation
3. Gluon Splitting

In ISAJET, next-to-leading order heavy quark production is approximated from the simple lowest order 2 parton to 2 parton reactions. For example, flavor excitation has one heavy quark in the final state (Fig 5.2b) and gluon splitting has no heavy quarks in the final state (Fig 5.2c). Flavor excitation and gluon splitting were simulated through initial and final state parton evolution. Flavor creation is two heavy quarks in the final state (Fig 5.2a). One can compare the before mentioned diagrams to the ones calculated by the MNR program (Section 2.2.6) in Fig. 2.1. The above $b\bar{b}$ production mechanisms have distinct final state topologies. Fig. 5.3 illustrates the azimuthal separation for the $b\bar{b}$ pair for the distinct processes produced by ISAJET. The accepted events correspond to dimuons whose muons had $|\eta| < 1$ and $P_T > 3$ GeV/c. These distributions were obtained as follows: from the ISAJET jet identification numbers we labeled flavor creation events to be one jet 5 and the other -5; gluon splitting with both jets to have id 9; flavor excitation events with both jets to have id 0.

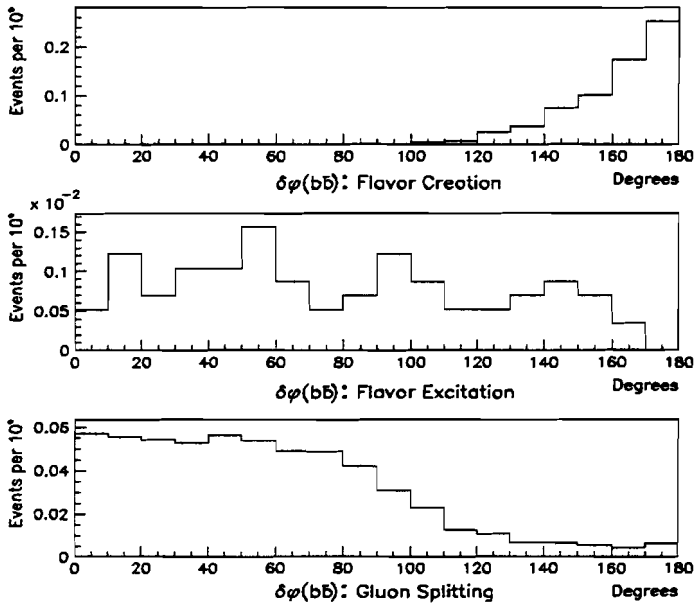

Figure 5.3: The azimuthal separation of the $b\bar{b}$ system for Flavor Creation, Flavor Excitation and Gluon Splitting as modeled by ISAJET. The distributions are normalized to unity.

5.1.3 Hadronization

Colored quarks and gluons can be regarded as free for a hard collision but subsequent color forces organize them into colorless hadrons (mesons and baryons) since color confinement in QCD postulates that only color-singlet hadronic states are observable. The formation of color-singlet hadrons is called *fragmentation* or *hadronization*. Fragmentation cannot be calculated from fundamental principles since it is governed by soft non-perturbative QCD. Several empirical models have been formulated. ISAJET used the independent fragmentation ansatz originally proposed by Feynman and Field [74]. In this fragmentation model a hadron was formed from a quark q of momentum p and an antiquark $\bar{q}'$ generated from q's color field with the light quark ratio being $u : d : s = 0.4 : 0.4 : 0.2$. The ratios indicate the small probability of the s quark to be produced in the color field since it is heavier than the u and d quarks (a gluon was fragmented with the ratios

$u : d : s = 0.43 : 0.43 : 0.14$). The q' and $\bar{q}'$ were given an average transverse momentum of 350 MeV and were combined with equal probability to form a 0^- or 1^- meson which was approximately correct for light mesons, however may have underestimated the fraction of heavy vector mesons. The momentum fraction carried by of the resultant hadron was defined to be

$$z = \frac{E^{\rm had} + p_{||}^{\rm had}}{E^q + p^q} \ , \tag{5.4}$$

where E_i are the energies for the hadron and quark respectively, $p_{||}^{\rm had}$ denotes the longitudinal momentum of the hadron and p^q is the momentum of the quark. The determination of the momentum fraction z was obtained either from the fragmentation distribution function for light quarks and gluons:

$$f(z) = 1 - a + a(b+1)(1-z)^b \quad a = 0.96,\ b = 3 \ ,$$

or the Peterson form [84]:

$$f(z) = \frac{1}{z[1 - 1/z - \epsilon/(1-z)]^2} \ ,$$

for heavy quarks (ϵ scales with the quark mass, m_q: $\epsilon = k_q^2/m_q^2$, where k_q denotes the quark's transverse momentum). This procedure was then iterated for the new leftover quark q', from the $q'\bar{q}'$ pair, with momentum $(1-z)p$. Baryons were formed by the generation of diquark pairs with a total probability of 0.08.

Even though independent hadronization incorporated most of the important features of jet fragmentation there were serious limitations. Namely, since a massless parton was fragmented into massive hadrons the momentum four vector was not conserved. The conservation of energy and momentum for the hadrons was imposed in ISAJET by the recalculation of all the energies by a scale factor in the hadron's rest frame. Also, flavor was not conserved since hadrons with longitudinal momentum less than zero were discarded. Furthermore, since jet fragmentation was done independently, a collinear branching of a

quark into a quark and gluon results in a larger multiplicity than into a single quark even if the quark-gluon mass was small.

5.1.4 Beam Jet Fragmentation

After the hard scattered event was generated hadrons from spectator beam jets were evolved. While PYTHIA used an extension of the Lund colored string scheme, ISAJET used a scheme based on the Abramovskii, Kanchelli and Gribov (AKG) sum rules [85]. The AKG idea reproduced the experimental observation from minimum-bias data of long range rapidity correlations and a broad multiplicity distribution. In contrast to the original notion of multiparticle production based on the idea of particle creation from the vacuum, which lead to short range rapidity correlations and a Poisson multiplicity distribution, the AKG method used the idea of *cut Pomerons*.

5.2 Detector Simulation

Once a sample of simulated $p\bar{p}$ events was generated, one modeled the detector's response and organized the digitized output information in the same format as the data acquisition system. Detector simulation described the effects due to the passage of elementary particles traveling through matter and took into account various possible physical processes a particle may likely undergo. Physics processes modeled were for example delta-ray production, multiple coulomb scattering, electron and muon bremsstrahlung, and particle decays. A full simulation of the DØ detector was important for several reasons. Namely, to study:

- The geometrical acceptances for the various physics processes;
- The systematic effects of information smearing to determine the resolutions for various physics signals;
- Signal and background physics processes in order to enhance event selection criteria and optimize the signal-to-background ratio.

5.2.1 DØGEANT

DØGEANT was a customized version of the CERN program GEANT [86], which was a general package for simulating the interactions between particles and various detectors. DØGEANT took into account the geometrical volume boundaries and all physical effects due to the nature of the particles through the DØ detector. The DØGEANT geometry simulated the muon and tracking chambers in great detail down to the level of sense wires, cathode material, support structures, *etc.* As for the Calorimeter, a full simulation of all the uranium plates and argon gaps was usually not done because of the inordinate computer processing time required to track many particles through its volume. Instead, the geometry of the structure supports and individual calorimetric modules was preserved but the modules were modeled as homogeneous blocks of uranium-G10-argon mixture. As a result, the sampling fluctuations and attenuation of electromagnetic energy, and the hadron to electron response (compensation) were added after the showering of each track. Furthermore, electromagnetic showers were evolved until the individual secondary particle energies fell below 200 MeV at which point the energies were determined from parametrizations.

5.2.1.1 Refinements to DØGEANT

The output from DØGEANT needed further refinement in order to have a better representation of the data. Specifically, the package NOISY [87] handled cell-by-cell modifications to the Calorimeter's response due to uranium and electronic noise, and event pileup resulting from multiple interactions and signal tails of previous events. Secondly, and of principle importance to this analysis, we used the MUSMEAR package [88] which took into account the muon chamber drift time resolution, pad latch inefficiencies and misalignment with respect to other muon chambers. These muon chamber corrections were needed for a better characterization of the muon system's momentum resolution. The to the Calorimeter and

the muon system were stored in a new GEANT output file.

5.2.1.1.1 NOISY At the typical Run 1A luminosities, there are on average 1.2 interaction vertices per beam crossing. Consequently, the energy deposited in the Calorimeter from the other interactions, uranium noise and electronic fluctuations was be added to the energy of events of primary interest. To model these contributing factors to the energy measurement one processed the GEANT output with the NOISY package. Pileup of events and multiple interactions were simulated by using a second input stream of Monte Carlo generated minimum-bias (Section 4.2) events. Assuming the average number of interactions per beam crossing (N) a Poisson probability ($P(N, N')$) was calculated for getting N' interactions per beam crossing. Appropriately weighted by this probability a sufficient number of events were read from the second input stream and added cell-by-cell to the current Monte Carlo generated event. To simulate detector and uranium noise NOISY used the experimental data from dedicated runs with beam off. For such runs, the pedestal distributions were made separately for each pseudorapidity and calorimeter layer, merged in azimuthal angle and north/south in pseudorapidity. One created a histogram for each individual merged sector distribution and generated a random number based on the histogram distribution. The pedestal counts were converted to units of GeV and added cell-by-cell to the cells which corresponded to the specific distribution.

5.2.1.1.2 MUSMEAR The muon momentum resolution after the Monte Carlo events are processed through DØGEANT is

$$\left(\frac{\delta p}{p}\right)^2 = (0.18)^2 + (0.001p)^2 \ .$$

For muon momenta in the range of 40–50 GeV/c this corresponded to a resolution of 7–9%. The actual resolution was of order 15–22%, as parametrized by Equation 4.23. For a

more realistic representation of the muon resolution, the MUSMEAR package first smeared the raw muon GEANT hits in order to worsen the drift time and the time division position electronic resolutions. The respective values for the drift time and the time division position resolutions were 70 μm and 20 cm for the data used for this thesis (Run 1A). In contrast, the previously mentioned resolutions used by DØGEANT were 20 μm and 12 cm. Second, MUSMEAR eliminated some hits in order to simulate chamber inefficiencies. DØGEANT assumed 100% chamber efficiency, while the data indicated that the central muon chambers were about 90% efficient. Finally, MUSMEAR modified the muon geometry files used by DØReco, to deliberately misalign the muon chamber positions. One spread the positions of the muon modules contained in the muon geometry constant files by a gaussian distribution. A misalignment value of 3 mm, the width of the gaussian, was needed in order for the mass distributions for $Z \rightarrow \mu^+\mu^-$ and $W^\pm \rightarrow \mu^\pm\nu$ Monte Carlo events to agree with data reconstructed with DØReco version 11.

5.2.2 Trigger Simulation

After detector simulation of the Monte Carlo sample (and event reconstruction), the next step was to model the trigger performance with the processed events. Trigger simulation was accomplished by the use of the TRIGSIM package, which was a composition of L1SIM and L2SIM packages. L1SIM simulated the Level 1 trigger elements—the AND-OR network of the respective Level 1 calorimeter and muon components. L2SIM was the actual Level 2 software code and the same trigger configuration files as used during data collection. We processed the Monte Carlo events for this analysis with TRIGSIM version 7.2. The details of trigger version 7.2 will be discussed in Section 6.2.1.

5.3 Generated Monte Carlo Samples

Up to now, our Monte Carlo discussion has concentrated on the generic physics event generation and detector simulation. Now we will describe the different specific types of Monte Carlo samples used for this analysis, which helped us in our understanding of the collected data sample. We generated both signal and background physics events to best characterize our observations. The physics processes simulated were:

- J/ψ from Bottom Production Model (BPM)
- J/ψ from Charmonium Production Model (CPM)
- Dimuons and trimuons from heavy flavor $Q\bar{Q}$ production
- Dimuons from Drell-Yan production
- Dimuon from decays of low mass mesons ($\rho, \phi, \omega, \eta, \eta'$)
- Dimuons from pion/kaon decays

For all of the above processes, ISAJET version 6.49 and DØGEANT version 3.14 was used for the generation and detector simulation. The hard scattering process chosen to generate all the Monte Carlo types, except for CPM and Drell-Yan, was *TWOJET*. The TWOJET option in ISAJET was an approximation to α_s^2 QCD processes[3], which gave rise in lowest order to two high P_T jets. Processes included were, for example,

$$g + g \rightarrow g + g$$

$$g + q \rightarrow g + q$$

$$g + g \rightarrow q + \bar{q}, \cdots$$

[3]If one does not force either jet to decay into one exclusive state, *e.g.* $b_{jet} \rightarrow B^0$.

Masses were neglected for the charm and lighter quarks but were taken into account for the bottom and top quark. The momentum transfer scale (Q^2) was taken to be

$$Q^2 = \frac{2stu}{s^2 + t^2 + u^2} \ ,$$

where s, t, and u are the usual Mandelstam variables[4]. The summary of the required muon kinematic cuts and the number of generated events for each Monte Carlo samples are tallied in Table 5.1. It must be noted that an important mechanism for the production of J/ψ at Tevatron energies, the Fragmentation Mechanism [89], was not simulated because no Monte Carlo package was presently available.

GENERATED MONTE CARLO SAMPLE	
Muon Kinematic Requirements at Generation Stage	
$P_T^\mu > 3$ GeV/c & $\lvert\eta^\mu\rvert < 1$	
Process	Number of Events
B-J/ψ	48841
χ_c-J/ψ	18814
$Q\bar{Q}$	48681
Drell-Yan	22453
Low Mass Mesons	8624
π/K	18046

Table 5.1: Summary of Generated Monte Carlo Events

For expeditious and efficient detector simulation for the various Monte Carlo samples, and to be in agreement with the kinematic and fiducial volume specifications used for this analysis, we required the muons to have P_T greater than 3 GeV/c and to be within $|\eta| < 1$. Finally, the GEANT output, with MUSMEAR and NOISY included, was reconstructed and the Monte Carlo events were analyzed in exactly the same way as the data.

[4]For a scattering process of the form $AB \to CD$, $s = (p_A + p_B)^2$, $t = (p_A - p_C)^2$ and $u = (p_A - p_D)^2$, where p_i are the respective four-vectors for the four particles.

5.3.1 Simulation of J/ψ from the BPM

The physics process used to generate J/ψ from the Bottom Production Model, with the muonic decay of the J/ψ, was

$$p\bar{p} \rightarrow b + X \rightarrow \mathrm{J}/\psi + X \rightarrow \mu^+\mu^- + X \ .$$

The P_{T} range for the two jets in the hard scattering process was 7 GeV/c $< P_{\mathrm{T}}^{\mathrm{jet}} <$ 80 GeV/c. Events were evolved up to ten times requiring the existence of a bottom quark in the event. Once an event had the desired quark, various attempts at hadronization were made until a J/ψ was present in the event. Afterwards, the J/ψ was forced to decay to a pair of opposite sign muons ($\mu^+\mu^-$), with the muons satisfying the kinematic requirements of Section 5.3. The BPM J/ψ invariant mass and P_{T} spectra as generated by ISAJET, and the same distributions after the events were reconstructed, are illustrated in Fig. 5.4.

5.3.2 Simulation of J/ψ from the CPM

A modified version of ISAJET was used in order to simulate the production of J/ψ via the charmonium production mechanism. The modified ISAJET was called the ISACHI package. The difference between the two Monte Carlo generators was that ISACHI used the hard scattering matrix elements calculated by Humpert [106] instead of that by Combridge [90]. The Humpert matrix elements simulated the cascade production of J/ψ's via the following processes

$$p\bar{p} \rightarrow \chi_{c_0} + X \rightarrow \mathrm{J}/\psi + \gamma + X, \quad \mathrm{Br}(\chi_{c_0} \rightarrow \mathrm{J}/\psi + \gamma) = 0.66\%$$

$$p\bar{p} \rightarrow \chi_{c_1} + X \rightarrow \mathrm{J}/\psi + \gamma + X, \quad \mathrm{Br}(\chi_{c_1} \rightarrow \mathrm{J}/\psi + \gamma) = 27.3\%$$

$$p\bar{p} \rightarrow \chi_{c_2} + X \rightarrow \mathrm{J}/\psi + \gamma + X, \quad \mathrm{Br}(\chi_{c_2} \rightarrow \mathrm{J}/\psi + \gamma) = 13.5\%$$

As in the BPM case, the J/ψ was forced to decay to $\mu^+\mu^-$ pairs, with the muons satisfying the kinematic requirements of Section 5.3. The P_{T} range chosen for the χ_{c} states

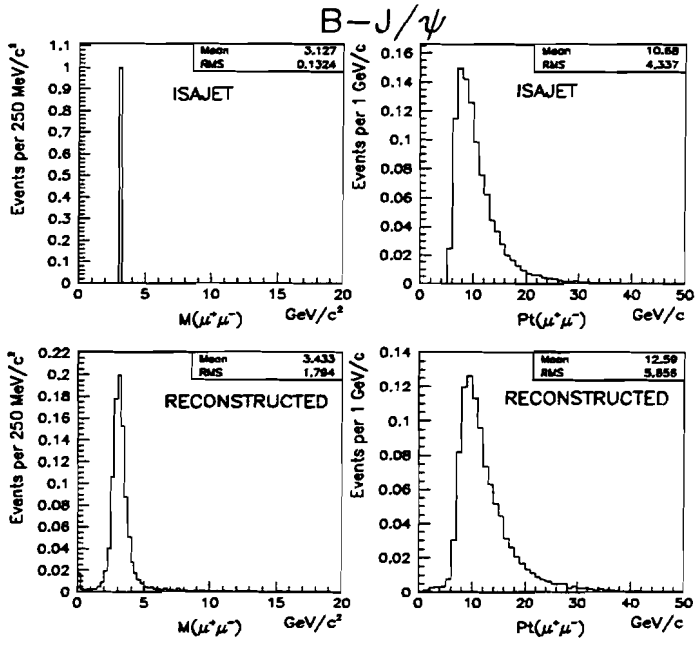

Figure 5.4: The comparison of the BPM J/ψ invariant mass and P_T spectra before and after reconstruction. The top row is the generated distributions, whereas the bottom row is the reconstructed distributions. All four histograms are normalized to unity.

was 4 GeV/c $< P_T^{\chi_c} <$ 40 GeV/c. The CPM Jψ invariant mass and P_T spectra as generated by ISACHI, and the same distributions after the events were reconstructed, are illustrated in Fig. 5.5.

5.3.3 Simulation of Heavy Flavor $Q\bar{Q}$ Production

Two basic semileptonic B-hadron decay topologies produce multimuon events. Namely, parallel B semileptonic decays, and sequential B semileptonic decays. The production of dimuons in parallel decays is via the process

$$p\bar{p} \rightarrow b\bar{b} \rightarrow \begin{array}{l} \bar{c} + \mu^+ + \nu_\mu \\ \hookrightarrow \quad c + \mu^- + \bar{\nu}_\mu \ . \end{array}$$

For the case of sequential decays, dimuons are produced according to the process

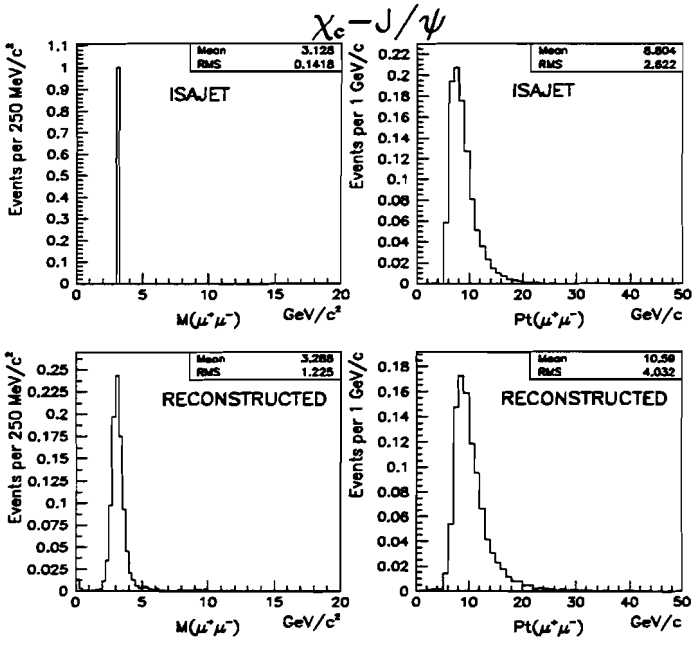

Figure 5.5: The comparison of the CPM J/ψ invariant mass and P_T spectra before and after reconstruction. The top row is the generated distributions, whereas the bottom row is the reconstructed distributions. All four histograms are normalized to unity.

$$p\bar{p} \rightarrow b \rightarrow c + \mu^- + \bar{\nu}_\mu$$
$$\hookrightarrow s + \mu^+ + \nu_\mu$$

or its charge conjugate. ISAJET version 6.49 assumed 12% for the semimuonic branching ratios for the B and D-mesons[5].

Opposite sign dimuons were produced if one of the b-quarks decays sequentially or if both b-quarks decay in parallel. For the latter case, same sign dimuons were not produced because ISAJET version 6.49 does not model $B\bar{B}$ mixing. To simulate $B\bar{B}$ mixing we randomly changed the sign of one of the muons from a selected sample of generated $Q\bar{Q}$ dimuon events. We made sure that the muons came from a B_d^o and B_s^o mesons. Same sign dimuons were produced if one of the b-quarks decayed sequentially, with an electron created

[5]The current values are [91]: Br($B \rightarrow \mu\nu_\mu$) = 10.3 ± 0.5% and Br($D \rightarrow \mu\nu_\mu$) = 10 ± 2.6%

in the first intermediate step of the decay, while the other jet decayed directly into a muon.

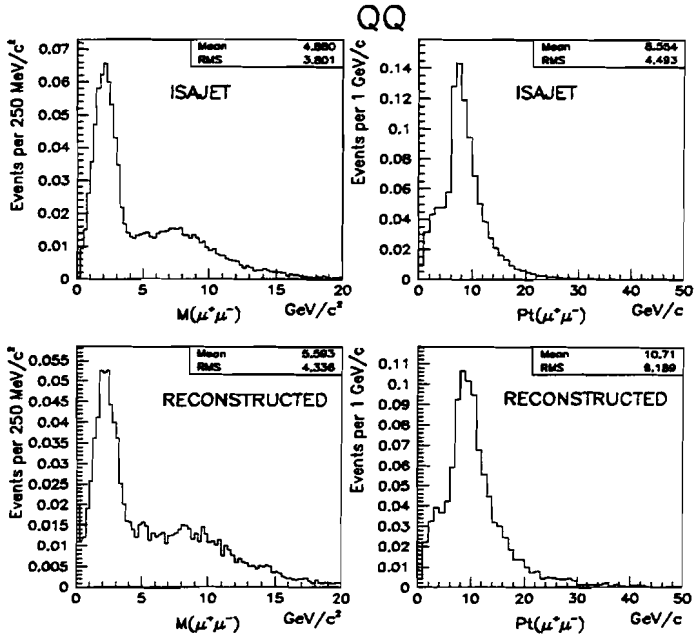

Figure 5.6: The comparison of the $Q\bar{Q}$ invariant mass and P_T spectra before and after reconstruction. The top row is the generated distributions, whereas the bottom row is the reconstructed distributions. All four histograms are normalized to unity.

In the case of leading-order $b\bar{b}$ production, one can distinguish dimuons between the two processes because of different kinematic characteristics. Parallel decays produce dimuons with relatively small P_T and large 3-dimensional opening angles. Sequential decays produce dimuons with larger values of P_T and smaller 3-dimensional opening angles. However, for next-to-leading order $b\bar{b}$ production the distinction becomes more difficult because of the smaller azimuthal angle separation between the two b-quarks (Figs. 9.16).

Dimuon events can also arise from the decay of $c\bar{c}$ quarks. To distinguish between $b\bar{b}$ and $c\bar{c}$ events, several topological characteristics can be utilized. For example, since b-quark fragmentation is harder than c-quark fragmentation the resulting B-mesons will carry a larger fraction of the initial quark momentum than the resulting D-mesons. Also,

the average transverse momentum of b-quarks will be larger than c-quarks since $\langle P_T^q \rangle \sim m_q$. Furthermore, due to the higher b-quark mass the transverse momentum of decay muon relative to the heavy quark axis will be larger for muons from b decays. The P_T range for the two jets in the hard scattering process was 4 GeV/c $< P_T^{jet} <$ 80 GeV/c. Events were evolved up to ten times requiring the existence of a bottom and/or charm quark in the event. Once an event had the desired quark, various attempts at hadronization were made until a dimuon was present in the event. The $Q\bar{Q}$ invariant mass and P_T spectra as generated by ISAJET, and the same distributions after the events were reconstructed, are shown in Fig. 5.6.

In order for a trimuon event to be produced one of the two b-quarks had to decay sequentially, while the other b-quark decayed semimuonicly, as depicted by (or its charge conjugate):

$$\begin{array}{lll} p\bar{p} \rightarrow & b\bar{b} \rightarrow & \bar{c} + \mu^+ + \nu_\mu \\ & \hookrightarrow & c + \mu^- + \bar{\nu}_\mu \\ & & \hookrightarrow \; s + \mu^+ + \nu_\mu \; . \end{array}$$

To enhance the statistical sample of Monte Carlo trimuons events, ISAJET was modified to select dimuons that originated from sequential decay. This was accomplished by:

1. requiring the muons of the dimuon to arise from the B/D-meson chain;
2. restricting the dimuon invariant mass to the 1-6.2 GeV/c^2 range; and
3. asking for $|\eta_{\mu\mu}| \leq 0.8$ and $P_T^{\mu\mu} > 7$ GeV/c (with the muon restrictions of Section 5.3).

The daughter lepton from the other $b(\bar{b})$ semileptonic decay was required to have a $P_T > 3.5$ GeV/c and to be within $|\eta| < 1$. If the lepton was an electron, then the ISAJET

particle identification number and mass was changed to the muon's identification number and mass.

5.3.4 Simulation of Drell-Yan Production

ISAJET provided the option to select the Drell-Yan process. ISAJET included both leading order:

$$q\bar{q} \rightarrow \gamma^* \rightarrow \mu^+\mu^- ,$$

and next-to-leading order:

$$\begin{aligned} q\bar{q} &\rightarrow \gamma^* g \rightarrow \mu^+\mu^- g \\ qg &\rightarrow \gamma^* q \rightarrow \mu^+\mu^- q \\ \bar{q}g &\rightarrow \gamma^* \bar{q} \rightarrow \mu^+\mu^- \bar{q} , \end{aligned} \tag{5.5}$$

Drell-Yan processes. We restricted the *mass* of the virtual photon to be between 0.28–20 GeV/c^2 to produce the desired dimuon invariant mass range for our study. The muons satisfied the kinematic requirements of Section 5.3. In order to simulate both leading order and next-to-leading order event topologies the transverse momentum range of the virtual photon was 0 GeV/c $< P_T^\gamma <$ 80 GeV/c. Similar to the dimuon characteristics in leading order $b\bar{b}$ events, dimuons produced in leading order Drell-Yan production have small P_T and large 3-dimensional opening angles. On the other hand, next-to-leading order Drell-Yan events produce dimuons with larger P_T and smaller 3-dimensional opening angles, as is the case for next-to-leading order $b\bar{b}$ events.

For lowest order Drell-Yan process, ISAJET defined the QCD evolution scale (Λ_{QCD}) equal to the *mass* of the virtual photon, while Λ_{QCD} is set equal to the P_T of the virtual photon for the higher order processes. The Drell-Yan invariant mass and P_T spectra as generated by ISAJET, and the same distributions after the events were reconstructed, are shown in Fig. 5.7.

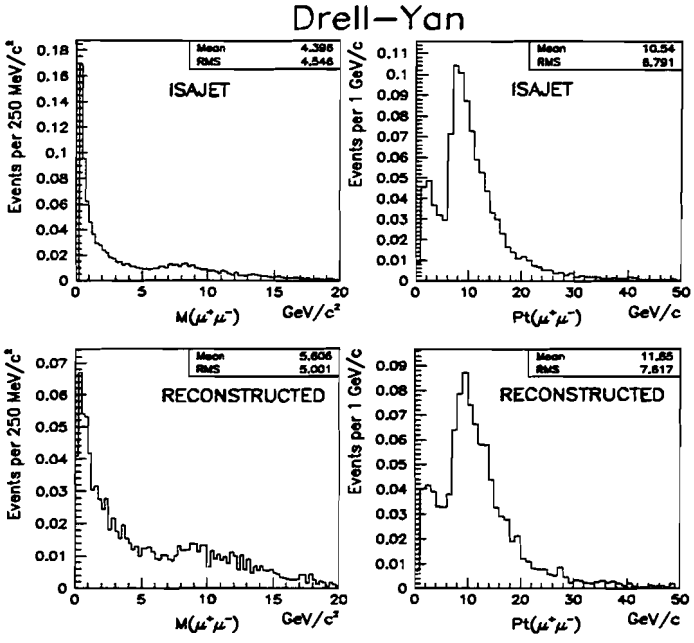

Figure 5.7: The comparison of the Drell-Yan invariant mass and P_T spectra before and after reconstruction. The top row is the generated distributions, whereas the bottom row is the reconstructed distributions. All four histograms are normalized to unity.

5.3.5 Simulation of Low Mass Mesons

The ISAJET generator was modified to produce low mass mesons, *e.g.* $\rho, \phi, \omega, \eta, \eta'$, to include their respective muonic decays. The P_T range for the two jets in the hard scattering process was between 10 GeV/c–80 GeV/c. Various attempts at hadronization were made until a low mass meson was present in the event. Afterwards, the meson was forced to decay to a $\mu^+\mu^-$ pair, with the muons satisfying the kinematic requirements of Section 5.3. The low mass mesons invariant mass and P_T spectra as generated by ISAJET, and the same distributions after the events were reconstructed, are shown in Fig. 5.8.

5.3.6 Simulation of Pion/Kaon Decays

Since quark and gluon jets have large multiplicity of pions and kaons, multimuon events can arise from the combination of a muon from a b-quark plus a muon from a pion/kaon

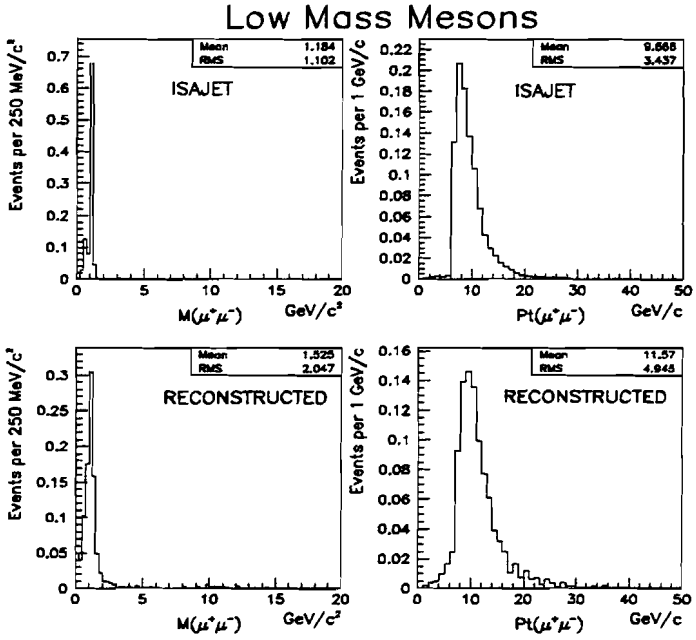

Figure 5.8: The comparison of the Low Mass Mesons invariant mass and P_{T} spectra before and after reconstruction. The top row is the generated distributions, whereas the bottom row is the reconstructed distributions. All four histograms are normalized to unity.

decay[6]. Muons from the leptonic decays of pions ($\pi \rightarrow \mu\nu_{\mu}$, Br = 99.99%) and kaons ($K \rightarrow \mu\nu_{\mu}$, Br = 63.51%; $K^{\circ}_{\mathrm{L}} \rightarrow \pi^{\pm}\mu^{\mp}\nu_{\mu}$, Br = 27%) were simulated by utilizing the heavy quark $Q\bar{Q}$ dimuon Monte Carlo events discussed in Section 5.3.3. Essentially, to increase the number of muons from pion/kaon decay in heavy flavor events one randomly selected a pion or kaon from a $b\bar{b}$ or $c\bar{c}$ event that had at least one semileptonic decay muon and decayed the meson if $P_{\mathrm{T}}^{\pi/K} > 3$ GeV/c and $|\eta^{\pi/K}| < 0.9$. For the chosen meson, the decay was appropriately weighted with a probability value which took into account the branching fraction, decay length, transverse momentum and mass of the meson, and the cylindrical radius of the decay volume of the DØ detector [92]. As before, the kinematic conditions in Section 5.3 had to have been satisfied by two of the muons in the event. The π/K invariant

[6]The decay probability for a pion and kaon in the DØ detector is respectively $\mathcal{P} = 0.015/P_{\mathrm{T}}^{\pi}$ and $\mathcal{P} = 0.070/P_{\mathrm{T}}^{\mathrm{K}}$ [109].

mass and P_T spectra as generated by ISAJET, and the same distributions after the events were reconstructed, are shown in Fig. 5.9.

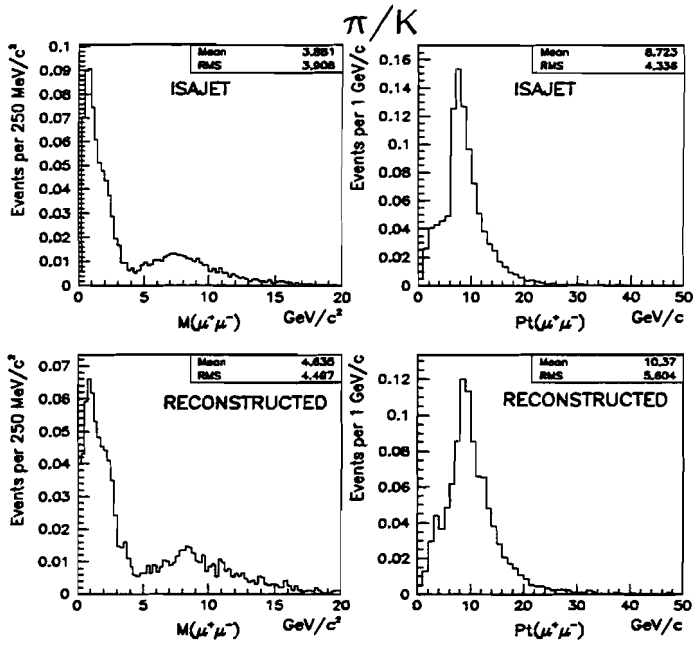

Figure 5.9: The comparison of the π/K invariant mass and P_T spectra before and after reconstruction. The top row is the generated distributions, whereas the bottom row is the reconstructed distributions. All four histograms are normalized to unity.

5.4 MNR Program

Since ISAJET provides only an approximate simulation of next-to-leading order processes any proper comparison of the data with theory must be accomplished via a Monte Carlo program which explicitly calculates leading and next-to-leading order diagrams. To calculate next-to-leading order heavy quark cross sections we used the Mangano, Nason and Ridolfi (MNR) program [93]. The program performs the analytic next-to-leading order $\mathcal{O}(\alpha_s^3)$ calculation for the production of heavy quarks carried out by Nason, Dawson and Ellis (NDE) [25][7]. For a heavy quark (c, b or t-quark), the MNR program calculates the single

[7]ISAJET does not calculate NLO matrix elements for heavy quark production (Section 5.1.2).

inclusive distributions $d\sigma/dy$ and $d\sigma/dP_{\rm T}$, the double (correlated) differential distributions and the total cross section. The calculation includes the Born term for producing a $Q\bar{Q}$ to $\mathcal{O}(\alpha_s^2)$, the virtual corrections to the Born cross section to $\mathcal{O}(\alpha_s^3)$, and the cross section for producing a $Q\bar{Q}$ pair plus a light parton to $\mathcal{O}(\alpha_s^3)$ [94]. The result of the calculation was a set of formulae that were easily implemented in a partonic Monte Carlo model, which generated the appropriately weighted partonic events with a heavy quark-antiquark pair and events with the pair plus an extra parton (*e.g.* a gluon, a light quark or antiquark). Subprocesses, such as

$$g + g \rightarrow Q + \bar{Q}\,, \quad g + g \rightarrow Q + \bar{Q} + g$$

$$q + \bar{q} \rightarrow Q + \bar{Q}\,, \quad g + \bar{q} \rightarrow Q + \bar{Q} + g$$

$$g + q \rightarrow Q + \bar{Q} + q\,, \quad g + \bar{q} \rightarrow Q + \bar{Q} + \bar{q}\,,$$

were included to orders $\mathcal{O}(\alpha_s^2)$ and $\mathcal{O}(\alpha_s^3)$. One can consider the MNR program as giving the *exact* $\mathcal{O}(\alpha_s^3)$ result for heavy quark cross section even when complicated kinematical cuts were imposed upon the final state partons[8]. However, one must note that the MNR program was not an event generator for heavy quark production.

[8]The program fails whenever finite order calculations are expected to fail.

Chapter 6

EVENT SELECTION

The data sample used for this thesis was collected during the 1992–1993 Tevatron run (Run 1A). To enhance the events of interest for our physics study, muon identification quality requirements were imposed on the data to minimize fake muon candidate tracks. In this chapter we will discuss the selection criteria used to obtain the data sample for our multimuon[1] study.

6.1 Offline Event Filters

The 12.7 million Run 1A events were streamed for the various DØ physics groups by the use of FORTRAN filter codes provided by the respective groups. This analysis used the B2M[2] (b-physics dimuon) stream—both for the DST and STA output files. Additional streaming was performed by the author to obtain a more manageable data set. The filter codes passed "good" dimuon events based upon quality muon criteria. In the proceeding two sections we will describe the selection criteria used for the two filters.

[1]The author has defined the following notational convention used throughout this thesis: 2μ are generic dimuons, whereas $\mu\mu$ are low mass dimuons.

[2]B2M filter code was primarily written and maintained by the author during Run 1A.

6.1.1 B2M Stream

The extraction of multimuon events began with the implementation of the B2M filter to the entire Run 1A data set, which corresponded to an integrated luminosity ($\mathcal{L}$) of $13 \pm 0.70\,\mathrm{pb}^{-1}$. First, the filter required the number of reconstructed muon candidates, the number of PMUO ZEBRA banks, to be between 2 and 5. The upper limit of 5 was chosen from the experience gained from event scanning. Once an event had the required number of muon candidates we imposed the following minimum muon quality selection criteria for two of the muons in the event:

- Muon quality flag word 4 (IFW4[3]) equal to 0 or 1 with the sum of their respective IFW4 less than 2. IFW4 indicated the goodness of fit for the muon candidate track. For example, a good muon track had a good vertex projection and sufficient number of hits along the track for a good fit in both the bend and non-bend views;

- Calorimetric confirmation with a minimum ionizing particle (MIP confirmation). Specifically, the observed deposited energy in the Calorimeter along the cells traversed by the muon candidate plus two nearest neighboring cells to be greater than 1 GeV ($E^{\mathrm{Tot}}_{\mathrm{2NN}} \geq 1$ GeV).

If two muon tracks satisfied the above requirements, then the dimuon system needed to have a 3-dimensional opening angle less than 160° in order to minimize the acceptance of cosmic ray events. However, if the opening angle was greater than 160°, then at least one of the muons of the pair had to have had a crossing time with respect to the $p\bar{p}$ collision less than 100 ns.

When a pair of muons passed all the stated criteria then the event was accepted by the B2M filter. Approximately, 6% of the Run 1A data was filtered into the B2M stream.

[3] See section 4.6.

6.1.2 Subfilter

Further selection conditions were imposed on the B2M data set to obtain a more tractable dimuon event pool. First, we eliminated "bad" runs[4]. Second, we implemented a subfilter which defined a good dimuon. In addition to the B2M requirements, the following requisites were used in the definition of a good dimuon event:

- Muons comprising the dimuon to be within the fiducial volume of $|\eta^{\mu}| \leq 1.7$;
- The invariant mass of the dimuon candidate less than 200 GeV/c^2.

The reduction of cosmic ray contamination was addressed with the requirement that the difference in azimuth ($\Delta\phi^{2\mu}$) between the two track candidates was less than 160° or the difference in the polar angles ($\Delta\theta^{2\mu} = \theta^{\mu_1} + \theta^{\mu_2} - 180°$) was greater than 20°. The phi and theta angles were calculated from the measured direction cosines outside the toroids for each respective muon track candidate.

The subfilter decreased the B2M stream by a factor of 1.25, which corresponded to 4% of the Run 1A data or about 500,000 multimuon events. Figure 6.1 illustrates the progression of passed opposite sign dimuons for the two filters for 1.5 pb^{-1} of data. No trigger requirement was imposed. The top histogram illustrates the reduction of the data of the two filtering steps.

6.2 Analysis Quality Criteria

To insure good multimuon candidate events we imposed various quality selections at the analysis stage. The selection criteria used for this analysis can be described into two general categories: 1) global event standards; and 2) muon and dimuon quality identification standards.

[4] See appendix A for the good run list.

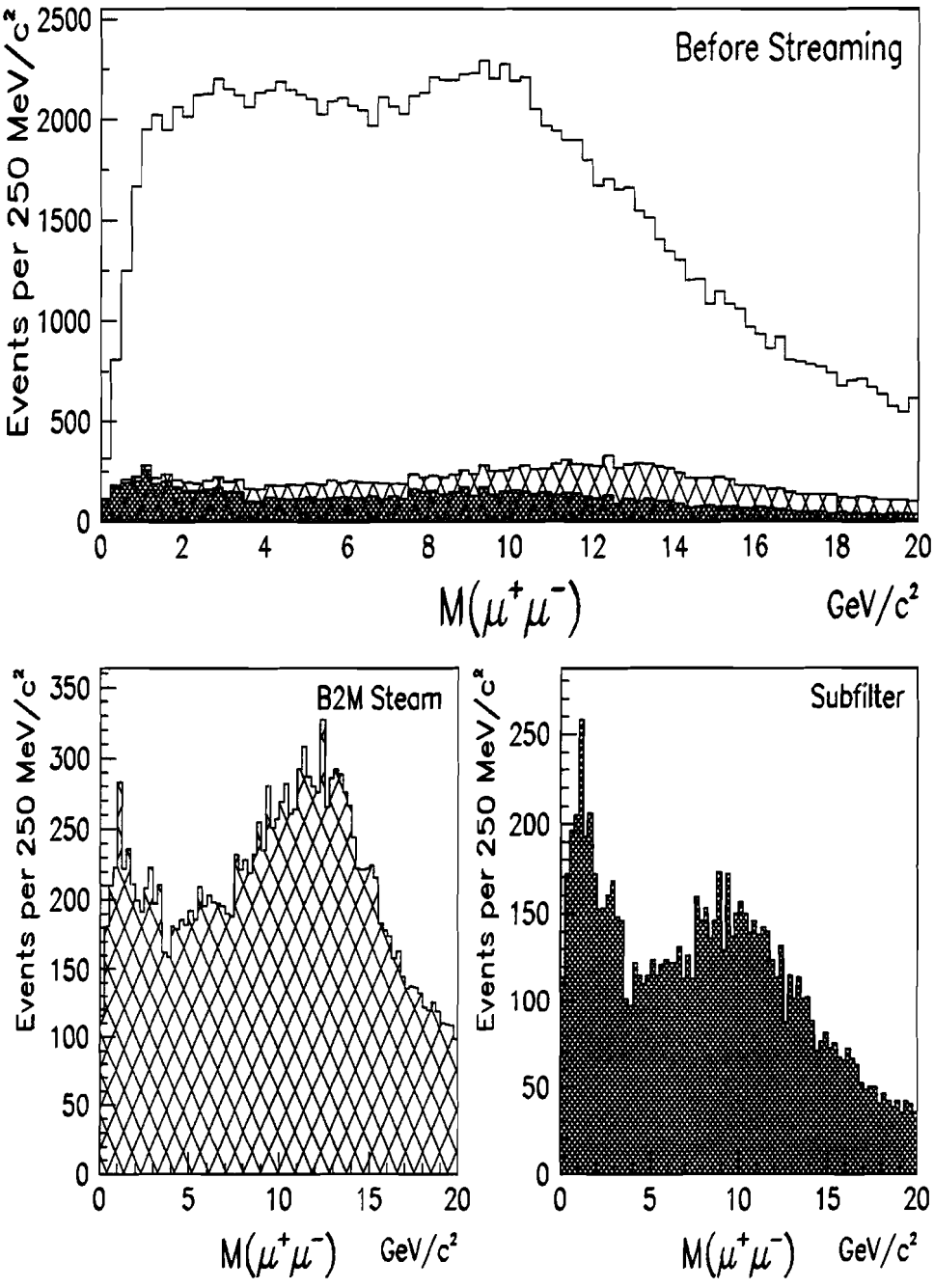

Figure 6.1: Streaming Progression of DØ's Run 1A $\mu^+\mu^-$ Mass Spectrum

6.2.1 Global Event Criteria

Beginning with the data set selected by the subfilter, the first analysis step to enhance quality multimuon events was the imposition of four global event criteria.

- The first global condition for an event was the requirement of the MU2HIGH trigger. Accepted events satisfied the MU2HIGH Level 1 hardware trigger and the MU2HIGH Level 2 software filter. The MU2HIGH hardware trigger called for the logical combination of two muons within $|\eta^{\mu}| < 1.7$, with each track having hit at least two of the three WAMUS layers, and the Main Ring vetos MRBSLOSS[5] and MICROBLANK[6]. The MU2HIGH filter required two muon candidates each having $P_{\mathrm{T}}^{\mu} > 3$ GeV/c contained within $|\eta^{\mu}| < 1.7$. In addition, the filter rejected potential multimuon events if two tracks had $\Delta\theta^{2\mu} > 160°$ and $\Delta\phi^{2\mu} > 170°$. An event was also vetoed if a predetermined combination of hits were found in the opposite side of the muon system in an area (60 cm in the bend view by 150 cm in the non-bend view) pointed by the *BC* segment of a Level 2 muon track candidate. Furthermore, an event was passed by the MU2HIGH filter if one of the two muons had quality of *tight* (IFW4 = 0) and the other had quality of *common* (IFW4 = 1) or better. The requisite of the trigger had an $\mathcal{L} = 11.5 \pm 0.62$ pb^{-1}.
- The second global event selection was the "post-shutdown" data. Runs numbered 60000 and beyond were exclusively used because the MU2HIGH trigger was stable. The integrated luminosity for the post-shutdown MU2HIGH data sample was 6.73 ± 0.36 pb^{-1}.

[5]Losses from the Main Ring will show up in the detector since the Main Ring passes through DØ. Hence, the losses are rejected. The largest losses occur when the protons are injected into the Main Ring and again 0.3 seconds later when the protons pass through *transition* (the acceleration of leading relativistic particles in a bunch in order to prevent the bunch from blowing up longitudinally). These losses were dealt with by vetoing a 0.4 second window commencing at injection, continuing through transition and providing recovery time for the Calorimeter and Muon high voltage. The resultant dead time was approximately 17%.

[6]This term protects against Main Ring losses even after injection. Events were vetoed if a Main Ring bunch was within $\pm$ 800 ns of a $p\bar{p}$ collison. The resultant dead time was roughly 8%.

- The third global benchmark for an event is a variable defined to be

$$\frac{\text{Total Number of Muon Hits}}{\text{Total Number of Muon Modules Hit}}.$$

  If the ratio was greater than 2.5 or if an event had more than 130 muon hits, then the event was rejected.

- The fourth, and final, global event standard cut was the exclusion of events with multi (3, 4, or 5) same sign muons.

6.2.2 Muon and Dimuon Criteria

The first aspect of muon and dimuon identification standards for this analysis was the geometric restriction made on the muon and dimuon candidates with respect to the well understood region of the muon detector. Muons track candidates had to be within the fiducial volume of $|\eta^{\mu}| \leq 1$ (central region—CF). Furthermore, we required the dimuon to be bounded in $|\eta^{2\mu}| \leq 0.8$. Furthermore, we excluded the phi range 80–110° for the muon candidate tracks because of poor chamber performance within that phi region (Section 7.2.3). We also restricted the muon transverse momentum within the range of $3.3 \leq P_{\mathrm{T}}^{\mu} \leq 25$ GeV/c. Third muon candidates had no upper limit placed. The lower limit corresponded to the minimum P_{T} value to pass through the Calorimeter and magnetic toroid in the CF; the upper limit was introduced to insure a good momentum resolution from Monte Carlo studies. For the dimuon system, we did not require a P_{T} cutoff for dimuons with mass greater than 6.25 GeV/c^2 (in order to accept dimuons from $b\bar{b}$ parallel decays). However, low mass dimuons needed to have a minimum P_{T} of 6.6 GeV/c.

To separate reconstructed muon candidate tracks which did or did not originate from a $p\bar{p}$ interaction point we imposed the following muon selection criteria:

- Muon quality flag IFW4 equal to 0 or 1. If IFW4 equalled 1, then we insisted that the track had a good bend and non-bend fit;

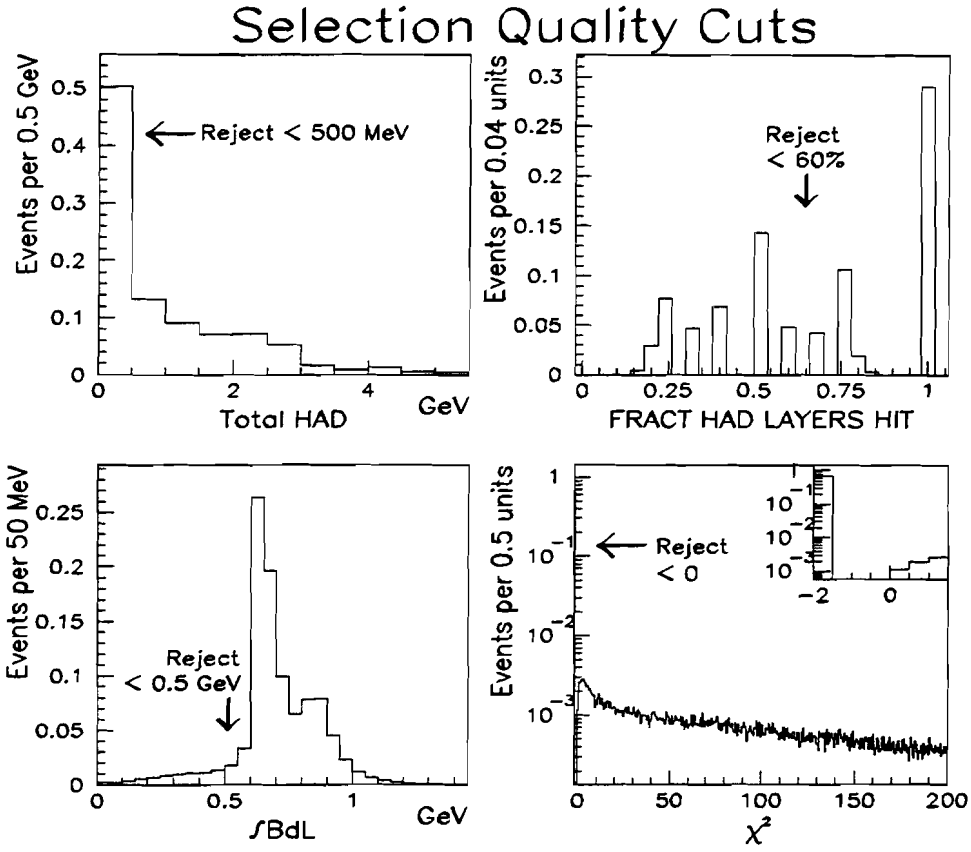

Figure 6.2: Muon Quality Selection Cuts. The plots are all normalized to unity.

- MIP confirmation. Specifically, the fraction of hadronic layers peregrinated by the muon to be greater than 60% and the sampled hadronic energy greater than 500 MeV for 3×3 calorimeter cell arrangement (direct hit cells plus one nearest neighboring cell) along the eta-phi direction of the muon track candidate. Both of these values were obtained from the MTC (Muon Tracking in the Calorimeter) package [95];

- Good momentum determination by the integral of the magnetic field induction vector along the path of the muon track—$\int \vec{B} \cdot d\vec{l}$. We required $\int \vec{B} \cdot d\vec{l} \geq$ 0.5 GeV for muons comprising the dimuon and 0.2 GeV for the third muon in trimuon events;

- A minimum number of hits per muon detector layer was required for each muon candidate track. For example, CF muon tracks could have no *A*-layer hits but needed at least 2 hits in each of the *B* and *C*-layers;

- The χ^2/d.o.f. > 0 from the global fit for the muon candidate (Section 4.6).

A summary of the above selection criteria is given in Table 6.1, whereas Table 6.2 enumerates the surviving Run 1A multimuon events, with their respective number of dimuon and trimuon candidates, at the various stages of rejection.

On occasion two tracks where within close proximity of each other for various physics processes (*e.g.* decay of low mass vector mesons). In order not to over estimate the deposited hadronic energy for track candidates the energy for the tracks were corrected if a muon was within an annular cone of radius 0.2 of another muon candidate. The correction was the subtraction of the other muon track's expected hadronic energy deposition (determined from Monte Carlo studies) from the muon track's hadronic energy.

To discriminate against *ghost* muon tracks (tracks mistakenly reconstructed due to a high density of hits) we compared two quality indicators between the closely spaced tracks. If two tracks were within $\Delta\phi^{2\mu} \leq 0.05^\circ$ or $\Delta\theta^{2\mu} \leq 0.05^\circ$ of each other, then we kept the track which had the smallest IFW4 or chisquare value. As an assurance to eliminate combinatorial background muons the 3-dimensional opening angle of the dimuon had to be greater than two degrees.

Finally, the author scanned the event displays of over 2000 multimuon events[7] to help determine some of the selection analysis cuts (*e.g.* ghost track cut, hits per muon detector layer) and to remove any surviving bad events which passed the selection criteria—in particular trimuon candidates. Figure 6.5 is an example of a bad event which passed all the good multimuon selection criteria. As one can clearly see two of the muons were back-to-back—

[7] Over the span of three years.

evident from the tracks and MIP traces. Furthermore, the central detectors did not have many tracks which pointed to the vertex even though there was a lot of deposited energy in the calorimeter along the direction of the muon candidates. Even though each respective filter had a cosmic rejection cut this event exemplified an accepted cosmic event. Therefore, it was decided early in the analysis that visual confirmation of the passed multimuon events was necessary to remove remaining cosmic and other bad events. In particular, scanning helped reduced 67% of the passed offline selected trimuon events (see Table 6.2). A few of the criteria used to determine a good multimuon event were:

- The matching of central detector hits to the muons that do not point to the primary vertex;
- The assurance of the MIP confirmation along the trajectory path of the muons. There may have been readout problems of the calorimeter cells, to either side of the muons, typically resulting in an over estimate of the measured "deposited" energy (hot cells: Section 4.4).

An example of a good dimuon event is shown in Fig. 6.6.

Figure 6.3 was the resulting opposite/same sign dimuon mass distributions after the imposition of the above criteria. In the opposite sign spectrum, one can clearly see a J/ψ peak. The left shoulder of the J/ψ peak indicates dimuons produced from the cascade decay of b-quarks, next-to-leading order Drell-Yan production, and low mass resonant mesons. To the right of the J/ψ peak indicates dimuons from parallel semileptonic decay of heavy quarks, upsilon and leading order Drell-Yan production. The like sign dimuon high mass spectrum is principally due to the semimuonic parallel decay and/or the $B\bar{B}$ mixing of the b and $\bar{b}$-quarks and whereas the low mass dimuons are primarily from next-to-leading-order heavy flavor production, *e.g.* gluon splitting. In addition, both dimuon spectra—high and low mass—have dimuons resulting from the combination of prompt plus decay muons.

Trigger		MU2HIGH	
		Muon	**Dimuon**
Kinematic	$\|\eta\|$	≤ 1	≤ 0.8
	ϕ	$80° < \phi$ or $\phi > 110°$	—
	P_T	3.3-25 GeV/c [a]	$\geq$ 6.6 GeV/c for $M_{2\mu} \leq 6$; none for $M_{2\mu} > 6$
	3-D angle	—	$\geq 2°$
Muon Quality		MIP = hadronic fraction ≥ 0.6 and $E^{had}_{3\times3\ cells} \geq 0.5$ GeV	
		IFW4 = 0 or 1 [b]	
		$\int \vec{B} \cdot d\vec{l} \geq 0.5$ GeV [c]	
		$\chi^2 \geq 0$	
		Hits along track	

Table 6.1: Muon and Dimuon Selection Criteria

[a] No upper limit for third muon

[b] If IFW4 equalled 1, then we insisted that the track had a good bend and non-bend fit.

[c] 0.2 GeV for third muon

	Candidate 2μ Events	**Candidate 3μ Events**	$\mathcal{L}$ (pb^{-1})
Entire Run 1A Data Set	12.7×10^6	NA	13.2 ± 0.70
B2M Filter	7.6×10^5	NA	
Subfilter	5×10^5	NA	
MU2HIGH Trigger	186362	40624[a]	11.5 ± 0.62
Post Shutdown MU2HIGH	43079	12230[a]	6.73 ± 0.36
All Global Event Cuts	27861	3302[a]	
Analysis Cuts	1973	27	
After Scanning	1919[c]	9	

Table 6.2: Reduction of Run 1A Multimuon Data Sample

[a] No cuts on 3rd μ

Background subtraction has not been done for either mass distributions.

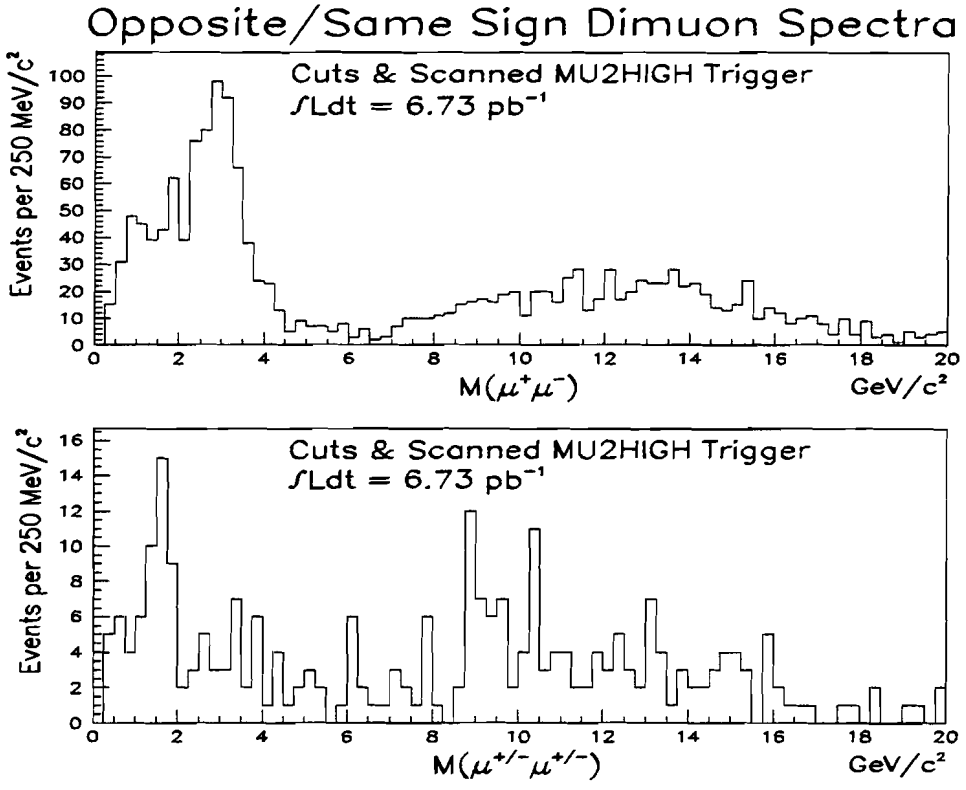

Figure 6.3: Dimuon opposite/same sign mass spectra after the imposition of all the quality selection criteria.

Run 1A was DØ's first test and physics run. Consequently, run conditions and the detector's response were not anticipated and understood. For example, we did not have enough available tools to veto cosmic rays at the trigger level. As a result, we needed to spend a considerable amount of time devising offline cuts to reduce the triggered data. Even with one's "final" data sample scanning was necessary. The experienced gained from DØ's inaugural run was valuable for the consecutive runs (1B and 1C). Among the improvements were the installation of scintillator counters and the counters use in the hardware trigger, along with the MIP requirement in Level 2, to help reject cosmic rays and spurious muon tracks, better comprehension of the muon chamber performance to maximize their usage

and refinements to DØReco to reduce bogus muon candidates.

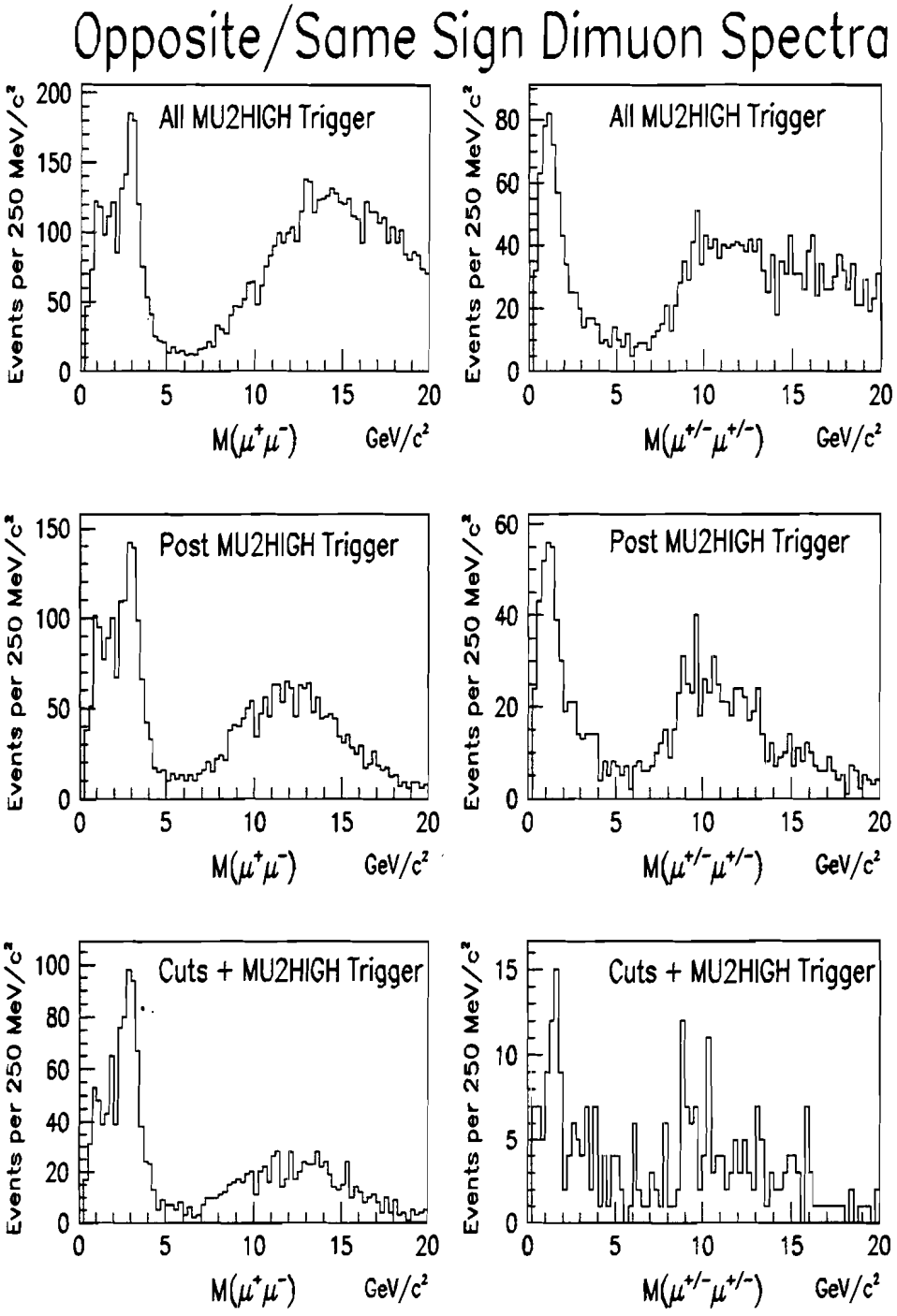

Figure 6.4: The progression of the dimuon mass spectra at various stages of the MU2HIGH requirement.

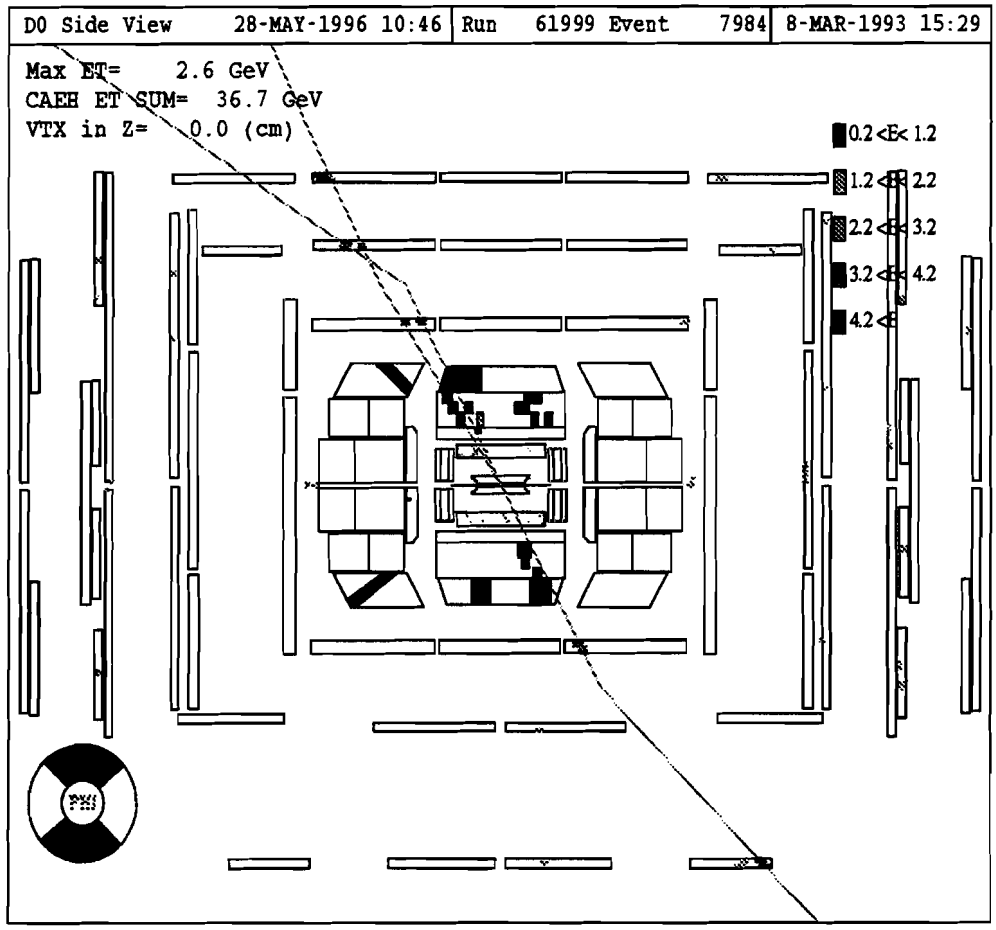

Figure 6.5: A cosmic event which passed all of our selection criteria. This event, and other cosmic and poor quality events, were only eliminated by scanning.

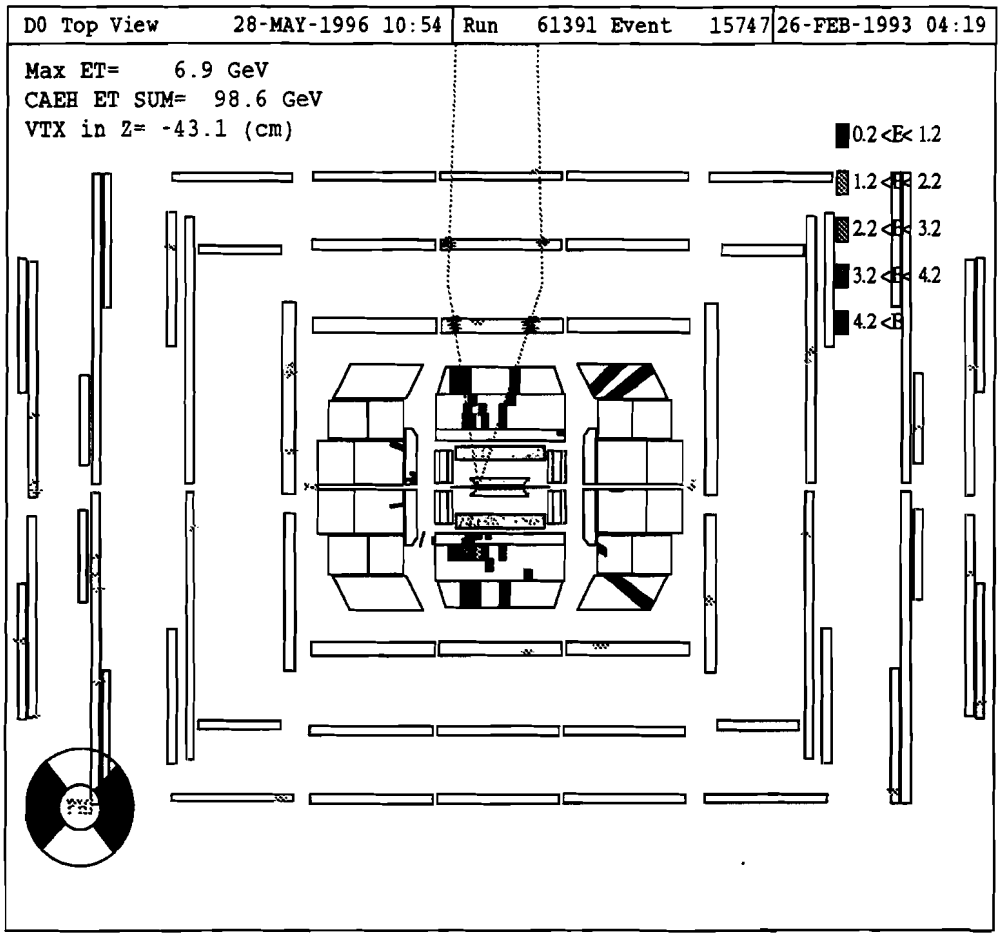

Figure 6.6: An example of a good dimuon event. Note the associated calorimeter traces for each muon track.

Chapter 7

DETERMINATION OF ACCEPTANCES, EFFICIENCIES AND SYSTEMATICS

"Did nothing in particular, and did it very well." W. S. Gilbert

A reality of high energy experimental physics research is that not all produced physics events will be observed for analysis. Limitations, such as detector acceptance, and trigger, reconstruction and offline selection criteria efficiencies, must be taken into account in order to arrive at meaningful results. This chapter will address the efficiency and acceptance corrections needed for our multimuon analysis, and the systematic uncertainty associated with those emendations.

7.1 Acceptances

As stated in Section 5.3, in order to avoid high inefficiencies in running DØGEANT we imposed kinematic cuts on the ISAJET generated Monte Carlo muons. Such being the case, we needed to correct for the dimuon acceptance for those events which failed to survive the muon kinematic requirements. Figure 7.1 is the acceptance curves, as a function of dimuon P_{T}, for the J/ψ and $Q\bar{Q}$ Monte Carlo sets.

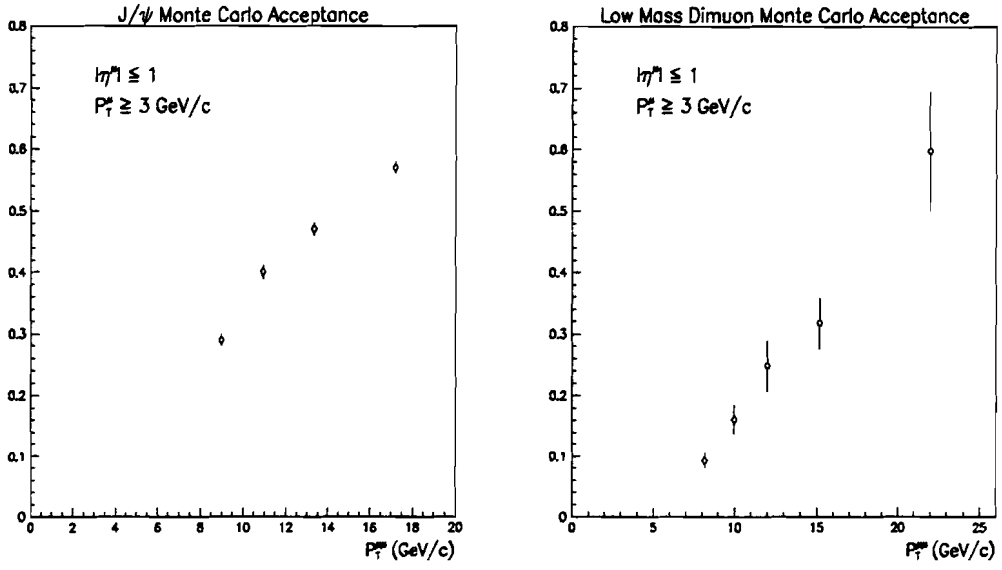

Figure 7.1: Monte Carlo Acceptance for J/ψ and Low Mass Dimuons

7.1.1 Azimuthal "Hole"

As alluded to in Section 7.2.3, the chambers with the lowest efficiency were the ones in the vicinity of the Main Ring pipe. Hence, we excluded in our analysis of the Monte Carlo events muons that occupied the azimuthal fiducial volume between 80–110°. This correction corresponded to a 92% correction factor per muon.

7.2 Efficiencies

Trigger and offline reconstruction efficiencies to be discussed were arrived by using the generated J/ψ[1] and $Q\bar{Q}$ Monte Carlo events, while the selection criteria efficiencies were determined from the data. Recall that the simulated events were processed through a complete detector simulation and processed with the same DØReco version as the data. The efficiencies to be discussed are presented in the order the corrections were applied and the efficiency curves are plotted in the respective bins for the two above mentioned dimuons

[1] A weighted average of 60% B-J/ψ and 40% χ_c-J/*psi*. Justification stated in Chapter 9.

we principally studied (see Sections 9.2 and 9.3 for the decided upon bin P_T divisions).

7.2.1 MU2HIGH Trigger

Details of MU2HIGH's hardware and software specifications were presented in Section 6.2.1. In summary, the MU2HIGH requirements were

- Level 1: two muons with $|\eta^{\mu}| < 1.7$;
- Level 2: two muons with $P_T^{\mu} > 3$ GeV/c and $|\eta^{\mu}| < 1.7$.

The efficiency determination was accomplished by the use of the TRIGSIM package (Section 5.2.2). We simulated the hardware and software configuration for trigger version 7.2 with the J/ψ and $Q\bar{Q}$ Monte Carlo events. Table 7.1 lists the integrated MU2HIGH trigger efficiencies for the respective Monte Carlo samples. Figure 7.2 illustrates the combined L1×L2 efficiency for each Monte Carlo set as a function of dimuon P_T.

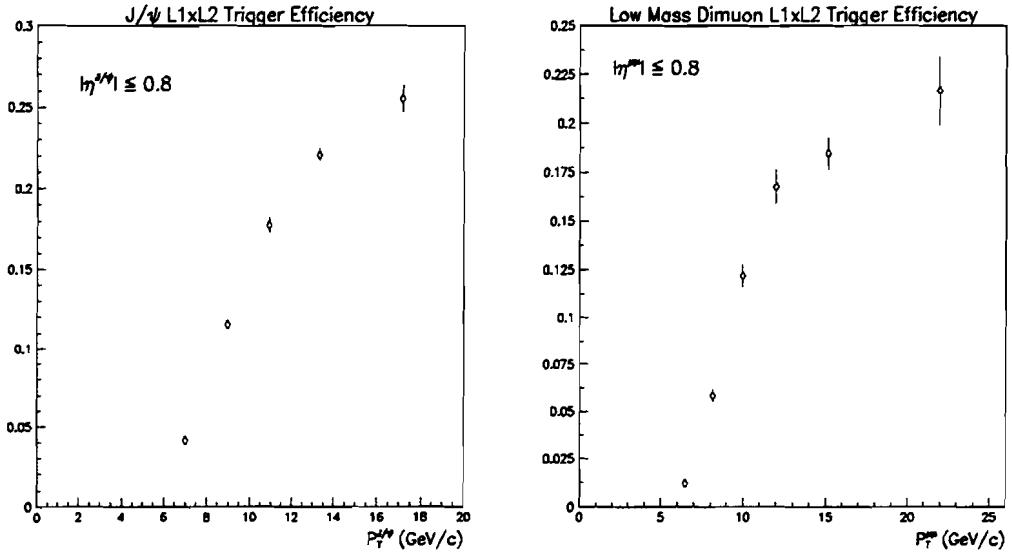

Figure 7.2: Trigger Efficiency for J/ψ and Low Mass Dimuons

Physics Process	Level 1	Level 2	L1·L2
J/ψ	0.187 ± 0.002	0.705 ± 0.012	0.132 ± 0.002
$Q\bar{Q}$	0.152 ± 0.002	0.588 ± 0.013	0.089 ± 0.002

Table 7.1: Integrated MU2HIGH Level 1 and Level 2 Trigger Efficiencies

7.2.2 Reconstruction

Once an event satisfied the MU2HIGH trigger we studied what was the probability of the given dimuon to be constructed by DØReco. The kinematic requirements on the muons were $|\eta| < 1$ and $P_T > 3.3$ GeV/c. In order to arrive at the reconstruction efficiency for the J/ψ and $Q\bar{Q}$ Monte Carlo samples we assured the parentage of the muons composing the dimuon, *i.e.* ISAJET muons from b-meson decays were matched to the closest reconstructed track[2]. The reconstruction efficiencies for the respective Monte Carlo sets are shown in Fig. 7.3.

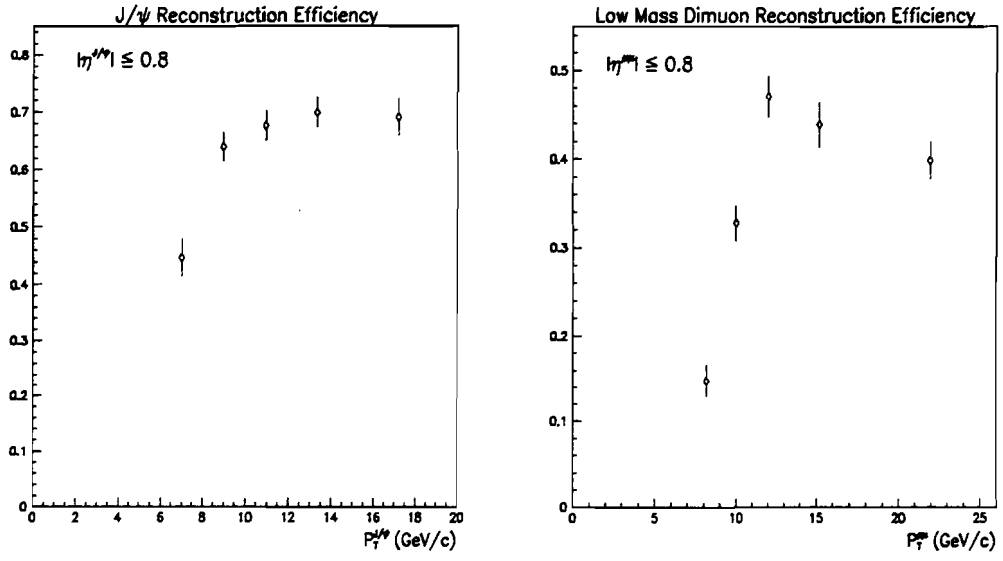

Figure 7.3: Reconstruction Efficiency for J/ψ and Low Mass Dimuons

[2]We defined the closest reconstructed track as follows:

$$\Delta\left(\theta_\mu^{ISAJET} - \theta_\mu^{RECO}\right) \leq 10^\circ \quad \text{and} \quad \Delta\left(\phi_\mu^{ISAJET} - \phi_\mu^{RECO}\right) \leq 10^\circ .$$

7.2.3 Muon Chambers

Even though we processed the generated Monte Carlo events with the MUSMEAR package (Section 5.2.1.1.2), to account for chamber inefficiencies, the simulated chamber efficiency did not agree with the actual one measured from calibration runs. The discrepancy between the simulation and the data was due to the fact that the MUSMEAR package did not model the debris deposited on the wires of the proportional drift tubes[3] [96]. The deposited debris was produced from a chemical reaction between the muon chamber's gas mixture and the Glasteel[4]. The reaction was induced by the radiation from the $p\bar{p}$ collision. As a result, we accounted for the disagreement by introducing an additional efficiency of $81 \pm 6\%$ per muon track.

7.2.4 Offline Selection Criteria

We have addressed what are the efficiencies for triggering and reconstructing dimuons from $Q\bar{Q}$ and J/ψ processes. The next step was to separate good dimuons from bogus dimuons in our data set. This was accomplished by the five imposed offline selection criteria discussed in the previous chapter, which were:

1. IFW4;
2. MIP confirmation;
3. $\int \vec{B} \cdot d\vec{l}$;
4. Hits on track per layer;
5. χ^2.

To get a quantitative sense, the efficiencies for the offline cuts were determined from data since the processed Monte Carlo events did not "truly" simulate every detector response, *e.g.* degradation of the tracking chamber's hits was not mimicked because no package was

[3]This was discovered in the summer of 1994.

[4]Polyester and epoxy copolymer sheets with chopped glass fibers.

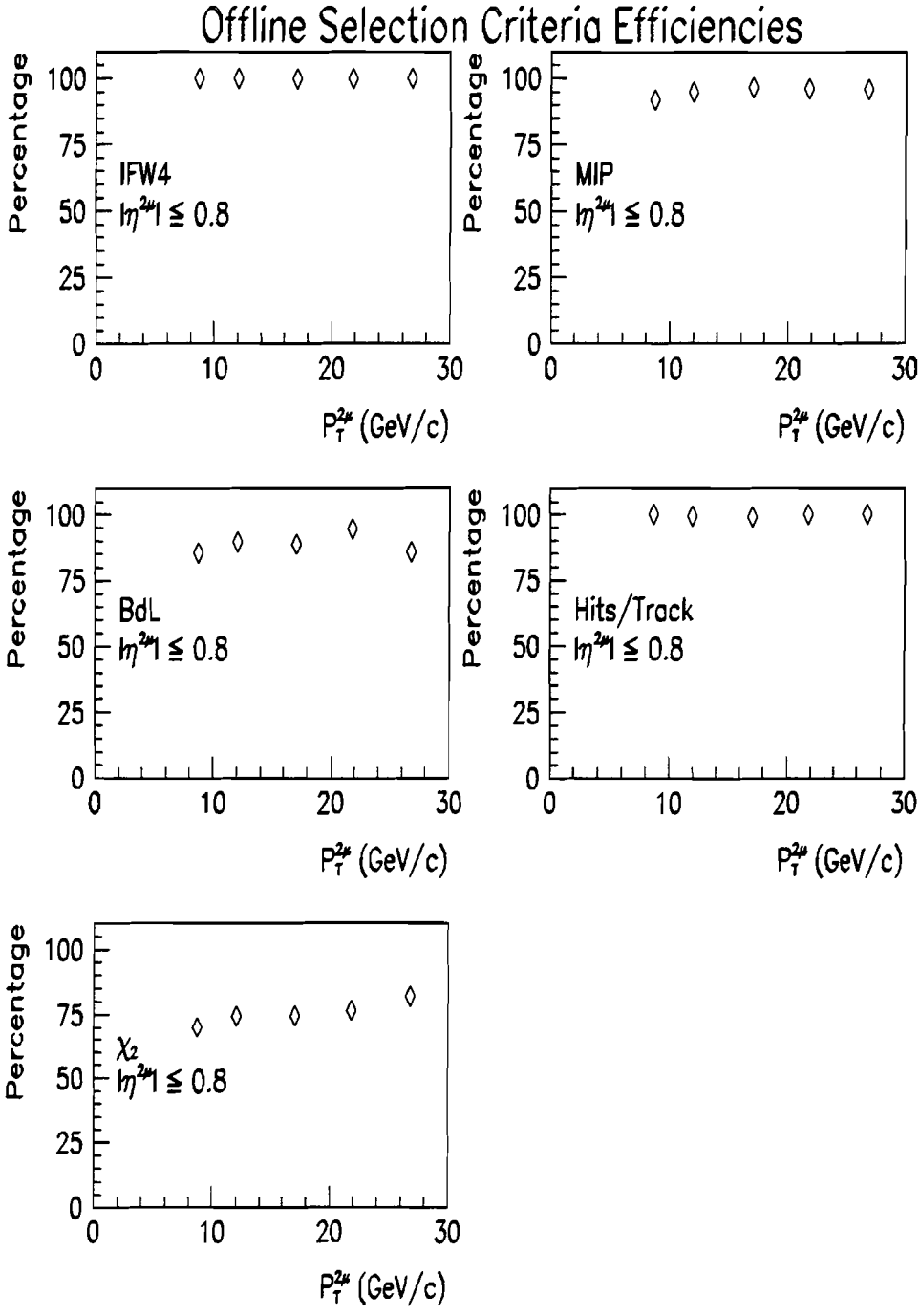

Figure 7.4: Efficiencies for the Five Offline Cuts

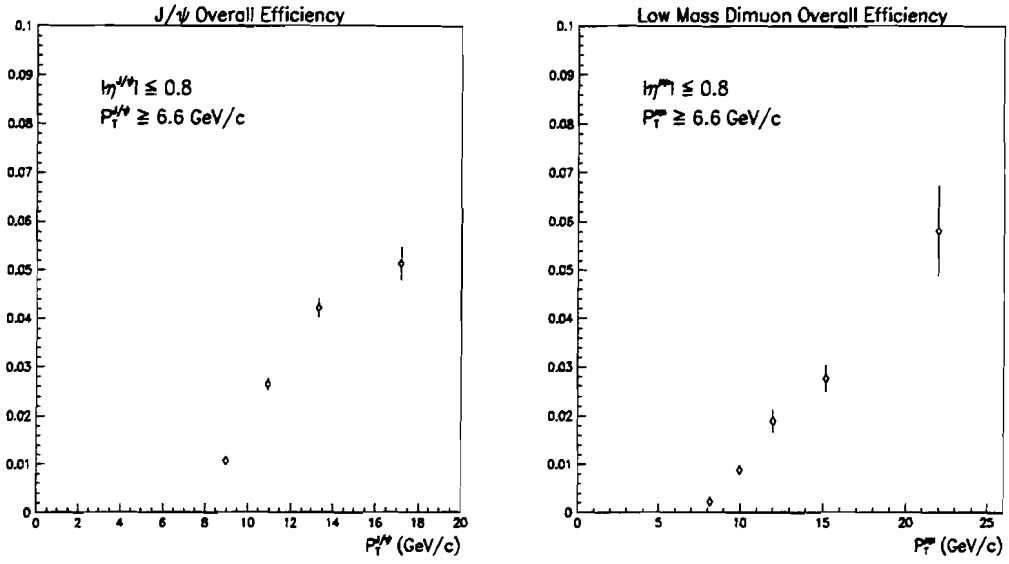

Figure 7.5: Overall Detection Efficiency for J/ψ and Low Mass Dimuons

available at the time of this thesis. Therefore, we decided to use the data as the principle means for our offline cuts efficiency study. However, for our overall efficiency (Section 7.3) we used our generated Monte Carlo events.

Commencing with the data which passed the subfilter (Section 6.1.2), we selected a best measured subset of dimuon events—to ensure a negligible component of background muons in the data—by the imposition of the above listed cuts on MU2HIGH triggered events. Each offline cut was relaxed in turn and the fraction of the events lost was noted. The efficiencies are shown in Fig. 7.4 as a function of dimuon P_T.

7.3 Overall Acceptances and Efficiencies

We have discussed all of the pertinent acceptances and efficiencies for our multimuon analyses. Their convolution described the probability of detecting a muonic decayed J/ψ or a semi-muonic decayed $Q\bar{Q}$ in our data set. Figure 7.5 displays the respective detection curves for the two physics processes of interest. These plots were integral in measuring

our sequential dimuon and inclusive J/ψ cross Sections to be presented in Chapter 9. It must be stressed, we did not take the product of the previous trigger, offline selection cuts and reconstruction histograms. The overall efficiency for the three mentioned criteria were respectively obtained from the generated J/ψ and $Q\bar{Q}$ Monte Carlo samples. Essentially, for each Monte Carlo set, the overall efficiency was calculated as a ratio of the number of events satisfying all cuts simultaneously to the number of events allowed as input. Therefore, we should have accounted for any possible correlation between cuts.

What is evident from the respective plots is that neither efficiency curve has a plateau. Unfortunately, the efficiency for the majority of our dimuons were on the ascending portion of the curves. Dimuons from J/ψ's had a slightly better detection efficiency than dimuons from $Q\bar{Q}$ decays.

7.4 Systematic Errors

Even though we corrected for all crucial factors which diminished the observation of multimuon events no determination is absolutely assured. Uncertainties were associated with those corrections. Hence, we studied the robustness for each efficiency factor presented in this chapter.

7.4.1 MU2HIGH Trigger Systematic Error

Verification of the efficiencies listed in Table 7.1 was done in [92]. A comparison of the hardware and software trigger was made between data events with one and two muons. It was concluded that the Monte Carlo events modeled data very well for Level 1. However, for Level 2 a 15% discrepancy was found for trigger version 7.3 and a 8% difference for version 7.2. Since the data analyzed in this thesis was predominately taken with trigger version 7.2 we estimated a 10% correction was needed with a 5% associated uncertainty.

Source	Systematic Error (%)
Monte Carlo Statistics	5–10
Trigger Simulation	5
Chamber Efficiency	10
Offline Cuts	6
Luminosity	5.4
Unfolding P_T Spectrum	5–10

Table 7.2: Sources of Systematic Errors

7.4.2 Offline Selection Criteria Systematic Error

The systematics for the offline selection cuts were determined from Monte Carlo events. We defined good Monte Carlo dimuons by the before mentioned requisites and events that passed the MU2HIGH trigger. Once again, we relaxed each cut in turn to determine their respective efficiency. Comparing the efficiencies measured from the data and Monte Carlo events, the uncertainty estimation for IFW4, MIP, $\int \vec{B} \cdot d\vec{l}$, and hits on track cuts was less than 2% for each; the error for the χ^2 cut was of the order 6%. Because of correlations between the various cuts, the systematic error for the overall offline cuts was taken to be 6%.

7.4.3 Additional Systematic Errors

In addition to the two discussed systematic errors the integrated luminosity had an uncertainty of 5.4%. This value was common to all DØ's Run 1A analyses and was due to the uncertainties on the total inelastic cross section at Tevatron energies [97]. Another uncertainty was attributed to the unfolding of the dimuon's transverse momentum spectrum (to be presented in the Sections 9.2 and 9.3). This was arrived by comparing the smeared and unsmeared dimuon P_T spectra for the different bins used in our study. We estimated the bin dependent uncertainty to be 5–10%. Finally, an important systematic error in our

analysis was the limited statistic of Monte Carlo events. The error bars quoted for the efficiency and acceptance plots account for this uncertainty.

The systematic errors stated in this chapter are summarized in Table 7.2.

Chapter 8

STATISTICAL METHODS

"Mathematics, rightly viewed, possesses not only truth, but supreme beauty—a beauty cold and austere like that of sculpture." Bertrand Russell

The basic principles of statistical inference involve the notions of experiment, outcome, sample space, event and probability. In High Energy Physics, like in all of physics, it is assumed that each measurement is independent of any preceding one. It is also assumed that there is an underlying physics mechanism determining the nature of the data. If the underlying physics mechanism is known, then the probability that certain outcomes occurred can be calculated (probability theory). Statistics is concerned with the application of probability theory to data. One uses statistical methods on data to infer which physics mechanism generated it and to associate probabilities to the various mechanisms.

In this chapter, we will discuss the two statistical methods employed in this thesis, the Maximum Likelihood Method and Bayes Decision Theory, to decipher the relative contributions of various dimuon production mechanisms in the data and the deconvolution of the dimuon momentum spectrum to arrive at the b-quark cross section.

8.1 Maximum Likelihood Method

A widely used method of parameter estimation is the maximum likelihood method (MLM). For families of discrete or continuous distributions, the probability of obtaining

the particular sample that has been observed can be computed and then those values of the parameters that maximize the probability can be chosen as estimates[1]. In our application, physics distributions of different processes are parametrized to arrive at normalized probability distribution functions (PDF). To distinguish various physics processes one combines the different PDF to form a correctly normalized likelihood function which is maximized with respect to coefficients that serve to normalize the contribution of each physics process. Symbolically, the likelihood function is

$$\pounds = \prod_{i=1}^{nevent} \left(\sum_{j=1}^{nproc} A_j \prod_{k=1}^{nvar} f_{jk}(x_{ik}) \right) , \tag{8.1}$$

where x_{ik} represent the k^{th} physics variable for the i^{th} event whose normalized distribution for the j^{th} process is given by the PDF $f_{jk}(x_{ik})$ and A_j represent normalizing coefficients for the j^{th} process. Equation 8.1 holds for a set of uncorrelated variables. A more complicated expression has to be used for the correlated case.

Using the constraint that the sum of the estimates for the various physics processes must add up to the total number of the observed events, the A_j maybe rewritten in terms of independent parameters. For example, if p_j are the independent parameters, then for six physics processes the re-expression of the A_j is:

$$\begin{aligned}
A_1 &= p_1 \\
A_2 &= (1-p_1)p_2 \\
A_3 &= (1-p_1)(1-p_2)p_3 \\
A_4 &= (1-p_1)(1-p_2)(1-p_3)p_4 \\
A_5 &= (1-p_1)(1-p_2)(1-p_3)(1-p_4)p_5 \\
A_6 &= (1-p_1)(1-p_2)(1-p_3)(1-p_4)(1-p_5) \ .
\end{aligned} \tag{8.2}$$

By minimizing $-\ln \pounds$ with respect to the p_i we obtained likelihood estimates of the

[1]Although symbolically the same, the likelihood in the discrete situation is a probability, but in the continuous case it is a measure of the density of probability at the sample point.

A_j which measure the contributed amount for j^{th} processes. The actual minimization was performed with the use of the MINUIT package [98].

The attractive features of the MLM to physicists [99] are:

1. Invariance under parameter transformation: regardless of the functional form one uses for a PDF the MLM is free of arbitrariness in the minimization procedure;
2. Consistency: the MLM estimates will converge towards the true values when one has a large input data sample;
3. Unbiassedness: for any size data set, the estimates will be distributed with a mean equal to the true estimates' value;
4. Sufficiency: the MLM produces the estimate with the minimum attainable variance;
5. Efficiency: the variance of the MLM estimators can not be arbitrarily small;
6. Uniqueness: every solution of the likelihood equation corresponds to a minimum of the likelihood function;
7. Asymptotic normality of the MLM estimators: the estimates are asymptotically normally distributed about their true values.

8.1.1 Parametrization

In order to employ the MLM one needs to describe the dissimilar physics distributions, *e.g.* invariant mass and transverse momentum spectra for dimuon system, by their respective PDF. The various physics processes considered were modeled by Monte Carlo events, with full detector and trigger simulation, and offline selection criteria imposed, as discussed in Chapter 5. We parametrized the physics distributions for each of the physics processes to arrive at the "best" functional representation—probability distribution function. In the proceeding sections we detail how we attained the PDF for the disparate distributions.

8.1.1.1 One-Dimensional Parametrization

The parametrization of one-dimensional (1-D) physics distributions was obtained by the use of a CERN FORTRAN subroutine, HQUAD [100], which is interfaced with PAW [101] in order to utilize PAW's Application Visualization System (AVS) [102]. HQUAD represents the input distribution in multiquadric radial basis functions (MRBF). The creator of the algorithm, implemented in HQUAD, has shown [103] that MRBF are extremely suitable to describe event densities. The author of the paper demonstrated that MRBF are:

- Smooth: follow statistically significant variations where necessary in a non-abrupt way, continuous to all orders and behaving close to linearly elsewhere;
- No-nonsense: no uncontrolled, unnecessary or erratic departures from the input distributions;
- Unbiased: follow statistically significant variations faithfully while ignoring insignificant ones;
- Economical: the number of basis functions is determined primarily by the statistical significance of the input distribution and not by the dimensionality of the input distribution (*i.e.* 1-D, 2-D or 3-D);
- Positive: ensures the functional form of the event densities to be always positive.

PAW's AVS was crucial because it allowed one to visualize the fitted analytic function to the various distributions. By manually adjusting the *sensitivity* and *smoothness* parameters one chose the best functional representation for the different distributions for each of the considered physics processes. The resulting functions were normalized and used as the PDF.

8.1.1.2 Two-Dimensional Parametrization

In contrast to the one-dimensional case, two-dimensional distributions (2-D) are more problematic to parametrize because of their increased statistical fluctuations. Even though

multiquadric radial basis functions can be used to represent a 2-D distribution, the events of the Monte Carlo samples used are not uniformly distributed to get reliable functional forms. Instead, the 2-D PDF we used was a grid appropriately normalized to the number of events for the respective two-dimensional distribution.

8.2 Bayes Decision Theory

To arrive at a governing process' distribution from the observed measurements, *e.g.* the determination of the produced transverse momentum spectrum from its reconstructed P_{T} spectrum, Bayes' Theorem [105] provides an estimation procedure to unfold experimental distributions. An advantage of Bayes' Theorem is that there is no dependence on the theoretical shape of the distribution to be unfolded. Bayes' procedure simply describes how the true spectrum maps into the distorted spectrum. Another benefit of the theorem is that it allows an error analysis based on the input smearing distribution and the number of events in the input distribution to compute uncertainties in the number of umsmeared events.

Bayes' Theorem has two suppositions:

1. there are several independent causes, C_i $(i = 1, 2, \ldots, n_c)$, which can produce one effect, E;
2. one knows the initial probability of the causes $P(C_i)$ and the conditional probability if the i^{th} cause to produce the effect $P(E|C_i)$.

Given the above conditions, the theorem states if one observes a single effect, then the probability that it is due to the i^{th} cause is proportional to the probability of the cause times the probability of the cause to produce the effect. Mathematically, the theorem can be written as

$$P(C_i|E) = \frac{P(E|C_i) \cdot P(C_i)}{\sum_{l=1}^{n_C} P(E|C_l) \cdot P(C_l)} \ . \tag{8.3}$$

For our specific application, the cause C_i was the $P_{\mathrm{T}}^{\mathrm{true}}$ of the produced dimuon, the effect E was the dimuon's reconstructed $P_{\mathrm{T}}^{\mathrm{meas}}$, and $P(E|C_i)$ was the mapping between the two spectra. Subdividing the distributions into k intervals we can reformulate Equation 8.3 into

$$\left(\frac{\mathrm{d}N}{\mathrm{d}P_{\mathrm{T}}}\right)^{\mathrm{true}} = \sum_{j=1}^{k} \frac{P(E_j|C_i)\cdot P(C_i)}{\sum_{l=1}^{nc} P(E_j|C_l)\cdot P(C_l)} \cdot \left(\frac{\mathrm{d}N}{\mathrm{d}P_{\mathrm{T}}}\right)_j^{\mathrm{meas}} \quad . \tag{8.4}$$

The Bayesian approach gives a convenient way of incorporating prior information about the contributing effects which distort data, such as detector response. Since it is the aim of the experimentalist to extract the true distribution from the distorted data, a comprehensive knowledge of the overall effects is required. We used Monte Carlo events, which were processed with full detector and trigger simulation, and survived our offline selection criteria, to arrive at such an understanding, thus obtaining $P(E|C_i)$. The application of Bayes' multidimensional unfolding method allowed us to arrive at the "true" dimuon P_{T} distribution from the measured one.

Chapter 9

DIMUONS & TRIMUONS

"Science arises from the discovery of identity amidst diversity." W. J. Jevons

Dimuons were copiously produced at the Tevatron by various physics mechanisms. The task at hand was to distinguish the different processes in order to identify dimuons from heavy quark production. The differentiation was achieved by the employment of the Maximum Likelihood Method. We restricted ourselves to dimuons in the invariant mass range of 0.25–6.25 GeV/c^2, with the kinematic requirements of $P_T^{2\mu} > 6.6$ GeV/c and $|\eta^{2\mu}| < 0.8$. From our fit we extracted the low mass dimuon production cross section and studied dimuons associated with jets in order to separate Leading-Order and Next-to-Leading-Order QCD processes. Moreover, as a complementary identifier of heavy quark events we searched for an associated third muon in the dimuon events and studied some trimuon topological characteristics.

9.1 Dimuon Production Processes

From the many different sources of low mass dimuons this thesis focused on two dimuon production mechanisms—J/ψ and the semimuonic decay of b-quarks. J/ψ's are produced from direct charmonium [106], weak decay of a B-hadrons [107, 94] and parton fragmentation into charmonium states [89]. We only modeled the first two mechanisms for J/ψ

production. At the time of this analysis no parton fragmentation generator existed. Ultimately, we were only interested in J/ψ from b-quarks in order to study the quark's production cross section. As for the case of the semimuonic decay of b-quarks there are two distinct decay modes: 1) parallel decay of both b-quarks; and 2) sequential decay of one b branch. Schematically, the three pertinent sources of dimuons for our study are

$$\begin{aligned} p\bar{p} \rightarrow\ & b \rightarrow J/\psi + X \\ & \quad\ \hookrightarrow \mu^+\mu^- \end{aligned}$$

$$\begin{aligned} p\bar{p} \rightarrow\ & b\bar{b} \rightarrow \bar{c} + \mu^+ + \nu_\mu \\ & \quad\ \hookrightarrow\ c + \mu^- + \bar{\nu}_\mu \end{aligned}$$

$$\begin{aligned} p\bar{p} \rightarrow\ & b \rightarrow c + \mu^- + \bar{\nu}_\mu \\ & \quad\ \hookrightarrow\ s + \mu^+ + \nu_\mu \ . \end{aligned}$$

The discrimination of different dimuon sources was accomplished by the employment of the Maximum Likelihood Method (MLM), as discussed in Chapter 8. We simultaneously fitted contributions of six modeled dimuon processes (Chapter 5), which were:

1. J/ψ from Bottom Production Model (BPM);
2. J/ψ from Charmonium Production Model (CPM);
3. Dimuons from heavy flavor $Q\bar{Q}$ production including the effect of B°-$\bar{B}^\circ$ mixing[1];
4. Dimuons from Drell-Yan production;
5. Dimuon from decays of low mass mesons ($\rho, \phi, \omega, \eta, \eta'$);
6. Dimuons from pion/kaon decays.

From the listed simulated physics processes, we studied and optimized the choice of variables used for the MLM fit. The variables chosen were the invariant mass for both opposite

[1]We took the weighted average for the mixing of B_d and B_s mesons. B_d mixes 15.6% of the time, while B_s mixes 62% of the time. In addition, we used the measurements that B_d and B_s are approximately 85% and 15% of the B mesons. Therefore, the mixing Monte Carlo events were combined with the non-mixed $b\bar{b}$ events in proportion to the world mixing average of $85\% \cdot 15.6\% + 15\% \cdot 62\% \approx 22.6\%$.

and same sign dimuons, and the dimuon's transverse and parallel momenta relative to an associated jet[2] axis (P_T^{rel} and momentum fraction Z).

The same sign mass spectrum was principally used to constrain π/K dimuons and to a lesser extent the occurrence of misidentification of the muon's sign. The mixing Monte Carlo events were essential because they helped distinguish between same sign π/K and $Q\bar{Q}$ dimuons. For each type of Monte Carlo events the same and opposite sign mass spectra were histogramed together, with a 6.25 GeV/c^2 shift to separate them.

The resultant histograms were parametrized to obtain the probability distribution functions (PDF). These PDFs took into account the expectation of the experimental low mass dimuons of being due to one of the six modeled processes; this included the chance of the dimuon being observed as a same sign dimuon. Figure 9.1 are the respective invariant mass parametrizations for the various Monte Carlo samples. It must be noted that we shifted the two J/ψ mass parametrizations by 100 MeV in order to fit the data.

The variables P_T^{rel} ($= P^{2\mu}\sin\theta^{rel}$) and Z ($= P^{2\mu}\cos\theta^{rel}/|P^{2\mu+jet}|$) could only be defined for dimuons associated with a jet. We looked at jet candidates with cone size of 0.7 in $\eta \times \phi$ space and required the potential candidate associated jets the standard quality cuts as discussed in Section 4.4.

A dimuon was considered associated to a jet if the radius, in $\eta \times \phi$ space, between the jet and dimuon was less than 0.7 units ($\mathcal{R} = \sqrt{\Delta\eta^2 + \Delta\phi^2}$). Once an association was made a "dimuon+jet" system was defined. First, we calculated the radial distance between the jet and each muon comprising the associated dimuon. If either muon, or both, was within $\mathcal{R} = 0.7$ of the jet, then the associated muon(s)'s expected energy loss was(were) subtracted from the jet's 4-momentum vector. Finally, the associated muon(s)'s 4-momentum was(were) added vectorially to the jet's 4-momentum hence defining the dimuon+jet system.

[2]See Section 4.4 for definition of a jet and quality variables.

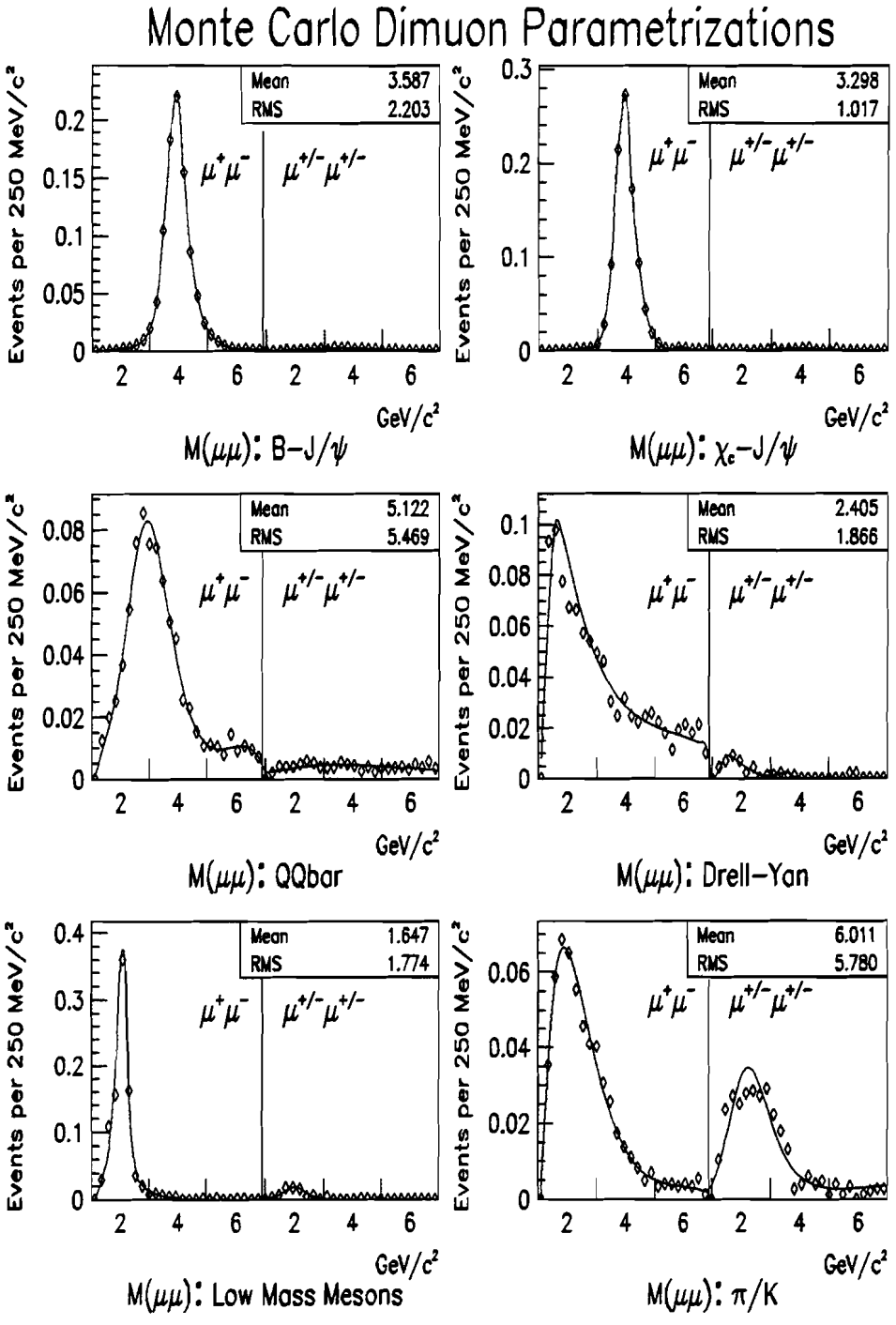

Figure 9.1: Normalized Monte Carlo Dimuon Mass Parametrizations

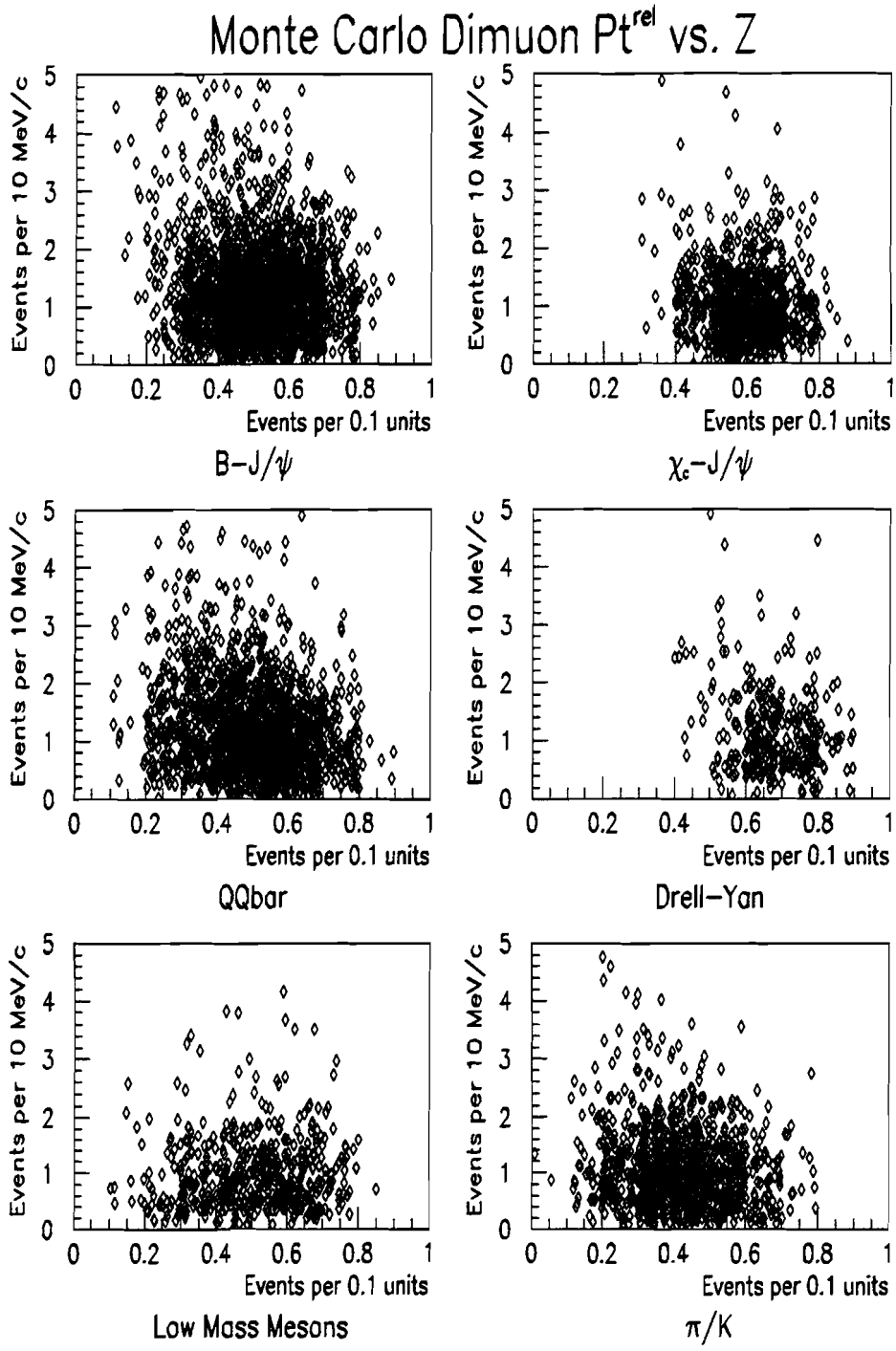

Figure 9.2: Monte Carlo Scatter Plots for the Dimuon P_T^{rel} and Momentum Fraction

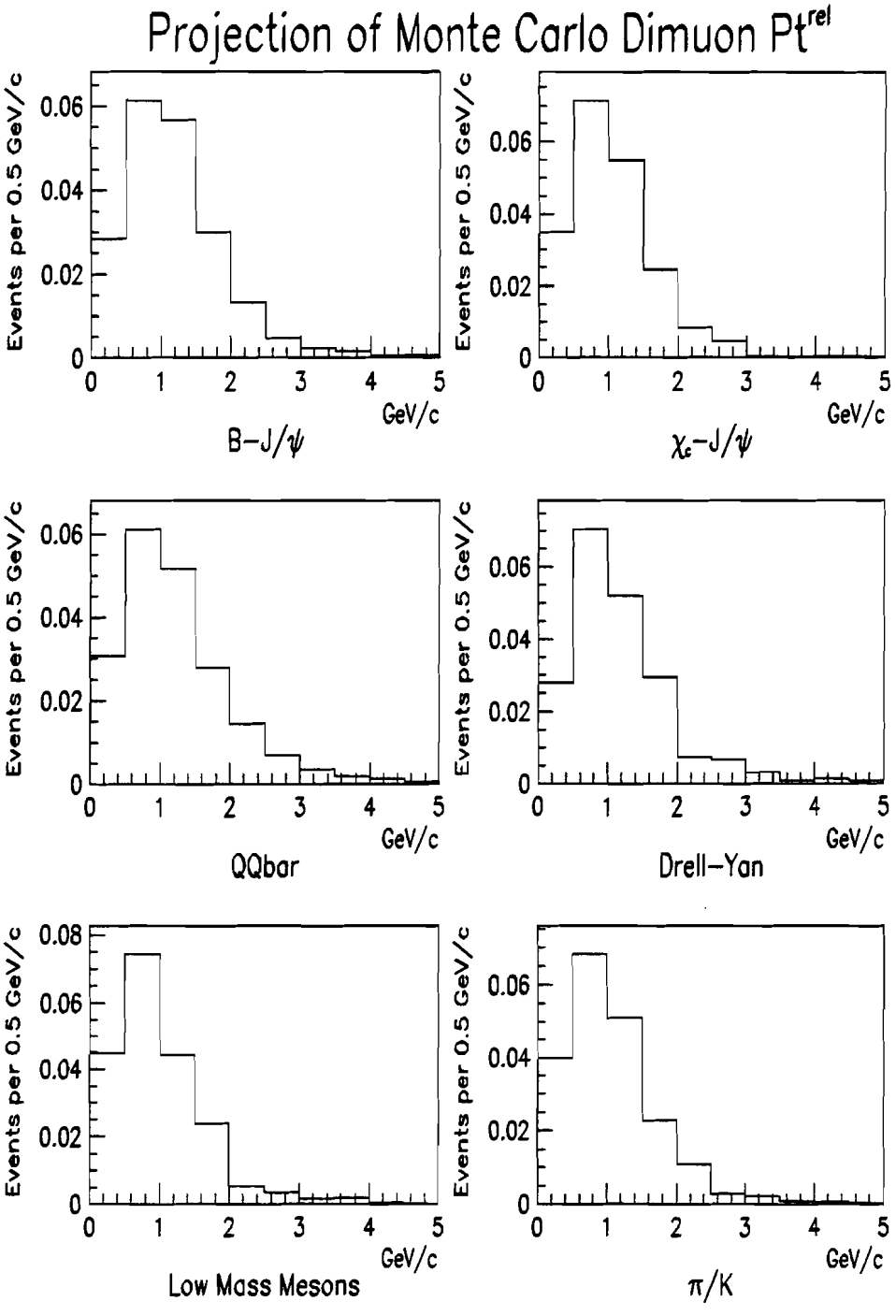

Figure 9.3: Monte Carlo Dimuon P_T^{rel} Distribution

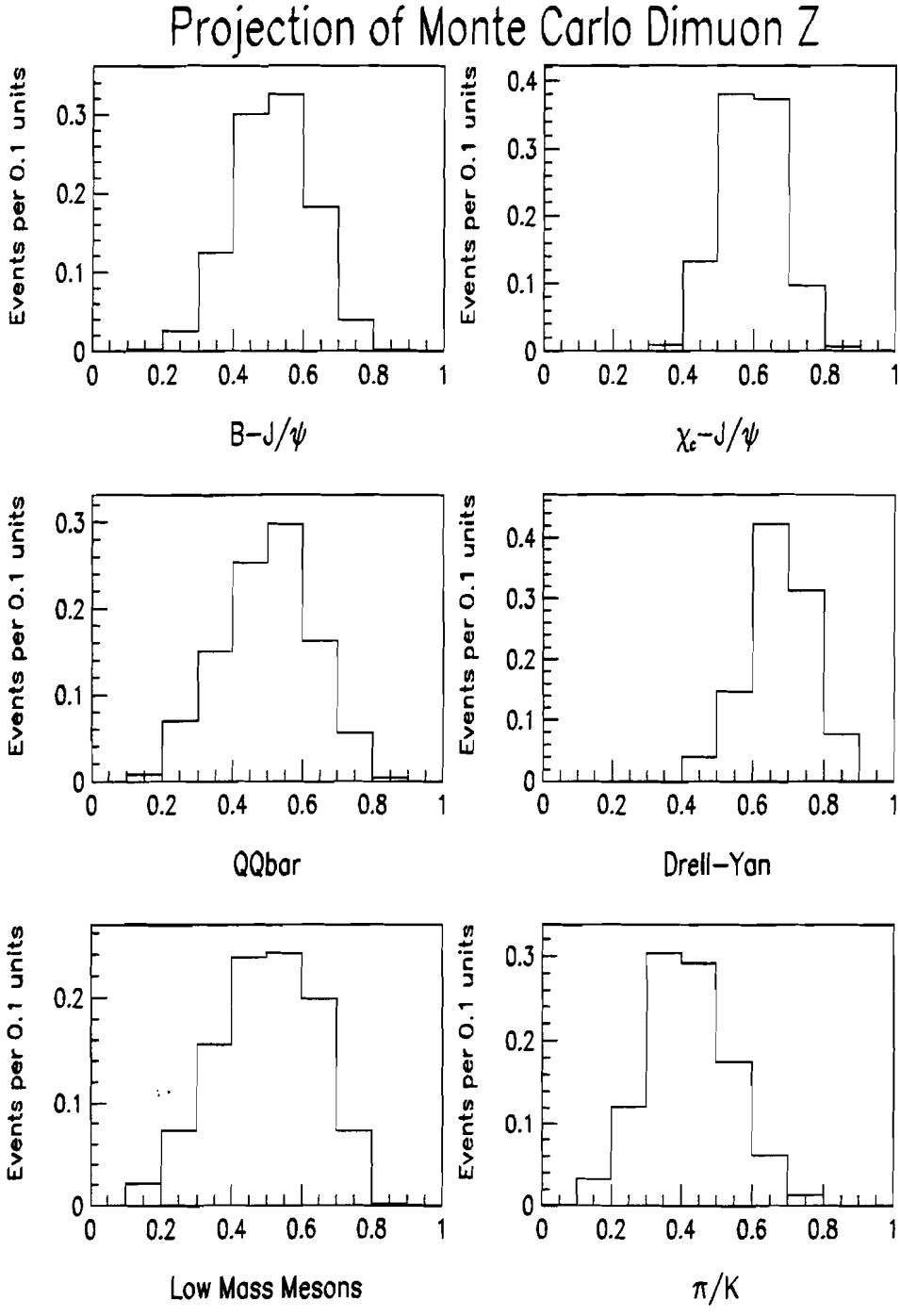

Figure 9.4: Monte Carlo Dimuon Momentum Fraction Distribution

Physics Process	Jet Association (%)
B-J/ψ	85
χ_c-J/ψ	68
$Q\bar{Q}$	70
Drell-Yan	34
Low Mass Mesons	81
π/K	76

Table 9.1: Jet Association Percentage for the Processed Monte Carlo Events

To calculate $P_{\rm T}^{\rm rel}$ and Z one determined the relative angle ($\theta^{\rm rel}$) between the momentum vectors of the dimuon and dimuon+jet system. Dimuons not associated with jets were assigned negative values for $P_{\rm T}^{\rm rel}$ and Z. This was important to separate Drell-Yan dimuons from the other processes which had a higher probability of jet association (see Table 9.1). The two fragmentation variables were used to define a 2-dimensional grid as the second PDF for the MLM fit. The scatter plots in Fig. 9.2 are the respective distributions for the six Monte Carlo simulations. Figures 9.3 and 9.4 illustrate the $P_{\rm T}^{\rm rel}$ and Z projections for the six Monte Carlo sets.

The distinctive shapes of the fragmentation distribution, in particular the Z, combined with the probability of jet association, was a powerful complementary discriminator to the mass distributions to discern the various modeled processes in our data.

After all offline cuts were imposed we arrived at a total of 982 low mass dimuon events: 876 opposite sign and 106 same sign. The resultant fit to the dimuon spectra is shown in Fig. 9.5, while the fits to the Z and $P_{\rm T}^{\rm rel}$ spectra are shown in Fig. 9.6. The break down of the physics processes is listed in Table 9.2. The statistical errors quoted account for all correlations between the processes because we utilized the full covariance matrix that resulted from the fit. Performing the fit separately without π/K and $Q\bar{Q}$ processes, and varying the width of the J/ψ's was how we determined the stated systematic errors.

Physics Process	Fitted Number of Events	Percent Contribution
B-J/ψ	215 ± 24 (stat) ± 41 (sys)	22
χ_c-J/ψ	144 ± 21 (stat) ± 25 (sys)	15
QQ	260 ± 30 (stat) ± 95 (sys)	26
Drell-Yan	135 ± 19 (stat) ± 40 (sys)	14
Low Mass Mesons	32 ± 10 (stat) ± 14 (sys)	3
π/K	196 ± 20 (stat) ± 50 (sys)	20

Table 9.2: Fitted Dimuon Contributions

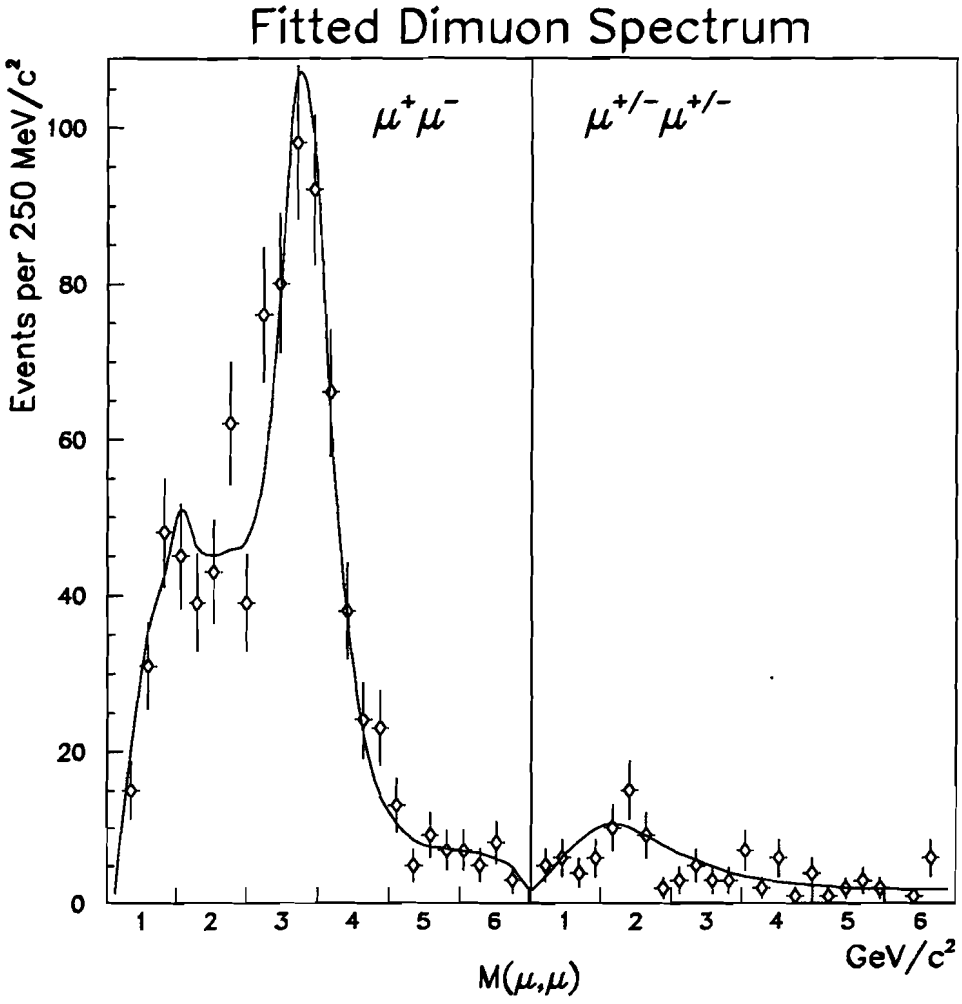

Figure 9.5: Resultant maximum likelihood fit to the opposite/same sign dimuon mass spectra.

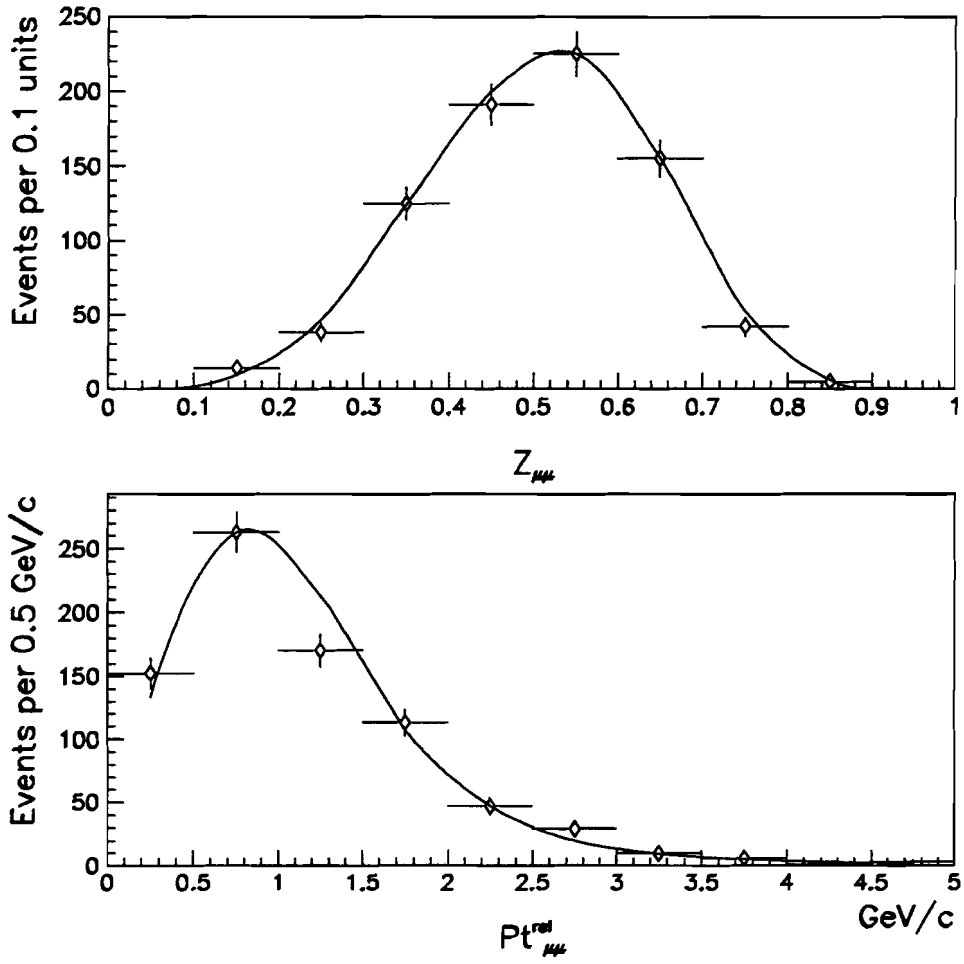

Figure 9.6: Resultant maximum likelihood fit to the opposite/same sign dimuon momentum fraction Z (top) and P_T^{rel} (bottom).

Figure 9.7 shows the plots of the negative log likelihood versus the primary fit parameters p_k ($k = 1 \ldots 5$). One can see that each plot has a good parabolic behavior in the neighborhood of its corresponding minimum.

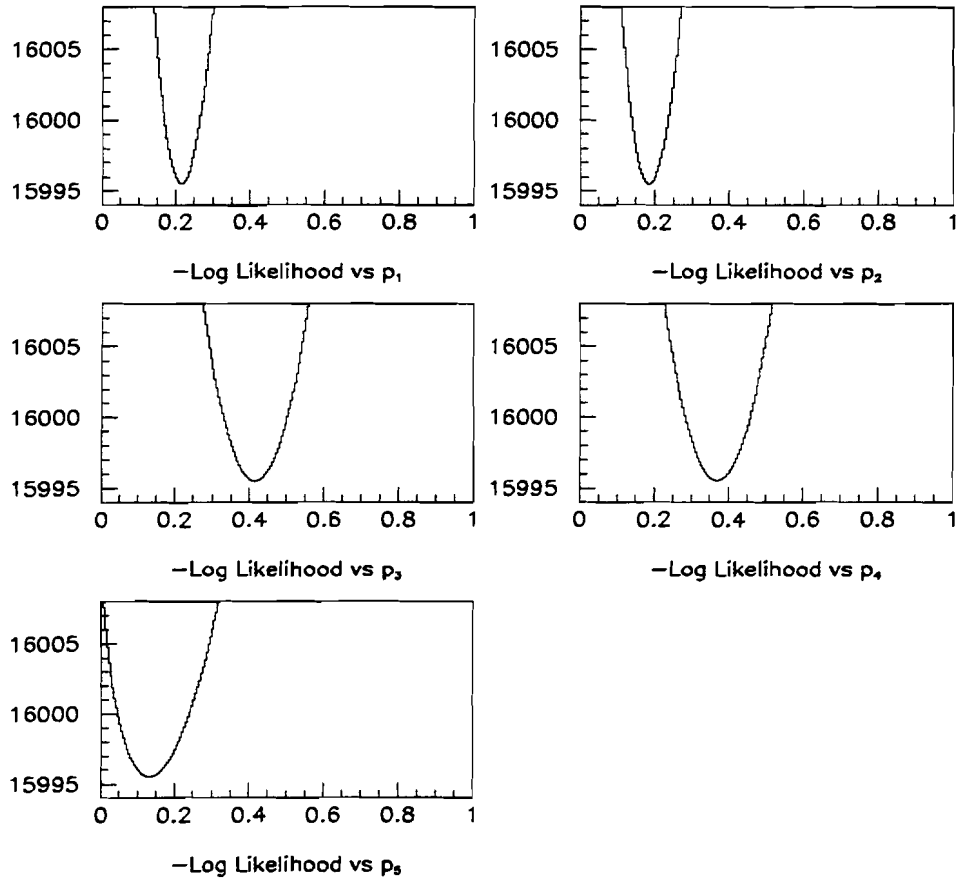

Figure 9.7: Negative Log Likelihood vs. Primary Fit Parameters p_k

To verify the validity of the fitted normalized coefficients A_j we used the probability that a given event is due to a particular process to predict the dimuon P_T spectrum. The probability that the i^{th} event was due to the j^{th} process was calculate by

$$\mathcal{P}_{i,j} = \frac{A_j \cdot mass(i,j) \cdot zptrel(i,j)}{\sum_j A_j \cdot mass(i,j) \cdot zptrel(i,j)} . \tag{9.1}$$

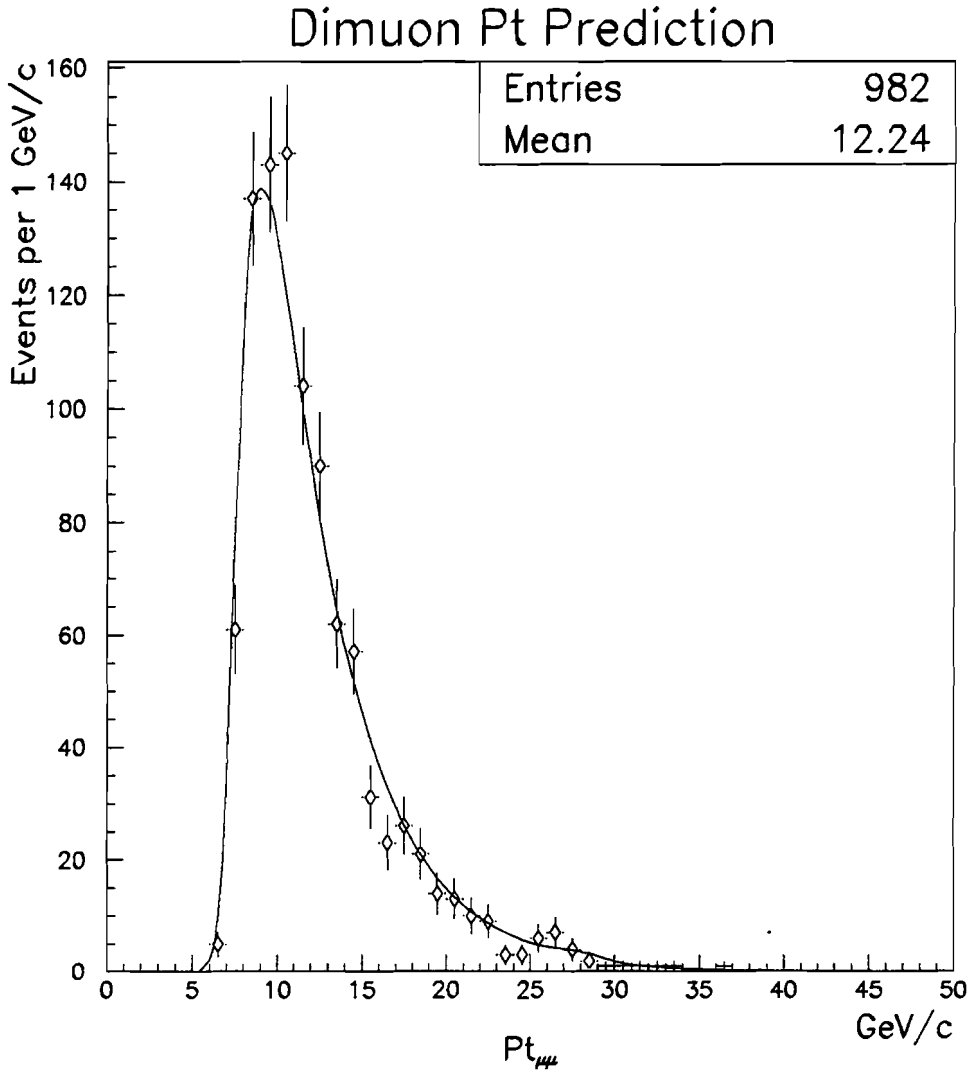

Figure 9.8: The comparison of the experimentally measured low mass dimuon P_T spectrum to the prediction from the maximum likelihood fit.

As shown in Fig. 9.8, our prediction for the dimuon P_T spectrum was in good agreement with the measured spectrum.

9.2 The Low Mass Dimuon Production Cross Section

The differential cross section, as a function of P_T, is expressed as

$$\frac{d\sigma}{dP_T} = \frac{\text{Num of Events}}{\epsilon \cdot \mathcal{L} \cdot \Delta\text{bin}} . \tag{9.2}$$

From the MLM fit we estimated 260 ± 44 $Q\bar{Q}$ low mass dimuons. Using Equation 9.2 and the overall efficiency for $Q\bar{Q}$ dimuons stated in Chapter 7 we calculated the low mass dimuon production cross section.

However, before we proceeded with that measurement we had to obtain the "true" low mass dimuon P_T spectrum. This was achieved by the application of Bayes' Theorem (Chapter 8) by unfolding the fitted P_T spectrum. The unfolded P_T distribution is shown in Fig. 9.9.

We choose to quote our cross section in the following P_T bins: 7–9, 9–11, 11–13, 13–19 and 19–26 GeV/c. The statistical error per P_T bin was calculated from the square root of N_e—the number of statistically equivalent events. This was calculated as

$$N_e = \frac{(\sum_i W_i)^2}{\sum_i (W_i)^2} , \tag{9.3}$$

where the sum is over all events that fell into the given low mass dimuon P_T bin and W_i is the probability, computed as in Equation 9.1, for a given event to be a low mass dimuon.

Table 9.3 summarizes the differential low mass cross section we measured. The integrated low mass dimuon cross section is

$$\text{Br}(B \to D\mu\nu) \cdot \text{Br}(D \to s\mu\nu) \cdot \sigma(p\bar{p} \to B + X) = 6.04 \pm 0.70\ (\text{stat}) \pm 2.21\ (\text{sys})\ \text{nb}$$

$$P_T^{\mu\mu} > 7.0\ \text{GeV/c},\ |\eta^{\mu\mu}| < 0.8 .$$

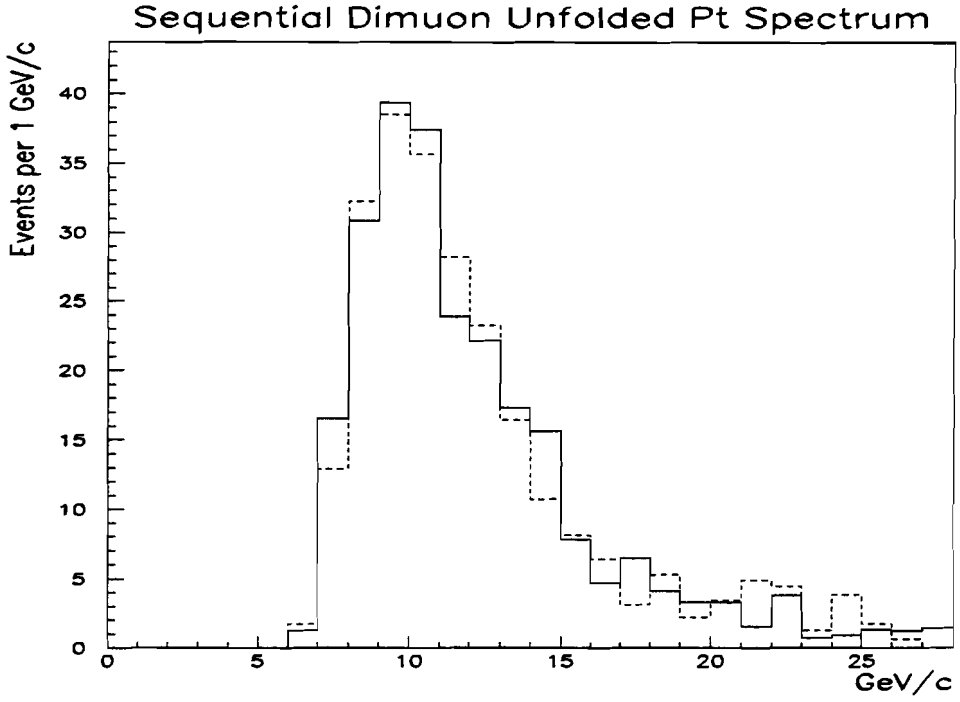

Figure 9.9: The solid line is the measured low mass dimuon P_T spectrum, while the dash-dot line is the unsmeared spectrum. Increase in the number of events above 20 GeV/c is due to unsmearing of events with very large measured P_T's.

$P_T^{\mu\mu}$ Bin (GeV/c)	$\langle P_T^{\mu\mu} \rangle$ (GeV/c)	$N_{\mu\mu}$	Efficiency (%)	$Br \cdot (d\sigma/dP_T)_{\mu\mu}$ (pb/(GeV/c))
7–9	8.16	50 ± 11 (stat) ± 11 (sys)	0.22 ± 0.03	1858 ± 372 (stat) ± 470 (sys)
9–11	9.99	76 ± 13 (stat) ± 16 (sys)	0.88 ± 0.10	711 ± 110 (stat) ± 166 (sys)
11–13	12.00	59 ± 12 (stat) ± 12 (sys)	1.89 ± 0.24	255 ± 47 (stat) ± 67 (sys)
13–19	15.18	54 ± 10 (stat) ± 10 (sys)	2.75 ± 0.27	53 ± 9 (stat) ± 14 (sys)
19–26	21.97	24 ± 9 (stat) ± 4 (sys)	5.80 ± 0.94	10 ± 3 (stat) ± 4 (sys)

Table 9.3: Low Mass Dimuon Differential Cross Section for $|\eta^{\mu\mu}| < 0.8$

9.3 The J/ψ Inclusive Production Cross Section

As a consistency check that the low mass dimuon cross section analysis was done correctly we independently determined the inclusive J/ψ differential production cross section as a function of the J/ψ's P_T.

The result of the MLM fit indicated that the inclusive number of J/ψ's was 359 ± 57. To extract the inclusive J/ψ cross section the dimuon P_T spectrum was unfolded. Once again we applied Bayes' Theorem to obtain the true J/ψ P_T distribution. Figure 9.10 is the unfolded transverse momentum distribution. The decided upon P_T bins were 8–10, 10–12, 12–15 and 15–20 GeV/c. We modified Equation 9.3 to compute the statistical error per stated P_T bins[3]. The efficiency per bin was a weighted average efficiency from the B and χ_c produced J/ψ Monte Carlo events[4]. Our measured differential cross sections are listed in Table 9.4. The corresponding integrated inclusive J/ψ cross section is

$$\begin{aligned} \mathrm{Br}(\mathrm{J}/\psi \to \mu\mu) \cdot \sigma(p\bar{p} \to \mathrm{J}/\psi + X) \;&=\; 2.46 \pm 0.22\,(\mathrm{stat}) \pm 0.63\,(\mathrm{sys})\ \mathrm{nb} \\ & P_T^{\mathrm{J}/\psi} > 8.0\ \mathrm{GeV/c}\,,\ |\eta^{\mathrm{J}/\psi}| < 0.8\,. \end{aligned}$$

DØ's published inclusive J/ψ production cross section [108] for $P_T^{\mathrm{J}/\psi} > 8.0$ GeV/c and $|\eta^{\mathrm{J}/\psi}| < 0.6$ is $2.08 \pm 0.17\,(\mathrm{stat}) \pm 0.46\,(\mathrm{sys})$ nb. Accounting for the larger psuedo-rapidity coverage studied in this analysis, approximately a factor of 0.6/0.8, the two results are consistent.

---

[3]
$$N_c = \frac{\left(\sum_i (W_i(B\text{–}\mathrm{J}/\psi) + W_i(\chi_c\text{–}\mathrm{J}/\psi))\right)^2}{\sum_i (W_i(B\text{–}\mathrm{J}/\psi) + W_i(\chi_c\text{–}\mathrm{J}/\psi))^2}$$

[4]From our dimuon mass fit we determined the contribution of J/ψ's was 60% B-meson and 40% χ_c decays.

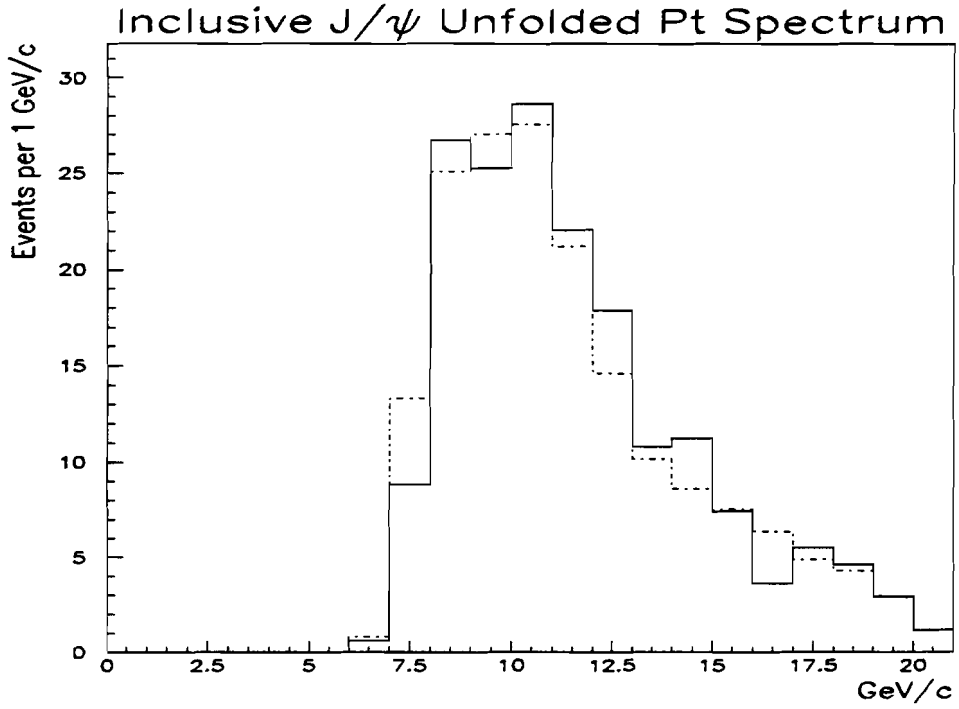

Figure 9.10: The solid line is the measured J/ψ P_T spectrum, whereas the dash-dot line is the unsmeared spectrum.

$P_T^{J/\psi}$ Bin (GeV/c)	$\langle P_T^{J/\psi} \rangle$ (GeV/c)	$N_{J/\psi}$	Efficiency (%)	Br $\cdot (d\sigma/dP_T)_{J/\psi}$ (pb/(GeV/c))
8–10	8.98	98 ± 14 (stat) ± 6 (sys)	1.07 ± 0.06	749 ± 97 (stat) ± 89 (sys)
10–12	10.93	92 ± 13 (stat) ± 6 (sys)	2.64 ± 0.13	284 ± 36 (stat) ± 34 (sys)
12–15	13.33	59 ± 10 (stat) ± 4 (sys)	4.22 ± 0.20	76 ± 12 (stat) ± 9 (sys)
15–20	17.19	52 ± 11 (stat) ± 4 (sys)	5.13 ± 0.33	33 ± 6 (stat) ± 5 (sys)

Table 9.4: Inclusive J/ψ Differential Cross Section $|\eta^{J/\psi}| < 0.8$

9.4 Dijet Spectroscopy

Low mass dimuons associated with a jet provide a high purity tag for b-quarks. Combining the tagged jet with another energetic jet in the event allows us to study the $b\bar{b}$ system. For our study we concentrated on opposite sign dimuons associated with a jet. We denote $\mathrm{J}\mu^+\mu^-\mathrm{J}$ to be the dijet system of interest, where $\mathrm{J}\mu^+\mu^-$ represents the jet tagged with the dimuon and J the other jet. The $\mathrm{J}\mu^+\mu^-$ object is most likely to result from the $b(\bar{b})$-quark decay, whereas the other jet is either a $\bar{b}$(b)-quark or gluon.

The analysis of the $\mathrm{J}\mu^+\mu^-\mathrm{J}$ system is interesting for several reasons:

1. To investigate $b\bar{b}$ production (correlations), in particular contributions from NLO QCD diagrams;
2. To establish a $Z \to b\bar{b}$[5] signal never seen before at the Tevatron. In addition to the verification of the Z cross section, such a signal is very valuable from the technical point of view of studying the energy scale and resolution of the DØ detector;
3. To search for a production of new particles decaying into the $b\bar{b}$ system, *e.g.* Higgs[6].

Even though we used the entire Run 1A MU2HIGH data, an integrated luminosity of $11.5 \pm 0.62\ \mathrm{pb}^{-1}$, we suffered from limited statistics of $\mathrm{J}\mu^+\mu^-\mathrm{J}$ events. Therefore only

[5]The expected Z signal was estimated to be as

$$N(Z \to b\bar{b} \to \mu^+\mu^-) =$$
$$2 \cdot \sigma(Z \to q\bar{q}) \cdot \mathrm{Br}(Z \to b\bar{b}) \cdot \mathrm{Br}(B \to D + \mu) \cdot \mathrm{Br}(D \to s + \mu) \cdot \mathcal{L} \cdot \epsilon_{\mu\mu} \cdot \epsilon_{dijet} =$$
$$2\,(7\ \mathrm{nb})(0.2)(0.103)(0.1)(11470\ \mathrm{nb}^{-1})(0.04)(0.5) \approx 6\,,$$

where the factor of 2 reflects that one of the two jets can be tagged. We estimated the combined dimuon acceptance and detection efficiency $\epsilon_{\mu\mu}$ by taking a weighted average, with the weights determined from our dimuon fit, for the corresponding acceptance times efficiency for the J/ψ and low mass dimuons. The jet efficiency $\epsilon_{\mathrm{dijet}}$ was obtained from [109].

[6]This study got a strong encouragement from the DØ collaboration in November 1995 when first a bump was observed by in the $\mathrm{J}\mu^+\mu^-\mathrm{J}$ topology in the Run 1B data and at the same time there were news about CDF and ALEPH had potential evidence for Higgs decaying into $b\bar{b}$.

the first goal was attainable. To perform this analysis we selected dijet systems, where one jet was tagged with a low mass dimuon, in an attempt to separate the dijet invariant mass spectrum into leading-order (LO) and next-to-leading-order (NLO) QCD processes.

With the usual jet selection criteria listed in Section 4.4, three additional cuts were imposed on the jets:

1. $|\eta^{\text{jet}}| < 1$;
2. the associated jet: $E_{\text{T}} \geq 10$ GeV;
3. the second jet: $E_{\text{T}} \geq 12$ GeV.

The two jets were required to be the first or second highest E_{T} ranked jets in the event. The tagged jet had its energy corrected as described in Section 9.1. After all the cuts were imposed we had 604 J$\mu^+\mu^-$J events.

Once again we used the MLM to discern between the QCD orders. For this fit, the Monte Carlo events used were:

1. Dimuons from LO (flavor creation) $b\bar{b}$ production;
2. Dimuons from NLO (flavor excitation and gluon splitting) $b\bar{b}$ production;
3. J/ψ from Bottom Production Model (BPM);
4. Dimuon from decays of low mass mesons ($\rho, \phi, \omega, \eta, \eta'$);
5. Dimuons from pion/kaon decays.

The optimized variables used for this particular MLM fit were the dijet[7] and opposite sign dimuon invariant masses. For each of the five modeled processes we parametrized the two mass distributions to obtain the PDFs needed for the MLM fit (Fig. 9.11 and 9.12). As one can see from the figures these variables are good discriminators between LO and NLO QCD processes, *e.g.* the mean dijet mass for the two are respectively 61 and 74 GeV/c^2, while each has a distinct dimuon mass distribution.

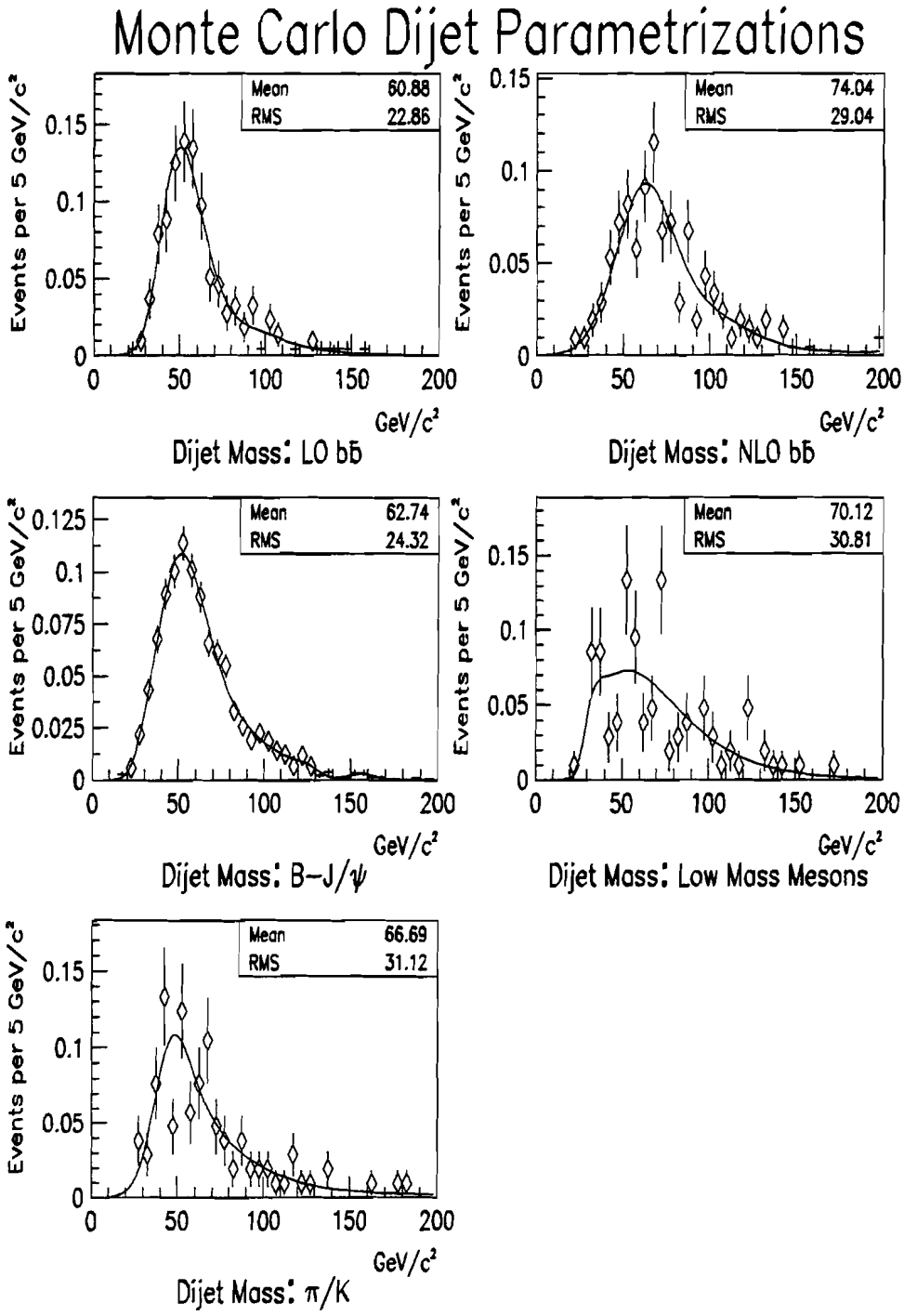

Figure 9.11: Normalized Monte Carlo Dijet Mass Parametrizations

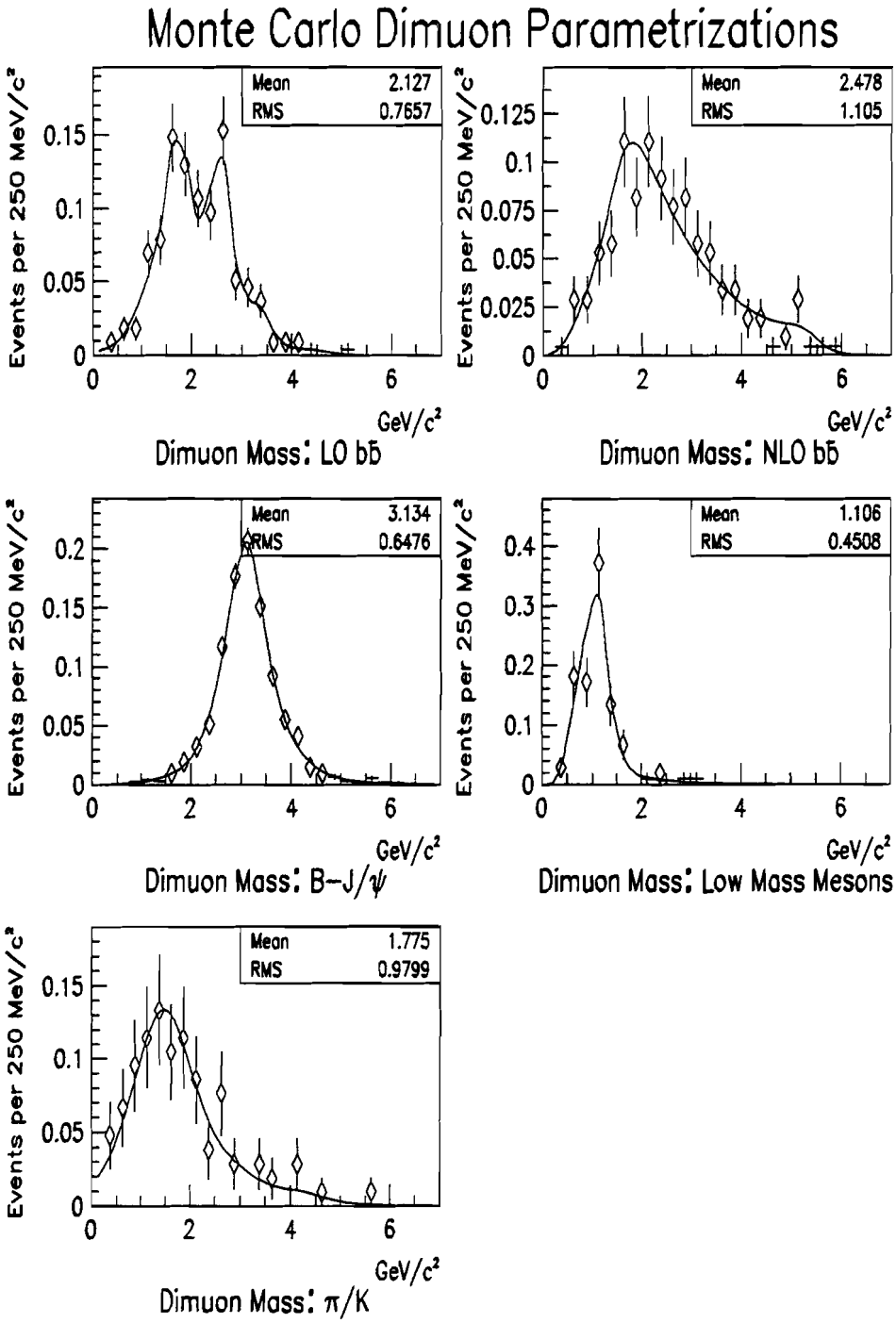

Figure 9.12: Normalized Monte Carlo Dimuon Mass Parametrizations

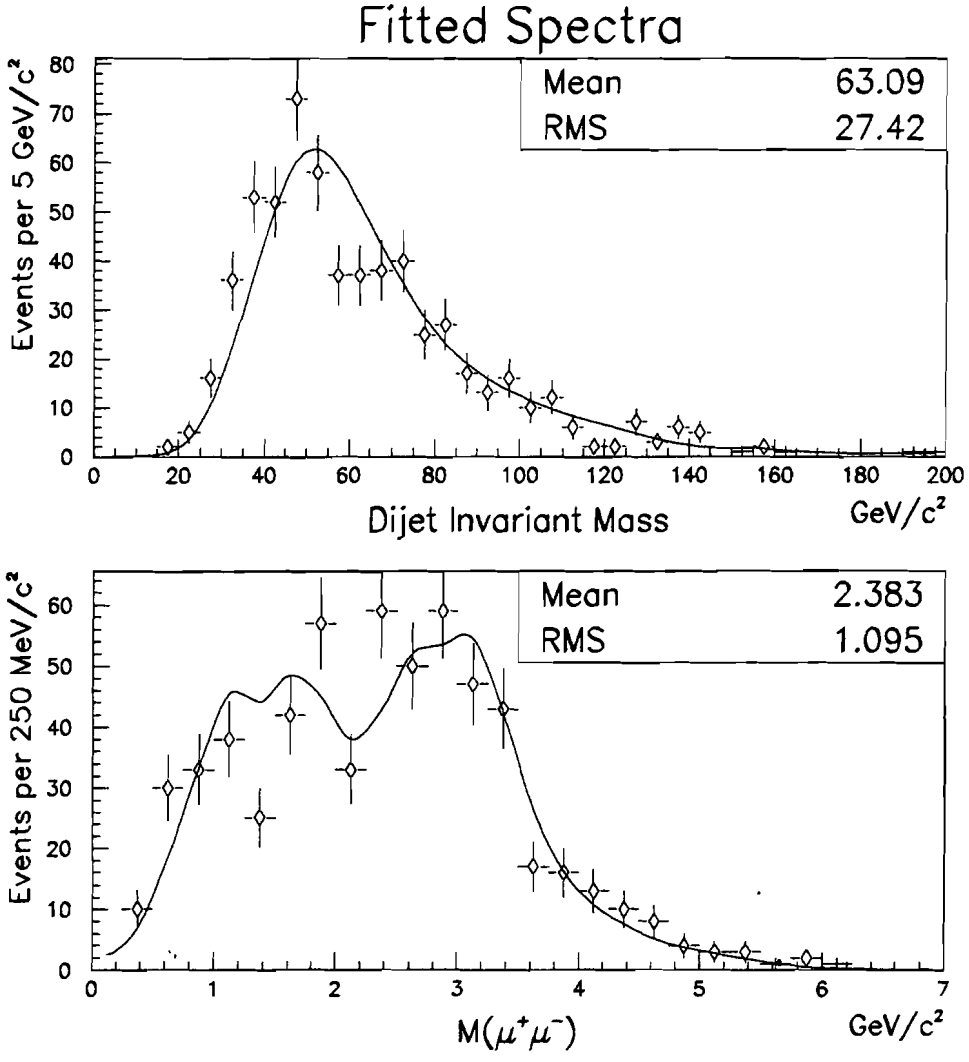

Figure 9.13: Maximum Likelihood Fit to the Dijet and Dimuon Invariant Mass Spectra

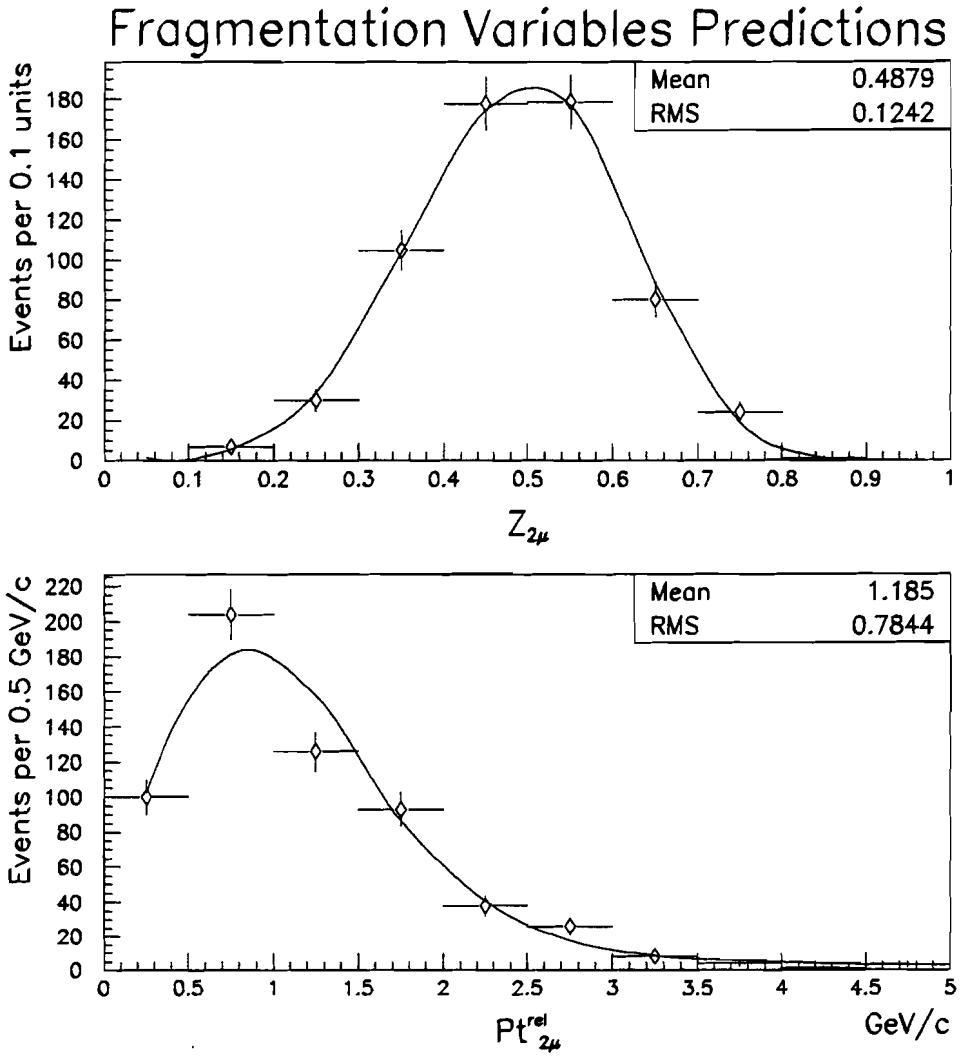

Figure 9.14: Maximum Likelihood Fit Dimuon's P_T^{rel} and Z Predictions

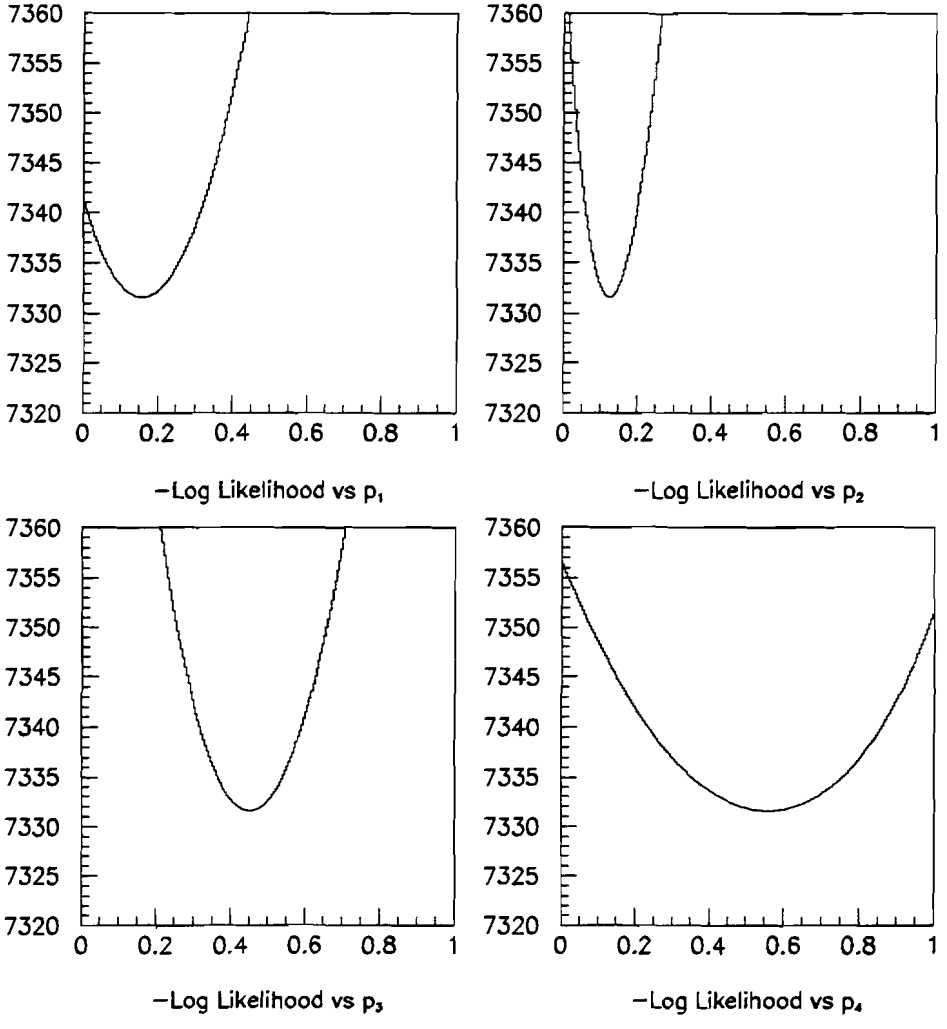

Figure 9.15: Negative Log Likelihood vs. Primary Fit Parameters p_k

The resultant fit is shown in Fig. 9.13 and the break down of the fitted processes is given in Table 9.5. Clearly, one does not see a resonance structure. Once again, the full covariance matrix from the fit was used to calculate the statistical errors, while the systematic errors were obtained by modifying the widths of the PDFs.

Indicators that the MLM achieved a good fit are the plots of the negative log likelihood versus the primary fit parameters p_k ($k = 1 \ldots 4$), Fig. 9.15 (good parabolic minima), and the respective predictions for the dimuon's $P_{\mathrm{T}}^{\mathrm{rel}}$ and Z, Fig. 9.14 (good agreement with the measured spectra). Another independent confirmation for the robustness of our dijet invariant mass fit, the ratio of B-J/ψ to $Q\bar{Q}$ (the sum of LO and NLO processes: $0.33/0.40 \approx 0.83$) events agrees with the same ratio from our dimuon invariant mass fit presented in Section 9.1 ($0.22/0.26 \approx 0.85$). Hence, we concluded that our fit well described the J$\mu^+\mu^-$J topology with the five above mentioned physics models.

Physics Process	Fitted Number of Events	Percent Contribution
LO $b\bar{b}$	136 $\pm$ 44 (stat) $\pm$ 17 (sys)	23
NLO $b\bar{b}$	105 $\pm$ 34 (stat) $\pm$ 13 (sys)	17
B-J/ψ	201 $\pm$ 22 (stat) $\pm$ 5 (sys)	33
Low Mass Mesons	65 $\pm$ 22 (stat) $\pm$ 11 (sys)	16
π/K	97 $\pm$ 27 (stat) $\pm$ 15 (sys)	11

Table 9.5: Fitted Dijet Contributions

9.5 Trimuons

Trimuon events are excellent candidates to study $b\bar{b}$ production. Their energetic final state muons provide a clean signature to identify $b\bar{b}$ pairs because they tag each b-quark—one quark decays into one muon while the other quark decays into two muons as depicted by the following (and their respective charge conjugate)

[7]The jets themselves were treated as massless.

$$
\begin{array}{lll}
p\bar{p} \rightarrow & b\bar{b} \rightarrow & \bar{c} + \mu^+ + \nu_\mu \\
 & \hookrightarrow & c + \mu^- + \bar{\nu}_\mu \\
 & & \hookrightarrow \; s + \mu^+ + \nu_\mu
\end{array}
$$

$$
\begin{array}{lll}
p\bar{p} \rightarrow & b\bar{b} \rightarrow & \bar{c} \rightarrow \bar{s} + \mu^- + \bar{\nu}_\mu \\
 & \hookrightarrow & c + \mu^- + \bar{\nu}_\mu \\
 & & \hookrightarrow \; s + \mu^+ + \nu_\mu
\end{array}
$$

$$
\begin{array}{lll}
p\bar{p} \rightarrow & b\bar{b} \rightarrow & \bar{c} + \mu^+ + \nu_\mu \\
 & \hookrightarrow & \mathrm{J}/\psi + X \\
 & & \hookrightarrow \; \mu^+\mu^-
\end{array}
$$

Obviously, this analysis was a natural extension of our dimuon analysis presented in Section 9.1. What follows is a discussion of our trimuon analysis.

9.5.1 Trimuon Event Selection

The event selection for trimuons was performed in two steps. First, "good" dimuon events, between the invariant mass of 1.2–6.25 GeV/c^2, were selected. The second step was the identification of an accepted third muon for those allowed dimuon events. The kinematic cuts placed on the third muon was that its $P_{\mathrm{T}} > 3.3$ GeV/c and $|\eta| < 1$. Table 6.1 summarized the pertinent event, muon and dimuon selection criteria used for our trimuon analysis.

The restriction of the dimuon invariant mass was to minimize the contamination of fake trimuons when dimuons from low mass vector mesons or Drell-Yan production were combined with a muon from a B-meson, charge pion/kaon ($\pi^{\pm}/K^{\pm}$) decay or a spurious track.

As discussed in Section 6.2.2, we scanned our multimuon events. The scanning for our trimuons events was crucial. It resulted in a rejection of 67% of the events which passed our

analysis cuts (see Table 6.2). Therefore, after the imposition of the listed cuts and scanning we found nine[8] trimuon events in our Run 1A post shutdown data set.

9.5.2 Event Topologies

We examined various topological characteristics of our trimuon events. First, we looked at the azimuthal separation between the dimuon and 3rd muon. This separation reflects the $b\bar{b}$ system. Second, we examined the fraction of momentum carried off by the dimuon and third muon from their respective parent b-quarks.

9.5.2.1 Azimuthal Separation Between Dimuon and Third Muon

The topology of leading-order and next-to-leading-order heavy quark events are quite distinct. The azimuthal separation between the quarks for leading-order production correspond to back-to-back configuration while for next-to-leading-order events the quarks are closer in azimuth (see Fig. 9.16). Studying the azimuth separation between our trimuon events allowed us to probe the $b\bar{b}$ system angular correlation.

The azimuthal difference between the dimuon and third muon ($\delta\phi(\mu_{12},\mu_3) = (\phi_{\mu_{12}} - \phi_{\mu_3})$) was calculated for our trimuon event candidates. The resultant histogram is shown in Fig. 9.17. Due to the limited statistics we cannot quantitatively state what fraction of our events are due to LO and NLO production. On the other hand, qualitatively one can see that it appears that the majority of our candidates strongly indicate LO production.

9.5.2.2 Momentum Fraction Carried by the Dimuon and Third Muon

The decay products of the hadronized b-quark carry off a percentage of the jet's momentum. Therefore, it was natural to study what fraction of b-quarks' momentum was taken away by the dimuons and third muons in our trimuon event candidates.

[8] One event had two combinations satisfying our definition of a trimuon.

9.5. TRIMUONS

To arrive at the momentum fraction Z for the dimuon and 3rd muon we performed the following steps:

1. Utilized the MTC package [95] to obtain the ϕ and η directions of the hit calorimeter towers along the direction of the dimuon and 3rd muon;
2. Summed the energy around the dimuon and 3rd muon within an annular cone of 0.7;
3. Defined the "dimuon+energy" and "3rd muon+energy" systems for the respective dimuon and 3rd muon annular cones. For each system, we added the muon's momentum to and subtracted the expected energy loss of the muon from the annular cone's energy if the muon was within a radial distance of 0.7;
4. Calculated Z $(= P^{\text{object}} \cos\theta^{\text{rel}} / |P^{\text{object+energy}}|)$.

θ^{rel} is the relative angle between the vectors of the object and object+energy system, where object is either the dimuon or 3rd muon.

Instead of associating jets to the dimuon and third muon, we decided on the above procedure because not all b-quarks will be reconstructed due to the 8 GeV cutoff required at the reconstruction stage (Section 4.4). Regardless if the jet was reconstructed its energy was deposited into the calorimeter and the information retrievable from the appropriate ZEBRA banks.

The comparison of the dimuon and third muon Z distributions between data and Monte Carlo events are shown in Fig. 9.18. We concluded, in spite of the limited Monte Carlo and data statistics, that there is reasonable agreement in the shapes for the respective distributions.

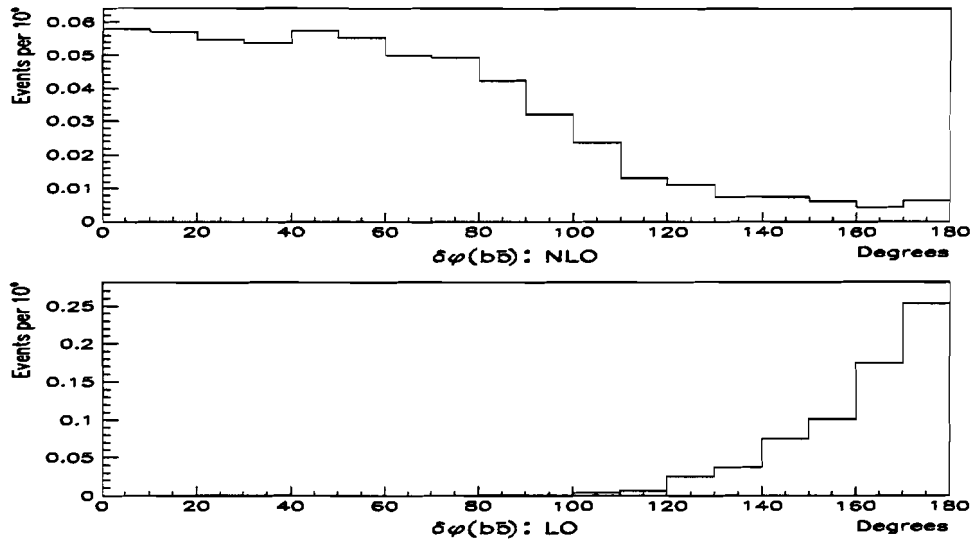

Figure 9.16: ISAJET prediction of the $b\bar{b}$ system azimuthal separation for next-to-leading-order and leading-order production. The accepted events correspond to dimuons whose muons had $|\eta| < 1$ and $P_T > 3$ GeV/c.

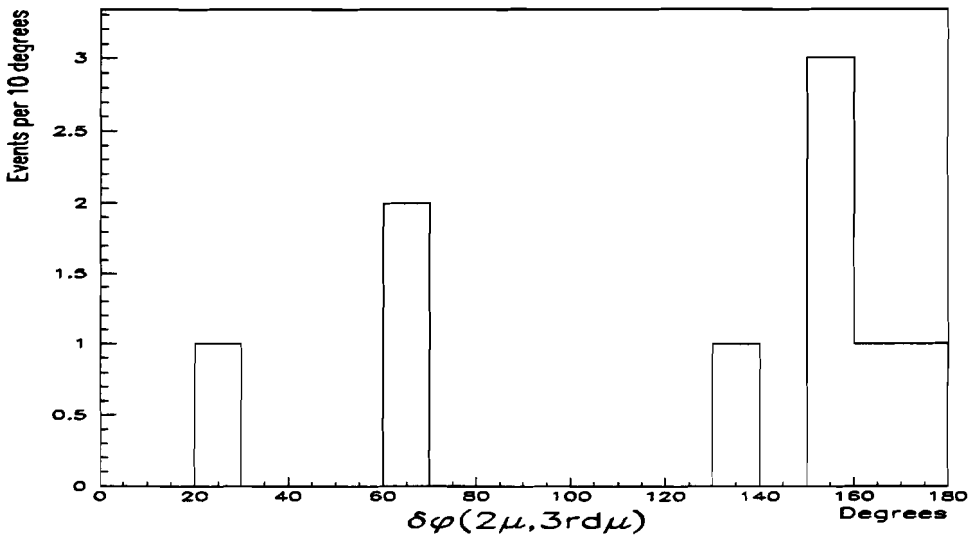

Figure 9.17: The azimuthal difference between the dimuon and third muon for our Run 1A trimuon candidates.

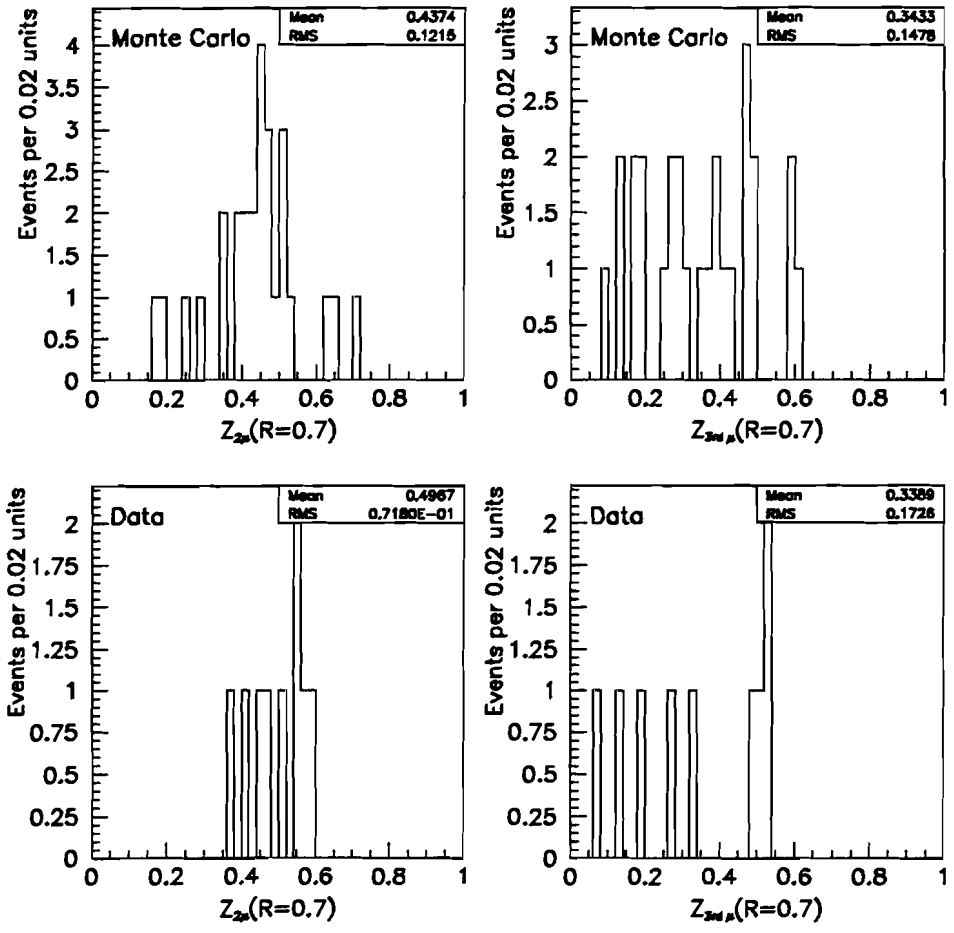

Figure 9.18: Monte Carlo and data comparison of the momentum fraction (Z) for trimuon events. The left side are the respective distributions for the dimuon and the right side are the respective distributions for the third muon.

Chapter 10

BEAUTY PRODUCTION AND THE DETERMINATION OF THE QCD COUPLING CONSTANT ALPHA STRONG

"From one thing know ten thousand things." Miyamoto Musashi

The aim of this thesis was to study b-quark production in order to perform a qualitative and quantitative test of perturbative QCD (pQCD) at the Tevatron. Using our dimuon and trimuon results, presented in the previous chapter, we measured the inclusive single b-quark and correlated $b\bar{b}$ production cross sections. Furthermore, from DØ's b-quark cross section measurements we performed a χ^2 fit to various theoretical predictions to determine pQCD's coupling constant alpha strong (α_s) and demonstrated the running nature of α_s.

10.1 Inclusive b-Quark Cross Section

Our first test of pQCD was to measure the inclusive b-quark cross section from the low mass dimuon and J/ψ samples.

10.1.1 Inclusive b-Quark Cross Section from Low Mass Dimuons

In order to convert the low mass dimuon cross section to the b-quark cross section, for the rapidity region $|y^b| < 1$, we needed to retrace the hadronization and decay undergone by the b-quarks. The extrapolation scheme implemented was developed by UA1 [29]. We began with the expected b-quark cross section and allowed one of the quarks to hadronize

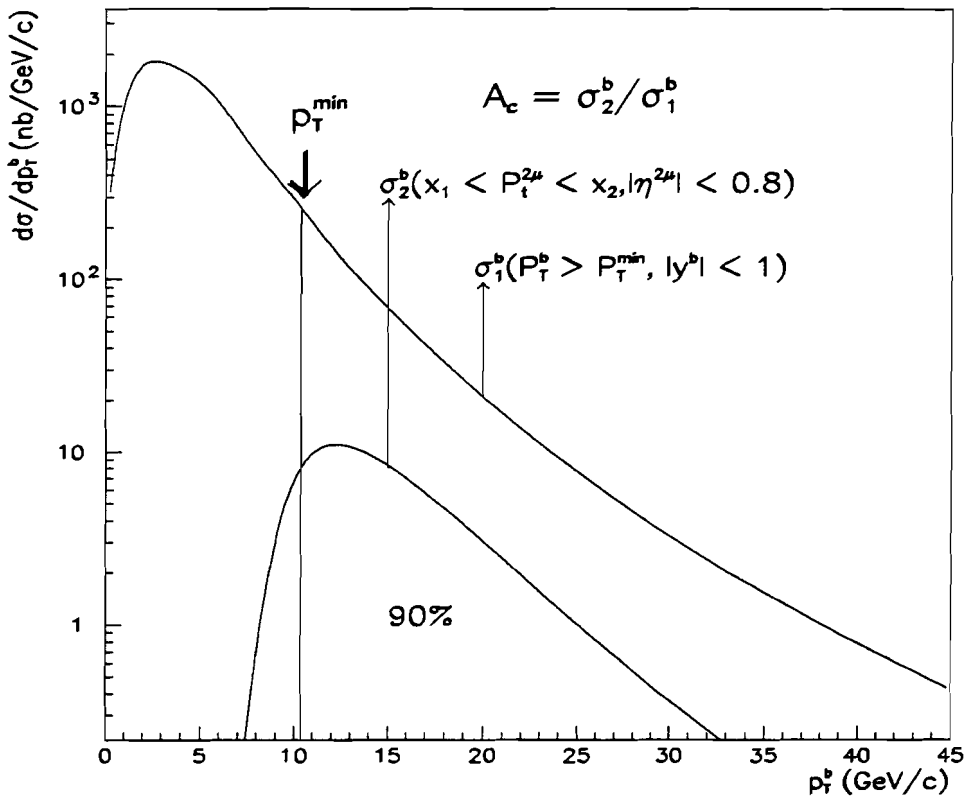

Figure 10.1: Illustration of the method used to convert the dimuon spectrum into the b-quark production cross section.

and decay into low mass dimuons. We applied a P_T cut to the dimuon and plotted the surviving parent b-quark P_T spectrum. Based on this distribution, we defined P_T^{min} such that 90% of the accepted b-quarks had their transverse momentum greater than that value (Fig. 10.1). Therefore, our integrated b-quark cross section was quoted above a certain minimum value P_T^{min}. Naturally, the estimation of P_T^{min} is dependent on a Monte Carlo generator. The generator used was the MNR program (5.4) which evaluated NLO heavy quark cross section predictions by Nason, Dawson and Ellis (NDE) [25]. The program was modified to hadronize the b-quarks and to decay the final state hadrons.

The b-quark cross section was determined from the following relation

$$\sigma\left(p\bar{p} \to b + X,\ P_{\mathrm{T}}^{b} > P_{\mathrm{T}}^{\mathrm{min}},\ |y^{b}| < 1\right) = \frac{\sigma(p\bar{p} \to \mu\mu + X,\ P_{\mathrm{T}}^{\mu\mu} > \mathrm{c})}{2 \cdot \mathrm{Br}(b \to \mu\mu + X) \cdot A_{\mathrm{c}}}\ , \tag{10.1}$$

where the acceptance A_{c} was defined to be

$$A_{\mathrm{c}} = \frac{\sigma^{\mathrm{MC}}\left(p\bar{p} \to b + X,\ |y^{b}| < 1,\ P_{\mathrm{T}}^{\mu\mu} > c\right)}{\sigma^{\mathrm{MC}}\left(p\bar{p} \to b + X,\ |y^{b}| < 1\right)}\ . \tag{10.2}$$

In order to use Equation 10.2, we calculated the integrated low mass cross section and determined A_{c} for each P_{T} range listed in Table 9.3. In addition, the branching fraction for the muonic cascade of a b-quarks is [110]

$$\mathrm{Br}(B \to D\mu\nu) \cdot \mathrm{Br}(D \to s\mu\nu) \ = \ 1.03 \times 10^{-2} \ \pm \ 2.72 \times 10^{-3}\ .$$

Our measured b-quark cross sections from low mass decays are summarized in Table 10.1. The systematic errors quoted for the A_{c}'s were estimated by varying the structure function and the b-quark fragmentation parametrization[1].

Figure 10.2 compares our measured b-quark cross section to NLO QCD predictions given by the MNR program. The MRSDØ structure function was used for all three theoretical curves. The MNR program defined the factorization and renormalization scales to be

$$\mu = \mu_{\mathrm{R}} = \mu_{\mathrm{F}} = C\sqrt{m_{b}^{2} + \langle P_{\mathrm{T}}^{b} \rangle^{2}} = C\mu_{\mathrm{o}},$$

where m_{b}^{2} and C were specified by the author (we chose $m_{b}^{2} = 4.75\ \mathrm{GeV/c^{2}}$ for our studies). The central curve had the μ scale set to one and the value of Λ_{5} equal to 140 MeV. The theoretical uncertainties were produced by varying the μ scale and Λ_{5}, namely $\mu = \mu_{\mathrm{o}}/2$ and $\Lambda_{5} = 187$ MeV for the top curve, and $\mu = 2\mu_{\mathrm{o}}$ and $\Lambda_{5} = 100$ MeV for the lower curve. The measured results are not in agreement with the central theoretical prediction; they are in better accord with the upper theoretical curve.

[1]The parameter ϵ in the Peterson fragmentation function.

$P_T^{\mu\mu}$ Range (GeV/c)	P_T^{min} (GeV/c)	A_c (%)	$\sigma^b(P_T^b > P_T^{min}, \|y^b\| < 1)$ (nb)
7–9	10.40	9.2 ± 1.3	1954 ± 430 ± 618
9–11	13.38	7.9 ± 1.1	878 ± 151 ± 272
11–13	16.00	6.4 ± 0.9	389 ± 79 ± 132
13–19	20.88	5.7 ± 0.8	272 ± 50 ± 89
19–26	29.41	5.6 ± 0.8	58 ± 22 ± 27

Table 10.1: b-Quark Cross Section from Low Mass Dimuons

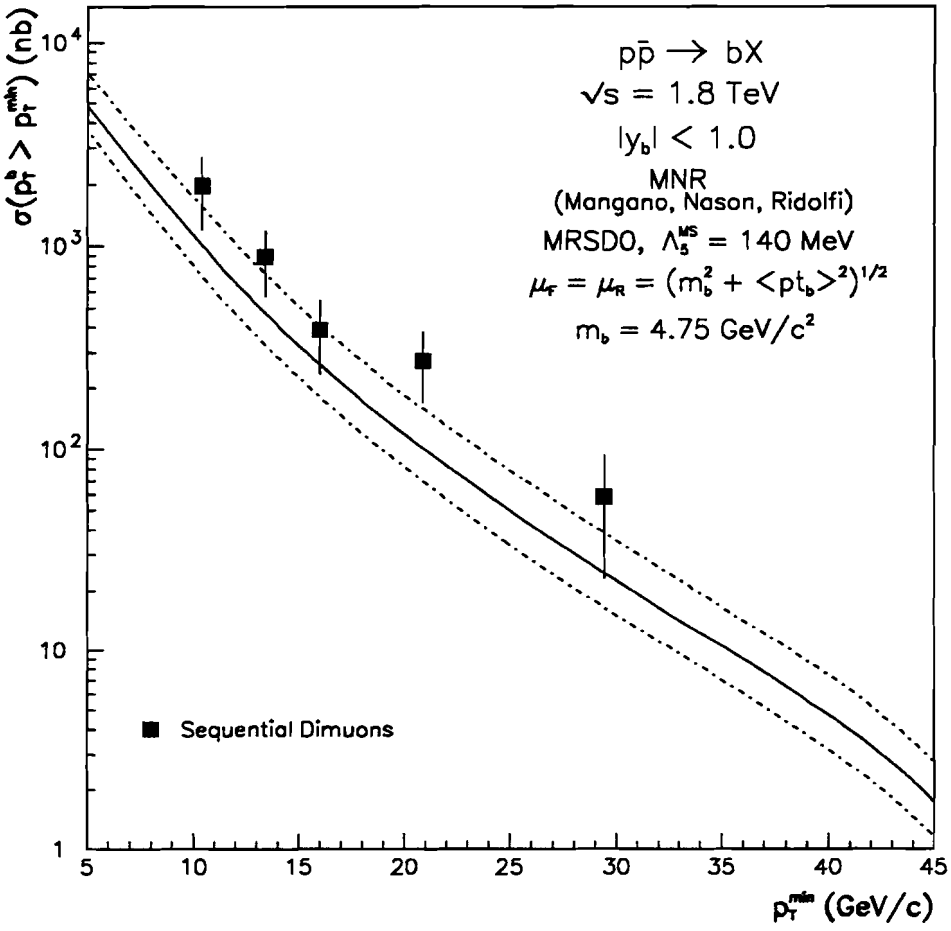

Figure 10.2: b-Quark Cross Section from Low Mass Dimuons

10.1.2 Inclusive b-Quark Cross Section from J/ψ

From our independently measured inclusive J/ψ cross section we computed the integrated b-quark cross section. The prescription discussed in Section 10.1.1 was followed with the following important difference. The numerator in Equation 10.1 was replaced by

$$F_b \cdot \sigma\left(p\bar{p} \rightarrow \mathrm{J}/\psi + X,\ P_{\mathrm{T}}^{\mathrm{J}/\psi} > \mathrm{c}\right) \ ,$$

where F_b is the fraction of J/ψ's produced from the weak decay of b-hadrons. Values of F_b for the different J/ψ P_{T} ranges listed in Table 10.2 was taken from CDF's study on the separation of J/ψ production mechanisms [111]. The product of the branching fractions for each particular decay mode is [110]

$$\mathrm{Br}\,(B \rightarrow \mathrm{J}/\psi) \cdot \mathrm{Br}\,(\mathrm{J}/\psi \rightarrow \mu\mu) \ = \ 7.76 \times 10^{-4} \ \pm \ 1.07 \times 10^{-4} \ .$$

Table 10.2 summarizes our b-quark cross section measurement from the J/ψ sample and the theoretical comparison of these measured cross section values is shown in Fig. 10.3. The theory curves are the same as in Fig. 10.2. Once again, our measurement is consistently above the central prediction.

10.1.3 The Current Status of b-Quark Production Cross Section

The b-quark inclusive production cross section has been measured in $p\bar{p}$ collisions by three experiments (UA1, DØ, and CDF UA1) at two different center of mass energies ($\sqrt{s}$ = 0.63, 1.8 TeV). What follows is a brief overview of the current status of b-quark production.

DØ determined 24 inclusive b-quark production cross section measurements in five different channels with the 1992–1993 Tevatron collider run data set. Figure 10.4 summarizes the various measurements compared to pQCD NLO calculations. The theory curves in the figure were described in Section 10.1.1. All of the DØ measurements are consistently above

$P_T^{J/\psi}$ Range (GeV/c)	P_T^{min} (GeV/c)	A_c (%)	F_b (%)	$\sigma^b\left(P_T^b > P_T^{min},\ \lvert y^b\rvert < 1\right)$ (nb)
8–10	9.95	14.7 ± 2.1	28.0 ± 6.0	1837 ± 263 ± 523
10–12	12.15	12.2 ± 1.7	33.0 ± 11.0	988 ± 140 ± 381

Table 10.2: b-Quark Cross Section from $J/\psi \rightarrow \mu^+\mu^-$

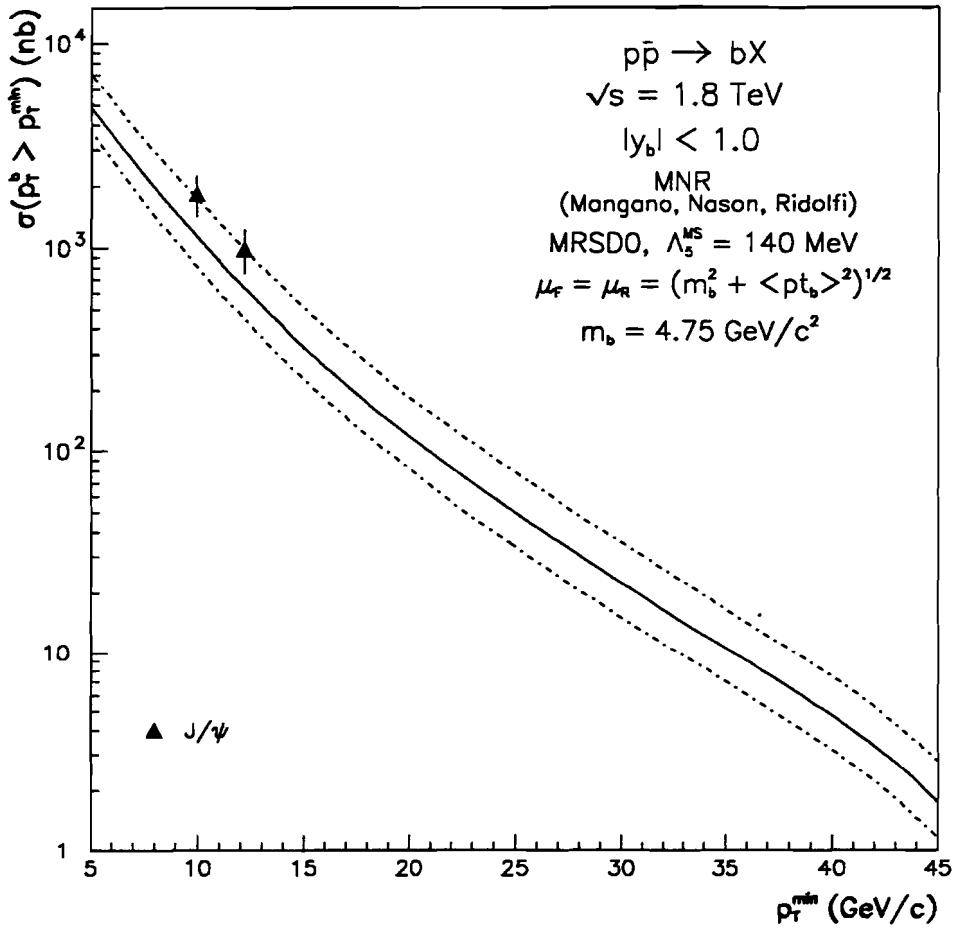

Figure 10.3: b-Quark Cross Section from J/ψ

the central prediction. Similar measurements were carried out by the CDF collaboration [113] at the Tevatron, as shown in Fig. 10.5 [30]. The CDF measurements are also in disagreement with the central NLO QCD prediction. The first b-quark production cross section measurements at $p\bar{p}$ collisions were performed by UA1 [29]. Their results are shown in Fig. 10.6. UA1 measurements are also above the central NLO QCD prediction. All three experiments agree in shape with pQCD NLO calculations but are higher in normalization than the central theoretical curve. The experiments agree with the upper edge of the theoretical prediction.

A quantitative comparison between theory and the DØ's and UA1's measurements is shown in Figs. 10.7 and 10.8. The two experiments' measurements were divided by the central value of the respective theory predictions. In both cases, the ratios are 1.6–1.8 above central theory predictions. One can only conclude that the pQCD calculations systematically underestimate b-quark production for $\sqrt{s} = 630$ GeV and 1.8 TeV.

10.2 $b\bar{b}$ Correlated Cross Section

The measurement of the integrated $b\bar{b}$ correlated production cross section provides another test of NLO QCD calculations. This determination was an extension of our trimuon analysis presented in the previous chapter.

Monte Carlo Type	Background Estimate (%)
J/ψ	26 ± 7.12
QQ	17 ± 7.35

Table 10.3: Trimuon Background Estimate

Even though we scanned all our trimuon candidates this did not assure these events originated from the decay of the b and $\bar{b}$-quarks. Only cosmic ray events and fake tracks were eliminated. The principal surviving background source for our trimuon events was

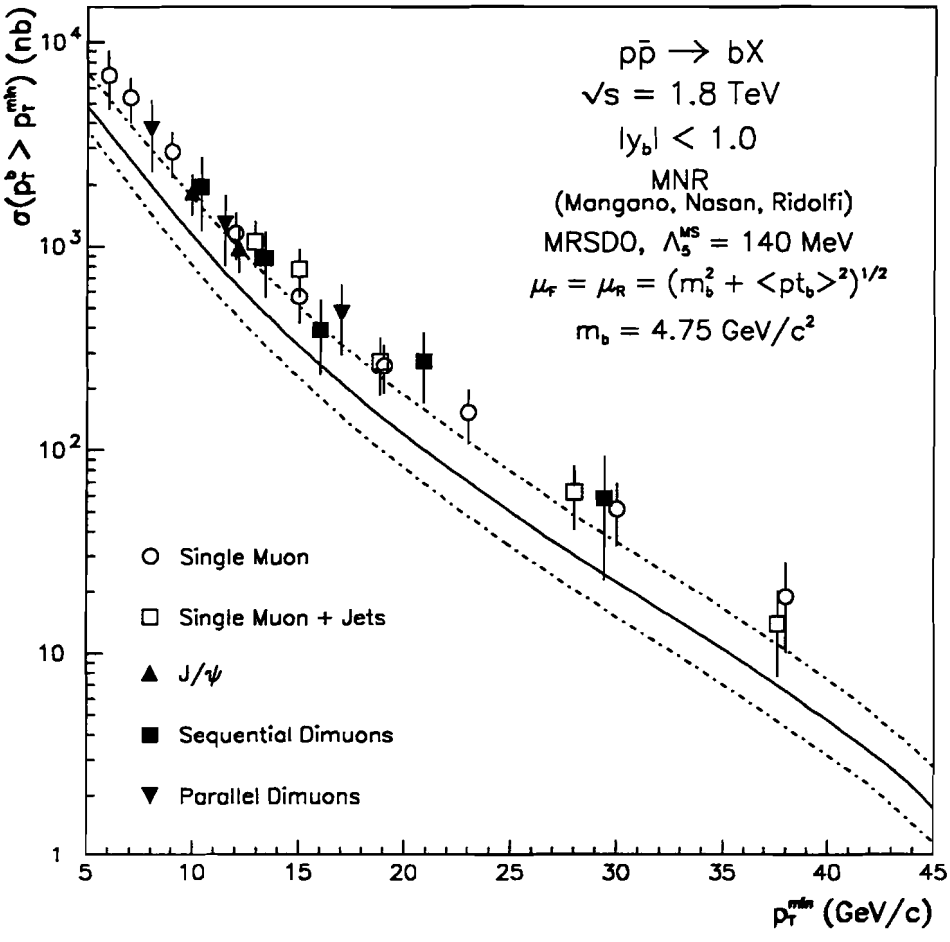

Figure 10.4: DØ Run 1A Inclusive b-Quark Production Cross Section Measurements

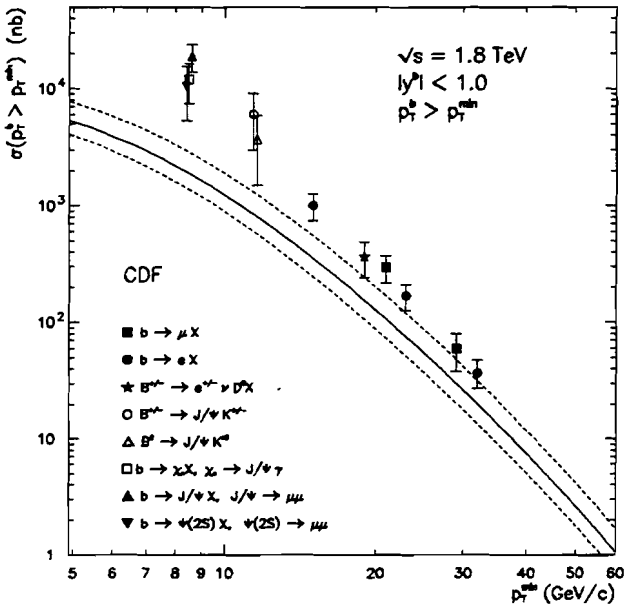

Figure 10.5: CDF Inclusive b-Quark Cross Section Measurements

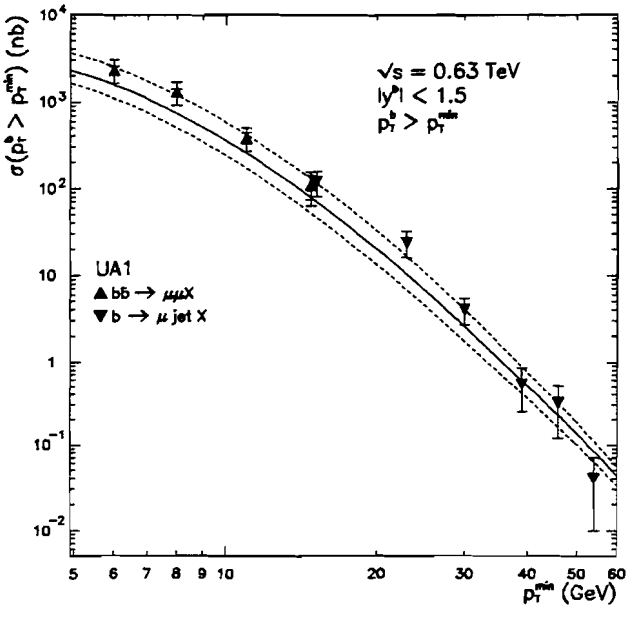

Figure 10.6: UA1 Inclusive b-Quark Cross Section Measurements

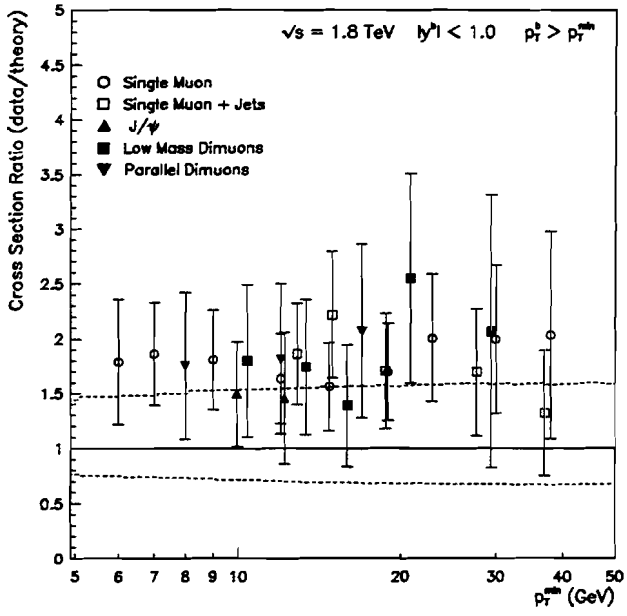

Figure 10.7: Data/Theory Ratio for DØ's b-Quark Production Cross Section Measurements

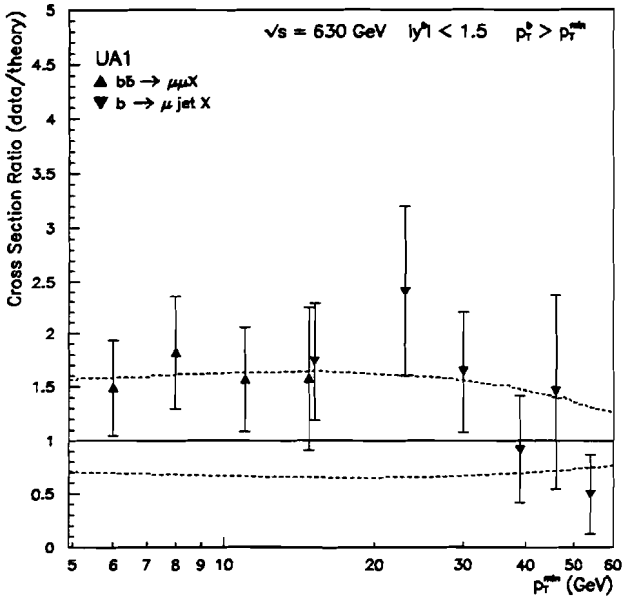

Figure 10.8: Data/Theory Ratio for UA1's b-Quark Production Cross Section Measurements

muons from $\pi^{\pm}/K^{\pm}$ decays. We calculated the background for the previous mentioned contaminant from the b produced J/ψ and $Q\bar{Q}$ Monte Carlo samples (Chapter 5). The analysis of the Monte Carlo events assured the parentage of the muons composing the dimuon, *i.e.* ISAJET muons from b-meson decays were matched to the closest reconstructed track (Section 7.2.2). Then we counted the third muon candidates which had a matching ISAJET track and those that did not. Table 10.3 itemizes the before mentioned Monte Carlo samples and the estimated background contribution for a third muon candidate. We took the average of the expected background for the two Monte Carlo samples and arrived at 6.3 ± 3 trimuon events in $\mathcal{L} = 6.73 \pm 0.36$ pb^{-1}.

To calculate the $b\bar{b}$ cross section we used the expression

$$\sigma\Big(|\eta^{b_1}| < 1;\ |\eta^{b_2}| < 1;\ P_{\rm T}^{b_1} > 10\ {\rm GeV/c};\ P_{\rm T}^{b_2} > 10\ {\rm GeV/c}\Big) = \frac{N^{3\mu}}{2 \cdot {\rm BR} \cdot \epsilon \cdot \mathcal{L}}\ , \qquad (10.3)$$

where ϵ is the product of the acceptance and the overall efficiency for detecting a third muon. The acceptance included:

1. The correction factor needed to account for the rejected dimuon events during ISAJET generation;
2. The correction factor to observe the $b\bar{b}$ system for the exclusion of the muons within the azimuthal fiducial volume of 80–110°.

The overall efficiency is the convolution of the trigger, reconstruction and offline selection efficiencies. We determined the acceptances and efficiencies from the J/ψ and $Q\bar{Q}$ Monte Carlo events. Table 10.4 tallies the breakup of ϵ.

We separated Br $\cdot\ \epsilon$ into

$$\Big[({\rm Br} \cdot \epsilon)_{{\rm J}/\psi}\ +\ ({\rm Br} \cdot \epsilon)_{Q\bar{Q}}\Big]\ ,$$

because the b-branch that decayed semimuonicly does not hadronize any differently if its conjugate partner decayed into a dimuon via a muonic decay of the J/ψ or a sequential

Process	MC Accep (%)	ϕ Accep (%)	Efficiency (%)
J/ψ	14.64 $\pm$ 1.61	81.94 $\pm$ 0.88	0.20 $\pm$ 0.05
$Q\bar{Q}$	3.53 $\pm$ 0.15	81.94 $\pm$ 0.88	0.15 $\pm$ 0.04

Table 10.4: $3^{rd}\mu$ Acceptances and Detection Efficiencies

muonic cascade. Therefore, our measured $b\bar{b}$ correlated cross is

$$\sigma\left(|\eta^{b_1}| < 1;\ |\eta^{b_2}| < 1;\ P_T^{b_1} > 10\ \text{GeV/c};\ P_T^{b_2} > 10\ \text{GeV/c}\right) \ = \ 0.71 \ \pm \ 0.38 \ \mu\text{b} \ .$$

The theoretical range for the correlated cross section for the above stated kinematic requirements is 0.23–0.49 μb. Our measured result is approximately 44% higher than the theoretical predicted upper limit. CDF has measured the $b\bar{b}$ correlated cross section as a function of the P_T for one of the b-quarks [112]. The shape of the measured points compared to the theoretical curve are in agreement, but the normalization is higher for the data by a factor greater than two. Therefore, both experiments indicate that $b\bar{b}$ production is not completely understood.

10.3 Measurement of Alpha Strong

In Section 10.1 we presented our inclusive b-quark production cross section measurement from dimuons originating from low mass b-quark and J/ψ decays, and it was shown that the NDE calculations gave a satisfactory description of the data. Since we demonstrated that these pQCD calculations are valid, in this section we will present our analysis of fitting the measured points, plus all of DØ's inclusive b-quark measurements (Fig. 10.4), to extract the value of $\alpha_s(M_Z)$.

10.3.1 Fitting Procedure

The determination of α_s was as follows:

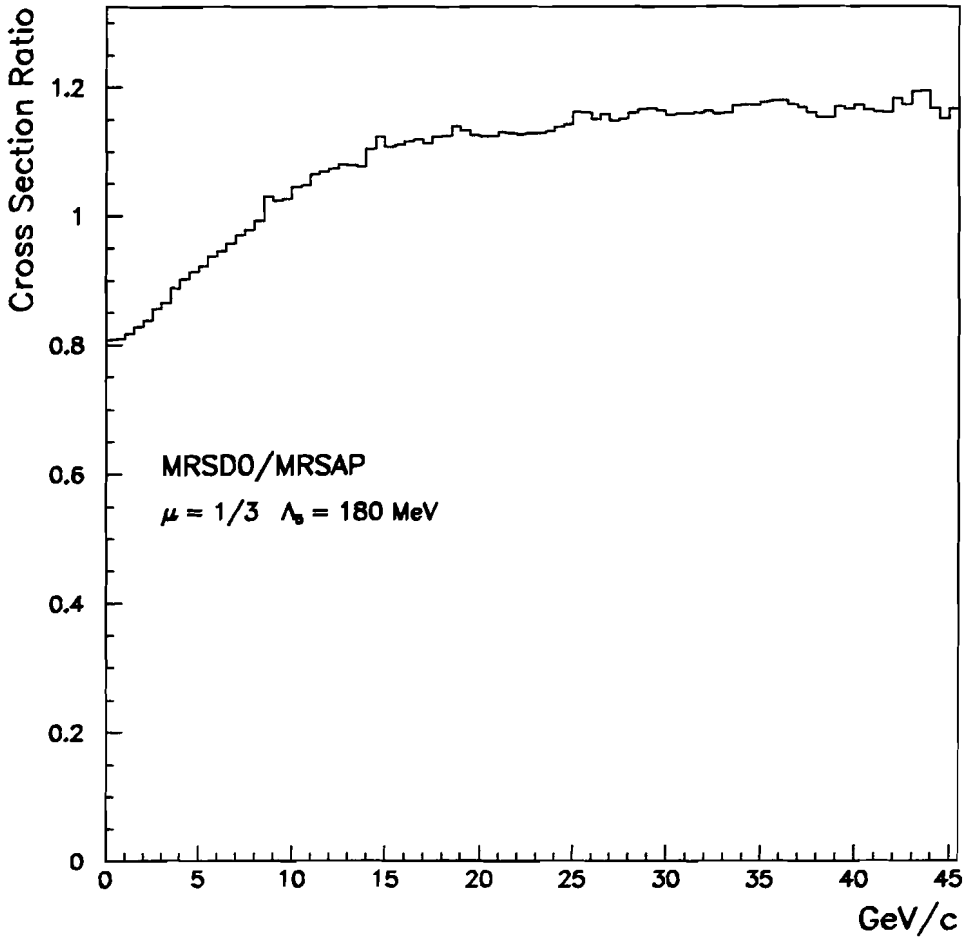

Figure 10.9: Ratio of $\sigma^b(|y| < 1)_{\mathrm{MRSD}\emptyset}/\sigma^b(|y| < 1)_{\mathrm{MRSA'}}$

Channel	P_T^{min} (GeV/c)	$\sigma^b(\|y^b\|<1)$ (nb)	$\delta\sigma_{stat}$ (nb)	$\delta\sigma_{sys}$ (nb)	$\delta\sigma^b_{tot}$ (nb)	$\delta\sigma^b_{corr\,tot}{}^a$ (nb)
Single Muon[b]	6	6884	90	2203	2205	1828
	7	5362	97	1341	1344	941
	9	2895	58	724	726	508
	12	1167	43	292	295	208
	15	567	34	142	146	104
	19	258	21	65	68	49
	23	152	16	41	44	35
	30	51	9	15	17	15
	38	19	6	6	9	8
Single Muon + Jet[c]	13	1060	32	265	267	188
	15	770	39	200	204	150
	19	270	24	81	85	69
	28	62	9	19	21	18
	37	14	3	5	6	6
J/ψ[d]	10	1837	263	523	585	484
	12	988	140	381	406	365
Low Mass Dimuons[d]	10	1954	430	618	753	667
	13	878	151	272	311	268
	16	389	79	132	154	137
	21	272	50	89	102	89
	29	58	22	27	35	33
Parallel Dimuons[e]	8	3749	56	1327	1440	1274
	12	1294	18	455	489	430
	17	471	55	171	180	159

Table 10.5: DØ Run 1A Inclusive b-Quark Production Cross Section Measurements

[a] Removal of the common systematic errors ($\approx$ 18%).
[b] See [114]
[c] See [109]
[d] This thesis
[e] See [115]

1. We performed a χ^2 fit of the measured b-quark cross section data to various theoretical distributions and plotted their respective χ^2 value as a function of Λ_5;
2. We fitted the χ^2 values to obtain its minimum and determined the corresponding $\Lambda_5^{\min}$;
3. From $\Lambda_5^{\min}$, we used Equation 2.14 to calculate $\alpha_s(M_Z)$.

The expected b-quark cross section distributions were obtained from the MNR program. For each μ scale we produced a family of curves for various Λ_5 values. For example, for $\mu = \mu_o/2$ we generated 40 theory curves varying the QCD parameter Λ_5 from 140 to 335 MeV in steps of 5 MeV.

The following relation was used to calculate the χ^2 for each theoretical curve

$$\chi_i^2 = \frac{1}{n}\sum_{j=1}^{n}\left\{\frac{1}{\delta\sigma_j^b}\left[f_i^{\Lambda_5}\left(P_{T_j}^{\min}\right) - \sigma_j^b\right]\right\}^2 . \tag{10.4}$$

$f_i^{\Lambda_5}$ are the parametrized MNR curves for the different Λ_5 values and they are evaluated at every $P_{T_j}^{\min}$ corresponding to its respective inclusive b-quark cross section measurement, σ_j^b ($j = 1 \ldots 24$). We computed the χ_i^2, and then the values were fitted to obtain $\Lambda_5^{\min}$. For our cited case of $\mu = 0.5$, we had forty χ_i^2 points to fit.

10.3.2 $\alpha_s(M_Z)$

We executed the above procedure for $\mu = (\mu_o/4, \mu_o/3, \mu_o/2, \mu_o)$ and for two sets of structure functions, MRSDØ and MRSA$'$. The ratio between the predicted inclusive b-quark production cross sections using the two parton distribution functions is shown in Fig. 10.9 for $\mu = \mu_o/3$ and $\Lambda_5 = 180$ MeV. The range of Λ_5 which we used to generate the theoretical curves for each value of μ for the two PDFs is listed in Table 10.6, while Figs. 10.10 and 10.11 are the χ^2 distributions for the different μ's for each respective PDF. Figures 10.12 and 10.13 are the best fitted MNR curves for the four $\Lambda_5^{\min}$ for the two PDFs.

Having determined $\Lambda_5^{\min}$ we were able to calculate $\alpha_s(M_Z)$ via Equation 2.14. The results are shown in Table 10.7. The uncertainties quoted for each Λ_5^{min} were obtained from the fit, while the uncertainties for the α_s's were obtained by calculating $\alpha_s(M_Z)$ at $(\sigma_j^b \div 1.18)$ and $(\sigma_j^b \times 1.18)$, and taking half of their difference. The factor 1.18 represents the size of the removed common systematic errors, which were

1. Luminosity 5.4%
2. Muon Chamber Efficiency 10%
3. b-quark Fragmentation Parameterization 14% .

As one can readily see the respective $\Lambda_5^{\min}$ and $\alpha_s(M_Z)$ values obtained with the structure functions MRSDØ and MRSA$'$, for each μ scale, are in good agreement. However, the range of $\Lambda_5^{\min}$ is big, a 200% increase from $\mu = \mu_o/4$ to $\mu = \mu_o$. Since Λ_5 is the "fundamental measure" of α_s such a dramatic increase is disturbing. In addition, the $\alpha_s(M_Z)$ measurements for $\mu_o/4, \mu_o/3, \mu_o/2$ are in accord with the world averages for $\alpha_s(M_Z)$ (0.117 ± 0.005) and Λ_5 (195^{+65}_{-50}), whereas for μ scale equal to μ_o is several standard deviations above the world average. Therefore, we can conclude that $\mu = 1$ is not a good subtraction point. Furthermore, for the remaining μ scales our data alone do not allow us to separate the effects of varying μ scale and α_s, Figs. 10.14 and 10.15.

	MRSDØ		MRSA$'$	
μ	Range of Λ_5 (MeV)	Step Size (MeV)	Range of Λ_5 (MeV)	Step Size (MeV)
1/4	95–180	2.5	100–220	5
1/3	120–230	5	130–250	5
1/2	140–335	5	160–405	5
1	250–700	10	300–600	10

Table 10.6: The range and step size of Λ_5 to generate each family of μ for the two PDFs.

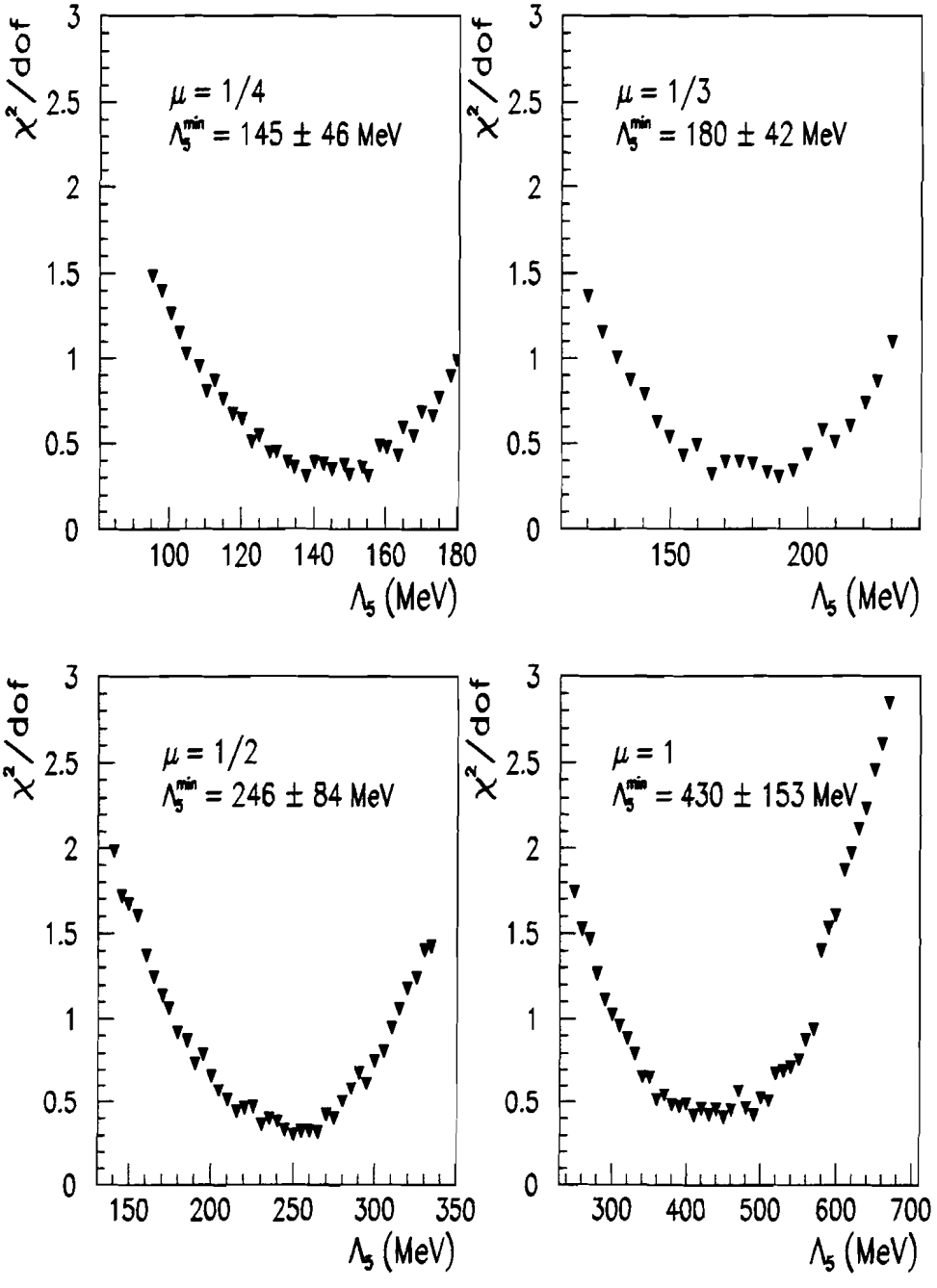

Figure 10.10: χ^2 distributions for the four μ's for the MRSDØ structure function.

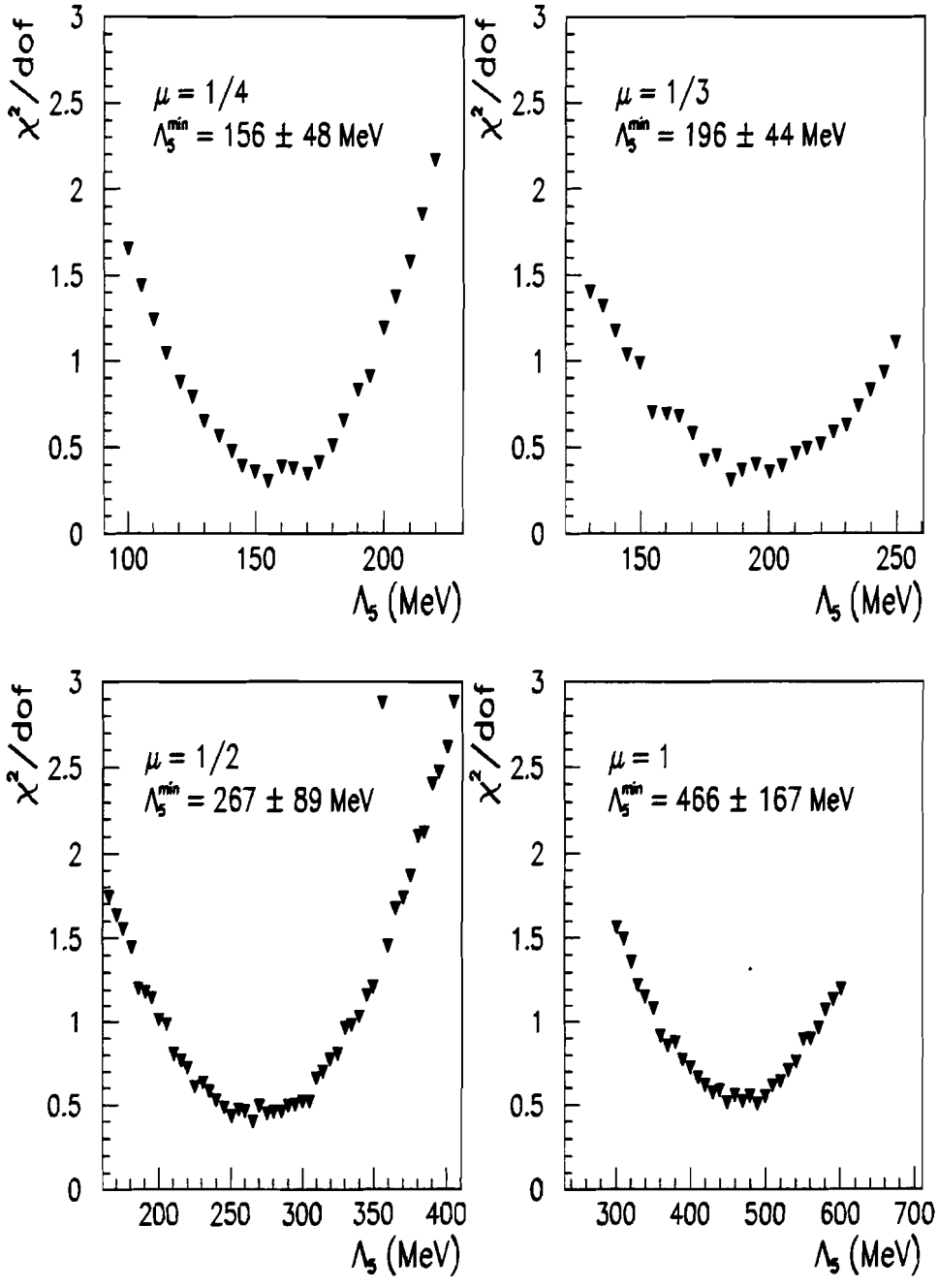

Figure 10.11: χ^2 distributions for the four μ's for the MRSA$'$ structure function.

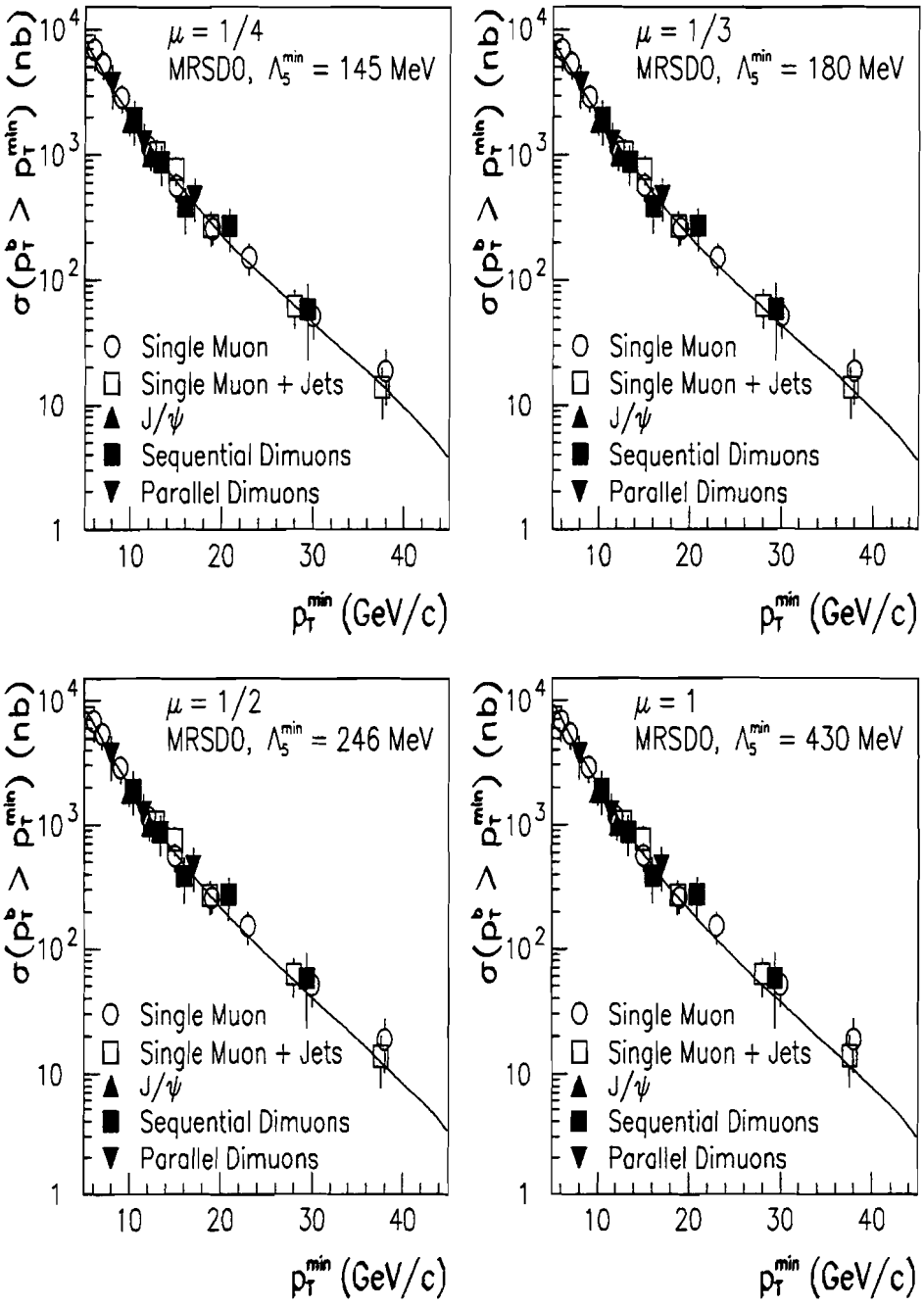

Figure 10.12: Fitted theoretical curves for the four μ's for the MRSDØ structure function.

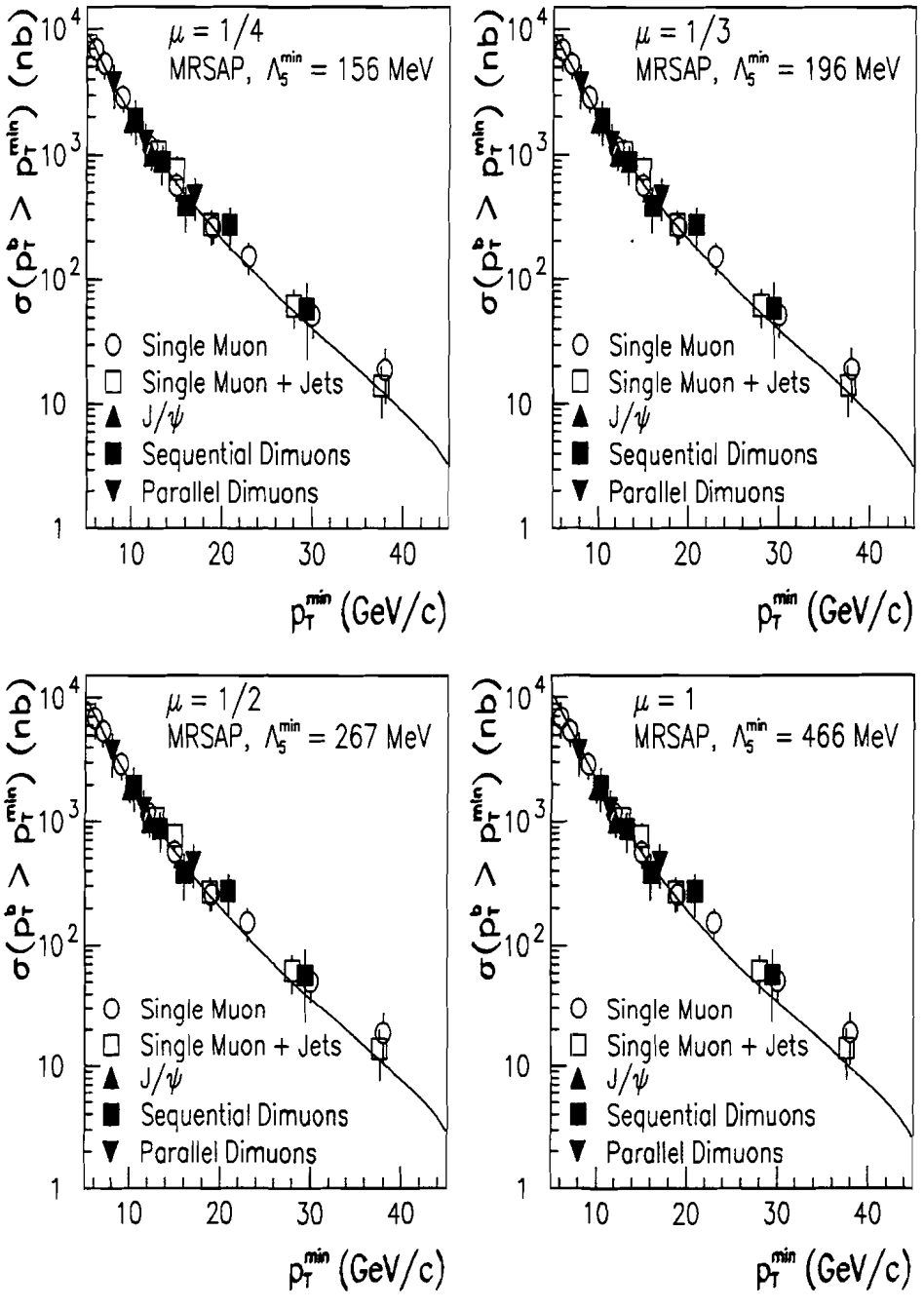

Figure 10.13: Fitted theoretical curves for the four μ's for the MRSA$'$ structure function.

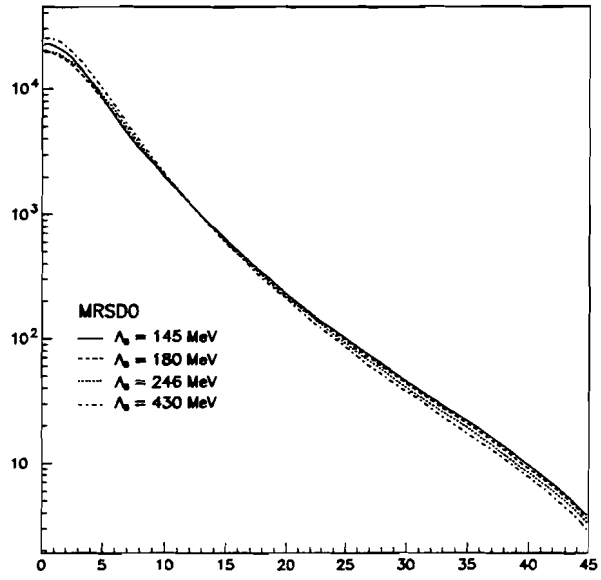

Figure 10.14: Comparison of the fitted theoretical curves for the MRSDØ structure function.

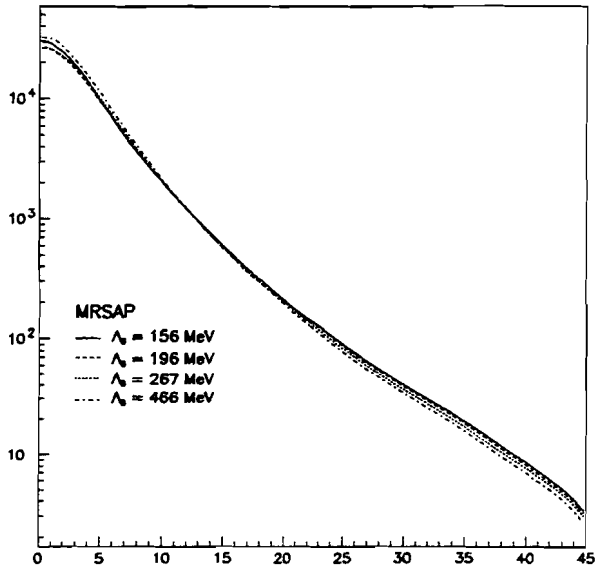

Figure 10.15: Comparison of the fitted theoretical curves for the MRSA$'$ structure function.

	MRSDØ		MRSA′	
μ	$\Lambda_5^{\min}$ (MeV)	$\alpha_s(M_Z)$	$\Lambda_5^{\min}$ (MeV)	$\alpha_s(M_Z)$
1/4	145 ± 46	0.111 ± 0.004	156 ± 48	0.112 ± 0.003
1/3	180 ± 42	0.114 ± 0.004	196 ± 44	0.115 ± 0.004
1/2	246 ± 84	0.119 ± 0.004	267 ± 89	0.121 ± 0.004
1	430 ± 153	0.131 ± 0.005	466 ± 167	0.132 ± 0.006

Table 10.7: Values of α_s for the different μ's for each PDF. Errors listed do not include the uncertainties due to the fit procedure and $\Lambda_5^{\min}$.

10.4 The Running of Alpha Strong

The running of α_s is an important prediction of pQCD. To test this prediction one must have different α_s measurements for various Q. We accomplished this by utilizing DØ's 24 b-quark cross section points (σ_i^b:Table 10.5) and the eight generated families of theory curves. The large P_T range of σ_i^b provides DØ a unique opportunity to perform this analysis.

Our study focused on the use of the leading order formula for the evolution of α_s,

$$\alpha_s(Q) = \frac{\alpha_s(Q_o)}{1 + b\alpha_s(Q_o)\ln(Q^2/Q_o^2)} . \tag{10.5}$$

Instead of fixing b to its QCD value of 0.61[2] and $\alpha_s(Q_o)$ to our determined values in the previous section (or the world average for that matter), we allowed them to be free parameters to be fitted from the data.

The first step was to evaluate α_s at each σ_i^b. Once again we used expression 2.14. For each σ_i^b we determined its respective value of $\Lambda_5^{\min}$ and Q. The value of $\Lambda_5^{\min}$ was obtained by interpellating σ_i^b between the two closest MNR curves, while Q was defined to be

$$Q = 2\sqrt{m_b^2 + \left(P_T^{\min}\right)^2} . \tag{10.6}$$

Having the $\alpha_s(Q)_i$ we performed a two parameter fit to the data. The results of the fit are

[2] $$b = \frac{11N_C - 2N_f}{12\pi} = \frac{(11 \cdot 3) - (2 \cdot 5)}{12\pi} = \frac{23}{12\pi}$$

	MRSDØ		MRSA′	
μ	b	$\alpha_s(Q_0)$	b	$\alpha_s(Q_0)$
1/4	$0.68 \pm 0.06 \pm 0.02$	$0.111 \pm 0.002 \pm 0.003$	$0.48 \pm 0.08 \pm 0.05$	$0.118 \pm 0.002 \pm 0.003$
1/3	$0.60 \pm 0.07 \pm 0.05$	$0.117 \pm 0.002 \pm 0.003$	$0.51 \pm 0.06 \pm 0.10$	$0.121 \pm 0.002 \pm 0.001$
1/2	$0.50 \pm 0.08 \pm 0.08$	$0.126 \pm 0.003 \pm 0.002$	$0.61 \pm 0.07 \pm 0.17$	$0.131 \pm 0.002 \pm 0.001$
1	$0.37 \pm 0.09 \pm 0.14$	$0.145 \pm 0.004 \pm 0.003$	$0.61 \pm 0.02 \pm 0.17$	$0.139 \pm 0.001 \pm 0.002$

Table 10.8: Fitted results of b and $\alpha_s(Q_0)$ for the MRSDØ and MRSA′ PDFs.

tallied in Table 10.8, and are shown in Figs. 10.16 and 10.17. The solid curves are from the resultant fit, whereas the dash-dot curves represents Equation 10.5 with b and $\alpha_s(Q_0)$ taken to be 0.61 and 0.117. As discussed is Section 10.3.2, the systematic errors for the parameters were obtained by separately fitting ($\sigma_i^b \div 1.18$) and ($\sigma_i^b \times 1.18$), and taking half of their difference, while the statistical error was determined from the fit of σ_i^b.

As one can see, we have clearly demonstrated the running nature of α_s. Our fitted values of the parameter b, for the different μ scales, indicate that α_s is inconsistent with being a constant ($b = 0$) by several standard deviations and consistent within one standard deviation with the transverse momentum dependence predicted by NLO QCD. In particular, our best agreement to the world average for $\alpha_s(M_Z)$ and the theoretical prediction of b was for MRSDØ structure function with μ scale equal to $\mu_0/3$: $b = 0.60 \pm 0.09$, $\alpha_s(Q_0) = 0.117 \pm 0.004$.

A similar analysis has been recently published by the UA1 collaboration studying b-quark production in $p\bar{p}$ collisions at $\sqrt{s} = 630$ GeV [21]. Their value for the parameter b is $0.79 \pm 0.16 \pm 19$. The larger uncertainties in the UA1 analysis reflect limited statistics of their sample and also the larger range of μ scales.

The interpretation of both results requires some caution for two reasons:

1. The individual values of α_{s_i} have been calculated from b-quark production cross section which where derived from the muon/dimuon differential production cross

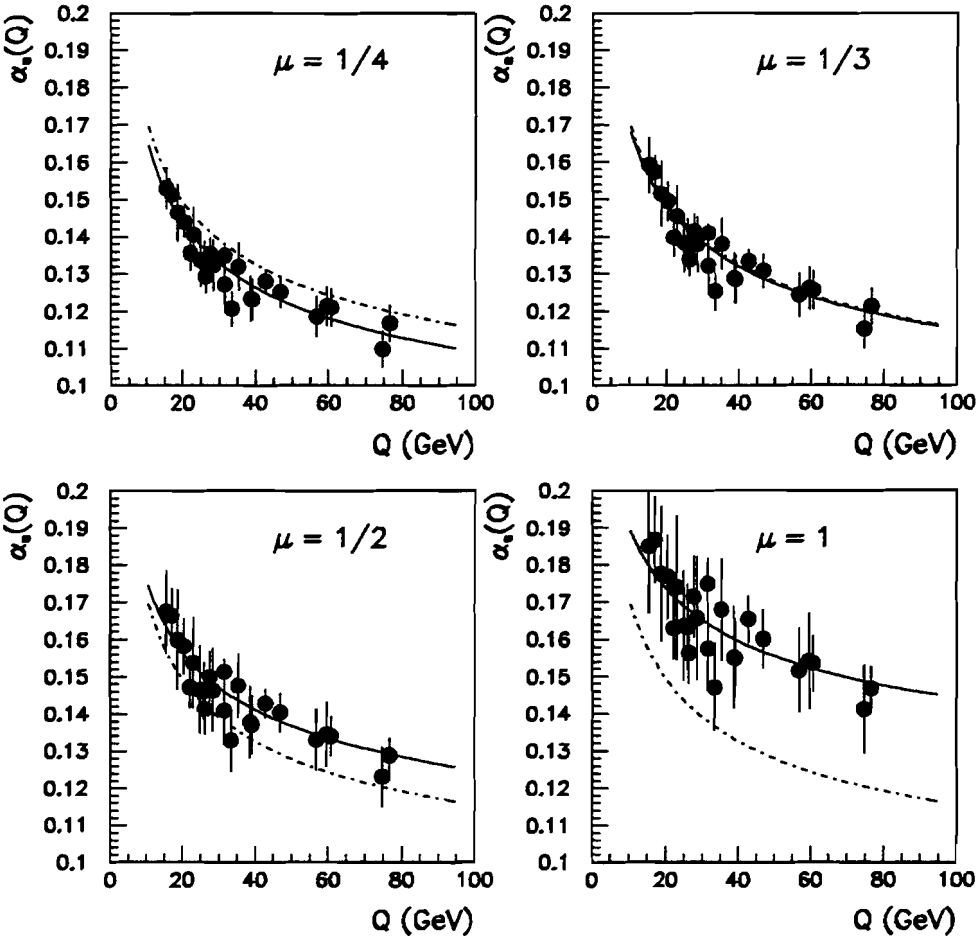

Figure 10.16: The running of α_s with DØ's Run 1A inclusive b-quark production cross section measurements for different μ scales with the MRSDØ structure function. The solid curves were determined from our two parameter fit, while the dash-dot curve corresponds to $b = 0.61$ and $\alpha_s(Q_o) = 0.117$.

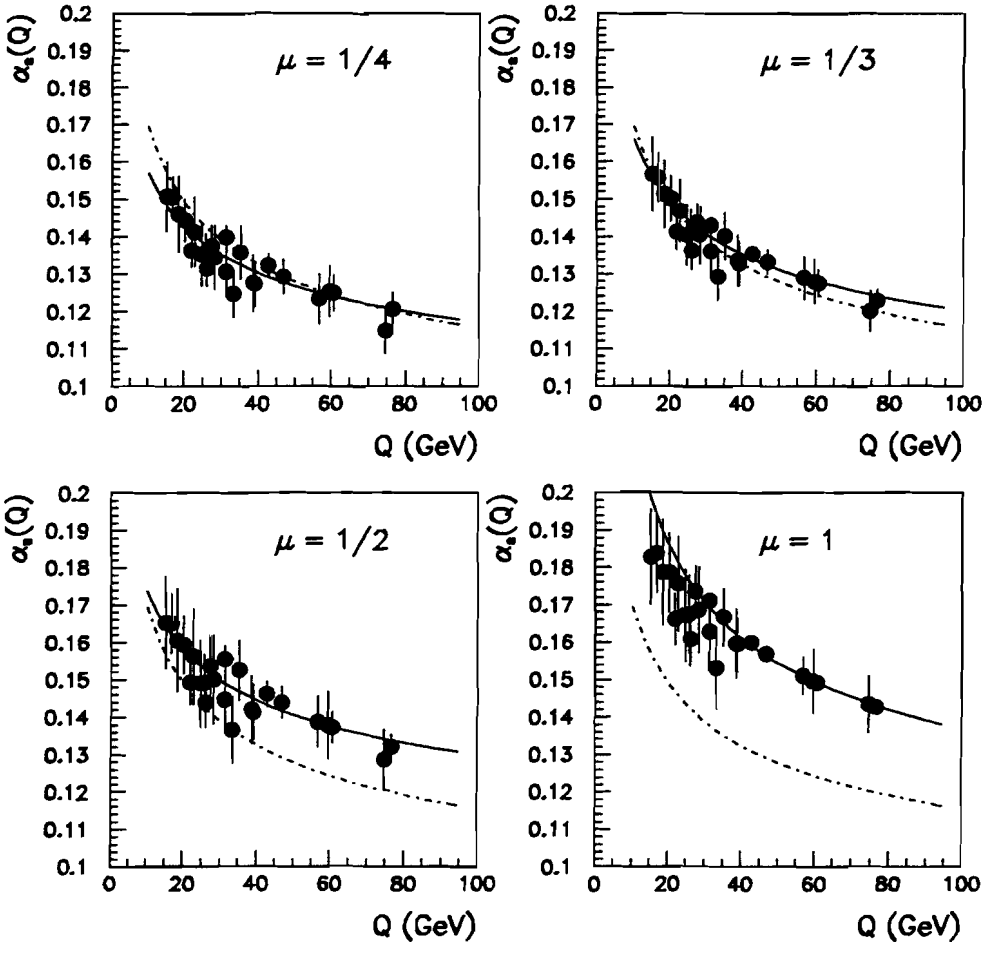

Figure 10.17: The running of α_s with DØ's Run 1A inclusive b-quark production cross section measurements for different μ scales with the MRSA$'$ structure function. The solid curves were determined from our two parameter fit, while the dash-dot curve corresponds to $b = 0.61$ and $\alpha_s(Q_0) = 0.117$.

sections using Monte Carlo events generated with a fixed value of Λ_5;

2. The Q^2 evolution of the used structure functions were done for the nominal value of $\Lambda_5 = 151$ and 152 MeV.

Therefore, our results do imply the internal consistency of the procedure. On the other hand, an absolute determination of the parameter b will require more work. We expect the effects of the structure functions to be minimal. We plan to remove the effects of the muon/dimuon b-quark transformation by directly fitting the muon and dimuon differential production cross sections.

Chapter 11

CONCLUSION

"There are two tragedies in life. One is to lose your heart's desire. The other is to gain it."
George Bernard Shaw

The focus of this thesis was the study of beauty production at $\sqrt{s} = 1.8$ TeV using data collected by the DØ collider detector with the primary goal of using our b-quark production results to test Quantum Chromodynamics (QCD).

During the 1992–93 Tevatron collider run the DØ detector collected 186 hundred thousand events triggered by the presence of two muons. This was the first physics run for the DØ collaboration and a lot of effort was put into understanding the detector. We selected 982 good low mass[1] dimuon events. This sample corresponded to a sensitivity of 6.73 events per picobarn.

We performed a maximum likelihood fit to discern various dimuon production processes, *e.g.* sequential semimuonic decay of b-quarks, J/ψ's from direct charmonium production and weak decay of B-hadrons, Drell-Yan production, *etc.* Using the results from our fit, we were able to measure the differential cross section for low mass dimuon production (Section 9.2) and to independently confirm DØ's published result [31] on the inclusive J/ψ differential cross section (Section 9.3). For the kinematic requirements of $P_T > 6.6$ GeV/c and $|\eta| < 0.8$

[1] The mass range of 0.25–6.25 GeV/c^2.

on the dimuons from low mass and J/ψ decays, the integrated low mass dimuon cross section was determined to be

$$\sigma(p\bar{p} \rightarrow B + X) \cdot \mathrm{Br}(B \rightarrow D\mu\nu) \cdot \mathrm{Br}(D \rightarrow s\mu\nu) = 6.04 \pm 0.70\,(\mathrm{stat}) \pm 2.21\,(\mathrm{sys})\ \mathrm{nb}$$
$$P_{\mathrm{T}}^{\mu\mu} > 7.0\ \mathrm{GeV/c},\ |\eta^{\mu\mu}| < 0.8\ ,$$

whereas the integrated inclusive J/ψ cross section was ascertained to be

$$\sigma(p\bar{p} \rightarrow \mathrm{J}/\psi + X) \cdot \mathrm{Br}(\mathrm{J}/\psi \rightarrow \mu\mu) = 2.46 \pm 0.22\,(\mathrm{stat}) \pm 0.63\,(\mathrm{sys})\ \mathrm{nb}$$
$$P_{\mathrm{T}}^{\mathrm{J}/\psi} > 8.0\ \mathrm{GeV/c},\ |\eta^{\mathrm{J}/\psi}| < 0.8\ .$$

Our next analysis was the inclusive integrated b-quark cross section measurement from our sequential dimuon and J/ψ cross sections (sections 10.1.1 and 10.1.2). This measurement was of great importance since earlier measurements by the CDF collaboration indicted a discrepancy with theory predictions [113]. The DØ collaboration took advantage of its good muon identification of its detector and has measured 24 b-quark cross section values over a wide b-quark transverse momentum range, using five different channels. This thesis described seven of these measurements in two channels. All of DØ's measurements are in good agreement with next-to-leading-order theoretical predictions and are also in agreement with the recalculated CDF measurements.

As a means to study both the b and $\bar{b}$-quarks we quantitatively studied the leading-order and next-to-leading-order contribution in dijet events, where one jet was tagged with a low mass dimuon (Section 9.4). From that study we determined that next-to-leading-order contributed a fraction of 0.43 ± 0.14 to the total of $b\bar{b}$ events.

Another method to identify the $b\bar{b}$ system was the search for an associated third muon in our dimuon events (Section 9.5). Eight trimuon events were found. We examined the azimuthal separation between the dimuon and 3rd muon, and studied what fraction of the b and $\bar{b}$-quark's momentum was carried off by the dimuon and third muon. From the trimuon

events, we determined the $b\bar{b}$ correlated cross section (Section 10.2). Our measured cross section was

$$\sigma\left(|\eta^{b_1}| < 1;\ |\eta^{b_2}| < 1;\ P_{\mathrm{T}}^{b_1} > 10\ \mathrm{GeV/c};\ P_{\mathrm{T}}^{b_2} > 10\ \mathrm{GeV/c}\right) \ = \ 0.71 \ \pm \ 0.38 \ \mu\mathrm{b}\ .$$

In order to test the validity of QCD we used DØ's inclusive b-quark cross section measurements to extract the strong running coupling constant (α_s) (Section 10.3.2) and to demonstrate its running nature (Section 10.4). If not for the recently published UA1 result based on smaller statistics [21], this would be the first attempt to exhibit the running of α_s using data from a single experiment.

By varying the renormalization and factorization scales ($\mu = \mu_{\mathrm{R}} = \mu_{\mathrm{F}} = C\mu_{\mathrm{o}} = C\sqrt{m_b^2 + \langle P_{\mathrm{T}}^b \rangle^2}$), the data were fitted to obtain the best value of the QCD parameter Lambda 5 (Λ_5). Next we used the fitted value Λ_5 to evaluate the strong coupling constant at the mass of the Z vector boson ($\alpha_s(\mathrm{M}_Z)$). The measured values ranged from 0.111–0.119 for values of the μ scales of $\mu_{\mathrm{o}}/4$–$\mu_{\mathrm{o}}/2$, when we used the MRSDØ structure functions (see Table 10.7). Our results agree very well with the world average of 0.117 ± 0.005. However, our data alone do not allow us to separate the effects of the changing μ scale and normalization of α_s.

Using the wide transverse momentum range of our measured b-quarks cross section points we studied the running of α_s. It turned out that the running property of α_s was less sensitive to the choice of the μ scale. Irrespective of the choice of μ values our data indicated that α_s is inconsistent with being a constant by several standard deviations and consistent within one standard deviation with the transverse momentum dependence predicted by NLO QCD. Therefore, a running α_s is a necessity for an accordant description of DØ's inclusive b-quark measurements within the framework of perturbative QCD. Further improvements in this analysis are underway.

Bibliography

[1] A. Rupert Hall and Marie Boas Hall, *A Brief History of Science* (1988).

[2] A.E.E. McKenzie, *The Major Achievements of Science* 2 vol. (1988).

[3] Sir Isaac Newton, *The Sceptical Chymist* (1661).

[4] C. D. Anderson, *Phys. Rev.* **43** (1933) 491.

[5] C. Albajar *et al.*, *Phys. Lett. B* **122** (1983) 103;

C. Albajar *et al.*, *Phys. Lett. B* **122** (1983) 476;

C. Albajar *et al.*, *Phys. Lett. B* **126** (1983) 398;

C. Albajar *et al.*, *Phys. Lett. B* **129** (1983) 130.

[6] P.A.M. Dirac, *Proc. Roy. Soc. Lon.* **A114** (1927) 243.

[7] E. Abers and B. W. Lee, *Phys. Rep. C*, **9** (1973) 1.

[8] C. N. Yang and T. D. Lee, *Phys. Rev.*, **96** (1954) 191.

[9] S. Gashow, *Nucl. Phys.*, **22** (1961) 579;

S. Weinberg, *Phys. Lett.*, **12** (1967) 132;

A. Salam, *Elementary Particle Physics*, N. Svartholm editor, (1968) 367.

[10] P. W. Higgs, *Phys. Lett.*, **12** (1964) 132;

P. W. Higgs, *Phys. Rev. Lett.* **13** (1964) 508.

[11] Michio Kaku, *Quantum Field Theory*, Oxford University Press (1993) 209.

[12] Paul Roman, *Advanced Quantum Theory*, Addison-Wesley (1965).

[13] F. J. Dyson, *Phys. Rev.* **75** (1949) 486;

J. C. Ward, *Phys. Rev.* **78** (1950) 182.

[14] N. N. Bogoliubov and O. Parasiuk, *Act Math.* **97** (1957) 227;

K. Hepp, *Comm. Math. Phys.* **2** (1966) 301;

W. Zimmerman, *Comm. Math. Phys.* **11** (1968) 1;

W. Zimmerman, *Comm. Math. Phys.* **15** (1969) 208.

[15] S. Weinberg, *Phys. Rev.* **118** (1960) 838.

[16] Michio Kaku, *Quantum Field Theory*, Oxford University Press (1993) 235.

[17] G. Altarelli and G. Parisi, *Nucl. Phys. B* **126** (1977) 298.

[18] G. 't Hooft, *Nucl. Phys. B* **33** (1971) 173;

G. 't Hooft, *Nucl. Phys. B* **35** (1971) 167.

[19] D. J. Gross and F. Wilczek, *Phys. Rev. D* **8** (1973) 3497;

H. D. Politzer, *Phys. Rev. Lett.* **26** (1973) 1346.

[20] G. 't Hooft, Conference on Lagrangian Field Theory, Marseille (1972) (unpublished).

[21] C. Albajar *et al.*, *Phys. Lett. B* **369** (1996) 46.

[22] E. Leader and E. Predazzi, *An Introduction to Gauge Theories and Modern Particle Physics* Cambridge University Press (1996) 53.

[23] R. P. Feynman, *Phys. Rev. Lett.* **23** (1969) 1415.

[24] G. Miller, *Phys. Rev. D* **5** (1972) 528.

[25] P. Nason, S. Dawson and R. K. Ellis, *Nucl. Phys. B* **303** (1988) 607.

[26] D. Kuebel, *Calculations of Bottom Quark Production at Hadron Colliders* ANL-HEP-TR-91-111 (1991).

[27] E. Leader and E. Predazzi, *An Introduction to Gauge Theories and Modern Particle Physics* Cambridge University Press (1996) 97.

[28] Michio Kaku, *Quantum Field Theory*, Oxford University Press (1993).

[29] C. Albajar *et al.*, *Phys. Lett. B* **213** (1988) 405;
C. Albajar *et al.*, *Phys. Lett. B* **256** (1991) 121;
C. Albajar *et al.*, *Z. Phys. C bf 61* (1994) 41.

[30] F. Abe *et al.*, *Phys. Rev. Lett.* **71** (1993) 2396;
F. Abe *et al.*, *Phys. Rev. Lett.* **71** (1993) 500;
F. Abe *et al.*, *Phys. Rev. Lett.* **69** (1992) 3704;
F. Abe *et al.*, *Phys. Rev. D* **50** (1993) 2537;
F. Abe *et al.*, *Phys. Rev. Lett.* **68** (1992) 3403;
F. Abe *et al.*, *Phys. Rev. D* **50** (1994) 4254.

[31] S. Abachi *et al.*, *Phys. Rev. Lett.* **74** (1995) 3548;
C. R. Murphy *et al.*, *Phys. Lett. B* **370** (1996) 239.

[32] J. Smith and W. K. Tung, *Proceedings of the Workshop on B Physics at Hadron Accelerators* (1993) 19.

[33] S. Abachi *et al.*, *Nucl. Instr. Meth.* **A338** (1994) 185.

[34] L. M. Lederman, *Scientific American* **264**(3) (Mar. 1991) 48.

[35] H. T. Edwards, *Ann. Rev. Nucl. Part. Sci.* **35** (1985) 605.

[36] FNAL Internal Note, **Design Report Tevatron 1 Project** (Sept. 1984).

[37] FNAL Internal Note, **A Report of the Design of the Fermi National Laboratory Superconducting Accelerator** (May 1979).

[38] William J. Thompson, Ph.D. Thesis, State University of New York at Stony Brook, *Search for the Top Quark in the Muon + Jets Channel at DØ* (1994) 111 (unpublished).

[39] D. Möhl *et al.*, *Phys. Rep.* **C58** (1980) 73.

[40] **Collider Run Sets World Luminosity Records** in *Fermilab Annual Report*, (1992) 9 (unpublished).

[41] R. C. Fernow, *Introduction to Experimental Particle Physics* Cambridge University Press (1986) 234.

[42] F. Sauli, **Principles of Operation of Multiwire Proportional and Drift Chambers** in T. Ferbel, editor, *Experimental Techniques in High Energy Physics* Addison-Wsley (1987) 79.

[43] A. R. Clark *et al.*, *Nucl. Inst. Meth.* **A261** (1987) 420.

[44] A. R. Clark *et al.*, *Nucl. Inst. Meth.* **A279** (1989) 243.

[45] A. R. Clark *et al.*, *Nucl. Inst. Meth.* **A315** (1992) 193.

[46] J. F. Detœuf *et al.*, *Nucl. Inst. Meth.* **A265** (1988) 157.

[47] J. F. Detœuf *et al.*, *Nucl. Inst. Meth.* **A279** (1989) 310.

[48] D. Buchholz *et al.*, *Nucl. Inst. Meth.* **A257** (1987) 556.

[49] R. C. Fernow, *Introduction to Experimental Particle Physics* Cambridge University Press (1986) 259.

[50] C. Fabjan, Calorimetry in High Energy Physics in T. Ferbel, editor, *Experimental Techniques in High Energy Physics* Addison-Wsley (1987) 257.

[51] C. Brown it et al., *Nucl. Inst. Meth.* **A279** (1989) 331.

[52] J. M. Butler it et al., *Nucl. Inst. Meth.* **A290** (1990) 122.

[53] Yu. M. Antipov it et al., *Nucl. Inst. Meth.* **A297** (1990) 121.

[54] G. S. Gao, R. Partridge, *IEEE Trans. Nucl. Sci.* **38** (1991) 286.

[55] M. Fortner *et al.*, *IEEE Trans. Nucl. Sci.* **38** (1991) 480.

[56] M. Abolins *et al.*, *IEEE Trans. Nucl. Sci.* **36** (1989) 384.

[57] M. Abolins, D. Edmunds, P. Laurens, B. Pi, *Nucl. Inst. Meth.* **A289** (1990) 543.

[58] D. Cutts *et al.*, *IEEE Trans. Nucl. Sci.* **36** (1989) 738.

[59] D. Cutts *et al.*, Operation of the DØ Data Acquistion System in *Proceedings of the Conference on Computing in High Energy Physics* Annecy, France (1992) 262.

[60] J. T. Linnemann *et al.*, The DØ Software Trigger in *Proceedings of the Conference on Computing in High Energy Physics* Annecy, France (1992) 199.

[61] CERN, *Zebra*, 1992. CERN Library Number Q100.

[62] T. Behnke, Ph.D. Thesis, State University of New York at Stony Brook, *The Central Drift Chamber for the DØ Experiment* (1989) (unpublished);

T. Pizzuto, Ph.D. Thesis, State University of New York at Stony Brook,
DØ Tracking Chamber Performance Studies (1991) (unpublished);
S. Rajagopalan, Ph.D. Thesis, Northwestern University,
The dE/dx Capabilities of the DØ Tracking System (1992) (unpublished);
J. Bantly, Ph.D. Thesis, Northwestern University,
The DØ Detector Forward Drift Chamber Performance and Physics Capability in the 1990 *FNAL Test Beam Run* (1992) (unpublished).

[63] S. Rajagopalan, Ph.D. Thesis, Northwestern University,
The dE/dx Capabilities of the DØ Tracking System (1992) (unpublished).

[64] D. Chakraborty, Ph.D. Thesis, State University of New York at Stony Brook,
A Search for $t\bar{t} \rightarrow electron + jets$ *Signature in* $p\bar{p}$ *Collisions at* $\sqrt{s} = 1.8$ *TeV with the DØ Detector* (1994) (unpublished).

[65] P. Bhat, "Low Energy Response of the DØ Calorimeter and Jet Energy Measurement", DØNote 1644, 1993 (unpublished).

[66] Gail Hanson *et al.*, *Physical Review Letters* **35** (1975) 1609.

[67] R. Astur, J. Blazey and D. Elvira, "A Study of Standard Jet Cuts and Efficiencies Using DØ Collider Data", DØNote 1763, 1993 (unpublished).

[68] M. Bhattacharjee *et al.*, "Efficiencies of the Standard Jet Cuts", DØNote 2197, 1994 (unpublished).

[69] J. J. Thomson, *London, Dublin and Glasgow Philosophical Magazine and Journal of Science* 5, 44 (1897) 269, 293.

[70] Carl D. Anderson and Seth Neddermeyer, *Physical Review* 50 (1936) 263;
Carl D. Anderson and Seth Neddermeyer, *Physical Review* 51 (1937) 884.

[71] Clyde Cowan, Frederick Reines *et al.*, *Science* 124 (1956) 103.

[72] Letter, W. Pauli to Lise Meitner, Hans Geiger, *et al.*, 4 December 1930;
W. Pauli, *Structure et Propriétés des Noyaux Atomiques*, Rapports et discussions du Septième Conseil de Physique, Institut International de Physique (Paris: Gauthier-Villars, 1934) 324.

[73] B. Anderson, G. Gustafson, G. Ingelman, T. Sjöstrand, *Phys. Rep.* **97** (1983) 31.

[74] R. D. Field, R. P. Feynman, *Nucl. Phys. B* **136** (1978) 1.

[75] G. Marchesini, B. R. Webber, *Nucl. Phys. B* **238** (1984) 1.

[76] B. R. Webber, *Nucl. Phys. B* **238** (1984) 492.

[77] J. D. Bjorken, *Particle Physics - Where Do We Go From Here?*
in *Beam Line*, **22** (1992) 11.

[78] Frank E. Paige, Serban D. Protopopescu, *ISAJET: A Monte Carlo Event Generator for pp and $\bar{p}p$ Reactions*, FERMILAB Computing Division PM0059 (1992).

[79] J. C. Collins, T. D. Gottschalk, *Assessment of Perturbative Monte Carlos for Hadron-Hadron Scattering*, Proceedings of Snowmass (1986) 303.

[80] Torbjörn Sjöstrand, *Phys. Lett. B* **157** (1985) 321.

[81] G. C. Fox, S. Wolfram, *Nucl. Phys. B* **168** (1980) 285.

[82] Torbjörn Sjöstrand, *Journ. Mod. Phys. A* **3** (1988) 751.

[83] G. Altarelli, G. Parisi, *Nucl. Phys. B* **126** (1977) 298.

[84] C. Peterson *et al.*, *Phys. Rev. D* **27** (1983) 105.

[85] V. A. Abramovskii, V. N. Gribov, O. V. Kancheli, *Sov. Journ. Nucl. Phys.* **18** (1974) 308.

[86] R. Brun *et al.*, *GEANT User's Guide*, CERN (1991).

[87] A. I. Mincer *et al.*, *The Noisy Package*, Internal DØ document (1993) (unpublished).

[88] T. Diehl, P. Quintas, *MUSMEAR Package*, Internal DØ document (1994) (unpublished).

[89] E. Braaten, T. C. Yuan, *Phys. Rev. Lett.* **71** (1993) 1673.

[90] B. L. Combridge, **Theoretical Approaches to Charm Hadroproduction**, Moriond Workshop 1982:451.

[91] Particle Data Group, *Phys. Rev. D* **71** (1994) 1173.

[92] Alexander B. Smith, Ph.D. Thesis, University of Arizona, *Measurement of the* Υ *and Drell-Yan Production Cross Section at* $\sqrt{s} = 1.8$ *TeV Using Dimuon* (1995) 151 (unpublished).

[93] M. L. Mangano, memo (unpublished).

[94] M. L. Mangano, P. Nason, G. Ridolfi, *Nucl. Phys. B* **373** (1992) 295.

[95] E. Gallas, "The MTC Package (Muon Tracking in the D0 Calorimeter)", DØNote 2066, 1994 (unpublished).

[96] H. Haggerty and T. Marshall, "Crud Removal from Muon Drift Chamber Wires", DØNote 2556, 1995 (unpublished).

[97] J. Bantly *et al.*, "Improvement to the DØ Luminosity Monitor Constant", DØNote 2544, 1995 (unpublished).

[98] F. James, *MINUIT Minimization Package Reference Manual*,
CERN Program Library Entry D506 (1994).

[99] A. G. Frodesen and O. Skjeggestad, *Probability and Statistics in Particle Physics*,
Universitetsforlaget (1979) 202.

[100] *HBOOK: Statistical Analysis and Histogramming*,
CERN Program Library Entry Y250 (1993).

[101] Physics Analysis Workstation, The Complete Reference,
CERN Program Library Entry Q121 (1993).

[102] Application Visualization System, Advanced Visual Systems Inc.

[103] John Allison, *Comput. Phys. Commun.* 77 (1993) 377.

[104] Carsten Peterson and Thorsteinn Rögnvaldsson, *An Introduction to Artifical Neural Networks*, LU TP 91-23 (1991).

[105] G. D'Agostini, *Nucl. Instr. Meth. A* **362** (1995) 487.

[106] R. Baier, R. Rückl, *Z. Phys. C* **19** (1983) 251;
B. Humpert, *Phys. Lett. B* **184** (1987) 105.

[107] H. Fritzsch, *Phys. Lett. B* **86** (1979) 343;
H. Fritzsch, *Phys. Lett. B* **86** (1979) 164;
E. Glover, *et al.*, *Phys. Lett. B* **185** (1986);
F. Halzen, *et al.*, *Phys. Rev. D* **30** (1984) 700.
P. Nason, S. Dawson, R. K. Ellis, *Nucl. Phys. B* **327** (1989) 49.
P. Nason, S. Dawson, R. K. Ellis, *Nucl. Phys. B* **303** (1988) 607;
R. Rückl, *Weak Decays of Heavy Flavors*, CERN Print (Oct. 1983);

M. Bauer, B. Stech, M. Wirbel, *Z. Phys. C* **34** (1987) 103;

J. Kuhn, S. Nussinov, R. Rückl, *Z. Phys. C* **5** (1980) 117;

J. Ellis, M. Gaillard, D. Nanopoulos, *Nucl. Phys. B* **100** (1975) 313;

M. Wirbel, B. Stech, M. Bauer, *Z. Phys. C* **34** (1987) 103;

M. Wirbel, B. Stech, M. Bauer, *Z. Phys. C* **29** (1985) 637;

G. Bodwin, *et al.*, *Phys. Rev D* **46** (1992) 3703.

[108] C. R. Murphy *et al.*, *Phys. Lett. B* **370** (1996) 239.

[109] Thorsten B. Huehn, Ph.D. Thesis, University of California Riverside,
A Measurement of Bottom Quark Production in $p\bar{p}$-Collision at $\sqrt{s} = 1.8$ TeV (1995)
100 (unpublished). Chapter 10: Beauty Production and Alpha Strong

[110] Particle Data Group, *Particle Physics Booklet* (1994).

[111] F. Abe *et al.*, *Fermilab Conference Preprint* 95/263-E (1995).

[112] F. Abe *et al.*, *Fermilab Conference Preprint* 95/223-E (1995).

[113] F. Abe *et al.*, *Nucl. Inst. Meth.* **A271** (1988) 387.

[114] S. Abachi *et al.*, *Phys. Rev. Lett.* **74** (1995) 3548.

[115] David K. Fein, Ph.D. Thesis, University of Arizona,
Measurement of the $b\bar{b}$ Cross Section and Correlations Using Dimuon Events in $p\bar{p}$ Collisions at $\sqrt{s} = 1.8$ TeV (1996) (unpublished).

Appendix A

Good Run List

54508	54569	54572	54576	54583	54598	54591	54593
54596	54604	54610	54616	54618	54619	54620	54621
54622	54623	54652	54654	54660	54665	54669	54670
54672	54674	54677	54700	54702	54703	54736	54759
54781	54784	54787	54788	54790	54807	54808	54871
54872	54875	54877	54962	54963	54965	54967	54978
54982	54998	54999	55000	55001	55002	55082	55083
55084	55190	55193	55195	55196	55199	55218	55289
55303	55304	55305	55333	55334	55335	55351	55353
55363	55364	55368	55369	55642	55653	55657	55673
55678	55684	55719	55725	55754	55755	55761	55762
55766	55780	55781	55782	55783	55809	55810	55824
55826	55827	55828	55853	55854	55881	55887	55888
55902	55908	55910	55936	55937	55943	56005	56006
56008	56009	56230	56231	56232	56233	56298	56299
56302	56303	56316	56393	56398	56412	56427	56428
56429	56478	56488	56490	56491	56637	56638	56639
56640	56641	56643	56666	56671	56672	56673	56683
56684	56686	56687	56695	56696	56697	56700	56701
56709	56710	56736	56738	56779	56810	56812	56813
56814	56846	56849	56854	56855	56860	56885	56891
56892	56904	56905	56907	56915	56918	56919	56920
56934	56935	58913	58923	58925	58926	58928	58931
58942	58943	58944	58953	58954	58956	58957	58970
58971	59005	59006	59018	59020	59028	59075	59076
59079	59080	59081	59100	59101	59102	59103	59154
59251	59252	59253	59254	59268	59274	59275	59276
59330	59331	59349	59350	59351	59373	59375	59377
59378	59390	59391	59407	59410	59420	59421	59432
59433	59434	59438	59442	59443	56939	56948	57022
57023	57034	57035	57036	57047	57049	57053	57057
57059	57065	57066	57067	57069	57070	57071	57072
57140	57162	57180	57183	57184	57188	57189	57262
57264	57268	57270	57272	57275	57292	57302	57322
57329	57331	57333	57335	57337	57339	57360	57361
57362	57363	57419	57423	57425	57427	57436	57437
57441	57442	57443	57451	57454	57455	57494	57496
57498	57499	57500	57512	57521	57545	57547	57549
57551	57603	57607	57609	57611	57613	57615	57621

57635	57636	58192	58193	58194	58203	58204	58205
58209	58225	58226	58227	58235	58250	58251	58254
58255	58262	58354	58356	58361	58362	58363	58364
58378	58380	58381	58382	58414	58415	58416	58417
58418	58436	58437	58438	58439	58440	58442	58445
58448	58455	58458	58795	58796	58799	58810	58812
58813	58814	58820	58823	58826	58827	58859	58860
58861	58862	58863	58864	58867	58882	58886	58906
58909	58912	58481	58486	58487	58488	58489	58519
58520	58521	58528	58540	58541	58542	58543	58546
58556	58557	58567	58737	58764	58766	58793	58794
57637	57638	57658	57659	57660	57680	57686	57688
57690	57694	57711	57756	57757	57758	57759	57760
57761	57769	57770	57950	57951	57952	57953	58002
58004	58006	58014	58018	58020	58021	58056	58059
58078	58084	58114	58124	58129	58141	58168	58169
58170	58191	60832	60833	60834	60835	60843	60853
60868	60869	60873	60876	60890	60891	60892	60893
60894	60912	60917	60939	60940	60941	60942	60979
61001	61004	61007	61010	61045	61063	61064	61139
61142	61143	61144	61149	61152	61155	61183	61197
61198	61208	61252	61256	61257	61259	61272	61273
61274	61275	61276	61297	61299	61300	61301	61304
61305	61344	61345	61346	61347	61351	61354	61380
61387	61388	61389	61391	61392	61396	61398	61399
61400	61401	61404	61405	61464	61468	61470	61471
61473	61474	61476	61477	61478	61514	61515	61528
61535	61539	61552	61554	61555	61585	61599	61600
61602	61606	61608	61618	61619	61620	61621	61622
61624	61646	61648	61650	61657	61661	61663	61668
61670	61684	61685	61704	61705	61706	61707	61708
61712	61819	61820	61821	61822	61823	61969	61996
61999	62001	62037	62039	62158	62159	62160	62161
62174	62175	62176	62197	62199	62293	62294	62302
62303	62307	62326	62328	62329	62331	62332	62333
62345	62348	62352	62401	62408	62410	62412	62414
62416	62418	62423	62429	62431	62433	62435	62437
62443	62446	62448	62450	62472	62473	62476	62478
62480	62482	62484	62508	62509	62510	62511	62512
62514	62517	62519	62520	62529	62530	62531	62532
62533	62534	62535	62536	62540	62548	62553	62556
62560	62562	62564	62569	62571	62630	62638	62639
62641	62643	62645	62647	62649	62651	62654	62655
62656	62657	62757	62758	62759	62792	62793	62794
62795	62838	62953	62963	62965	62966	62993	62995
62996	62997	63026	63027	63028	63057	63066	63068
63069	63070	63071	63072	63092	63093	63094	63095
63096	63097	63098	63113	63114	63115	63120	63121
63122	63123	63145	63147	63149	63151	63152	63153
63183	63185	63187	63188	63241	63243	63245	63247
63248	63250	63284	63285	63286	63287	63288	63375
63376	63400	63402	63456	63461	63464	63465	63485
63488	63490	63498	63499	63522	63531	63533	63535
63539	63542	63543	63544	63545	63621	63624	63625
63626	63627	63628	63629	63630	63631	63636	63718

63720	63723	63725	63727	63729	63730	63733	63734
63735	63737	63740	63742	63793	63794	63795	63796
63797	63798	63799	63800	63803	63822	63823	63824
63825	63826	63827	63830	63851	63853	63854	63855
63860	63861	63866	64086	64087	64090	64094	64096
64102	64103	64104	64105	64203	64220	64224	64250
64252	64253	64254	64255	64275	64276	64277	64278
64425	64426	64462	64463	64464	64466	64583	64584
64585	64606	64608	64610	64612	64679	64764	64777
64786	64796	64818	64834	64879	64881	64883	64896
64897	65099	65122	65123	65124	65125	65130	65131
65279	65285	65288	65358	65360	65365	65374	65377
65422	65423	65424	65425	65426	65427	65428	65429

APPENDIX A. GOOD RUN LIST

Appendix B

1995–1996 FERMILAB INDOOR SOCCER CHAMPIONS
PRERNA

PRERNA'S CHAMPIONSHIP ROSTER

Ian Adam	Gene Álvarez
Erfan Amidi	Linden Carmichael
Brajesh Choudhary	Eric Flattum
Rich Genik	Azriel Goldschmidt
José Luis González	Chang Lyong Kim
Bob Madden	Pat Mooney
Tetsuya Onogi	Danilo Pušeljić
Jamal Tarazi	Erich Varnes
Armand Zylberstejn	

PRERNA'S CHAMPIONSHIP SEASON

1995–1996 Indoor Record: 16 Wins 3 Losses 1 Tie (33 points)
266 Scored Goals 163 Allowed Goals (+103)

ROUND 1			ROUND 2		
Oct. 18	Prerna 17	Dynamo 3	Dec. 1	Prerna 19	Dynamo 4
Oct. 27	Prerna 10	Tigers 4[a]	Dec. 6	Prerna 12	Fermions 4
Nov. 1	Prerna 14	Fermions 7[b]	Dec. 15	Prerna 8	CDF 9
Nov. 8	Prerna 17	CDF 9	Jan. 10	Prerna 6	Chakra 13
Nov. 15	Prerna 19	Chakra 7	Jan. 19	Prerna 8	Tigers 14[c]
ROUND 3			**ROUND 4**		
Feb. 7	Prerna 16	Fermions 14	Mar. 22	Prerna 11	Tigers 5
Feb. 16	Prerna 10	Tigers 9[d]	Mar. 27	Prerna 18	Fermions 13
Feb. 21	Prerna 12	Dynamo 8	Apr. 5	Prerna 14	Dynamo 7
Feb. 28	Prerna 20	Chakra 11	Apr. 10	Prerna 0	Chakra 0[e]
Mar. 6	Prerna 18	CDF 12	Apr. 26	Prerna 17	CDF 10

[a]Played on 9 March 1996.
[b]Played on 31 January 1996.
[c]Played on 13 March 1996.
[d]Played on 1 May 1996.
[e]Tie was agreed by the captains.